Theoretical Analysis of Some Thin-Film Flows Over Complex Surfaces

This thesis is submitted to the University of Strathclyde for the
degree of Doctor of Philosophy in the Faculty of Science by

Abdulwahed Saleh Ali Alshaikhi
Department of Mathematics and Statistics
University of Strathclyde
Glasgow, UK

February 20, 2022

This thesis is the result of the author's original research. It has been composed by the author and has not been previously submitted for examination which has led to the award of a degree.

Signed:
Date:

Acknowledgements

I will first thank Almighty Allah, the compassionate, the almighty and merciful, who kindly supported me with courage and strength in completing my thesis.

It would have been impossible to write this thesis without the help and support of the kindest people around me, though it is only possible to acknowledge a few of them by name here.

I am grateful for the strong support from my family; in particular, my parents, brothers and sisters for all they have done for me, and my wife and my two children, who have been my fountain of strength.

For the success of this thesis, I am indebted to my supervisors, Prof. Stephen K. Wilson and Dr Michael Grinfeld, who gave me extensive support and assistance. I would like to thank both of them for the opportunity to study fluid mechanics and for introducing me to the field of thin film flow. I would also like to convey my heartfelt gratitude and sincere appreciation for guiding me through the completion of this thesis, with their invaluable advice, supervision, encouragement, and the benefit of their invaluable knowledge. I have no words that can adequately express my thanks for their outstanding work and immense patience while assisting in my progress. Beyond their direct help with this thesis, I am grateful for all the opportunities my supervisors provided me with allowing me to contribute to conferences and to benefit fully from academic life.

I would also like to express my utmost gratitude and give great thanks to my additional unofficial supervisor, Dr Brian R. Duffy, for all of his help during the completion of the work in Chapters 2 and 3. I am very grateful for his efforts, kindness and concrete aid.

I also take the opportunity to thank the Ministry of Education, Kingdom of Saudi Arabia and King Abdulaziz University for financial support for this thesis.

Abstract

In this thesis, three different aspects of thin-film flow over complex surfaces are investigated. First, locally-unidirectional rivulet flow on a slippery surface is considered. We study rivulets with prescribed flux and either fixed semi-width or fixed contact angle. In both cases we determined the effect of varying the slip length on the rivulet. We found that in the limit of strong slip, for a rivulet of a perfectly wetting fluid and a rivulet with constant width, the velocity becomes large and plug-like, and the rivulet becomes shallow, while for a rivulet with positive constant contact angle, the velocity becomes large and plug-like, and the rivulet becomes narrow and shallow. Second, rivulet flow over and through a permeable membrane is considered. We study rivulets with prescribed flux and either fixed semi-width or fixed contact angle. We found that whereas there is a physically realisable pendant rivulet solution only if the semi-width does not exceed a critical value, there are physically realisable sessile and vertical rivulet solutions for all values of the semi-width; moreover, a sessile rivulet with fixed semi-width has a finite maximum possible length which is attained in the limit of a wide rivulet. Lastly, patterns formed in a two-dimensional thin film with a Derjaguin-type disjoining pressure on a planar substrate with periodic wettability stripes is considered. Using Liapunov–Schmidt reduction, we study the local bifurcation structure of the problem for spatially homogeneous disjoining pressure and how the structure depends on the average film thickness. Using methods of local bifurcation theory and the continuation software package AUTO, we perform a continuation analysis of the steady state solutions and establish the existence of both nucleation and metastable regimes. The dependence of the steady state solutions on the wettability contrast are investigated for two forms of spatially non-homogeneous disjoining pressure.

Contents

Chapter 1

Introduction

In this thesis we will consider three different aspect of thin-film flow over complex surfaces. In Chapter 2 and 3 we will consider rivulet flow over a slippery substrate and over and through a permeable membrane, respectively, while in Chapter 4 we will consider aspects of two-dimensional thin-film flow over homogeneous and non-homogeneous substrates. In this introductory chapter we will introduce the key concepts of thin-film flow, rivulet flow, flow in porous media, and thin-film flow on complex surfaces required as a basis for the new results presented in the remainder of the thesis.

1.1 Thin-Film Flow

The deposition and flow of thin fluid films on homogeneous, heterogeneous, and porous substrates is ubiquitous in nature, and their characteristic lengths vary over a wide range, from nanometres to kilometres. A "thin film" in this context refers to a film that has a significantly smaller depth than width. This definition is important as it includes geophysical phenomena that are "thin" but not "small". Thin films are found in numerous industrial processes, and in many biological and geophysical contexts. Industrial contexts that involve thin fluid films include processes such as painting, printing, and coating. For example, Figure 1.1 depicts a fruit coated with a solidified film, which reduces cellular respiration and enhances fruit quality. As well as being of fundamental scientific interest in their own right, understanding of thin-film flows is

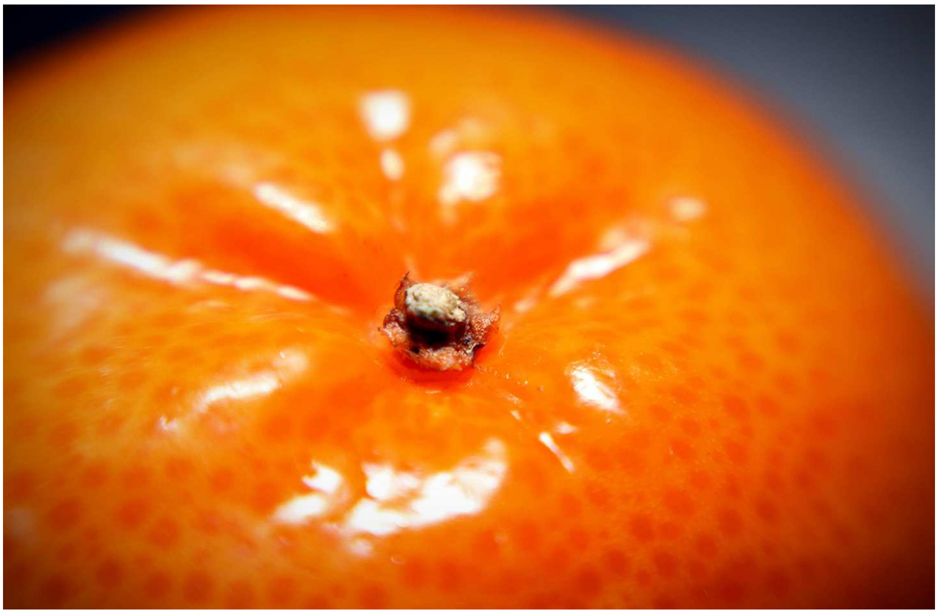

Figure 1.1: A fruit coated with a solidified film to reduce cellular respiration and enhance the fruit quality [110]. (Reproduced with permission.)

necessary for the control and safety of industrial processes.

We will now describe an important class of industrial processes involving thin-film flows. Coating is the industrial process of forming a fluid layer on a solid substrate. In such process, the solid substrate is completely or partially covered by layers of possibly different materials. Industrial coating is performed using a variety of methods and processes, including chemical vapor deposition (CVD), physical vapor deposition (PVD), and dip coating. CVD involves the exposure of a substrate to one or more materials which react chemically and create a deposition layer on the surface of the substrate to produce the desired coating [36]. Electron beam deposition is a form of PVD in which a target material is bombarded with an electron beam from a charged tungsten filament to evaporate and convert it to a gaseous state; this is followed by deposition of the evaporated material on the substrate surface to be coated. Dip coating involves depositing a layer of the material on a solid substrate by pulling the solid substrate out of a liquid reservoir [116]. Figure 1.2 shows an image of gloves removed from a tank during the dip coating process [1].

Another example of a thin-film flow can be found in many industrial applications

Figure 1.2: Image showing gloves removed from a tank during the dip coating process [1]. (Reproduced with permission.)

which involve the lubrication of moving solid machine parts. Lubrication is a process by which a thin layer of oil or another lubricating fluid is used to reduce the friction that would otherwise occur if moving parts came into contact. This is used in mechanical devices such as pistons and turbines [114].

With regard to biological processes, thin fluid films can appear in human beings in the form of sebum fluid that lubricates the surface of the skin, as mucus that protects and lubricates epithelium tissues such as in the stomach and intestines, as synovial fluid that lubricates joints, as tears that lubricate the eyes, and as plasma that lubricates the red blood cells in capillaries.

1.2 Thin-Film Flow Over Complex Surfaces

While much of the previous theoretical and experimental work on thin-film flow has, for obvious reasons, involved ideal (*i.e.* solid, impermeable and homogeneous) substrates, many of the substrates which occur in practice are complex (*i.e.* not ideal). Specifically, some substrates are porous while many others are non-homogeneous. It is the need for a better understanding of such situations that motivates the study of the problems analysed in the present thesis.

A porous medium is a material containing pores (small holes or voids), and such material can be characterized by properties such as permeability and porosity. Flows through porous media occur in a wide range of applications. Inkjet printing onto paper and textiles is an example of fluid spreading on a porous substrate. Another example is screen printing, in which a fluid is transferred onto a substrate such as a fabric or paper, using a permeable screen; the fluid transfers only to the areas the screen permits [117]. For example, in one application, graphene ink is pushed through a mesh screen to fabricate highly conductive graphene patterns on a substrate beneath the screen [43]. Water harvesting is another example that involves flow through a porous medium. In this method, storm water penetrates a porous asphalt surface, then enters a stone reservoir beneath, thereby reducing the water runoff. The water then infiltrates into the underlying soil, which results in improved water quality and restoration of groundwater supplies [32]. Flow in porous media is discussed further in Section 1.6.

Thin-film flows on chemically patterned substrates have been studied extensively with a view to control and direct fluid behaviour on a substrate. In this context, it is important to consider the role of surface heterogeneities and the wetting properties of the fluid in determining the behaviour of the film. Substrates with chemical patterning have many practical applications; notably, they are used in the construction of microfluidic devices and soft materials with a particular pattern (see, for example, Aimé and Ondarcuhu [78], Brasjen and Darhuber [16], Quake and Scherer [87] and Sehgal et al. [97]). One example of such applications is in the use of hydrophobic strip width to control microbubble size. Microbubbles are microscopic bubbles with a mean diameter of microns. They play a fundamental role in different applied fields. For example, in medicine they can be used to deliver drugs to a specific part of the body. Herrada et al. [44] proposed a technique to produce microbubbles of controlled sizes in a T-junction geometry. In this technique, a gaseous stream is injected into a channel transporting a liquid current with a hydrophobic strip printed on one of the channel surfaces. A rivulet is formed over that strip, and when the rivulet breaks up, a collection of microbubbles

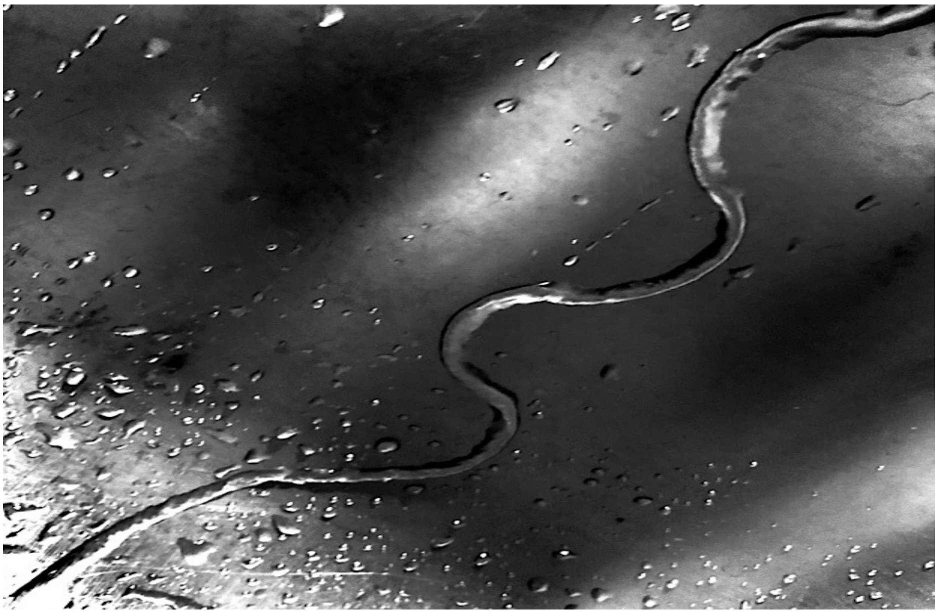

Figure 1.3: Water rivulet in a kitchen sink. Picture courtesy of Truog [111]. (Reproduced with permission.)

much smaller than the channel size is formed. Thin-film flow on non-homogeneous substrates will be discussed further in Section 1.7.

Before discussing flow in porous media in Section 1.6 and thin-film flow on non-homogeneous substrates in Section 1.7, we first review previous work on rivulet flow in Sections 1.3 and 1.4, and on the slip boundary condition in Section 1.5.

1.3 Rivulet Flow

A rivulet flow is a long, slender stream of fluid that flows predominantly in the direction of the longer length scale. The flowing and spreading of rivulets of fluid on a variety of substrates is an everyday occurrence in a wide range of situations, such as rivulets of water on a car windscreen, and in a kitchen sink (for example, Figure 1.3 shows a water rivulet meandering from a saturated sponge under a dripping tap in a kitchen sink). Some common examples of large but thin streams found in geophysical and environmental settings are the flow of a river, spreading flows of lava, and flows of mud (for example, Figure 1.4 shows a rivulet flow of lava in an open channel with overflows

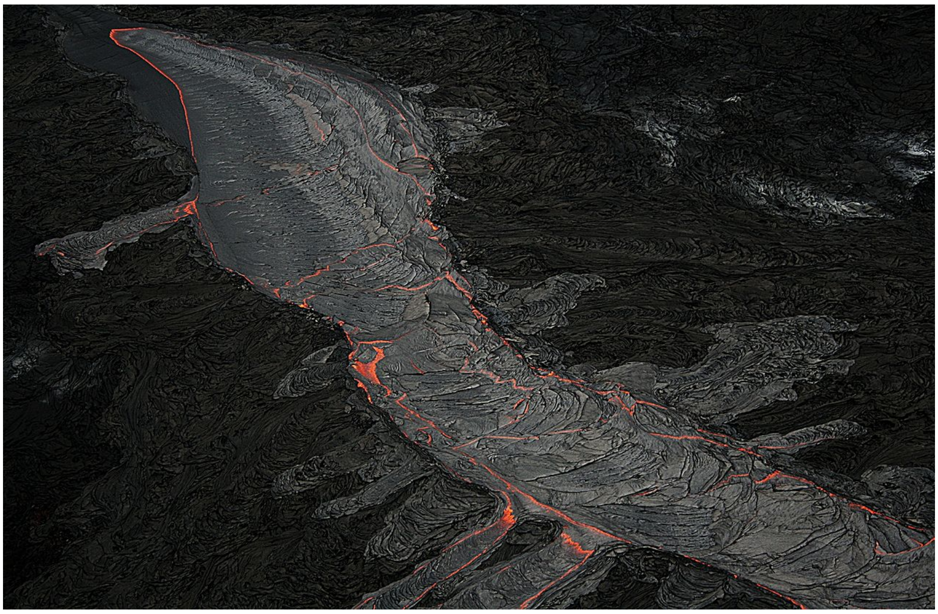

Figure 1.4: Rivulet flow of lava [49]. (Reproduced with permission.)

at both sides). Motivated by such flows, several authors have studied various aspects of rivulet flow. For example, Coussot et al. [24] and Wilson and Burgess [118] investigated flows of mud, and Griffiths [40] investigated flows of lava.

In Chapters 2 and 3 we will consider locally-unidirectional rivulet flow on a slippery substrate and over and through a porous membrane, respectively. Hence, in the following subsections, we discuss previous work concerning rivulet flow.

1.3.1 Review of previous literature on rivulet flow

The topic of gravity-driven rivulet flow down impermeable surfaces has been the subject of much theoretical and experimental work. Early work on this problem was undertaken by Towell and Rothfeld [108], who analysed theoretically and experimentally the steady, unidirectional flow of a uniform rivulet of Newtonian fluid as it flows down an inclined substrate. Towell and Rothfeld [108] derived the ordinary differential equation that describes the shape of the free surface, depending only on the surface tension of the fluid and on gravity, and obtained expressions for the shape of the free surface and the velocity profile within the rivulet. Their experimental measurements of rivulet flow of three different liquids, namely water, glycerol-water mixtures and n-dodecane, on an inclined glass substrate, support their theoretical predictions. For the same problem, Allen and Biggin [3] obtained the leading and first-order asymptotic solutions in the limit of a thin rivulet, and compared their asymptotic predictions with numerical solutions to the full problem.

Bentwich et al. [11] extended the method employed by Allen and Biggin [3] to obtain an analytical solution for the velocity distribution of unidirectional rivulet flow down a vertical substrate for large contact angles. They also obtained a polynomial approximation for the velocity distribution for the case of an inclined substrate, and found that, up to a contact angle of 140°, only the first four terms of the polynomial approximation can produce adequate velocity profiles.

Duffy and Moffatt [31] investigated the locally-unidirectional flow of a thin rivulet with a prescribed non-zero contact angle $\beta > 0$ and used this solution to analyse rivulet flow in the azimuthal direction with prescribed volume flux round a large horizontal cylinder. Their work demonstrates that the rivulet is wide, with finite thickness near the top of the cylinder, but it is narrow and deep near the bottom. This work will be reviewed in detail in Section 1.4.1. Subsequently, Wilson and Duffy [119] extended Duffy and Moffatt's [31] work to include the effect of substrate variation transverse to the direction of flow. Their study demonstrates that a rivulet can only run continuously from the top to the bottom of a large horizontal cylinder if the transverse profile of the substrate is a sufficiently shallow trough. Near the bottom of the cylinder, a rivulet is not possible if the profile is a deeper trough; near the top of the cylinder, a rivulet is not possible if the profile is a ridge.

Wilson and Duffy [120] described the flow of a thin rivulet with zero contact angle (*i.e.* a rivulet of a perfectly wetting fluid) in the azimuthal direction with prescribed volume flux over a large horizontal cylinder. This research reveals that no such rivulet is possible on the upper half of the cylinder. However, it also shows that there are infinitely many solutions corresponding to arrays of rivulets on the lower half of the cylinder, each of which is a suitably rescaled copy of the single-rivulet solution.

Perazzo and Gratton [85] considered unidirectional flow of a rivulet with constant width and derived exact solutions to the Navier–Stokes equations that describe the steady flow of a sessile rivulet down an inclined substrate. In particular, they compared the solutions for the cross section of the rivulet obtained by solving the full Navier–Stokes equations with the results of the lubrication approximation, and found that the global properties of the rivulet, such as the area of the cross section and the volume flux, are predicted quite accurately by the lubrication approximation.

Tanasijczuk et al. [104] built on the work of Perazzo and Gratton [85] to obtain exact solutions for both sessile and pendant rivulets for any profile of the substrate (transversally to the direction of flow).

Paterson et al. [83] studied the locally unidirectional flow of a thin rivulet with a prescribed width (*i.e.* with pinned contact lines) over a large horizontal cylinder. This work will be reviewed in detail in Subsection 1.4.2.

1.3.2 Experiments on and numerical simulations of rivulet flow

Much experimental and numerical simulation work on the flow of rivulets has been done by many authors. Zhang et al. [126] experimentally investigated the flow of fluid draining in a falling film microreactor. This microreactor is a reactor device consisting of a solid flat surface or a surface containing microchannels and used for numerous gas-liquid reactions. They observed three flow regimes; namely, corner rivulet flow, falling film flow with dry patches, and complete falling film flow.

Howell et al. [47] studied, both theoretically and experimentally, the flow of a thin rivulet draining down a flexible beam which is fixed at one end, as shown in Figure 1.5. They showed that the weight of the rivulet will increase the deflection of the beam and, as a result, enhance the spreading rate of the rivulet.

Three-dimensional numerical simulations of a fluid down an inclined substrate were conducted by Singh et al. [100] to calculate the interfacial area of rivulets under the variation of liquid properties, flow rates, substrate inclination angle, and contact angle. In particular, they found that the interfacial area for the rivulet flow decreases with increasing contact angle, whereas the height of the rivulet increases. They studied the impact of the flow rate, characterized by the Weber number, which is the ratio of

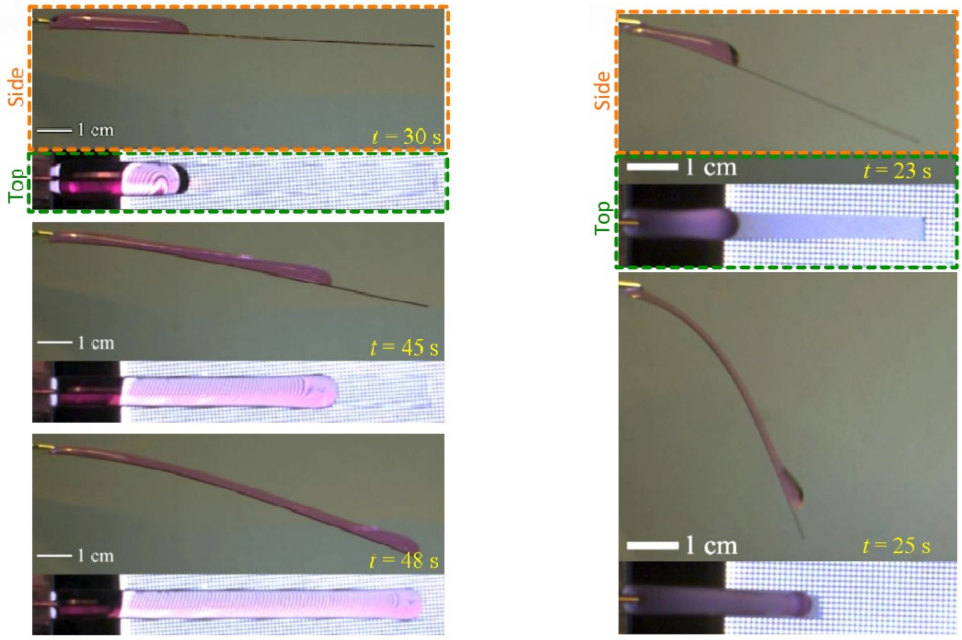

(a) Small beam deflection (b) Large beam deflection

Figure 1.5: Side and top images of the flow of a thin rivulet draining down a flexible beam, obtained by Howell et al. [47]. These images shows how the beam deformation over time and display two particular regimes, namely (a) small deflection and (b) large deflection. Reprinted from Howell et al. [47] with permission from Cambridge University Press.

inertia force and surface tension force, on the wetted area. In particular, at very low Weber numbers (< 0.05), a liquid droplet is formed and further increase in the Weber number develops the flow from droplet to rivulet and finally full film for Weber number (> 0.90), as shown in Figure 1.6.

Singh et al. [101] conducted three-dimensional simulations to study the breakup of a rivulet down an inclined substrate. They also conducted experiments for a rivulet flow down an inclined substrate to confirm the reliability of their simulations and showed that the simulations predictions compared well with experimental results. The flow of fluid draining down an inclined substrate was also investigated experimentally by Schmuki and Laso [95]. They examined the effects of the flux, inclination of the substrate, substrate material, liquid viscosity, and surface tension on the flow. They observed several different flow regimes, including continuous film flow, droplet flow, linear

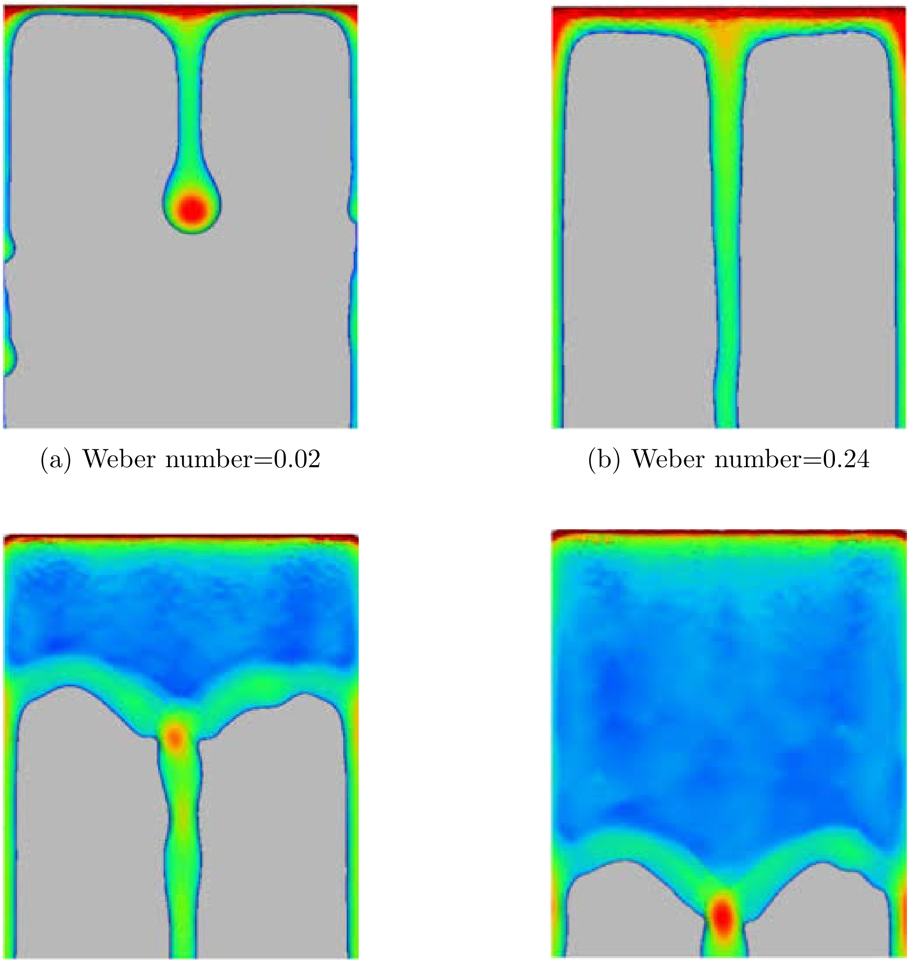

(a) Weber number=0.02

(b) Weber number=0.24

(c) Weber number=0.47

(d) Weber number=0.67

Figure 1.6: Illustration of various snapshots of the interface of film flow over an inclined plate for different Weber numbers ranging from droplet to rivulet and finally full film. Reprinted from Singh et al. [100], Copyright (2020), with permission from Elsevier.

rivulet, meandering rivulet, and pendulum rivulet regimes, as shown in Figure 1.7.

1.3.3 Stability of rivulet flow

The stability of various aspects of rivulet flow has been studied by many researchers. Several authors have studied the stability of rivulets by exploring whether or not it is energetically favourable for a rivulet to break up into sub-rivulets. Myers et al. [70] used lubrication theory to investigate the flow of a rivulet down an inclined substrate, subject to interfacial shear and gravity. They obtained analytical solutions for the free

Figure 1.7: Images of the flow regimes obtained experimentally by Schmuki and Laso [95], namely (from left to right) continuous film flow, droplet flow, linear rivulet, meandering rivulet, and pendulum rivulet. Reprinted from Schmuki and Laso [95] with permission from Cambridge University Press.

surface profile, velocity, and pressure. The energy of the rivulet was calculated in order to determine when it was energetically favourable for a gravity-driven rivulet to split into two sub-rivulets, and they conjectured that purely shear-driven rivulets are always stable and will never split.

Wilson and Duffy [121] explored the flow of a thin rivulet with prescribed flux on a vertical substrate, subject to uniform longitudinal surface shear stress. They calculated when it is energetically favourable for a rivulet to split into two narrower rivulets. Their findings disproved the conjecture of Myers et al. [70] that it is never energetically favourable for a purely shear stress driven rivulet to split.

Sullivan et al. [103] explored the steady, unidirectional flow of a perfectly wetting fluid on an inclined substrate, subject to a constant longitudinal shear stress. They investigated the stability of the rivulet, in particular, they also determined the conditions under which it is energetically favourable for a rivulet to split into one or more identical sub-rivulets.

Wilson et al. [122] studied the flow of both a film and a rivulet on a vertical substrate subject to a prescribed uniform longitudinal shear stress at the free surface. In particular, they determined when it is favourable for both a film to break up into a periodic array of rivulets and for a rivulet to break up into one or more sub-rivulets. They found that there is a critical thickness below which it is energetically favourable for a film to break up into rivulets, and there is a critical semi-width above which it is energetically favourable for a single rivulet to break up into sub-rivulets.

The flow of a rivulet down an inclined substrate may exhibit many different flow regimes, including the well-known phenomenon of meandering, which in general is observed upon increasing flow rate (see, for example, Culkin and Davis [26], Nakagawa and Scott [72], Nakagawa [71], Le Grand-Piteira et al. [61], Birnir et al. [13], Daerr et al. [27], and Couvreur and Daerr [25]).

1.4 Mathematical Modelling of a Unidirectional Rivulet Flow

In this section we review the previous mathematical modelling of unidirectional rivulet flow which forms the basis for the work described in Chapters 2 and 3. Consider the unidirectional steady gravity-driven flow of a rivulet of a Newtonian fluid with constant volume flux $Q = \bar{Q}$ down a planar substrate inclined at an angle α to the horizontal. Referred to a Cartesian system of coordinates $Ox'y'z'$, the substrate is at $z' = 0$, the x'-axis is in the direction of the flow, the y'-axis is horizontal and transverse to the direction of the flow, and the z'-axis is normal to the substrate. We take the free surface to be at $z' = h'$, where $h' = h'(y')$ is the rivulet thickness, and take the contact lines of the rivulet, where $h' = 0$, to be at $y' = \pm a'$, where a' is the semi-width of the rivulet, β' is the contact angle of the rivulet, and the thickness of the rivulet at $y' = 0$ by $h'_{\mathrm{m}} = h'(0)$. The fluid is assumed to have constant density ρ, viscosity μ and surface tension γ. The velocity $\mathbf{u}' = u'(y', z')\mathbf{i}$ and pressure $p'(y', z')$ of the fluid are governed by the mass conservation equation

$$\nabla' \cdot \mathbf{u}' = 0, \tag{1.1}$$

and the steady Navier–Stokes equation

$$\rho(\mathbf{u}' \cdot \nabla' \mathbf{u}') = -\nabla' p' + \rho \mathbf{g} + \mu \nabla'^2 \mathbf{u}', \tag{1.2}$$

where $\mathbf{g}$ is the body force due to gravity, and ∇' is the gradient operator.

Note that in general, the governing equations, namely the mass conservation equation (1.1) and the Navier–Stokes equation (1.2) must be solved numerically; however, by considering a sufficiently thin film of fluid we can apply the well-known lubrication approximation to the equations and boundary conditions and make analytical progress in the thin-film flow problem. The lubrication approximation leads to a set of equations which are simpler to solve than the full Navier–Stokes equations. Thus, in what follows we apply the lubrication approximation in order to replace the governing equations and obtain a general partial differential equation for the rivulet thickness h describing the flow of a rivulet of a Newtonian fluid.

We consider the flow of a thin rivulet with small contact angle $\beta' \ll 1$ for which the length scale in the z'-direction (denoted by $\delta\ell$) is much smaller than the length scale in the y'-direction (denoted by ℓ), where δ ($\ll 1$) is the transverse aspect ratio of the rivulet. We non-dimensionalise and scale the variables by writing:

$$\begin{gathered} y' = \ell y, \quad a' = \ell a, \quad \beta' = \delta\beta, \quad z' = \delta\ell z, \quad h' = \delta\ell h \\ h'_{\mathrm{m}} = \delta\ell h_{\mathrm{m}}, \quad u' = Uu, \quad Q' = \delta\ell^2 UQ, \quad p' = \delta\rho g\ell p, \end{gathered} \tag{1.3}$$

where g is the magnitude of acceleration due to gravity, $\ell = (\gamma/\rho g)^{1/2}$ is the capillary length, $U = \delta^2\rho g\ell^2/\mu$ is the appropriate velocity scale. With these scalings, the Navier–Stokes equations (1.2) become

$$u_{zz} + \sin\alpha = 0, \tag{1.4}$$

$$-p_y = 0, \tag{1.5}$$

$$-p_z - \cos\alpha = 0, \tag{1.6}$$

which are subject to the dimensionless boundary conditions which we discuss next. The no-slip condition at the interface between the fluid layer and the substrate $z = 0$ is

$$u = 0 \quad \text{on} \quad z = 0. \tag{1.7}$$

The continuity of stress condition on the free surface is,

$$[\underline{\underline{\sigma}} \cdot \mathbf{n}]_1^2 = K\gamma\, \mathbf{n} \qquad \text{on} \quad z = h, \tag{1.8}$$

where $\underline{\underline{\sigma}} = -p\mathbf{I} + \mu[\nabla\mathbf{u} + (\nabla\mathbf{u})^{\mathrm{T}}]$ is the stress tensor, $\mathbf{I}$ is the unit tensor, K is the mean curvature of the free surface, $\mathbf{n}$ is the unit vector normal to the free surface, and $[\phi]_1^2$ denotes the jump in the quantity ϕ going from region 1 just below the free surface to region 2 just above the free surface. The normal and tangential stress-balances at the free surface $z = h(y)$ given by (1.8) are

$$p = -\frac{\mathrm{d}^2 h}{\mathrm{d}y^2}, \tag{1.9}$$

$$u_z = 0, \tag{1.10}$$

The conditions of zero film thickness and the contact angle at the contact-lines $y = \pm a$ are

$$h = 0 \quad \text{and} \quad \frac{\mathrm{d}h}{\mathrm{d}y} = \mp\beta. \tag{1.11}$$

Solving equations (1.4) and (1.6) subject to the boundary conditions (1.7), (1.9) and (1.10) gives

$$u = \frac{\sin\alpha}{2}(2hz - z^2), \tag{1.12}$$

$$p = (h - z)\cos\alpha - \frac{\mathrm{d}^2 h}{\mathrm{d}y^2}. \tag{1.13}$$

Therefore the local flux $\bar{u}$ in the x direction is given by

$$\bar{u} = \int_0^h u \,\mathrm{d}z = \frac{\sin\alpha}{3} h^3, \tag{1.14}$$

and hence the volume flux of fluid along the rivulet, Q, is given by

$$Q = \int_{-a}^{a} \bar{u} \; \mathrm{d}y = \frac{2\sin\alpha}{3} \int_0^a h^3 \mathrm{d}y. \tag{1.15}$$

In the general case of non-zero contact angle $\beta > 0$, Duffy and Moffatt [31] showed that applying (1.5) to the solution for p given by (1.13) leads to a third-order ordinary differential equation for the rivulet thickness h, namely

$$\frac{\mathrm{d}}{\mathrm{d}y}\left(\frac{\mathrm{d}^2 h}{\mathrm{d}y^2} - h\cos\alpha\right) = 0, \tag{1.16}$$

which when integrated subject to (1.11) yields the free surface shape, $h = h(y)$, namely

$$h = \beta \times \begin{cases} \dfrac{\cosh ma - \cosh my}{m \sinh ma} & \text{for } 0 \le \alpha < \dfrac{\pi}{2}, \\ \dfrac{a^2 - y^2}{2a} & \text{for } \alpha = \dfrac{\pi}{2}, \\ \dfrac{\cos my - \cos ma}{m \sin ma} & \text{for } \dfrac{\pi}{2} < \alpha \le \pi, \end{cases} \tag{1.17}$$

and so, in particular, the maximum thickness of rivulet, $h_{\mathrm{m}} = h(0)$, is given by

$$h_{\mathrm{m}} = \beta \times \begin{cases} \dfrac{1}{m}\tanh\left(\dfrac{ma}{2}\right) & \text{for } 0 \le \alpha < \dfrac{\pi}{2}, \\ \dfrac{a}{2} & \text{for } \alpha = \dfrac{\pi}{2}, \\ \dfrac{1}{m}\tan\left(\dfrac{ma}{2}\right) & \text{for } \dfrac{\pi}{2} < \alpha \le \pi, \end{cases} \tag{1.18}$$

and the volume flux along the rivulet is given by

$$Q = 2\int_0^a \int_0^h u \,\mathrm{d}z \,\mathrm{d}y = \frac{\beta^3 \sin\alpha}{9m^4} f(ma), \tag{1.19}$$

where we have defined $m = |\cos\alpha|^{1/2}$. The function $f(ma)$ is given by

$$f(ma) = \begin{cases} 15ma\coth^3(ma) - 15\coth^2(ma) - 9ma\coth(ma) + 4 & \text{for } 0 \le \alpha < \dfrac{\pi}{2}, \\ \dfrac{12}{35}(ma)^4 & \text{for } \alpha = \dfrac{\pi}{2}, \\ -15ma\cot^3(ma) + 15\cot^2(ma) - 9ma\cot(ma) + 4 & \text{for } \dfrac{\pi}{2} < \alpha \le \pi. \end{cases} \tag{1.20}$$

In the special case of zero contact angle $\beta = 0$, Wilson and Duffy [120] showed that there is no rivulet solution for $0 \leq \alpha \leq \pi/2$ but for $\pi/2 < \alpha \leq \pi$ there are infinitely many solutions given by

$$a = \frac{n\pi}{m}, \qquad h = \frac{h_{\mathrm{m}}}{2}(1 - (-1)^n \cos my), \tag{1.21}$$

for $n = 1, 2, 3, ...$, and the maximum thickness of the rivulet h_{m} is given by

$$h_{\mathrm{m}} = \left(\frac{24m\bar{Q}}{5n\pi \sin\alpha} \right)^{\frac{1}{3}}. \tag{1.22}$$

Note that all of these solutions are physically realisable, but since the higher-branch solutions (*i.e.* those for $n = 2, 3, ..$) are simply appropriately re-scaled copies of the lowest-branch solution (*i.e.* $n = 1$) representing arrays of contiguous identical rivulets, we choose $n = 1$ without loss of generality in what follows.

1.4.1 Rivulet with constant contact angle ($\beta = \bar{\beta} > 0$)

Duffy and Moffatt [31] used the unidirectional flow solution (1.17)–(1.20) to describe the *locally* unidirectional flow with prescribed flux $Q = \bar{Q}$ down a slowly varying substrate, in particular the flow in the azimuthal direction from the top $\alpha = 0$ to the bottom $\alpha = \pi$ of a large horizontal cylinder, of a rivulet with constant contact angle $\beta = \bar{\beta}$ but slowly varying semi-width a. Note that α is now the local slope of the substrate, and also that "slowly varying" means that the longitudinal aspect ratio $\epsilon = \ell/R$, where R is the radius of the cylinder, satisfies $\epsilon \ll \delta$ so that $\epsilon/\delta \to 0$ in the limit $\epsilon \to 0$. Applying the condition of prescribed volume flux, $Q = \bar{Q}$ with Q given by (1.19), yields a transcendental algebraic equation for the semi-width a, which can generally be solved numerically. The solution (1.17) shows that, unlike in the case $\bar{\beta} = 0$ described above, solutions exist for both $0 \leq \alpha \leq \pi/2$ and $\pi/2 < \alpha \leq \pi$. In Figure 1.8 we show plots of the semi-width a given by solving (1.19) when $Q = \bar{Q}$ and the maximum thickness h_{m} given by (1.18) plotted as functions of the scaled angle α/π for a rivulet with constant contact angle $\beta = \bar{\beta} = 1$ for a range of values of $\bar{Q}$. In particular, Figure 1.8 illustrates that the rivulet becomes wide with finite thickness near the top of a large horizontal cylinder *i.e.* $\alpha = 0$, while it becomes infinitely deep and of finite width near

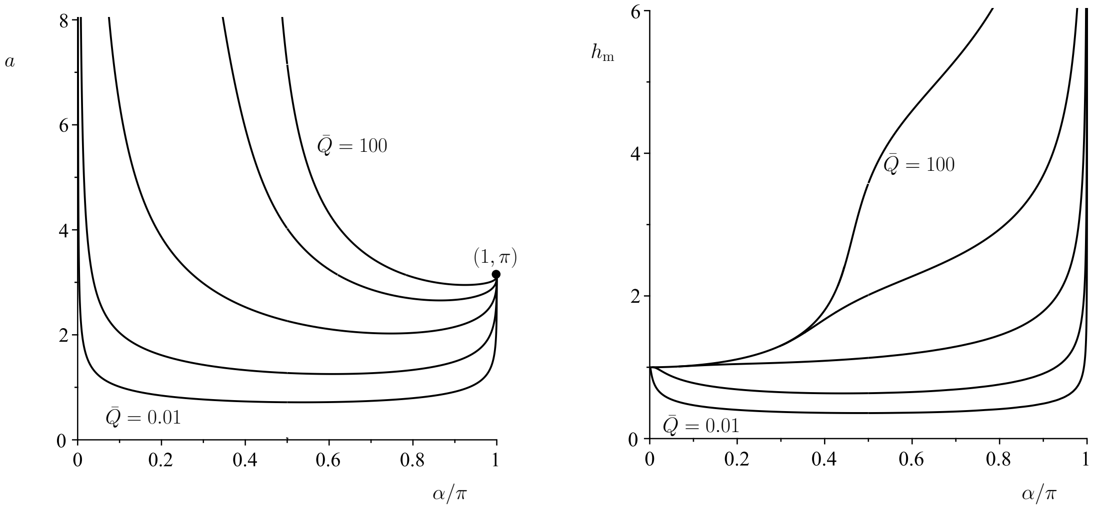

(a) (b)

Figure 1.8: Plots of (a) the semi-width a obtained by solving (1.19) when $Q = \bar{Q}$ and (b) the maximum thickness h_{m} given by (1.18) as functions of the scaled angle α/π for a rivulet with constant contact angle $\beta = \bar{\beta} = 1$ for $\bar{Q} = 0.01, 0.1, 1, 10, 100$.

the bottom of the cylinder, *i.e.* $\alpha = \pi$.

1.4.2 Rivulet with constant semi-width ($a = \bar{a} > 0$)

Paterson et al. [83] described the flow of a rivulet with constant semi-width $a = \bar{a}$ (> 0) (*i.e.* pinned contact lines) with slowly varying contact angle down a slowly varying substrate by using the solution (1.17)–(1.20) together with the solution for a rivulet of a perfectly wetting fluid given by (1.21). They showed that the behaviour of the rivulet in this case is qualitatively different from that of a rivulet with constant contact angle described in Subsection 1.4.1. In particular, setting $Q = \bar{Q}$ and $a = \bar{a}$ in (1.19) they obtained an explicit solution for β, namely

$$\beta = \left(\frac{9\bar{Q}m^4}{f(m\bar{a})\sin\alpha} \right)^{\frac{1}{3}}, \tag{1.23}$$

and showed that for a narrow rivulet with constant semi-width $a = \bar{a} \leq \pi$ a rivulet can run from the top ($\alpha = 0$) to the bottom ($\alpha = \pi$) of a large horizontal cylinder, but for a wide rivulet with constant semi-width $a = \bar{a} > \pi$ there is a critical value of α on the

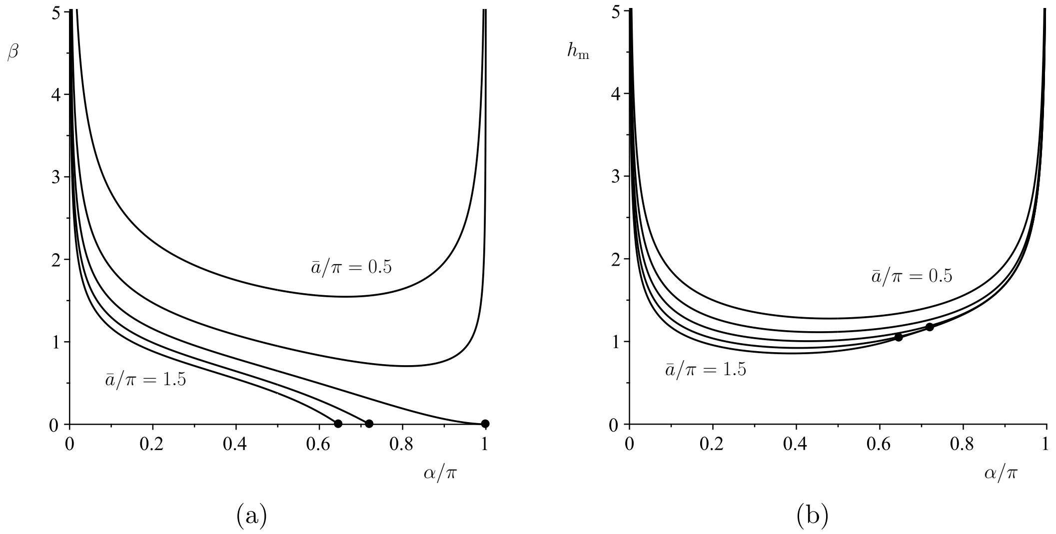

(a) (b)

Figure 1.9: Plots of (a) the contact angle β given by (1.23) and (b) the maximum thickness h_{m} given by (1.18) when $\bar{a} \leq \pi$ and given by (1.22) when $\bar{a} > \pi$ as functions of α/π for $\bar{a}/\pi = 0.5, 0.75, 1, 1.25, 1.5$ when $\bar{Q} = 1$. The dots ($\bullet$) denote the values of $\beta = 0$ and h_{m} at α_{depin} given by (1.24).

lower half of the cylinder, denoted by α_{depin} ($\pi/2 < \alpha_{\mathrm{depin}} < \pi$) and given by solving $m\bar{a} = \pi$ to obtain

$$\alpha_{\mathrm{depin}} = \cos^{-1}\left(-\frac{\pi^2}{\bar{a}^2}\right) \quad \text{for} \quad \bar{a} > \pi \tag{1.24}$$

at which the contact angle β is equal to zero and beyond which there is no physically realisable solution. In order to give an alternative description of the rivulet behaviour beyond $\alpha = \alpha_{\mathrm{depin}}$, Paterson et al. [83] assumed that the contact lines de-pin at $\alpha = \alpha_{\mathrm{depin}}$, and that thereafter the rivulet runs from $\alpha = \alpha_{\mathrm{depin}}$ to the bottom of the cylinder $\alpha = \pi$ with zero contact angle $\beta = 0$ with monotonically decreasing semi-width a. Figure 1.9 show plots of the contact angle β and the maximum thickness h_{m} as functions of α/π for a range of values of $\bar{a}/\pi$.

1.5 The Slip Boundary Condition

In Chapter 2 of this thesis, we consider rivulet flow over a slippery substrate. This section gives a brief overview of the slip boundary condition and, in particular, discusses the existence of slip over different surfaces and the effects of using a proper interfacial slip boundary condition, rather than the traditionally used no-slip boundary condition.

Slip is the motion of fluid particles relative to a solid boundary. It is commonly (and usually correctly) assumed that the appropriate boundary condition for a viscous fluid at a solid boundary is the no-slip condition, in which the fluid moves with the same tangential velocity as that of the boundary, and the no-penetration condition in which the normal component of the fluid velocity is the same as that of the boundary. The no-slip condition has long been accepted as the appropriate boundary condition in many (but not all) practical situations for the Navier-Stokes equations because in many situations effects of slip are too small to make a difference. However, in some practical situations where the material properties of the solid-liquid interface are important, such as patterned and structured surfaces (Ajaev et al. [2]), and superhydrophobic surfaces, which tend to strongly repel liquid droplets and remain completely dry (Schäffel et al. [94]), significant fluid slip has been observed. Slip can also occur when a thin film flows over a porous substrate, where a slip boundary condition can be used to describe the influence of porosity [10]. To model such slip at a boundary, the Navier slip boundary condition is usually introduced. Navier proposed a slip boundary condition in which the interface slip velocity, U_s, is proportional to the shear rate, according to

$$U_s = \lambda \frac{dU}{dz}, \tag{1.25}$$

where U is the tangential component of the fluid velocity, z is the normal coordinate and dU/dz is the shear rate [15]. He introduced the idea of a slip length, which quantifies the slip of a fluid at a solid boundary, here denoted by λ. The slip length λ is defined as the extrapolated distance below the boundary at which the fluid velocity is equal to zero, as shown in Figure 1.10. In particular, Figure 1.10(a) represents the no-slip boundary condition and shows that the velocity at the stationary solid boundary is equal to zero. Figure 1.10(b) represents the slip boundary condition and shows that the velocity at the stationary solid boundary, U_s, is nonzero, in which the velocity of the fluid matches the zero velocity of the wall at some distance λ below it. Figure 1.10(c) shows the perfect slip condition, in which the stationary solid boundary has no

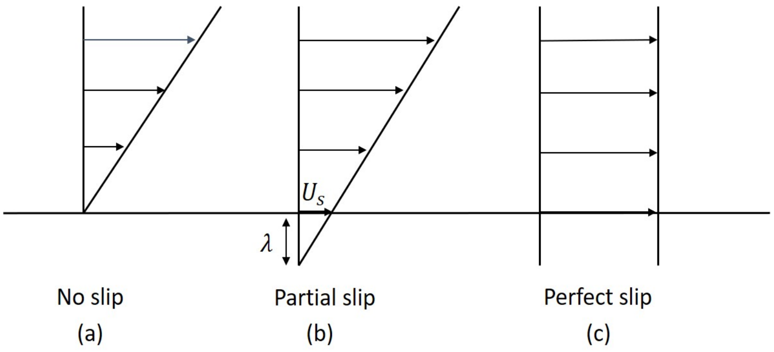

Figure 1.10: Diagram illustrating (a) no slip, (b) slip with interface slip velocity U_s and slip length λ, and (c) perfect slip at a solid-liquid interface. Reprinted by permission from Springer Nature: Nature [57], copyright 2007.

influence on the velocity profile.

Huh and Scriven [48] studied the movement of a three-phase contact line, *i.e.* the line where the interface of two fluid phases intersects the substrate, over a solid surface. They noted that applying the no-slip condition to flow close to the contact line leads to physically unacceptable stress and energy dissipation singularities at the contact line. To relieve the force singularity, Huh and Scriven [48] suggested allowing slip in the region of the contact line.

Lauga et al. [57] presented a comprehensive review of slip results from different experimental investigations. They discussed the validity of the no-slip boundary condition at a solid-liquid interface, focusing on measuring the magnitude of the slip length and its dependence on parameters such as surface roughness, wettability, dissolved gas and bubbles and shear rate. According to Lauga et al. [57], the phenomenon of slip is encountered in three different contexts. The first context is that of gas flow in devices with small dimensions. In general, the Knudsen number Kn is used to characterise the boundary condition for gas flow, with slip being important when $\mathrm{Kn} \gtrsim 0.1$. The second context arises in flows of certain non-Newtonian fluids such as polymer solutions. The third context involves Newtonian fluid flows near moving contact lines, where including slip is necessary to remove the singularities described earlier by Huh and Scriven [48]. These authors found that the slip lengths reported experimentally can range from several nanometres up to hundreds of nanometres and the impact of slip on systems with typical dimensions larger than tens of microns will be limited.

Finally, it has been experimentally observed that slip occurs on both hydrophobic and hydrophilic surfaces and the factors that affect the slip length are the shear rate, and contact angle [124].

Neto et al. [73] published a review of experimental studies on the boundary slip of Newtonian liquids on solid surfaces and considered the effects on the measured slip of surface roughness, wettability, and the presence of gaseous layers.

Biswal et al. [14] investigated the role of slip on evaporation of a thin liquid film in a microfluidic channel. The authors concluded that the film spreading and the total mass of evaporation increases with the increase in the slip length.

Chao et al. [19] studied the dynamics of thin-film flows down a uniformly heated or cooled cylinder with wall slippage. They reported that the slip boundary condition enhances the size and speed of the sliding droplets for the thin liquid films on the cylinder.

Nicholson et al. [74] analysed film flow dynamics in which the film can be thin, motivated by an aero-engine application where an oil film flows at the bearing chamber walls. They developed an extended model for rimming flow driven by surface shear within a stationary cylinder. In particular, they replaced the no-slip condition with a slip boundary condition imposed upon the chamber surface and compared the results obtained to cases with no-slip condition from previous studies of rimming flows. Additionally, they investigated the influence of wall slip on the transition between smooth film solution and pooling solution, where fluid accumulates in a recirculation in the bottom of the cylinder. Their study shows that increasing the slip length results in a significant thinning of the film flow profile toward domain boundaries. In particular, the film profile shows a significantly deeper pooling solution when the slip length is comparable to the film height. A summary of slip lengths from experimental studies was collated by Nicholson et al. [74] and is reproduced here as Table 1.1 which shows that an infinite slip length is expected in the presence of an air only interface [73] and gives details of observed slip for a variety of surfaces and fluids.

Large slip lengths (*i.e.* low friction) have been reported on superhydrophobic sur-

Table 1.1: Summary of the slip lengths from experimental studies. Reprinted from Nicholson et al. [74], with the permission of AIP Publishing.

Author	Fluid	Substrate	Slip length
Lauga et al. [57]	Water	Dimethyldichlorosilane coated glass	1μm $-$ 10μm
	Mercury	Trimethlychlorosilane coated quartz	70nm
	Propanedial vacuum	Silica	1μm
Lee et al. [62]	Water	Hydrophobic polymer surface	1.7μm
Neto et al. [73]	Water	Air	$\infty\mu$m
Zhu and Granick [127]	Deionized water	Octadecyltriethoxysilane	2.5μm
	Tetradecane	Octadecyltriethoxysilane	1.5μm
	Tetradecane mix	Mica	1.0μm
Ou et al. [80]	Water	Ultrahydrophobic silicon	20μm
Choi and Kim [21]	Water	Ultrahydrophobic silicon	20μm
	30wt.% glycerin	Ultrahydrophobic silicon	50μm
Aurelian et al. [8]	Oil	Hydrophobic substrate	0.013mm
Maali and Bhushan [67]	Water	Superhydrophobic surface	20μm

faces [89]. Rothstein [89] discussed the use of superhydrophobic surfaces and demonstrated that such surfaces can significantly reduce drag in both laminar and turbulent flows by accommodating large slip velocity near the surface, and hence affect different important technologies such as microfluidic devices. The slip length in such surfaces can be up to hundreds of μm [51].

Lee et al. [62] conducted a review of published literature on boundary conditions for flow on rough and structured surfaces, surfaces with chemical patterns, surfaces bearing nanobubbles and superhydrophobic surfaces, and discuss how these properties can affect the slip length. In particular, they showed that experiments on superhydrophobic surfaces show a significant drag reduction on a macroscopic scale, which can be interpreted as a slip on the surface.

Sochi [102] reviewed slip at the solid-liquid interface and pointed out that the magnitude of slip is affected by properties such as viscosity and density, the physical and chemical properties of the surface such as wettability and roughness, the geometry of the flow system, and to the ambient conditions, such as temperature and pressure. Sochi [102] also showed experimental evidence that supports the large values of slip length due to the presence of gaseous films or pockets on the surface.

1.6 Flow in Porous Media

1.6.1 Small-scale flows in porous media

In Chapter 3 of this thesis we consider rivulet flow over and through a porous membrane. This section discusses flow in a porous medium and, in particular, the appropriate boundary conditions at the interface between a fluid and a porous medium.

Large scale-flows, such as tidal motion over a sandy beach, the possible escape of liquidised carbon dioxide sequestered in porous underground reservoirs, and the flow of lava over fractured bedrock, have motivated several authors to use theoretical and experimental approaches to address different aspects of the flow of fluid over a porous substrate. However, the motivation for the work described in the present thesis is small-scale flows. Therefore, in addition to the examples given in Section 1.1, we will now give several other examples of small-scale flows through porous media. Small-scale flows can arise in different applications. Of the many applications, the following seem to us the most significant and promising: absorption of agrochemicals, printing, dyeing textiles and fog-harvesting, which we now describe briefly.

Tredenick et al. [109] investigated the process of the absorption of pesticides by the leaves of plants. They introduced a mathematical model to simulate the absorption of ionic agrochemicals, such as pesticides, herbicides and fertilizers through aqueous pores in plant cuticles in order to enhance the efficacy of the agrochemicals. They found that the most important component determining absorption was the cuticle structure, including the tortuosity and density of the aqueous pores.

Another application connected with coating and inkjet printing onto porous receivers, such as paper, was studied by Clarke et al. [23]. They modelled the spreading and imbibtation into a porous surface of an inkjet drop. The model was experimentally verified for water droplets and droplets of an aqueous solution of glycerol and hexelene glycol over a range of microporous filter membranes. They found that, as the average pore size increased, the rate of decrease of droplet volume increased in all of the experiments.

Shamey and Zhao [98] discussed and reviewed dyeing processes, such as in dyeing textiles. In such an application, a dye solution imparts its colour to a textile fibre, and under suitable conditions, the dye is absorbed by the fibre.

Another interesting application is the flow of condensed water on mesh fog-harvesting devices. Such devices can be used as a technology to generate water through fog harvesting.

Park et al. [81] investigated the fog-collection efficiency of woven meshes with a range of surface coatings. They developed a model to predict the overall fog-collection efficiency of the meshes and found that mesh type and pattern can affect the fog collection on the mesh. They created a design chart which can be used to select an optimal mesh to enhance the fog collection.

1.6.2 Darcy's equation

Modelling small-scale flows such as discussed in the previous subsection requires an accurate description of fluid flow through the porous medium. Many of the authors who have considered problems involving a fluid flow over and/or through a porous substrate have used Darcy's equation to describe the flow in the porous medium (see, for example, Pascal [82] and Sadiq et al. [92]). Pioneering work on flow through a porous medium was performed by Darcy [28], who experimentally investigated the flow of water in a vertical steel column filled with layers of sand [68]. The results of Darcy's experiments indicated that there is a relationship between the fluid volume flux per unit area $\mathbf{U}$ (now known as the Darcy velocity) through the porous medium, the permeability k, the fluid viscosity μ, the pressure gradient in the porous medium ∇P, the fluid density ρ, and the acceleration due to gravity $\mathbf{g}$. This relationship is now known as Darcy's equation and is given by

$$\mathbf{U} = -\frac{k}{\mu}\left(\nabla P - \rho\mathbf{g}\right). \tag{1.26}$$

For high-porosity porous media, Brinkman [18] generalised Darcy's equation by adding an extra viscous term (now known as the Brinkman term) in which viscous shear effects are accounted for. The new equation, the Darcy–Brinkman equation, is given by

$$\nabla P = -\frac{\mu}{k}\mathbf{U} + \mu' \nabla^2 \mathbf{U}, \tag{1.27}$$

where μ' is an effective viscosity, a parameter with the dimensions of viscosity.

1.6.3 Boundary conditions at the interface

Next we consider the boundary conditions at the interface between flow in a porous medium and that of a fluid layer. A variety of different modelling assumptions have been made by previous researchers. One such assumption, valid for materials with small permeability, is to regard the surface of the porous medium as a solid surface containing small holes, and apply the no-slip boundary condition. The no-slip condition was used in several studies dealing with a porous medium adjacent to a fluid. However, for materials with larger permeability, significant slip occurs and so the no-slip condition is not appropriate.

Beavers and Joseph [10] examined the interfacial boundary conditions for a Poiseuille flow through and over a homogeneous porous medium. The main goal of their experimental studies was to obtain accurate measurements of the flow rate through a long porous block and through a small uniform gap immediately above the block. Two different porous media (namely, low-density nickel foametal and aloxite) were used. Beavers and Joseph [10] suggested that there is a boundary layer at the interface over which the transition in velocity takes place, and that the effect of this boundary layer can be replaced by a slip condition at the interface, as shown in Figure 1.11, which illustrates that across the permeable lower wall the velocity changes rapidly from its value u at the wall to the Darcy value given by equation (1.26). Based on their experiments, the authors proposed the following slip boundary condition, now called the Beavers-Joseph condition,

$$\frac{\partial u}{\partial z} = \frac{\alpha}{\sqrt{k}}\,(u - U) \quad \text{on} \quad z = 0, \tag{1.28}$$

where z is the direction perpendicular to the interface, u is the tangential velocity component in the fluid parallel to the interface, U is the tangential Darcy velocity component obtained from the Darcy equation (1.26), and α is the slip coefficient which

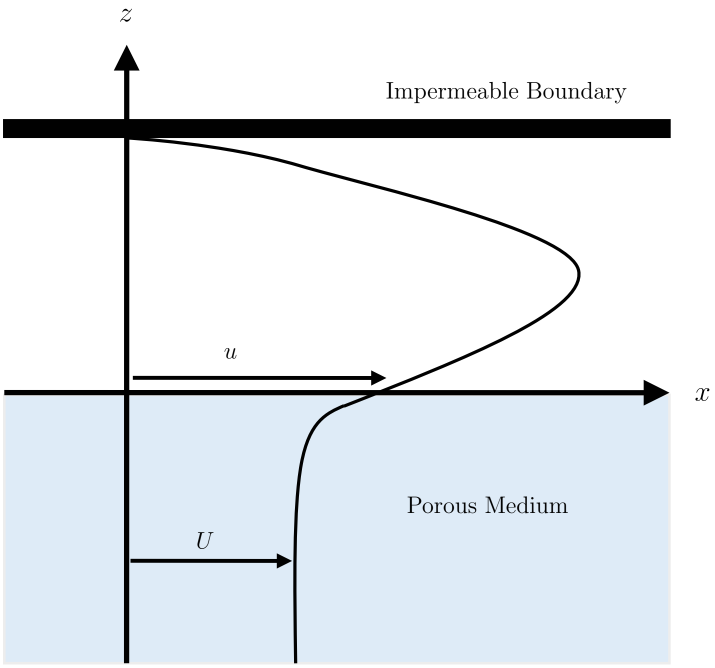

Figure 1.11: Velocity profile for the unidirectional flow of a fluid through a horizontal channel formed by a permeable lower wall and an impermeable upper wall, as examined by Beavers and Joseph [10].

is a dimensionless parameter depending on the structure of the porous medium.

Saffman [93] provided a theoretical justification for the boundary condition proposed by Beavers and Joseph [10]. He generalized Darcy's equation (1.26) to non-planar geometries which was not considered by Beavers and Joseph [10] and obtained the following boundary condition

$$u = \frac{\sqrt{k}}{\alpha}\frac{\partial u}{\partial z} + O(k), \tag{1.29}$$

indicating that the tangential velocity term in the porous medium (*i.e.* the U in equation (1.28)) is much smaller than the tangential velocity in the fluid parallel to the interface in the Beavers–Joseph equation (1.28), and therefore this term may be neglected.

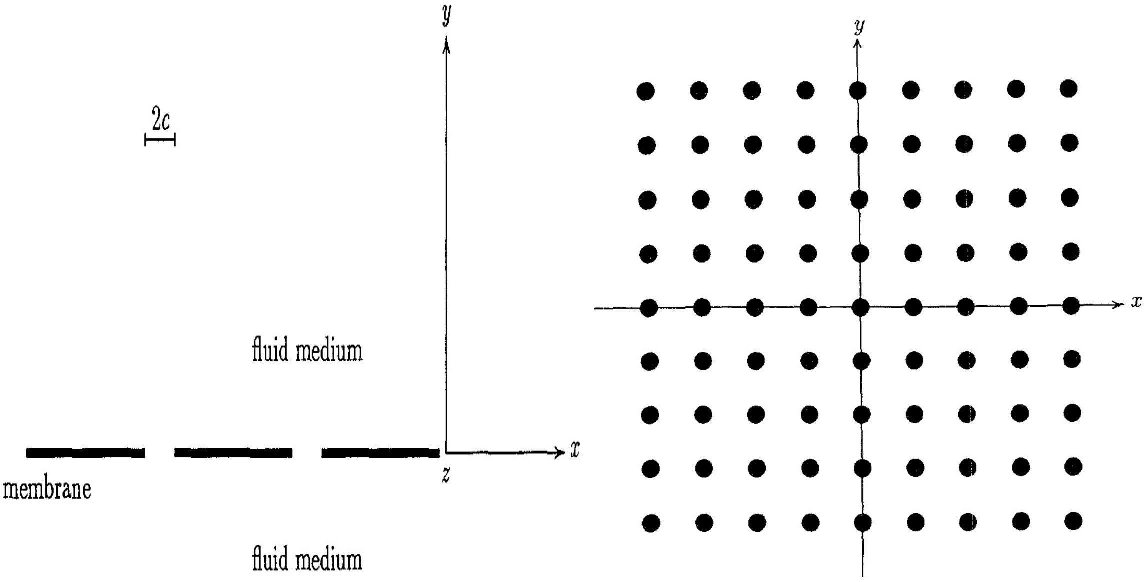

(a) (b)

Figure 1.12: Diagram illustrating (a) a membrane with a series of periodically distributed slits of width $2c$ and immersed in an infinite fluid medium and (b) diagram of a membrane with a square array of circular holes, as examined by Tio and Sadhal [107]. Reprinted by permission from Springer Nature: Nature [107], copyright 1994.

1.6.4 Flow of a fluid over and through a porous inclined plane

Next we consider the flow of a fluid over and through a porous membrane. In particular, we describe different types of membrane, where fluid can penetrate. Tio and Sadhal [107] studied both the flow through a thin membrane driven by the difference in pressure between the two sides of the membrane, and the flow parallel to the membrane. This study considered two types of model. The first model was a membrane with a series of periodically distributed slits of equal width, while the second was a membrane with a regular square and hexagonal array of circular holes, as shown in Figure 1.12. They obtained a formula relating the flow rate to the pressure drop across the membrane in the case of flow through the membrane. Then, for the case of flow parallel to the membrane, these authors considered both transverse and parallel shear flows on each side of the membrane and obtained a formula that expressed the relationship between the slip velocity and the shear stress as a function of porosity.

Davis and Hocking [29] considered the spreading and imbibition of two-dimensional droplets on permeable substrates. A number of different imbibition scenarios were considered and the main objective of the study was to determine the evolution of the droplet and specifically the lifetime of the drop and the position of the contact lines. Among these scenarios, they investigated the flow and spreading of a two-dimensional fluid sheet down an inclined substrate, which is impermeable before and permeable after the origin. To describe the permeable substrate, the authors used a simple model in which the substrate acts as a porous membrane of uniform thickness d and is modelled as an array of vertical pores of constant width $2b$ with a number density n per unit width. They also assumed that the flow in each pore is driven by pressure gradient. Following these assumptions the vertical velocity component at the top of the substrate indicates that the flow through the substrate is proportional to the pressure on the substrate as

$$w = -\frac{kp}{\mu}, \tag{1.30}$$

where $k = nb^2/3d$. They found that, as the fluid moves over the porous membrane, it gradually passes through it, until the entire fluid is completely imbibed by it. They demonstrated that the length of the fluid sheet (*i.e.* the distance over which the fluid is completely absorbed) on the porous part of the membrane increases as the permeability of the substrate decreases. However, there are some errors and inconsistencies in some aspects of this analysis. Therefore, we will revisit this problem as a limiting case of the rivulet problem solved in Chapter 3 of the present thesis.

Espín and Kumar [34] developed a model for the spreading of a droplet on a permeable substrate. They incorporate surface roughness and used a modified boundary condition, derived from Darcy's equation (1.26), for liquid imbibition in their model, which can be applied to other situations like flow down an inclined plane. In this model, they used a precursor film and two-term disjoining pressure (see Section 1.8) to describe the behaviour of the contact line of the droplet. In particular, in order to remove the need for thickness-dependent permeability, which has been used in similar studies to prevent imbibition of the precursor film, they derived the imbibition condition such that the thickness of the substrate and the precursor film above the substrate are considered. Espín and Kumar [35] described the influence of external shear and substrate permeability on droplet motion on an inclined substrate by imposing the same boundary conditions as those used in their earlier work. It has been shown experimentally by the authors that as droplet speed increases, the droplets go through different wetting transitions in which the droplet goes from a round footprint shape and a tear-drop shape to smaller droplets formed by a pearling process. In this process, the droplet stretches its shape and forms a liquid tail that breaks up into smaller droplets (pearls) and separated completely from the main droplet (*i.e.* the leading droplet). They found that in the presence of strong external shear, which opposes the droplet motion, the droplet can remain stationary on the inclined substrate and has a shape similar to the shape of a droplet on a horizontal substrate. Activating the external shear at a later time during the pearling process, can reduce the speed of the leading droplet and cause the smaller droplet to move upward. For the substrate permeability effects, they observed that the liquid absorption caused droplets to change their shape and motion due to the mass loss. In particular, the substrate permeability has a significant impact on droplet wetting transitions as it suppresses the pearling process.

If the assumption of small permeability is made, then one can decouple the dynamics of the fluid layer and the fluid flow through the porous medium. This approach is known as a “one-sided” model in which the effect of substrate permeability is incorporated as a boundary condition. Another approach is to use a “two-sided” model in which the fluid layer and porous layer are treated separately. In that case, the Stokes equations govern the flow of the clear fluid, while either the Darcy equation (1.26) or Darcy–Brinkman equation (1.27) describe the flow in the porous medium, with boundary conditions imposed at the fluid-substrate boundary. Because Darcy’s equation (1.26) does not take into account fluid-fluid viscous interactions which become important very close to the interface and/or when the permeability becomes large, Le Bars and Worster [60] introduced a viscous transition zone below the porous interface, inside the porous medium, within which the Stokes equation still applies down to a depth δ, and obtained a new condition at the fluid-porous interface which takes into account fluid-fluid viscous interactions at the interface in the following form:

$$u(x, y, -\delta) = U(x, y, -\delta), \tag{1.31}$$

where $\delta = c\sqrt{k}$ is the length scale of the transition zone and c is a constant.

The one-sided approach was used by Pascal [82] who examined the linear stability of a fluid flowing on a porous inclined substrate. He imposed the Beavers–Joseph condition (1.28) at the fluid-substrate boundary, together with Darcy's equation (1.26) governing the flow through the porous medium. In this work, the author neglected the flow in the porous medium by assuming $k/d^2 \ll 1$, where k is again the permeability and d is the vertical length scale of the fluid layer. The results show that an increase in the permeability of the substrate enhances the instability of the flow.

Sadiq and Usha [91] explored the effect of surface tension, using the same model and with the same assumptions as Pascal [82]. They described the flow of a fluid layer on an inclined porous substrate and, by performing a linear stability analysis, they obtained the same results as Pascal [82] in the absence of surface tension effects, in which they demonstrated that the fluid flow on a porous inclined substrate is more unstable than that on a rigid inclined substrate.

Sadiq et al. [92] investigated the stability of a fluid film flow down a heated porous inclined substrate, using Darcy's law to describe the flow through the porous medium. This study also used the same one-sided model as Pascal [82] to examine the combined effects of the gravity, capillary force, and permeability of the porous medium on the film. They showed that the role of permeability is to increase the amplitude of the disturbance leading to the destabilization of the film. It was found that an increase in the permeability of the porous medium led to an oscillatory behaviour.

Liu and Liu [65] similarly examined the linear stability of the flow of a fluid layer on a porous inclined substrate. This study extended Pascal's [82] one-sided model to a two-sided model by incorporating the Darcy velocity (1.26) in the porous medium which was not considered by Pascal [82] and compared the results of the two different approaches. The results highlight the fact that the two models are in good agreement only when permeability is very low.

Thiele et al. [106] analysed the stability of a thin fluid film flowing down a heated porous substrate. The study employed the Darcy–Brinkman equation (1.27) to describe the flow in the porous medium, and utilised a stress jump boundary condition at the porous-fluid interface proposed by Ochoa-Tapia and Whitaker [77]. Thiele et al. [106] showed that, in certain conditions, the porous layer can be replaced by an effective slip boundary condition at the porous-fluid interface. The authors analysed the effects of the thickness of the porous medium on the stability of the film flow, ultimately proposing a relation between the slip length and the thickness and properties of the porous substrate. The results of their study show that the one-sided model is accurate only when the permeability is sufficiently low and the porous substrate is sufficiently thin.

Nong and Anderson [76] described a thin fluid film on a permeable contact lens, which is modelled as a rigid porous layer of constant thickness. At the surface of the contact lens, they considered two slip models: Beavers–Joseph condition (1.28) and the Le Bars–Worster condition (1.31). The study investigated the influence of various effects, including contact lens thickness, lens permeability, slip, and gravity. The authors ultimately demonstrated that an increase in lens thickness, permeability, or slip length/depth in both slip models increases the film thinning rate (*i.e.* the rate at which the film thickness decreases) and, therefore, the possibility of film rupture.

Researches which take account of the flow of fluid into and/or out of the porous layer are relevant to our work, for example, the work by Ramon et al. [88], Knox et al. [54, 55] and Venerus [113] on porous squeeze-film flow. Knox et al. [54] considered squeeze-film flow of a thin layer of fluid between a flat impermeable surface moving vertically under a constant load and a flat thin porous bed coating a stationary flat impermeable surface. They assumed that the flow in the porous medium was governed by Darcy's law and imposed the Beavers–Joseph condition, together with the continuity of normal stress at the fluid-porous medium interface. They obtained an implicit expression for the fluid layer thickness as a function of time and an explicit expression for the contact time at which the two surfaces come into contact. In particular, they showed that increasing permeability reduced the contact time between the two surfaces. Knox et al. [55] extended their earlier work to study a curved impermeable surface. In particular, they investigated the influence of changing the shape of the impermeable surface.

Venerus [113] investigated the squeeze-film flows between porous and impermeable disks. They considered two configurations: (a) a sealed-face configuration where the upper surface of the porous disk is impermeable, and (b) a sealed-edge configuration where the upper surface of the porous disk is permeable and in contact with a reservoir. Darcy's law is assumed in the porous disk, while the flow in the liquid film is described by lubrication theory and allows for slip between the porous disk and liquid film. The author obtained expressions for velocity and pressure fields and showed that for a constant applied load, the contact time decreased as the disk permeability increased in both configurations.

Let us summarise the implications for our work of the research briefly reviewed above. The existence of the classical no-slip boundary condition has been adopted in many theoretical works. However, the existence of slip at the solid surfaces was established in many experiments as we discussed in the previous sections and, therefore, it is more appropriate to use a slip boundary condition. In particular, in Chapter 2 we will consider small-scale locally unidirectional gravity-driven rivulet flow down an inclined slippery substrate and hence an appropriate slip condition is considered. As we mentioned at the beginning of this section, in Chapter 3 we consider thin rivulet flowing over and through a permeable membrane. In particular, we consider the flow within the membrane and derive a boundary condition on the substrate similar to these of the "one-sided" model used by some of the previous authors described above where the flow through the permeable membrane is govern by Darcy's equation (1.26).

Note that, as far as we are aware, thus far there has been no previous theoretical work on rivulet flow over and through a porous substrate.

1.7 Thin Films on Non-Homogeneous Substrates

In Chapter 4 of this thesis we consider stationary solutions of a thin-film equation describing the flow on homogeneous and on non-homogeneous substrates. This section gives a brief overview of studies that focused on thin-film flow on non-homogeneous substrates and, in particular, the use of such substrates in determining the behaviour of fluid films. Dust and chemical contamination on surfaces are examples of naturally heterogeneous surfaces in which patches of surface properties are generated that are different from the surrounding substrate. In industrial and experimental situations heterogeneous solid surfaces can be constructed by using a flat surface with spatially periodic variation of chemical properties (*i.e.* patterned surfaces), such as stripes of an ultra thin film of gold, or by structured surfaces with periodic variations of topography, such as periodic arrays of parallel grooves or arrays of pillars of circular cross section [2, 63].

Organic semiconductors are semiconductors which use organic molecules, such as carbon, rather than silicon for their material. Organic semiconductors have become a very important field, both in science and in industrial research; in particular, for their applications in electronic devices, including organic light emitting diodes (OLEDs), sensors, organic solar cells (OSCs), lasers and transistors. Organic semiconductors are of major interest due to lower production cost, easy fabrication, flexibility and the lightness of the structures. In general, design of such devices involves the use of heterogeneous substrates. These substrates are prepared by a number of different methods, such as depositing a thin film of organic material on the substrate [64, 125].

Honisch et al. [46] theoretically modelled an experiment on organic semiconductors performed by Wang et al. [115]. In this experiment, the authors deposited thin layers of orange light-emitting organic molecules on a substrate, using an organic molecular beam deposition method, as shown in Figure 1.13. In this method, molecules are evaporated from a vacuum and subsequently condensed on the substrate. In order to control pattern formation, Wang et al. [115] used periodic gold stripes on a silicon oxide substrate and created high resolution triple colour patterns. Honisch et al. [46]

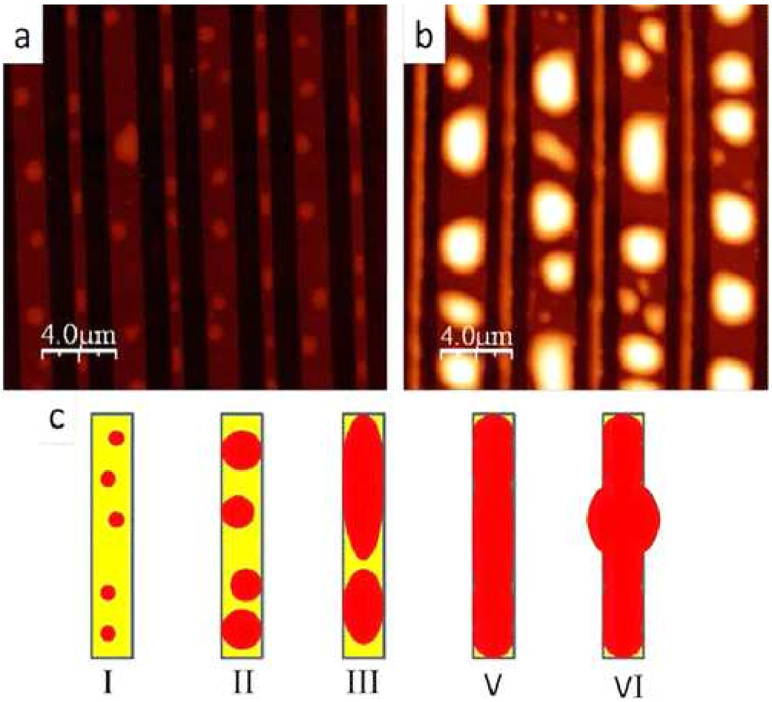

Figure 1.13: Different growth regimes during the deposition of organic molecules on a silicon oxide substrates patterned with Au stripes of alternating width. (a) Atomic force microscopy (AFM) image of 3 nm of organic molecules on Au stripes. (b) AFM image of 10 nm of organic molecules on Au stripes. (c) Sketches of the different growth regimes as amounts of deposited molecules increases: (I) random small droplets, (II) large droplets, (III) elongated drops, (V) the stripe is covered with a cylindrical ridge and (VI) bulges on both the stripe and the substrate. Reprinted with permission from Honisch et al. [46]. Copyright 2020 American Chemical Society.

formulated a thin-film equation that describes the evolution of the height profile of the layer of deposited molecules and used it to analyse the linear stability of stationary solutions. In particular, they analysed the influence of the wettability contrast, the mean film thickness (liquid volume), and the geometry of the stripe pattern on the stability of liquid ridges. Honisch et al. [46] performed numerical continuation and found two different types of instabilities, both of which were also observed in the experiment. For a small amount of deposited molecules, small droplets formed on the gold stripes, while for large amounts of deposited molecules, bulges formed which also covered part of the silicon oxide substrate.

Konnur et al. [56] studied the rupture of thin films on chemically heterogeneous substrates. In particular, they studied the case of an isolated circular patch with wetting properties different from the rest of the substrate. They solved an appropriate evolution equation numerically and found that, if the circular patch is less wettable than the rest of the substrate, then liquid flows away from the less wettable regions, while if the patch is more wettable than the rest of the substrate, the liquid tends to accumulate and form droplets. In addition, they found that the presence of chemical heterogeneities can destabilize and rupture the thin film, and the time to rupture on the heterogeneous patch is independent of the size of the patch.

Kargupta and Sharma [52] investigated dewetting on chemically patterned substrates. They considered a substrate consisting of alternating less wettable and more wettable stripes and used a spatially periodic disjoining pressure (see Section 1.8) to model the heterogeneity of the substrate. In particular, they explored numerically the effect of the periodicity interval (*i.e.* the distance between two stripes) and the stripe width on the dewetting structure. They found that a successful templating on a striped substrate, in which the pattern of the substrate is transferred into the pattern of liquid structure, can be achieved if the periodicity interval of the substrate is very close to the characteristic lengthscale of the instability. This therefore ensures dewetting on every less wettable site on the patterned substrate (*i.e.* number of dewetting sites equals the number of dewetted stripes). Finally, regarding the influence of the stripe width, they showed that good templating can be achieved only if the stripe width does not exceed an upper limit, otherwise the templating of the substrate will breakdown.

In order to determine the right conditions for good templating, Kargupta and Sharma [53] continued their investigations of dewetting of liquid films for different types of substrate patterns. Instead of simple stripe pattern they considered periodic arrays of square and rectangular blocks of wettability different from the rest of the substrate, as well as checkerboard patterns of alternating more and less wettable blocks, as shown in Figure 1.14. In addition they considered templating of complex patterns, such as an N-shaped substrate pattern. They found that the best templating occurs when the following conditions are satisfied: (1) the pattern periodicity in x and y directions is more than a characteristic length scale of instability, (2) the less wettable area fraction is less than a transition value beyond which the liquid spills over the less

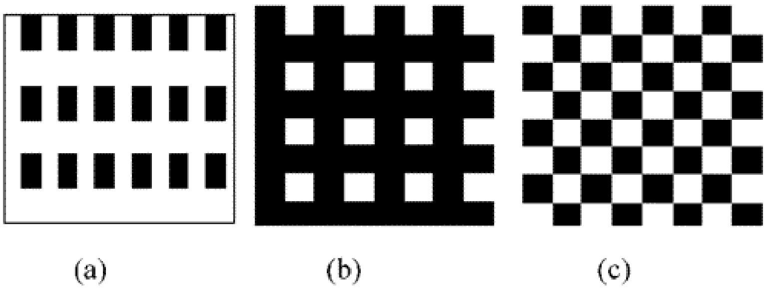

Figure 1.14: Different types of substrate patterns: (a) arrays of more wettable blocks on a less wettable substrate, (b) arrays of less wettable blocks on a more wettable substrate and (c) checkerboard pattern of more and less wettable blocks. Reprinted with permission from Kargupta and Sharma [53]. Copyright 2020 American Chemical Society.

wettable part, (3) the less wettable block width must be less than a transition width, and (4) the aspect ratio of the periodicity of the pattern is close to unity.

Sharma et al. [99] investigated the effect of the chemical heterogeneity of the substrate on the dewetting. They considered two different cases, namely a substrate containing a localized single heterogeneous patch and a periodically patterned substrate consisting of alternating less wettable and more wettable stripes. The main concern of the paper was to investigate how the substrate patterns are reproduced in the liquid film, and what are the conditions for the best templating. The results show that an increase in the width of the patch results in an increase in the rupture time. Furthermore, increasing the patch width further beyond a critical width leads to the formation of a single drop at the centre of the patch. The conditions for the best templating are similar to the results obtained in [52], in which the ideal templating is only possible if the substrate periodicity is larger than characteristic length scale of instability, and the less wettable stripe width is less than a transition stripe width.

Similarly to the previous studies, Thiele et al. [105] discussed the process of dewetting on a chemically patterned substrate. They studied the influence of the chemically patterned substrate on the dewetting and the solution structure of a thin liquid film on a substrate with a sinusoidal wettability pattern. In particular, the influence of varying the amplitude and periodicity of the chemical heterogeneity of the surface was considered. Thiele et al. [105] determined the stability of stationary periodic solutions for both homogeneous and heterogeneous substrates. They found that if the period of the heterogeneity is much smaller than a critical wavelength of the corresponding flat film on the homogeneous substrate, it is not possible to pin patterns to the heterogeneities. Conversely, a smaller critical wavelength will result in a weaker heterogeneity needed for the pattern to pin.

1.8 Disjoining Pressure

Studies of dewetting and spreading of a thin liquid film on a substrate are generally based on models involving an evolution equation of the thickness of the liquid film with a disjoining pressure term. Disjoining pressure describes the intermolecular forces arising from the interaction between the solid substrate and the fluid film. Depending on the particular situation being modelled, there are many forms of disjoining pressure, which may incorporate several interactions, such as the van der Waals forces and/or various types of short-range interaction terms.

The concept of a disjoining pressure has been applied in various systems including suspensions, foams, emulsions, and liquid films on solid surfaces. Various studies have considered the impact surface forces have on wetting and liquids spreading on solid substrates. The most common form of disjoining pressure used in these models is:

$$\Pi(h) = \frac{B}{h_*^n}\left[\left(\frac{h_*}{h}\right)^n - \left(\frac{h_*}{h}\right)^m\right], \tag{1.32}$$

where h is the film thickness, B and the exponents n and m are positive constants with $n > m > 1$. This disjoining pressure incorporates a thin wetted layer (*i.e.* a thin precursor layer) on the substrate of height h_*. This typically has a thickness of a few nanometres. Liquid-solid repulsion is represented by the first term and the corresponding attraction by the second term. Note that, when the disjoining pressure is only repulsive, it is called by some authors the conjoining pressure.

The interaction between the solid substrate and the fluid film can also be discussed in terms of the energy potential $U(h)$, where $U(h) = \int \Pi(h)\,\mathrm{d}h$. Figure 1.15 shows a plot of the disjoining pressure given by (1.32) and its corresponding potential for $B = 1$,

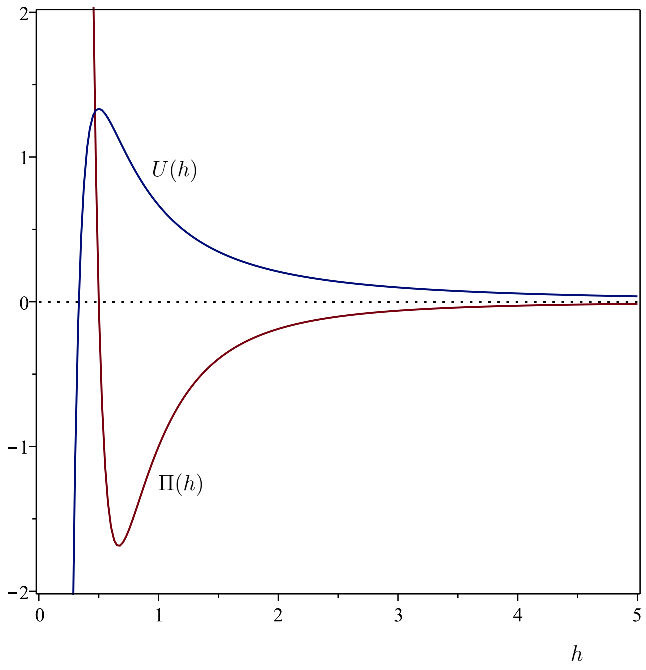

Figure 1.15: Plot of the disjoining pressure $\Pi(h)$ given by (1.32) and its corresponding energy potential $U(h)$ for $B = 1$, $h_* = 1/2$, $n = 4$ and $m = 3$.

$h_* = 1/2$, $n = 4$ and $m = 3$. In particular, Figure 1.15 illustrates that $\Pi(h_*) = 0$ that $\Pi(h)$ has a global minimum at $h = 4h_*/3 = 2/3$, and that the energy potential $U(h)$ has a global maximum at $h = h_*$.

The kind of disjoining pressure presented in (1.32), which incorporates both attractive and repulsive forces has been considered numerous times in thin film problems. Models with the exponent pair $(n, m) = (4, 3)$ have been considered frequently, while the 6–12 Lennard-Jones potential, which corresponds to the exponent pair $(n, m) = (9, 3)$ is also commonly used.

Attractive and repulsive surface forces can be used separately or in combination. Many studies have used only the attractive term, which, in general, leads to film rupture (*i.e.* the film thickness approaches zero in finite time), while the repulsive term tends to stabilise the film and prevent the fluid from reaching a zero thickness. Analytical and numerical difficulties due to a film of zero thickness may be prevented by using only the repulsive term [69].

Schwartz and Eley [96] proposed a numerical method that permits the calculation of the unsteady motion of droplets on heterogeneous substrates. In their study Schwartz and Eley [96] used an evolution equation which includes capillary, viscous, gravitational, and disjoining pressure forces. In particular, the disjoining pressure used was as in (1.32). Schwartz and Eley [96] used three different exponent pairs: (3,2), (4,3) and (9,3) to explore the effect of changing the disjoining exponents on the final droplet pattern. They found that the major observed difference between the three cases is the size of the droplet fragments. The authors studied axisymmetric spreading of a drop on a partially wetting substrate and found that similar to experiments, the contact angle does not affect the droplet spreading rates until the droplet has nearly stabilized (*i.e.* reached its equilibrium height).

Thin liquid films have been shown to rupture and merge into complex dewetting patterns when influenced by attractive and repulsive forces [12]. In their study Bertozzi et al. [12] focused on the effect of the disjoining/conjoining intermolecular forces exerted on a thin film. In their work, the disjoining pressure term had the form given by (1.32), with $B = 1$ and $h_* = \epsilon$, and represented as:

$$\Pi = \frac{1}{h^n} - \frac{\epsilon^{m-n}}{h^m} = \frac{1}{h^n}\left(1 - \left[\frac{\epsilon}{h}\right]^{m-n}\right), \tag{1.33}$$

where ϵ represents a small parameter. The study results show that the model's solutions have a similar qualitative structure for large set of (n, m) values.

Liu and Witelski [66] studied thin films on a chemically heterogeneous substrate. Unlike other studies, which modelled a sinusoidally-varying wettability of the substrate, they used stepwise wettability patterns modelled by a piecewise constant function. In their work, they considered the disjoining pressure as given in equation (1.32), with $B = \epsilon^2$, $h_* = \epsilon$, and the exponent pair $(n, m) = (4, 3)$ which has the form

$$\Pi(h) = \frac{\epsilon^2}{h^3} - \frac{\epsilon^3}{h^4}. \tag{1.34}$$

Based on the structure of the bifurcation diagram they obtained, their study categorized the 1-D steady-state solutions into six distinct but connected branches; small-thickness films, small-width droplets, pinned droplets, large-width droplets, confined droplets, and large-thickness films. A linear stability analysis established that confined droplets are the only unstable branch, while the rest of the branches are stable.

Thiele et al. [105] examined the dewetting of a thin liquid film on a chemically patterned substrate, using the wettability contrast as a control parameter as discussed in Section 1.7. They used a thin-film evolution model that included a spatially varying disjoining pressure given by:

$$\Pi(h) = \frac{2\kappa}{a}\mathrm{e}^{-h/l}\left(\frac{1}{a}\mathrm{e}^{-h/l} - 1\right). \tag{1.35}$$

The term a is a small dimensionless positive parameter that represents the wetting properties, l is the diffuse interface's length scale, and κ has the dimension of a spreading coefficient per length which represented by the heterogeneity

$$\kappa = \kappa_0\left(1 + \epsilon\xi(x)\right), \tag{1.36}$$

to make it spatially varying where $\xi(x) = \cos 2\pi x/P_{\text{het}}$ and ϵ and P_{het} correspond to the amplitude (*i.e.* wettability contrast) and the period of the heterogeneity.

Glasner and Witelski [37] examined two coarsening mechanisms that occur in dewetting films, mass exchange between droplets that influences the breakdown of individual droplets, and the spatial motion of the droplets that results in droplet collisions and merging events. They aimed to quantify the coarsening process. Using a disjoining pressure similar to the one given in equation (1.34), this study combined the effects of the intermolecular forces. This study suggested that, in certain regimes, isolated droplets can move substantially, which allows for droplet collisions as the mechanism responsible for coarsening.

Brasjen et al. [17] used numerical simulations and experiments to examine dewetting in thin liquid films on chemically heterogeneous substrates. The substrates included narrow and long hydrophobic stripes, with bigger hydrophilic domains separating them. They restricted their study to small contact angles θ which permitted the use of the lubrication approximation to identify the time evolution of the film thickness distribution. To represent the disjoining pressure, this study used the form given by (1.32), with

$$B = h_*^{n-1}\gamma(1-\cos\theta)\frac{(n-1)(m-1)}{(n-m)}, \tag{1.37}$$

so that equation (1.32) becomes

$$\Pi = \gamma(1-\cos\theta)\frac{(n-1)(m-1)}{(n-m)h_*}\left[\left(\frac{h_*}{h}\right)^n - \left(\frac{h_*}{h}\right)^m\right], \tag{1.38}$$

where γ is surface tension. In this study, the authors used the values $n = 3$, $m = 2$ and $h_* = 10$ nm. The authors demonstrated that there exist critical values of the film thickness, stripe width and contact angle so that when these critical values are not reached or are exceeded, dewetting does not occur. The study showed that the speed of the dewetting contact line on the substrate was strongly dependent on the contact angle; while being weakly dependent on the film thickness and the stripe width.

In Chapter 4, we revisit the results obtained by Honisch et al. [46] who considered a disjoining pressure of the form

$$\Pi(h) = \left(\frac{1}{h^6} - \frac{1}{h^3}\right)(1 + \rho G(x,y)), \tag{1.39}$$

where the function $G(x,y)$ models the non-homogeneity of the substrate and the parameter ρ is the wettability contrast. The disjoining pressure of the form (1.39) incorporates the wettability of the substrate in both attractive and repulsive forces. However, in Chapter 4 we incorporate the wettability of the substrate in either the attractive or the repulsive forces and study the dependence of the steady-state solutions on the wettability contrast.

1.9 Outline of Thesis

The outline of this thesis is as follows.

In Chapter 2, we analyse the steady flow of a thin and slender (*i.e.* slowly varying) rivulet of a Newtonian fluid down a slippery planar substrate. We follow the approaches of Duffy and Moffatt [31] and Paterson et al. [83], described in Subsections 1.4.1 and 1.4.2, and use the solutions for the unidirectional flow of a thin rivulet with prescribed constant volume flux down an inclined slippery planar substrate to describe the effect of slip on the locally unidirectional flow of a rivulet with constant width (*i.e.* pinned contact lines) but slowly varying contact angle as well as a rivulet with constant contact angle and slowly varying semi-width down a slowly varying substrate.

In Chapter 3, we analyse the steady locally unidirectional flow of a thin and slender rivulet over and through an inclined planar permeable membrane. We impose both a condition relating the normal component of the velocity of the fluid to the pressure drop across the membrane and a no-slip condition on the tangential component of the velocity of the fluid at the fluid/membrane interface in order to determine both the flow within and the shape of the rivulet. In particular, we use the solutions obtained to investigate the effect of the angle of inclination of the substrate and the permeability of the membrane on the length of the rivulet.

In Chapter 4, we build on the work of Honisch et al. [46] and consider patterns formed in a two-dimensional thin film on a planar substrate with a Derjaguin disjoining pressure and periodic wettability stripes. For the case of constant wettability, we elucidate the change in the global structure of branches of steady-state solutions as the average film thickness and the surface tension are varied. Using the continuation software package AUTO, we perform a continuation analysis of these steady-state solutions and establish the existence of both nucleation and metastable regimes, and discuss admissible forms of spatially non-homogeneous disjoining pressure.

1.10 Presentations and Publications

Aspects of the work described in Chapter 3 were presented at UK Fluids Conference held in Cambridge in the University of Cambridge from 27th to 29th August 2019, and at the 13th European Coating Symposium (ECS) held in Heidelberg, Germany from 8th to 11th September 2019. Aspects of the work described in Chapter 4 were presented at the British Applied Mathematics Colloquium (BAMC) held in Guilford in the University of Surrey from 10th to 12th April 2017, and at the 30th Scottish Fluid Mechanics Meeting held in Glasgow in the University of Strathclyde on 19th May 2017.

A full account of the work in Chapter 2 has been recently published in Physics of Fluids (Alshaikhi et al. [5]). A full account of the work contained in Chapter 3 has recently been published in Physical Review Fluids (Alshaikhi et al. [6]), and a full account of the work in Chapter 4 has recently been published online in the European Journal of Applied Mathematics (Alshaikhi et al. [4]).

Chapter 2

Rivulet Flow Over a Slippery Substrate

In this chapter we generalise the analysis of Duffy and Moffatt [31] and Paterson et al. [83], described in Subsections 1.4.1 and 1.4.2, to analyse rivulet flow over a slippery substrate, modelled using the Navier slip condition. We use the solutions for the unidirectional flow we described in Section 1.4 to analyse the effect of slip on the locally unidirectional flow with prescribed constant flux $Q = \bar{Q}$ (> 0) down a slowly varying substrate, for example, the flow in the azimuthal direction from the top $(\alpha = 0)$ to the bottom $(\alpha = \pi)$ of a large horizontal cylinder of a rivulet together with either prescribed constant semi-width $a = \bar{a}$ (> 0) (*i.e.* pinned contact lines) and slowly varying contact angle $\beta = \beta(\alpha)$ or prescribed constant contact angle $\beta = \bar{\beta}$ (≥ 0) and slowly varying semi-width $a = a(\alpha)$.

2.1 Problem Formulation

Similar to the analysis in Section 1.4, we consider unidirectional steady gravity-driven flow of a thin symmetric rivulet, *i.e.* the transverse aspect ratio of the rivulet is small, of a fluid with prescribed volume flux $\bar{Q}$ (> 0) down a slippery planar substrate inclined at an angle α $(0 \leq \alpha \leq \pi)$ to the horizontal, as sketched in Figure 2.1. The fluid is assumed to have constant density ρ, viscosity μ and surface tension γ. The velocity $\mathbf{u}'$

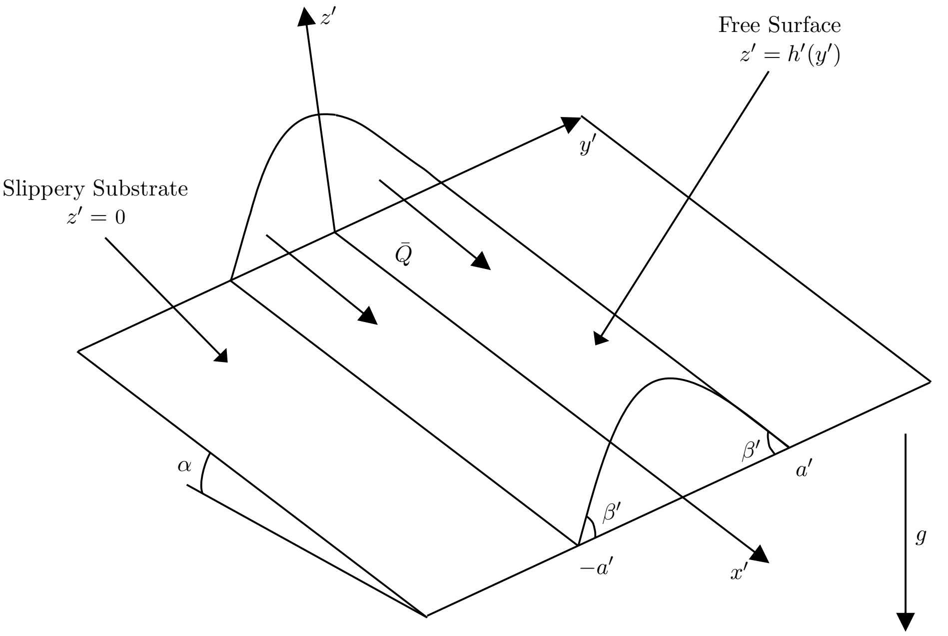

Figure 2.1: Unidirectional gravity-driven flow of a thin symmetric rivulet with semi-width a' (> 0), contact angle β' (≥ 0) and volume flux Q (> 0) down a slippery planar substrate inclined at an angle α ($0 \leq \alpha \leq \pi$) to the horizontal.

and pressure p' of the fluid are governed by the mass conservation and Navier–Stokes equations (1.1) and (1.2), respectively. Referred to Cartesian coordinate $Ox'y'z'$, the substrate is at $z' = 0$, the free surface profile of the rivulet is denoted by $z' = h'(y')$, the semi-width of the rivulet by a' and the contact angle of the rivulet by β'. In addition, the maximum thickness of the rivulet, which always occurs at $y = 0$ since the rivulet is symmetric about its centreline $y = 0$, is denoted by $h_{\mathrm{m}} = h(0)$. We non-dimensionalise and scale the variables according to

$$\begin{gathered} y' = \ell y, \quad a' = \ell a, \quad \beta' = \delta\beta, \quad z' = \delta\ell z, \quad h' = \delta\ell h, \quad h'_{\mathrm{m}} = \delta\ell h_{\mathrm{m}} \\ \lambda' = \delta\ell\lambda, \quad u' = Uu, \quad Q' = \delta\ell^2 UQ, \quad p' = \delta\rho g\ell p, \end{gathered} \tag{2.1}$$

where g is the magnitude of acceleration due to gravity, $U = \delta^2\rho g\ell^2/\mu$ is the appropriate velocity scale, and $\delta \ll 1$ is the transverse aspect ratio of the rivulet.

As we described in Section 1.4, for unidirectional flow, the velocity is of the form

$\mathbf{u} = u(y,z)\mathbf{i}$ and therefore the Navier–Stokes equation (1.2) reduces to

$$\sin\alpha + u_{zz} = 0, \quad -p_y = 0, \quad -p_z - \cos\alpha = 0, \tag{2.2}$$

which are to be solved subject to the dimensionless boundary conditions of slip between the fluid and the substrate $z = 0$, namely the Navier slip condition (1.25) as discussed in Section 1.5,

$$u = \lambda \frac{\partial u}{\partial z} \quad \text{on} \quad z = 0, \tag{2.3}$$

where λ (≥ 0) is the constant slip length, and the continuity of stress condition as discussed in Section 1.4,

$$[\underline{\underline{\sigma}} \cdot \mathbf{n}]_1^2 = K\gamma\,\mathbf{n} \quad \text{on} \quad z = h. \tag{2.4}$$

At the free surface $z = h(y)$, the unit normal vector, the tangent vector, and the curvature of the free surface are given by

$$\mathbf{n} = \frac{(-\delta h_y, 1)}{(1+\delta^2 h_y^2)^{1/2}}, \tag{2.5}$$

$$\mathbf{t} = \frac{(1, \delta h_y)}{(1+\delta^2 h_y^2)^{1/2}}, \tag{2.6}$$

$$K = \nabla \cdot \mathbf{n} = -\frac{(\delta/\ell) h_{yy}}{(1+\delta^2 h_y^2)^{3/2}}, \tag{2.7}$$

respectively. The normal and tangential components of (2.4) are

$$\mathbf{n} \cdot \underline{\underline{\sigma}} \cdot \mathbf{n} = K\gamma, \tag{2.8}$$

$$\mathbf{t} \cdot \underline{\underline{\sigma}} \cdot \mathbf{n} = 0. \tag{2.9}$$

From equations (2.8) and (2.9) we can obtain expressions for the normal and tangential stress balances, namely

$$p+\frac{2}{1+\delta^2h_y^2}[-\delta^3u_yh_y^2+\delta u_zh_y]=\frac{-{C_\mathrm{a}}^{-1}h_{yy}}{(1+\delta^2h_y^2)^{3/2}}, \tag{2.10}$$

$$u_z-\delta^2u_zh_y^2-2\delta^2u_yh_y=0, \tag{2.11}$$

where $C_\mathrm{a}=\rho g\ell^2/\gamma$ is the appropriate capillary number. At leading order in the limit $\delta\to 0$ the normal and tangential stress balances at the free surface $z=h(y)$ given by (2.10) and (2.11) reduce to

$$p = -C_\mathrm{a}^{-1}h_{yy}, \tag{2.12}$$

$$u_z = 0. \tag{2.13}$$

We define the capillary length ℓ by $\ell=(\gamma/\rho g)^{1/2}$ so that $C_\mathrm{a}=1$. In addition, h satisfies both the zero thickness and the contact angle conditions at the contact-lines $y=\pm a$, namely

$$h=0 \quad \text{and} \quad h_y=\mp\beta \quad \text{at} \quad y=\pm a. \tag{2.14}$$

At leading order in the limit of small transverse aspect ratio $\delta\to 0$ (*i.e.* for a thin rivulet) the governing equations are readily solved to yield the pressure,

$$p=\cos\alpha(h-z)-h_{yy}, \tag{2.15}$$

and the velocity of the fluid within the rivulet,

$$u=\frac{\sin\alpha}{2}\left[2h(z+\lambda)-z^2\right], \tag{2.16}$$

so that the local flux is given by

$$\bar{u}=\int_0^h u(y,z)\,\mathrm{d}z=\frac{\sin\alpha}{3}h^2(h+3\lambda). \tag{2.17}$$

Note that setting $z=0$ and $z=h$ in (2.16) yields the velocity at the substrate $u(y,0)=\lambda h\sin\alpha$ and the velocity of the free surface $u(y,h)=h(h+2\lambda)\sin\alpha/2$, respectively. When $\lambda = 0$ the analysis of Paterson et al. [83] discussed in Subsection 1.4.2 is recovered.

The present work draws from the previous studies on longitudinal shear stress studied by Wilson and Duffy [120], Sullivan et al. [103], Wilson et al. [122], and Paterson et al. [84] as discussed in Subsection 1.3.1, and especially focusses on the novel features of the current problem, namely, the rivulet's dependence on α, λ and Q.

In order to derive the asymptotics of the semi-width a, the contact angle β and the maximum thickness of rivulet h_{m} in various relevant limits, we use the mathematical software packages Maple and Mathematica. Note that the superscripts $-$ and $+$ which appear in some of the asymptotic results that follow indicate that the limit is a left-handed or right-handed one, respectively.

2.2 Perfectly Wetting Fluid ($\beta = 0$)

In the special case of a perfectly wetting fluid, $\beta = 0$, solving (2.15) with (2.14) shows that there is no solution for $0 \leq \alpha \leq \pi/2$, but for $\pi/2 < \alpha \leq \pi$ we have

$$a = \frac{\pi}{m}, \qquad h = \frac{h_{\mathrm{m}}}{2}\left(1 + \cos my\right), \qquad Q = \frac{\pi}{24m}\left(5h_{\mathrm{m}} + 18\lambda\right)h_{\mathrm{m}}^2 \sin\alpha, \tag{2.18}$$

where h_{m} denotes the maximum thickness of the rivulet, which occurs at $y = 0$. Note that the semi-width a is independent of both λ and $\bar{Q}$.

Setting $Q = \bar{Q}$ (where Q is given by (2.18)) yields a cubic equation for h_{m}, namely

$$h_{\mathrm{m}}^3 + \frac{18\lambda}{5}h_{\mathrm{m}}^2 - \frac{24\bar{Q}m}{5\pi\sin\alpha} = 0. \tag{2.19}$$

In the special case of zero slip length, $\lambda = 0$, we recover the real solution of (2.19) given by Wilson and Duffy [120] described in Section 1.4 and given by (1.22), while in the general case $\lambda > 0$, equation (2.19) has three real roots (two of them negative and one positive) when $0 < 25\bar{Q}m \leq 36\pi\lambda^3 \sin\alpha$, where the real positive solution is given by

$$h_{\mathrm{m}} = \frac{6\lambda}{5}\left\{2\cos\left[\frac{1}{3}\cos^{-1}\left(\frac{25\bar{Q}m}{18\pi\lambda^3\sin\alpha} - 1\right)\right] - 1\right\}, \tag{2.20}$$

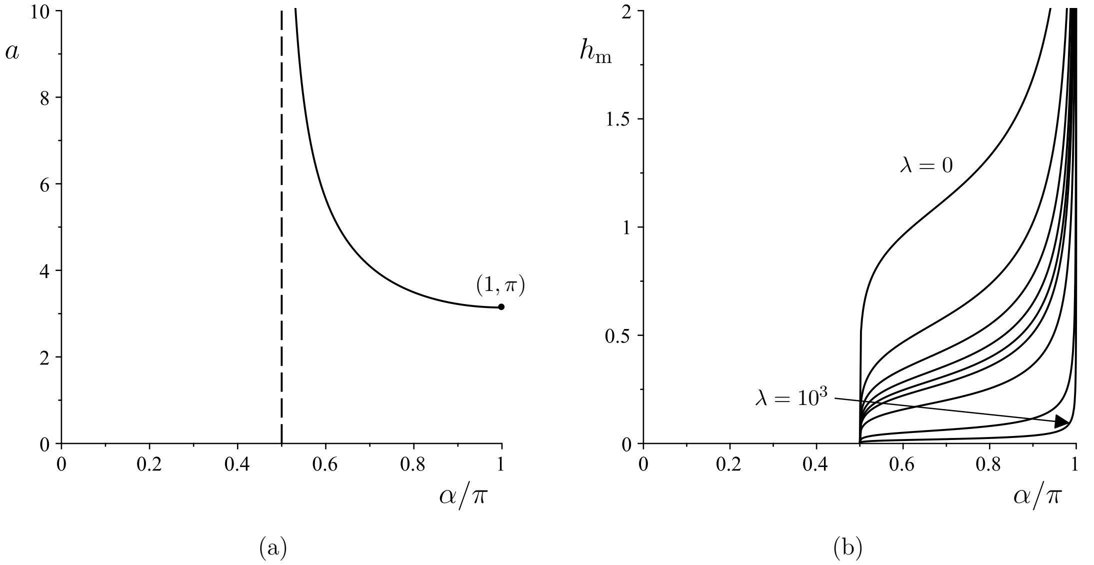

Figure 2.2: Plots of (a) the semi-width a given by (2.18) and (b) the maximum thickness h_{m} as functions of the scaled angle α/π given by (1.22) and (2.21) when $\bar{Q} = 1$ for $\lambda = 0, 1, 2, 3, 4, 5, 10, 100, 1000$ for a rivulet of a perfectly wetting fluid with $\beta = 0$.

and that when $25\bar{Q}m \geq 36\pi\lambda^3 \sin\alpha$ the solution is given by

$$h_{\mathrm{m}} = \frac{6\lambda}{5}\left\{2\cosh\left[\frac{1}{3}\cosh^{-1}\left(\frac{25\,\bar{Q}m}{18\pi\lambda^3\sin\alpha} - 1\right)\right] - 1\right\}, \tag{2.21}$$

(see Appendix A for details of the derivation of this solution).

Note that by replacing λ with $\tau/2\sin\alpha$ in equations (2.20) and (2.21) we recover the corresponding solutions obtained by Sullivan et al. [103] (their equations (A.2) and (A.5) with (A.6) and (A.7)) for their problem.

Figures 2.2 and 2.3 show plots of the semi-width a and the maximum thickness h_{m} as functions of the scaled angle α/π for various values of λ and $\bar{Q}$. We can get further insight into the behaviour of the semi-width a given by (2.18) and the maximum thickness h_{m} given by (1.22) and (2.21) by looking at the asymptotic behaviour of these equations. Specifically, Figure 2.2 shows that in the special case of zero slip length, $\lambda = 0$, the rivulet becomes wide and shallow according to

$$a \sim \pi\left(\alpha - \frac{\pi}{2}\right)^{-\frac{1}{2}} \to \infty \quad \text{and} \quad h_{\mathrm{m}} \sim \left(\frac{24\bar{Q}}{5\pi}\right)^{\frac{1}{3}}\left(\alpha - \frac{\pi}{2}\right)^{\frac{1}{6}} \to 0^{+} \tag{2.22}$$

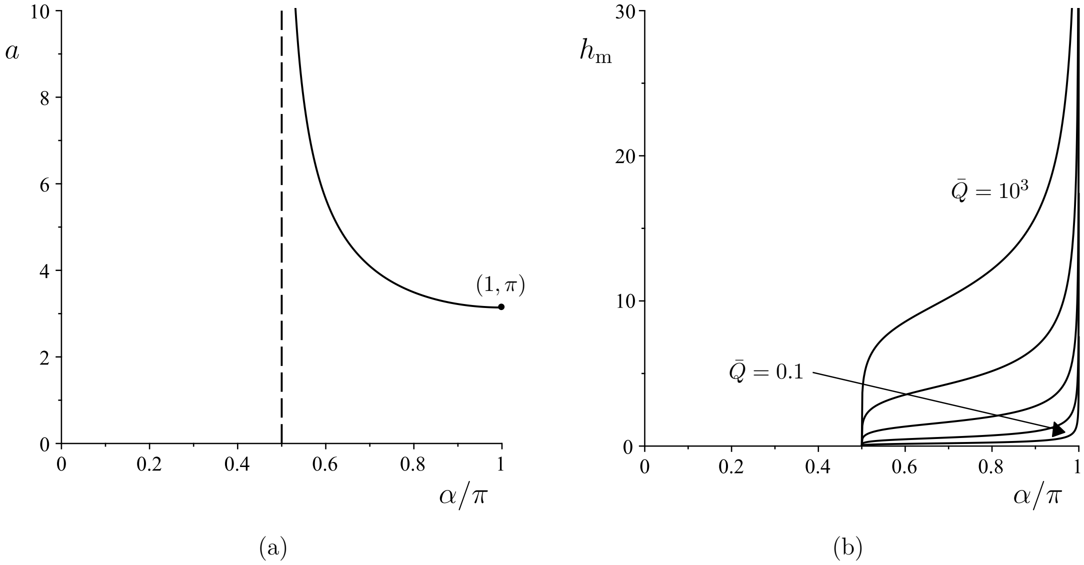

Figure 2.3: As Figure 2.2, except for $\bar{Q} = 0.1, 1, 10, 100, 1000$ when $\lambda = 1$.

as $\alpha \to \pi/2^+$, and deep with finite semi-width π according to

$$a = \pi + \frac{\pi}{4}(\pi-\alpha)^2 + O\left((\pi-\alpha)^4\right) \to \pi^+ \quad \text{and} \quad h_\mathrm{m} \sim \left(\frac{24\bar{Q}}{5\pi(\pi-\alpha)}\right)^{\frac{1}{3}} \to \infty \tag{2.23}$$

as $\alpha \to \pi^-$.

Note that the thin-film approximation is based on the assumption that the fluid is sufficiently thin, but since $h_\mathrm{m} \to \infty$ as $\alpha \to \pi^-$ in (2.23), this approximation ultimately fails and breaks down sufficiently close to $\alpha = \pi$.

In the general case, $\lambda > 0$, the rivulet becomes wide and shallow according to

$$a \sim \pi\left(\alpha - \frac{\pi}{2}\right)^{-\frac{1}{2}} \to \infty \quad \text{and} \quad h_\mathrm{m} \sim \left(\frac{4\bar{Q}}{3\pi\lambda}\right)^{\frac{1}{2}}\left(\alpha - \frac{\pi}{2}\right)^{\frac{1}{4}} \to 0^+ \tag{2.24}$$

as $\alpha \to \pi/2^+$, and deep with finite semi-width π according to

$$a = \pi + \frac{\pi}{4}(\pi-\alpha)^2 + O\left((\pi-\alpha)^4\right) \to \pi^+ \tag{2.25}$$

and

$$h_\mathrm{m} = \left(\frac{24\bar{Q}}{5\pi(\pi-\alpha)}\right)^{\frac{1}{3}} - \frac{6\lambda}{5} + O\left((\pi-\alpha)^{\frac{1}{3}}\right) \to \infty \tag{2.26}$$

as $\alpha \to \pi^-$.

Figure 2.2 also illustrates that h_m is a monotonically decreasing function of λ, and shows that the rivulet approaches its finite maximum thickness in the case $\lambda = 0$ given by (1.22) according to

$$h_\mathrm{m} = \left(\frac{24\bar{Q}m}{5\pi\sin\alpha}\right)^{\frac{1}{3}} - \frac{6}{5}\lambda + O\left(\lambda^2\right) \to \left(\frac{24\bar{Q}m}{5\pi\sin\alpha}\right)^{\frac{1}{3}^-} \tag{2.27}$$

as $\lambda \to 0^+$, and becomes shallow according to

$$h_\mathrm{m} = \left(\frac{4\bar{Q}m}{3\pi\lambda\sin\alpha}\right)^{\frac{1}{2}} - \frac{5\bar{Q}m}{27\pi\sin\alpha}\frac{1}{\lambda^2} + O\left(\frac{1}{\lambda^{\frac{7}{2}}}\right) \to 0^+ \tag{2.28}$$

as $\lambda \to \infty$.

Figure 2.3 also illustrates that h_m is a monotonically increasing function of $\bar{Q}$, and shows that the rivulet becomes shallow according to

$$h_\mathrm{m} = \left(\frac{4\bar{Q}m}{3\pi\lambda\sin\alpha}\right)^{\frac{1}{2}} - \frac{5\bar{Q}m}{27\pi\lambda^2\sin\alpha} + O\left(\bar{Q}^{\frac{3}{2}}\right) \to 0^+ \tag{2.29}$$

as $\bar{Q} \to 0^+$ and deep according to

$$h_\mathrm{m} = \left(\frac{24\bar{Q}m}{5\pi\sin\alpha}\right)^{\frac{1}{3}} - \frac{6\lambda}{5} + O\left(\left(\frac{1}{\bar{Q}}\right)^{\frac{1}{3}}\right) \to \infty \tag{2.30}$$

as $\bar{Q} \to \infty$.

2.3 Non-Perfectly Wetting Fluid ($\beta > 0$)

As discussed in Section 1.4, in the general case of non-perfectly wetting fluid, $\beta > 0$, Duffy and Moffatt [31] showed that applying (2.2b) to the solution for p given by (2.15) leads to a third-order ordinary differential equation for the free surface profile, namely

$$\frac{\mathrm{d}}{\mathrm{d}y}\left(\frac{\mathrm{d}^2 h}{\mathrm{d}y^2} - h\cos\alpha\right) = 0, \tag{2.31}$$

which when integrated subject to (2.14) yields the free surface shape, $h = h(y)$, given by (1.17), namely

$$h = \beta \times \begin{cases} \dfrac{\cosh(ma) - \cosh(my)}{m\sinh(ma)} & \text{for } 0 \le \alpha < \dfrac{\pi}{2}, \\ \dfrac{a^2 - y^2}{2a} & \text{for } \alpha = \dfrac{\pi}{2}, \\ \dfrac{\cos(my) - \cos(ma)}{m\sin(ma)} & \text{for } \dfrac{\pi}{2} < \alpha \le \pi, \end{cases} \tag{2.32}$$

where we have defined $m = |\cos\alpha|^{1/2}$.

In particular, the maximum thickness of rivulet, $h_{\mathrm{m}} = h(0)$, is given by (1.18), namely

$$h_{\mathrm{m}} = \beta \times \begin{cases} \dfrac{1}{m}\tanh\left(\dfrac{ma}{2}\right) & \text{for } \ 0 \le \alpha < \dfrac{\pi}{2}, \\ \dfrac{a}{2} & \text{for } \alpha = \dfrac{\pi}{2}, \\ \dfrac{1}{m}\tan\left(\dfrac{ma}{2}\right) & \text{for } \ \dfrac{\pi}{2} < \alpha \le \pi. \end{cases} \tag{2.33}$$

The volume flux along the rivulet is given by

$$Q = 2\int_0^a \int_0^h u \, \mathrm{d}z \, \mathrm{d}y = 2\int_0^a \bar{u} \, \mathrm{d}y = \frac{\beta^3 \sin\alpha}{9m^4} f(ma) + \frac{\lambda\beta^2 \sin\alpha}{m^3} g(ma), \tag{2.34}$$

where the function $f(ma)$ is given by

$$f(ma) = \begin{cases} 15ma\coth^3(ma) - 15\coth^2(ma) - 9ma\coth(ma) + 4 & \text{for } \ 0 \le \alpha < \dfrac{\pi}{2}, \\ \dfrac{12}{35}(ma)^4 & \text{for } \alpha = \dfrac{\pi}{2}, \\ -15ma\cot^3(ma) + 15\cot^2(ma) - 9ma\cot(ma) + 4 & \text{for } \ \dfrac{\pi}{2} < \alpha \le \pi, \end{cases} \tag{2.35}$$

and the function $g(ma)$ is given by

$$g(ma) = \begin{cases} 3ma\coth^2(ma) - 3\coth(ma) - ma & \text{for } \ 0 \le \alpha < \dfrac{\pi}{2}, \\ \dfrac{4}{15}(ma)^3 & \text{for } \alpha = \dfrac{\pi}{2}, \\ 3ma\cot^2(ma) - 3\cot(ma) + ma & \text{for } \ \dfrac{\pi}{2} < \alpha \le \pi. \end{cases} \tag{2.36}$$

Note, as discussed in Section 1.4, that the function $f(ma)$ was first obtained by Duffy

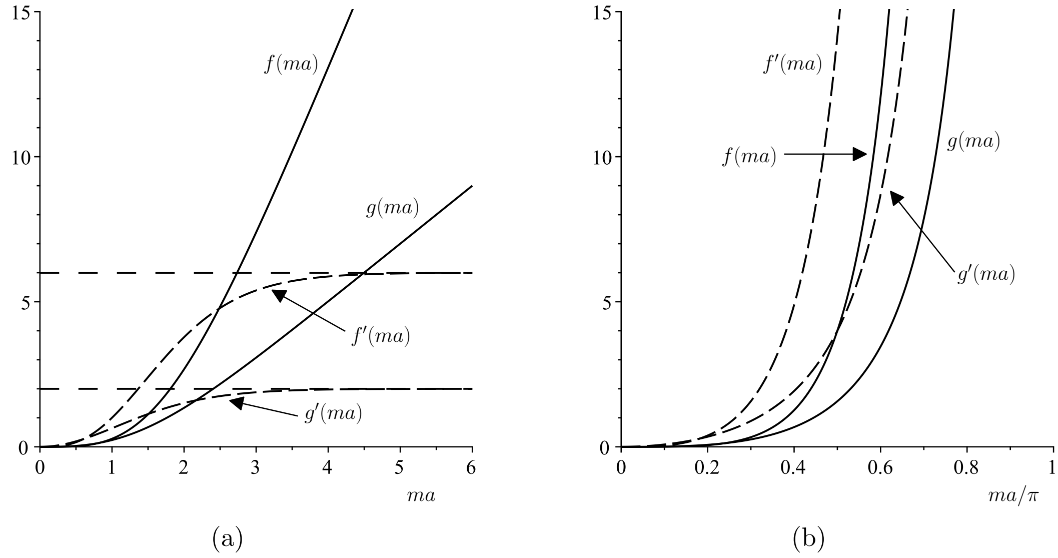

Figure 2.4: Plots of f and g (solid lines), defined by (2.35) and (2.36) respectively, together with their derivatives f' and g' (dashed lines) as (a) functions of ma for $0 \leq \alpha < \pi/2$ when $0 \leq ma < \infty$, and (b) functions of ma/π for $\pi/2 < \alpha \leq \pi$ when $0 \leq ma < \pi$. The horizontal dashed lines in (a) show the constant asymptotic values for f' and g' in the limit $ma \to \infty$.

and Moffatt [31] in their work on a rivulet of non-perfectly wetting fluid on a slowly varying substrate (their equation (14)) and the function $g(ma)$ was previously obtained by Sullivan et al. [103] in their work on a rivulet of perfectly wetting fluid subject to a longitudinal surface shear stress τ (their equation (2.16)) and by Paterson et al. [84] in their work on a rivulet of non-perfectly wetting fluid subject to a longitudinal surface shear stress τ (their equation (2.9)). For future reference we note that for $0 \leq \alpha < \pi/2$ both f and g are positive and monotonically increasing functions for $ma \geq 0$, while their derivatives f' and g' are also monotonically increasing functions such that $g'(ma) = 2$ and $f'(ma) = 6$ in the limit $ma \to \infty$. Figure 2.4(a) shows plots of f, g, f', and g' as functions of ma for $0 \leq \alpha < \pi/2$. For $\pi/2 < \alpha \leq \pi$ both f and g and their derivatives f' and g' are positive and monotonically increasing functions for $0 \leq ma < \pi$. Figure 2.4(b) shows plots of f, g, f', and g' as functions of ma/π for $\pi/2 < \alpha \leq \pi$. For future reference (especially when calculating asymptotic solutions) it is useful to note that in the limit $ma \to 0^+$

$$f(ma) = \begin{cases} \dfrac{12}{35}(ma)^4 - \dfrac{8}{105}(ma)^6 + O(ma)^8 & \text{for} \quad 0 \le \alpha < \dfrac{\pi}{2} \\ \dfrac{12}{35}(ma)^4 + \dfrac{8}{105}(ma)^6 + O(ma)^8 & \text{for} \quad \dfrac{\pi}{2} < \alpha \le \pi \end{cases} \tag{2.37}$$

and

$$g(ma) = \begin{cases} \dfrac{4}{15}(ma)^3 - \dfrac{4}{105}(ma)^5 + O(ma)^7 & \text{for} \quad 0 \le \alpha < \dfrac{\pi}{2} \\ \dfrac{4}{15}(ma)^3 + \dfrac{4}{105}(ma)^5 + O(ma)^7 & \text{for} \quad \dfrac{\pi}{2} < \alpha \le \pi. \end{cases} \tag{2.38}$$

In the limit $ma \to \infty$ for $0 \le \alpha < \pi/2$

$$f(ma) = 6ma - 11 + O(ma \exp(-2ma)) \tag{2.39}$$

and

$$g(ma) = 2ma - 3 + O(ma \exp(-2ma)). \tag{2.40}$$

In the limit $ma \to \pi^-$ for $\pi/2 < \alpha \le \pi$

$$f(ma) = \frac{15\pi}{(\pi - ma)^3} - \frac{6\pi}{(\pi - ma)} + O(\pi - ma) \tag{2.41}$$

and

$$g(ma) = \frac{3\pi}{(\pi - ma)^2} - \pi + O\left((\pi - ma)^2\right). \tag{2.42}$$

Note that by replacing $\lambda \sin\alpha$ with $\tau/2$ in equation (2.17) and equation (2.34) we recover expressions that coincide exactly with the corresponding expressions for $\bar{u}$ and Q obtained by Sullivan et al. [103] (their equations (2.12) and (2.14)) and Paterson et al. [84] (their equations (2.3) and (2.7)), but with a different velocity given by

$$u = \frac{\sin\alpha}{2}(2h - z)z + \tau z, \tag{2.43}$$

due to the different boundary conditions of no slip at the substrate, and prescribed non-zero tangential stress at the free surface ($i.e.$ $u_z = \tau$) used in their work.

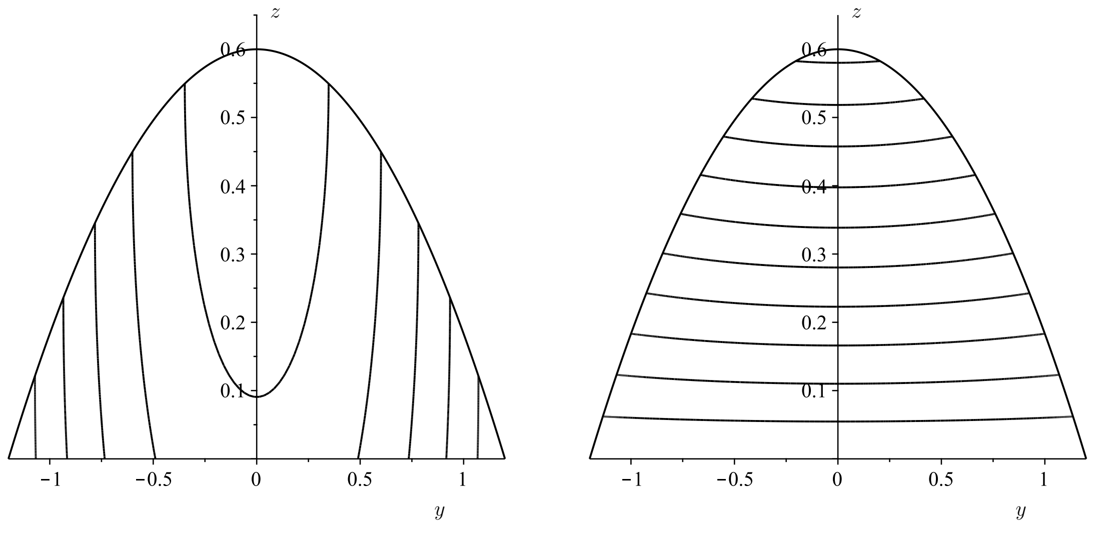

(a) (b)

Figure 2.5: Contour plots of the velocity $u(y, z)$ given by (a) equation (2.16) for the present problem with $\lambda = 2$ and by (b) equation (2.43) for the corresponding longitudinal shear stress problem with $\tau = 2\lambda \sin\alpha = 4$. In both cases $\alpha = \pi/2$, $a \simeq 1.1998, \beta = 1$ and $Q = 1$. The contour interval is 0.25 in both (a) and (b).

Figure 2.5 shows contour plots of the velocity u in the special case of a vertical substrate ($\alpha = \pi/2$) for the present problem given by (2.16) and for the corresponding shear-driven problem with $\tau = 2\lambda \sin\alpha$ given by (2.43) with the same values of $a \simeq 1.1998$, $\beta = 1$ and $Q = 1$. In particular, Figure 2.5 confirms that despite having the same local flux $\bar{u}$ and flux Q, the velocity profiles u are, as expected, qualitatively different.

Figure 2.6 shows contour plots of the velocity u given by (2.16) in the special case of a vertical substrate ($\alpha = \pi/2$), for a small and a large value of λ with the same values of β and Q (but different values of a). Specifically, in the limit of weak slip, $\lambda \to 0$, (as illustrated in Figure 2.6(a)) the velocity contours depend on both y and z and approaches the familiar semi-parabolic in z profile in the case $\lambda = 0$, namely $u \sim \sin\alpha(2h - z)z/2$, while in the limit of strong slip, $\lambda \to \infty$, (as illustrated in Figure 2.6(b)) the velocity profile is independent of z but not y and becomes plug-like in z, namely $u \sim \lambda h \sin\alpha$, and so the contours become straight lines perpendicular to the substrate.

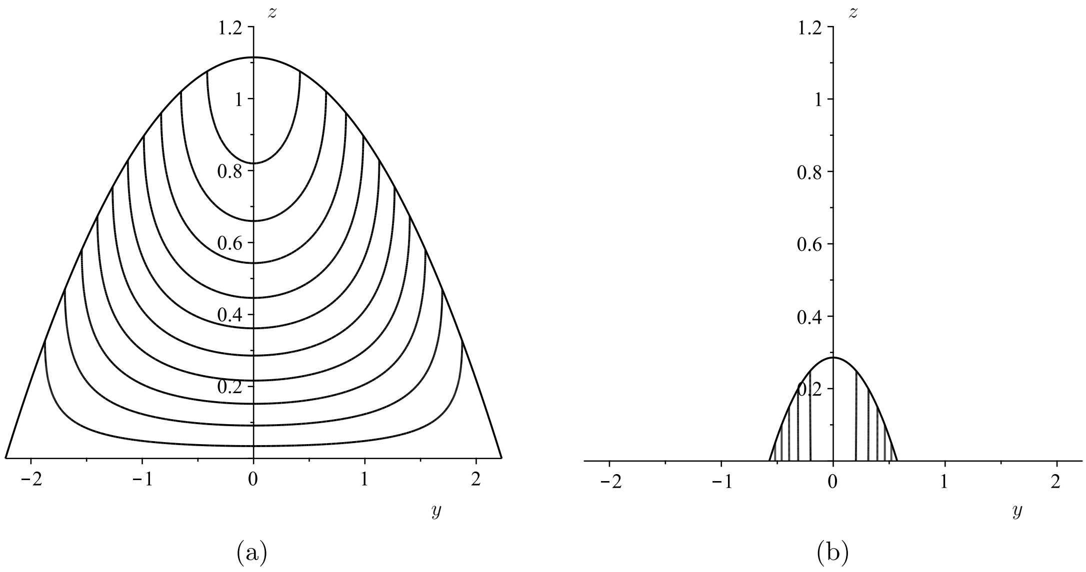

Figure 2.6: Contour plots of the velocity $u(y,z)$ given by equation (2.16) when (a) $\lambda = 0.02$ and $a \simeq 2.2293$ and (b) $\lambda = 20$ and $a \simeq 0.5716$. In both cases $\alpha = \pi/2$, $\beta = 1$ and $Q = 1$. The contour interval is 0.06 in (a) and 1 in (b).

2.4 A Rivulet with Constant Width $a = \bar{a}$ (> 0)

In this section we describe the steady, locally unidirectional flow of a slowly varying rivulet of non-perfectly wetting fluid with constant width $a = \bar{a}$ but slowly varying contact angle $\beta = \beta(\alpha)$. In Subsections 2.4.1 and 2.4.2 we follow the analysis of Paterson et al. [83] and show that, even in the general case $\lambda > 0$, we expect the behaviour of the rivulet to be qualitatively different for a narrow rivulet with $a = \bar{a} \le \pi$ and a wide rivulet with $a = \bar{a} > \pi$ as discussed in Subsection 1.4.2. Therefore, we treat these two cases separately in what follows. In Subsections 2.4.3–2.4.6 we describe the behaviour in the limits of weak slip, $\lambda \to 0^+$, strong slip, $\lambda \to \infty$, small flux, $\bar{Q} \to 0^+$, and large flux, $\bar{Q} \to \infty$, respectively.

If we set $Q = \bar{Q}$ with Q given by (2.34) and $a = \bar{a}$, then β can be determined exactly from the cubic equation for β, namely

$$\beta^3 + \frac{9\lambda m g(m\bar{a})}{f(m\bar{a})}\beta^2 - \frac{9\bar{Q}m^4}{f(m\bar{a})\sin\alpha} = 0. \tag{2.44}$$

Setting $\lambda = 0$ in equation (2.44) recovers the solution for β obtained by Paterson et al.

[83] given by (1.23), namely

$$\beta = \left(\frac{9\bar{Q}m^4}{f(m\bar{a})\sin\alpha} \right)^{\frac{1}{3}}, \tag{2.45}$$

and the maximum thickness h_{m} is given by (2.33) with β given by (2.45).

In the general case, $\lambda > 0$, the real positive solution of (2.44) for the contact angle β when $0 < \bar{Q}mf(m\bar{a})^2 \leq 12\lambda^3 g(m\bar{a})^3 \sin\alpha$ is

$$\beta = \frac{3\lambda\, mg(m\bar{a})}{f(m\bar{a})} \left\{ 2\cos\left[\frac{1}{3}\cos^{-1}\left(\frac{\bar{Q}mf(m\bar{a})^2}{6\lambda^3 g(m\bar{a})^3 \sin\alpha} - 1 \right) \right] - 1 \right\}, \tag{2.46}$$

and when $\bar{Q}mf(m\bar{a})^2 \geq 12\lambda^3 g(m\bar{a})^3 \sin\alpha$, the solution is given by

$$\beta = \frac{3\lambda\, mg(m\bar{a})}{f(m\bar{a})} \left\{ 2\cosh\left[\frac{1}{3}\cosh^{-1}\left(\frac{\bar{Q}mf(m\bar{a})^2}{6\lambda^3 g(m\bar{a})^3 \sin\alpha} - 1 \right) \right] - 1 \right\}, \tag{2.47}$$

with the corresponding solution for h_{m} is given by (2.33) with β given by (2.46) and (2.47) (see Appendix B for details of the derivation of this solution).

Note that by replacing λ with $\tau/2\sin\alpha$ in (2.46) we recover an expression that coincides exactly with the expression for β obtained by Paterson et al. [84] (their equations (5.6)) for their problem in the general case of strictly negative shear, $\tau < 0$, and in the limit $\lambda \to 0$ equations (2.46) and (2.47) reduce to the solution given by Paterson et al. [83] in (2.45).

2.4.1 A narrow rivulet with $a = \bar{a} \leq \pi$

In this section we will show that for a narrow rivulet with $\bar{a} \leq \pi$ for all values of $\bar{Q}$ and λ there is always a rivulet solution given by (2.45)–(2.47) and (2.33) in the interval $0 \leq \alpha \leq \pi$, and both its contact angle β and maximum thickness h_{m} have a single minimum. Figures 2.7 and 2.8 show plots of the contact angle β and the maximum thickness h_{m} given by (2.45)–(2.47) and (2.33) plotted as functions of the scaled angle α/π for a narrow rivulet with constant width $a = \bar{a} = 2$ $(< \pi)$ for a range of values of λ and $\bar{Q}$, respectively. In particular, Figures 2.7 and 2.8 illustrate that the rivulet

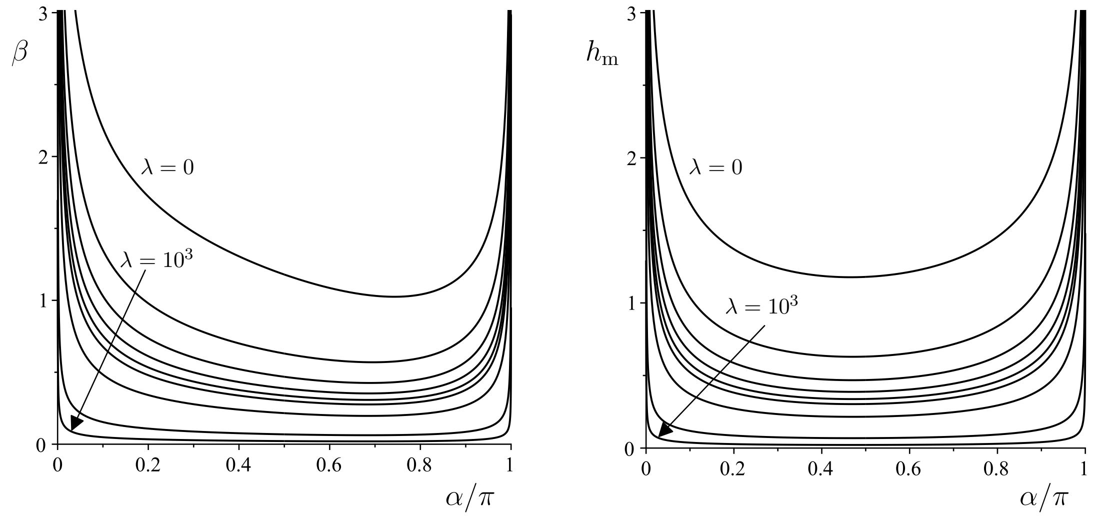

(a) (b)

Figure 2.7: Plots of (a) the contact angle β given by (2.45)–(2.47) and (b) the maximum thickness $h_{\rm m}$ given by (2.33) as functions of the scaled angle α/π for a narrow rivulet with constant width $a = \bar{a} = 2$ $(< \pi)$ for $\lambda = 0, 1, 2, 3, 4, 5, 10, 100, 1000$ when $\bar{Q} = 1$.

becomes deep according to

$$\beta \sim \left(\frac{9\bar{Q}}{f(\bar{a})\alpha}\right)^{\frac{1}{3}} \to \infty \quad \text{and} \quad h_{\rm m} \sim \left(\frac{9\bar{Q}}{f(\bar{a})\alpha}\right)^{\frac{1}{3}} \tanh\left(\frac{\bar{a}}{2}\right) \to \infty \tag{2.48}$$

as $\alpha \to 0^+$ and deep (except when $\bar{a} = \pi$ in which $\beta \to 0^+$ and $h_{\rm m} \to \infty$) according to

$$\beta \sim \left(\frac{9\bar{Q}}{f(\bar{a})(\pi - \alpha)}\right)^{\frac{1}{3}} \to \infty \tag{2.49}$$

and

$$h_{\rm m} \sim \left(\frac{9\bar{Q}}{f(\bar{a})(\pi - \alpha)}\right)^{\frac{1}{3}} \tan\left(\frac{\bar{a}}{2}\right) \to \infty \tag{2.50}$$

as $\alpha \to \pi^-$, recovering the corresponding results in the case $\lambda = 0$ obtained by Paterson et al. [83] (their equations (14) and (15)). Figure 2.7 also illustrates that both β and $h_{\rm m}$ are monotonically decreasing functions of λ, while Figure 2.8 illustrates that both β and $h_{\rm m}$ are monotonically increasing functions of $\bar{Q}$.

Figure 2.7(a) shows that the contact angle β has a single minimum, denoted by $\beta = \beta_{\rm min}$ and occurring at $\alpha = \alpha_{\rm min}$. Therefore, in Figure 2.9 we show plots of $\alpha_{\rm min}$ and $\beta_{\rm min}$

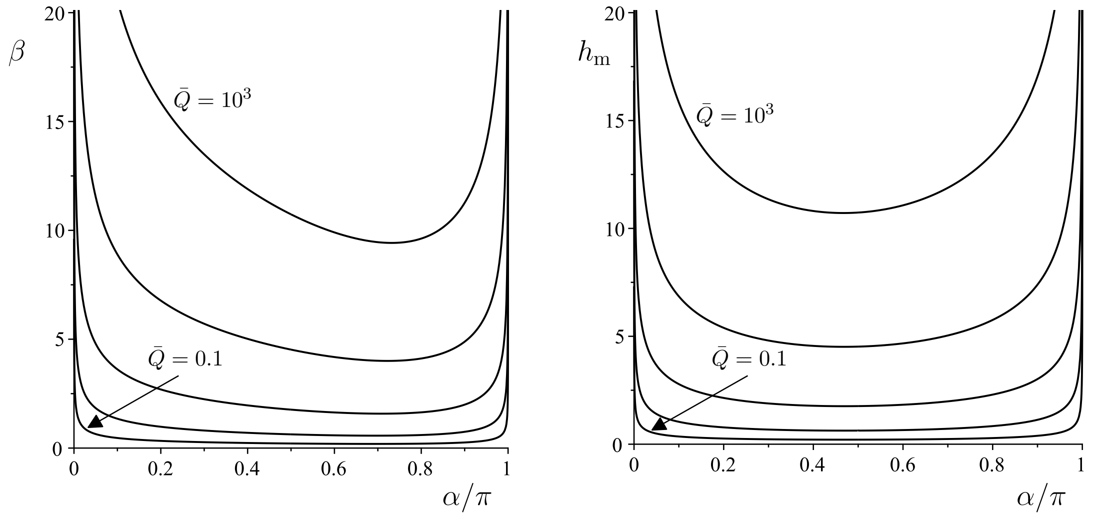

(a) (b)

Figure 2.8: As Figure 2.7, except for $\bar{Q} = 0.1, 1, 10, 100, 1000$ when $\lambda = 1$.

as functions of the slip length λ for a rivulet with constant semi-width $\bar{a} = 2$ $(< \pi)$ when $\bar{Q} = 1$. The dots indicate the corresponding values of $\alpha_{\mathrm{min}}/\pi$ and β_{min} in the special case $\lambda = 0$, and the dashed line in Figure 2.9(a) shows the corresponding value of $\alpha_{\mathrm{min}}/\pi$ in the limit $\lambda \to \infty$. In particular, Figure 2.9 illustrates that, in the limit of weak slip, $\lambda \to 0^+$, both $\alpha_{\mathrm{min}}/\pi$ and β_{min} are monotonically decreasing functions of λ satisfying

$$\alpha_{\mathrm{min}} \sim \alpha_0 - \frac{B_2'(\alpha_0)}{B_1''(\alpha_0)}\lambda \to \alpha_0^- \tag{2.51}$$

where

$$B_1(\alpha) = \left(\frac{9m^4\bar{Q}}{f(m\bar{a})\sin\alpha}\right)^{\frac{1}{3}} \quad \text{and} \quad B_2(\alpha) = -\frac{3mg(m\bar{a})}{f(m\bar{a})}, \tag{2.52}$$

and

$$\beta_{\mathrm{min}} \sim \left(\frac{9m_0^4\bar{Q}}{f(m_0\bar{a})\sin\alpha_0}\right)^{\frac{1}{3}} - \frac{3m_0 g(m_0\bar{a})}{f(m_0\bar{a})}\lambda \to \left(\frac{9m_0^4\bar{Q}}{f(m_0\bar{a})\sin\alpha_0}\right)^{\frac{1}{3}\,-} \tag{2.53}$$

where $m_0 = m(\alpha_0)$ and α_0 is given by

$$\alpha_0 = \pi - \cos^{-1}\left(\frac{\left[H^{-1}(\bar{a})\right]^2}{\bar{a}^2}\right), \tag{2.54}$$

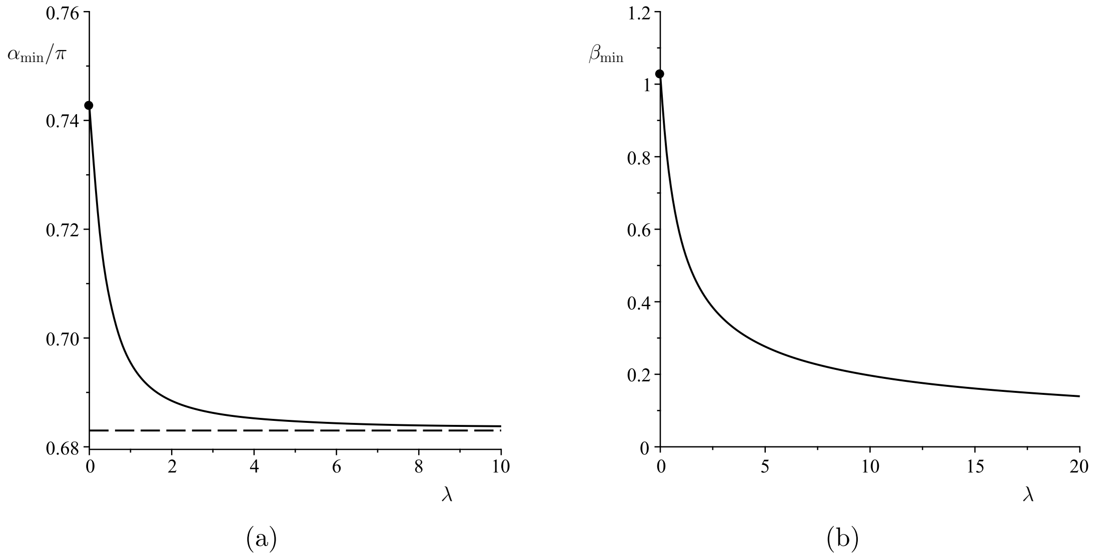

(a) (b)

Figure 2.9: Plots of (a) $\alpha_{\min}/\pi$ and (b) $\beta_{\min}$ as functions of the slip length λ for a rivulet with constant semi-width $\bar{a} = 2$ $(< \pi)$ when $\bar{Q} = 1$. The dots (●) indicate the corresponding values of (a) $\alpha_{\min}/\pi \simeq 0.74265$ and (b) $\beta_{\min} \simeq 1.02486$ in the special case $\lambda = 0$, and the dashed line in (a) shows the corresponding value of $\alpha_{\min}/\pi \simeq 0.6833$ in the limit $\lambda \to \infty$.

where H^{-1} is the inverse function for $H(x)$ given by

$$H(x) = x\left(\frac{xf'(x) - 2f(x)}{xf'(x) - 4f(x)}\right)^{\frac{1}{4}}, \tag{2.55}$$

where $x = m_0\bar{a}$.

In the limit of strong slip, $\lambda \to \infty$, we have

$$\alpha_{\min} \sim \alpha_0 - \frac{B_2'(\alpha_0)}{B_1''(\alpha_0)}\left(\frac{1}{\lambda}\right)^{\frac{3}{2}} \to \alpha_0^+ \tag{2.56}$$

where

$$B_1(\alpha) = \sqrt{\frac{m^3\bar{Q}}{g(m\bar{a})\sin\alpha}}, \quad B_2(\alpha) = -\frac{m^2\bar{Q}f(m\bar{a})}{18g^2(m\bar{a})\sin\alpha}, \tag{2.57}$$

and

$$\beta_{\min} \sim \sqrt{\frac{m_0^3\bar{Q}}{g(m_0\bar{a})\sin\alpha_0}}\left(\frac{1}{\lambda}\right)^{\frac{1}{2}} - \frac{m_0^2\bar{Q}f(m_0\bar{a})}{18g^2(m_0\bar{a})\sin\alpha_0}\left(\frac{1}{\lambda}\right)^{\frac{1}{2}} \to 0^+, \tag{2.58}$$

where α_0 is given by

$$\alpha_0 = \pi - \cos^{-1}\left(\frac{\left[W^{-1}(\bar{a})\right]^2}{\bar{a}^2}\right), \tag{2.59}$$

where W^{-1} is the inverse function for $W(x)$ given by

$$W(x) = x\left(\frac{xg'(x) - g(x)}{xg'(x) - 3g(x)}\right)^{\frac{1}{4}} \tag{2.60}$$

(see Appendix C for details of the derivation of this solution).

2.4.2 A wide rivulet with $a = \bar{a} > \pi$

For a wide rivulet with $a = \bar{a} > \pi$ for all values of $\bar{Q}$ and λ there is always a rivulet solution given by (2.45)–(2.47) and (2.33) only in the interval $0 \leq \alpha \leq \alpha_{\mathrm{c}}$, where the critical angle $\alpha = \alpha_{\mathrm{c}}(\bar{a})$ $(\pi/2 < \alpha_{\mathrm{c}} < \pi)$ is where the contact angle β reaches its minimum value of zero (*i.e.* $\beta = 0$ at $\alpha = \alpha_{\mathrm{c}}$). The critical angle $\alpha = \alpha_{\mathrm{c}}$ is given by solving $m\bar{a} = \pi$ to obtain

$$\alpha_{\mathrm{c}} = \cos^{-1}\left(-\frac{\pi^2}{\bar{a}^2}\right) \quad \text{for} \quad \bar{a} \geq \pi. \tag{2.61}$$

Note that α_{c} is independent of both $\bar{Q}$ and λ, and coincides exactly with the corresponding critical angle found by Paterson et al. [83] (their equation (19)) in the special case $\lambda = 0$ described in Subsection 1.4.2. From $\alpha = \alpha_{\mathrm{c}}$ to $\alpha = \pi$ we follow the analysis of Paterson et al. [83] which assumes that the contact lines de-pin at $\alpha = \alpha_{\mathrm{c}}$, *i.e.* the contact lines are no longer fixed, and assume that the rivulet runs with monotonically decreasing semi-width $a = \pi/m$ and zero contact angle according to the solution in the case $\beta = 0$ given by (2.18).

The behaviour of the contact angle β given by (2.45)–(2.47) for $0 \leq \alpha \leq \alpha_{\mathrm{c}}$ and by $\beta \equiv 0$ for $\alpha_{\mathrm{c}} \leq \alpha \leq \pi$ and the maximum thickness h_{m} given by (2.33) with β given by (2.45)–(2.47) for $0 \leq \alpha \leq \alpha_{\mathrm{c}}$ and by (1.22) and (2.21) for $\alpha_{\mathrm{c}} \leq \alpha \leq \pi$ when $a = \bar{a} > \pi$ is illustrated in Figures 2.10 and 2.11, which show plots of the contact angle β and the maximum thickness h_{m} as functions of α/π for various values of λ and $\bar{Q}$, respectively. The dots denote the values of $\beta = 0$ and $h_{\mathrm{m}} = h_{\mathrm{mc}}$ at $\alpha = \alpha_{\mathrm{c}}$ at which de-pinning

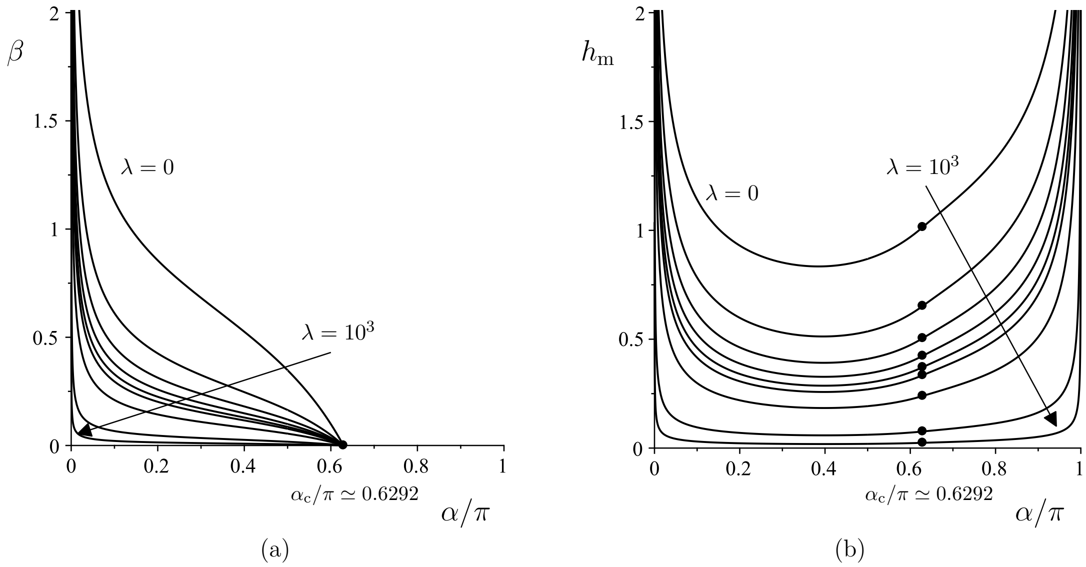

(a) (b)

Figure 2.10: Plots of (a) the contact angle β given by (2.45)–(2.47) for $\bar{a} = 5$, $0 \leq \alpha/\pi \leq \alpha_c/\pi \simeq 0.6292$ and by $\beta \equiv 0$ for $\alpha_c/\pi \leq \alpha/\pi \leq 1$ and (b) the maximum thickness h_m given by (2.33) with β given by (2.45)–(2.47) for $0 \leq \alpha/\pi \leq \alpha_c/\pi$ and by (1.22) and (2.21) for $\alpha_c/\pi \leq \alpha/\pi \leq 1$ as functions of the scaled angle α/π for a wide rivulet with constant width $a = \bar{a} = 5$ ($> \pi$) for $\lambda = 0, 1, 2, 3, 4, 5, 10, 100, 1000$ when $\bar{Q} = 1$. The dots (●) denote the values of $\beta = 0$ and $h_m = h_{mc}$ at $\alpha = \alpha_c$ at which de-pinning occurs.

occurs. In particular, Figures 2.10 and 2.11 illustrate that the rivulet becomes deep according to

$$\beta \sim \left(\frac{9\bar{Q}}{f(\bar{a})\alpha}\right)^{\frac{1}{3}} \to \infty \quad \text{and} \quad h_m \sim \left(\frac{9\bar{Q}}{f(\bar{a})\alpha}\right)^{\frac{1}{3}} \tanh\left(\frac{\bar{a}}{2}\right) \to \infty \tag{2.62}$$

as $\alpha \to 0^+$ and deep with finite semi-width π according to

$$a = \pi + \frac{\pi}{4}(\pi - \alpha)^2 + O(\pi - \alpha)^4 \to \pi^+ \tag{2.63}$$

and

$$h_m = \left(\frac{24\bar{Q}}{5\pi(\pi - \alpha)}\right)^{\frac{1}{3}} - \frac{6\lambda}{5} + O(\pi - \alpha)^{\frac{1}{3}} \to \infty \tag{2.64}$$

as $\alpha \to \pi^-$. Figure 2.10 also illustrates that both β and h_m are monotonically decreasing functions of λ, while Figure 2.11 illustrates that both β and h_m are monotonically increasing functions of $\bar{Q}$.

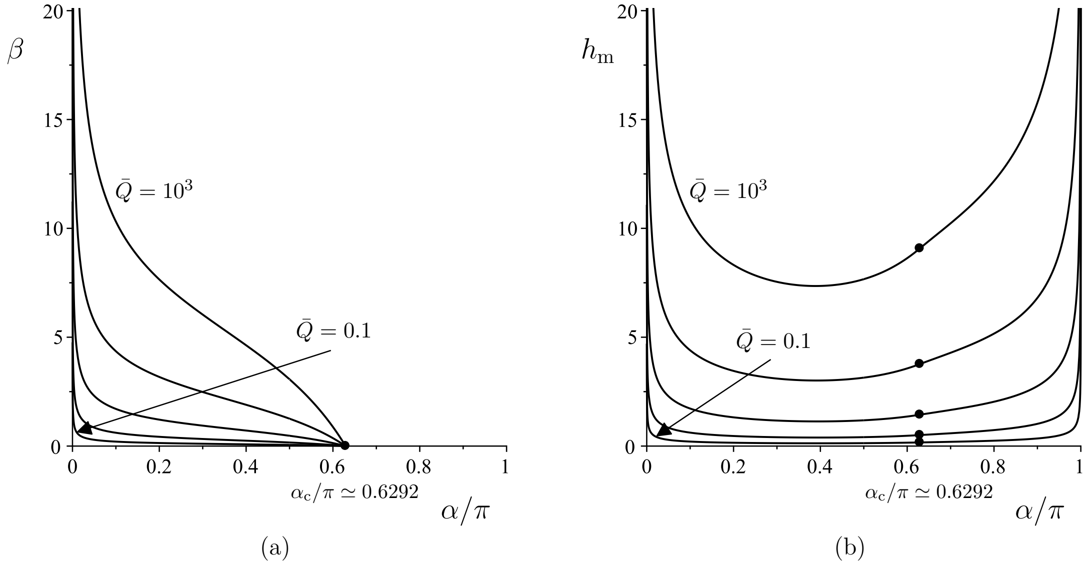

(a) (b)

Figure 2.11: As Figure 2.10, except for $\bar{Q} = 0.1, 1, 10, 100, 1000$ when $\lambda = 1$.

2.4.3 The limit of weak slip ($\lambda \to 0^+$)

In the limit of weak slip, $\lambda \to 0^+$, β and h_{m} take the forms

$$\beta = \beta_0 + \lambda\beta_1 + O\left(\lambda^2\right) \quad \text{and} \quad h_{\mathrm{m}} = h_{\mathrm{m}0} + \lambda h_{\mathrm{m}1} + O\left(\lambda^2\right). \tag{2.65}$$

For a narrow rivulet, the leading order terms β_0 and $h_{\mathrm{m}0}$ are given by

$$\beta_0 = \left(\frac{9\bar{Q}m^4}{f(m\bar{a})\sin\alpha}\right)^{\frac{1}{3}} \quad \text{and} \quad h_{\mathrm{m}0} = \left(\frac{9\bar{Q}m}{f(m\bar{a})\sin\alpha}\right)^{\frac{1}{3}} \tanh\left(\frac{m\bar{a}}{2}\right) \tag{2.66}$$

for $0 \le \alpha < \pi/2$,

$$\beta_0 = \left(\frac{105\bar{Q}}{4\bar{a}^4}\right)^{\frac{1}{3}} \quad \text{and} \quad h_{\mathrm{m}0} = \left(\frac{105\bar{Q}}{32\bar{a}}\right)^{\frac{1}{3}} \tag{2.67}$$

for $\alpha = \pi/2$,

$$\beta_0 = \left(\frac{9\bar{Q}m^4}{f(m\bar{a})\sin\alpha}\right)^{\frac{1}{3}} \quad \text{and} \quad h_{\mathrm{m}0} = \left(\frac{9\bar{Q}m}{f(m\bar{a})\sin\alpha}\right)^{\frac{1}{3}} \tan\left(\frac{m\bar{a}}{2}\right) \tag{2.68}$$

for $\pi/2 < \alpha \le \pi$, while for a wide rivulet, the leading order terms are the same as for a narrow rivulet for $0 \le \alpha < \alpha_{\rm c}$, and the same as for a perfectly wetting rivulet for $\alpha_{\rm c} \le \alpha \le \pi$ (*i.e.* the solution in the case of no slip $\lambda = 0$) in which

$$\beta_0 = 0 \quad \text{and} \quad h_{\rm m0} = \left(\frac{24\bar{Q}m}{5\pi \sin\alpha}\right)^{\frac{1}{3}}. \tag{2.69}$$

For a narrow rivulet, the first order terms β_1 and $h_{\rm m1}$ are given by

$$\beta_1 = -\frac{3mg(m\bar{a})}{f(m\bar{a})} \quad \text{and} \quad h_{\rm m1} = -\frac{3g(m\bar{a})}{f(m\bar{a})}\tanh\left(\frac{m\bar{a}}{2}\right) \tag{2.70}$$

for $0 \le \alpha < \pi/2$,

$$\beta_1 = -\frac{7}{3\bar{a}} \quad \text{and} \quad h_{\rm m1} = -\frac{7}{6} \tag{2.71}$$

at $\alpha = \pi/2$,

$$\beta_1 = -\frac{3mg(m\bar{a})}{f(m\bar{a})} \quad \text{and} \quad h_{\rm m1} = -\frac{3g(m\bar{a})}{f(m\bar{a})}\tan\left(\frac{m\bar{a}}{2}\right) \tag{2.72}$$

for $\pi/2 < \alpha \le \pi$, while for a wide rivulet, the first order terms are the same as for a narrow rivulet for $0 \le \alpha < \alpha_{\rm c}$, and the same as for a perfectly wetting rivulet for $\alpha_{\rm c} \le \alpha \le \pi$ in which

$$\beta_1 = 0 \quad \text{and} \quad h_{\rm m1} = -\frac{6}{5}. \tag{2.73}$$

2.4.4 The limit of strong slip ($\lambda \to \infty$)

In the limit of strong slip, $\lambda \to \infty$, a narrow rivulet becomes shallow according to

$$\beta \sim \left(\frac{\bar{Q}m^3}{\lambda \sin\alpha g(m\bar{a})}\right)^{\frac{1}{2}} \to 0^+ \quad \text{and} \quad h_{\rm m} \sim \left(\frac{\bar{Q}m}{\lambda \sin\alpha g(m\bar{a})}\right)^{\frac{1}{2}} \tanh\left(\frac{m\bar{a}}{2}\right) \to 0^+ \tag{2.74}$$

for $0 \le \alpha < \pi/2$,

$$\beta \sim \left(\frac{15\bar{Q}}{4\lambda\bar{a}^3}\right)^{\frac{1}{2}} \to 0^+ \quad \text{and} \quad h_{\rm m} \sim \left(\frac{15\bar{Q}}{16\lambda\bar{a}}\right)^{\frac{1}{2}} \to 0^+ \tag{2.75}$$

at $\alpha = \pi/2$, and

$$\beta \sim \left(\frac{\bar{Q}m^3}{\lambda \sin\alpha g(m\bar{a})}\right)^{\frac{1}{2}} \to 0^+ \quad \text{and} \quad h_{\mathrm{m}} \sim \left(\frac{\bar{Q}m}{\lambda \sin\alpha g(m\bar{a})}\right)^{\frac{1}{2}} \tan\left(\frac{m\bar{a}}{2}\right) \to 0^+ \tag{2.76}$$

for $\pi/2 < \alpha \leq \pi$, while for a wide rivulet, the solutions are the same as for a narrow rivulet for $0 \leq \alpha < \alpha_{\mathrm{c}}$, and the same as for a perfectly wetting rivulet for $\alpha_{\mathrm{c}} \leq \alpha \leq \pi$ in which

$$h_{\mathrm{m}} \sim \left(\frac{4\bar{Q}m}{3\pi\lambda \sin\alpha}\right)^{\frac{1}{2}} \to 0^+. \tag{2.77}$$

2.4.5 The limit of small flux ($\bar{Q} \to 0^+$)

In the limit of small flux, $\bar{Q} \to 0^+$, a narrow rivulet becomes shallow according to

$$\beta \sim \left(\frac{\bar{Q}m^3}{\lambda \sin\alpha g(m\bar{a})}\right)^{\frac{1}{2}} \to 0^+ \quad \text{and} \quad h_{\mathrm{m}} \sim \left(\frac{\bar{Q}m}{\lambda \sin\alpha g(m\bar{a})}\right)^{\frac{1}{2}} \tanh\left(\frac{m\bar{a}}{2}\right) \to 0^+ \tag{2.78}$$

for $0 \leq \alpha < \pi/2$,

$$\beta \sim \left(\frac{15\bar{Q}}{4\lambda\bar{a}^3}\right)^{\frac{1}{2}} \to 0 \quad \text{and} \quad h_{\mathrm{m}} \sim \left(\frac{15\bar{Q}}{16\lambda\bar{a}}\right)^{\frac{1}{2}} \to 0^+ \tag{2.79}$$

at $\alpha = \pi/2$, and

$$\beta \sim \left(\frac{\bar{Q}m^3}{\lambda \sin\alpha g(m\bar{a})}\right)^{\frac{1}{2}} \to 0^+ \quad \text{and} \quad h_{\mathrm{m}} \sim \left(\frac{\bar{Q}m}{\lambda \sin\alpha g(m\bar{a})}\right)^{\frac{1}{2}} \tan\left(\frac{m\bar{a}}{2}\right) \to 0^+ \tag{2.80}$$

for $\pi/2 < \alpha \leq \pi$, while for a wide rivulet, the solutions are the same as for a narrow rivulet for $0 \leq \alpha < \alpha_{\mathrm{c}}$, and the same as for a perfectly wetting rivulet for $\alpha_{\mathrm{c}} \leq \alpha \leq \pi$ in which

$$h_{\mathrm{m}} \sim \left(\frac{4\bar{Q}m}{3\pi\lambda \sin\alpha}\right)^{\frac{1}{2}} \to 0^+. \tag{2.81}$$

2.4.6 The limit of large flux ($\bar{Q} \to \infty$)

In the limit of large flux, $\bar{Q} \to \infty$, a narrow rivulet becomes deep according to

$$\beta \sim \left(\frac{9\bar{Q}m^4}{\sin\alpha f(m\bar{a})}\right)^{\frac{1}{3}} \to \infty \quad \text{and} \quad h_{\mathrm{m}} \sim \left(\frac{9\bar{Q}m}{\sin\alpha f(m\bar{a})}\right)^{\frac{1}{3}} \tanh\left(\frac{m\bar{a}}{2}\right) \to \infty \tag{2.82}$$

for $0 \le \alpha < \pi/2$,

$$\beta \sim \left(\frac{105\bar{Q}}{4\bar{a}^4}\right)^{\frac{1}{3}} \to \infty \quad \text{and} \quad h_{\mathrm{m}} \sim \left(\frac{105\bar{Q}}{32\bar{a}}\right)^{\frac{1}{3}} \to \infty \tag{2.83}$$

at $\alpha = \pi/2$, and

$$\beta \sim \left(\frac{9\bar{Q}m^4}{\sin\alpha f(m\bar{a})}\right)^{\frac{1}{3}} \to \infty \quad \text{and} \quad h_{\mathrm{m}} \sim \left(\frac{9\bar{Q}m}{\sin\alpha f(m\bar{a})}\right)^{\frac{1}{3}} \tan\left(\frac{m\bar{a}}{2}\right) \to \infty \tag{2.84}$$

for $\pi/2 < \alpha \le \pi$, while for a wide rivulet, the solutions are the same as for a narrow rivulet for $0 \le \alpha < \alpha_{\mathrm{c}}$, and the same as for a perfectly wetting rivulet for $\alpha_{\mathrm{c}} \le \alpha \le \pi$ in which

$$h_{\mathrm{m}} = \left(\frac{24\bar{Q}m}{5\pi\sin\alpha}\right)^{\frac{1}{3}} - \frac{6\lambda}{5} + O\left(\left(\frac{1}{\bar{Q}}\right)^{\frac{1}{3}}\right) \to \infty. \tag{2.85}$$

2.5 A Rivulet with Constant Contact Angle $\beta = \bar{\beta}$ (> 0)

In this section we describe the steady, locally unidirectional flow of a slowly varying rivulet of non-perfectly wetting fluid with constant contact angle $\beta = \bar{\beta} > 0$ but slowly varying semi-width $a = a(\alpha)$. In Subsections 2.5.1–2.5.4 we describe the behaviour in the limits of weak slip, $\lambda \to 0^+$, strong slip, $\lambda \to \infty$, small flux, $\bar{Q} \to 0^+$, and large flux, $\bar{Q} \to \infty$, respectively.

If we set $Q = \bar{Q}$ with Q given by (2.34) and $\beta = \bar{\beta}$ (> 0), we get a transcendental equation for a, namely

$$f(ma) + \frac{9\lambda m}{\bar{\beta}} g(ma) - \frac{9\bar{Q}m^4}{\bar{\beta}^3 \sin\alpha} = 0, \tag{2.86}$$

which, in general, can only be solved numerically.

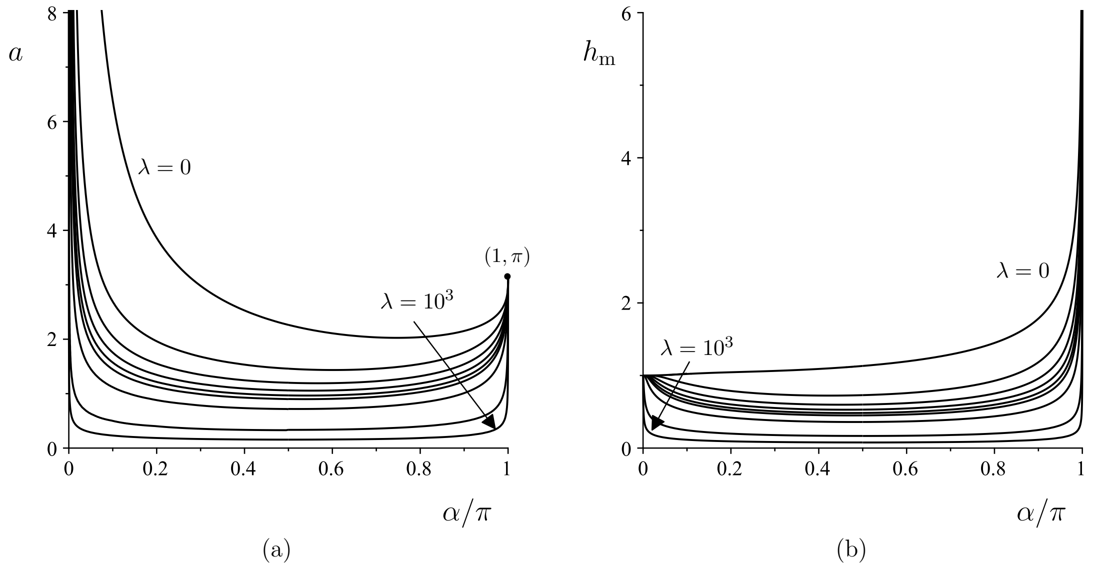

Figure 2.12: Plots of (a) the semi-width a obtained by solving (2.86) and (b) the maximum thickness h_m given by (2.33) as functions of the scaled angle α/π for a rivulet with constant contact angle $\beta = \bar{\beta} = 1$ for $\lambda = 0, 1, 2, 3, 4, 5, 10, 100, 1000$ when $\bar{Q} = 1$.

By setting $\lambda = 0$ in (2.86), we recover the solution of Duffy and Moffatt [31] in which the rivulet becomes infinitely wide at $\alpha = 0$ (*i.e.* $a \to \infty$ as $\alpha \to 0^+$) and its maximum thickness approaches the finite value $\bar{\beta}$, while the rivulet has a finite semi-width π at $\alpha = \pi$ and its maximum thickness becomes infinite (*i.e.* $h_\mathrm{m} \to \infty$ as $\alpha \to \pi^-$) according to

$$a \sim \frac{3\bar{Q}}{2\bar{\beta}^3\alpha} \to \infty \quad \text{and} \quad h_\mathrm{m} = \bar{\beta} + \frac{\bar{\beta}}{4}\alpha^2 + O(\alpha^4) \to \bar{\beta}^+ \tag{2.87}$$

as $\alpha \to 0^+$ and

$$a = \pi - \left(\frac{5\pi\bar{\beta}^3(\pi - \alpha)}{3\bar{Q}}\right)^{\frac{1}{3}} + O\left((\pi - \alpha)^2\right) \to \pi^- \tag{2.88}$$

and

$$h_\mathrm{m} = \left(\frac{24\bar{Q}}{5\pi(\pi - \alpha)}\right)^{\frac{1}{3}} + O\left((\pi - \alpha)^{\frac{1}{3}}\right) \to \infty \tag{2.89}$$

as $\alpha \to \pi^-$.

In the general case $\lambda > 0$, Figures 2.12 and 2.13 show plots of the semi-width a and the maximum thickness h_m as functions of the scaled angle α/π when $\bar{\beta} = 1$ for various

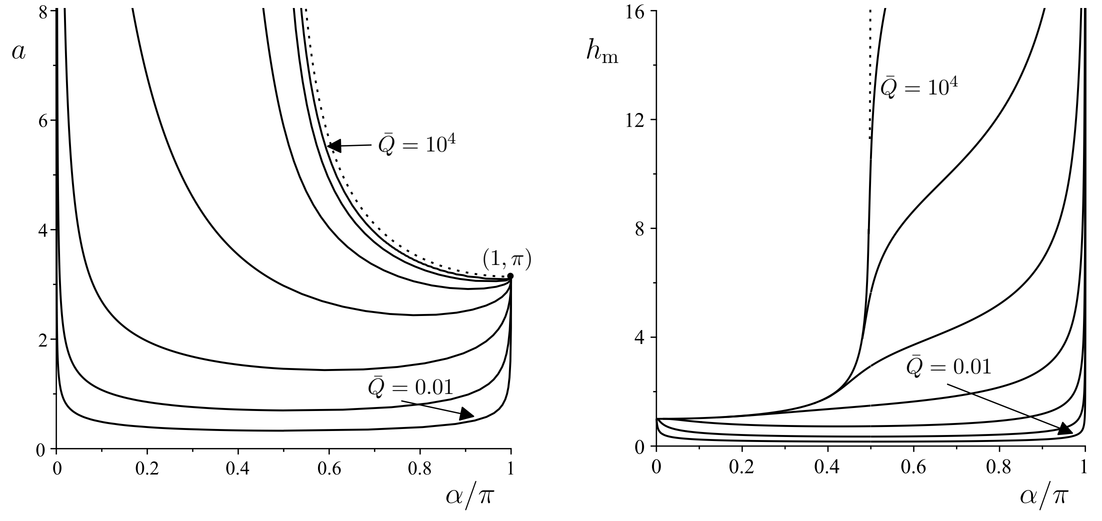

(a) (b)

Figure 2.13: As Figure 2.12, except for $\bar{Q} = 0.01, 0.1, 1, 10, 100, 1000, 10000$ when $\lambda = 1$. In (a) the dotted line denote the leading order solution for $a = \pi/m$ for $\pi/2 < \alpha \le \pi$ attained at leading order in the limit $\bar{Q} \to \infty$. In (b) the dotted line denotes the leading order solution for $h_{\rm m}$ for $0 < \alpha < \pi/2$ in the limit $\bar{Q} \to \infty$, namely $h_{\rm m} = \bar{\beta}/m$.

values of λ (≥ 0) when $\bar{Q} = 1$ in Figure 2.12 and for various values of $\bar{Q}$ when $\lambda = 1$ in Figure 2.13. In particular, Figures 2.12 and 2.13 illustrate that the rivulet becomes infinitely wide at $\alpha = 0$ (*i.e.* $a \to \infty$ as $\alpha \to 0^+$) and its maximum thickness approaches the finite value $\bar{\beta}$, while it becomes infinitely deep (*i.e.* $h_{\rm m} \to \infty$ as $\alpha \to \pi^-$) with finite semi-width π at $\alpha = \pi$ as shown in Figures 2.12 and 2.13 according to

$$a \sim \frac{3\bar{Q}}{2\bar{\beta}^2(\bar{\beta} + 3\lambda)\alpha} \to \infty \quad \text{and} \quad h_{\rm m} = \bar{\beta} + \frac{\bar{\beta}}{4}\alpha^2 + O\left(\alpha^4\right) \to \bar{\beta}^+ \tag{2.90}$$

as $\alpha \to 0^+$ and

$$a = \pi - \left(\frac{5\pi\bar{\beta}^3(\pi - \alpha)}{3\bar{Q}}\right)^{\frac{1}{3}} - \left(\frac{3\lambda^3\bar{\beta}^3\pi^2(\pi - \alpha)^2}{5\bar{Q}^2}\right)^{\frac{1}{3}} + O\left(\pi - \alpha\right) \to \pi^- \tag{2.91}$$

and

$$h_{\rm m} = \left(\frac{24\bar{Q}}{5\pi(\pi - \alpha)}\right)^{\frac{1}{3}} - \frac{6\lambda}{5} + O\left((\pi - \alpha)^{\frac{1}{3}}\right) \to \infty \quad \text{as} \quad \alpha \to \pi^-. \tag{2.92}$$

It can be shown numerically from (2.34) that there exists a critical flux $\bar{Q} = \bar{Q}_c(\lambda)$

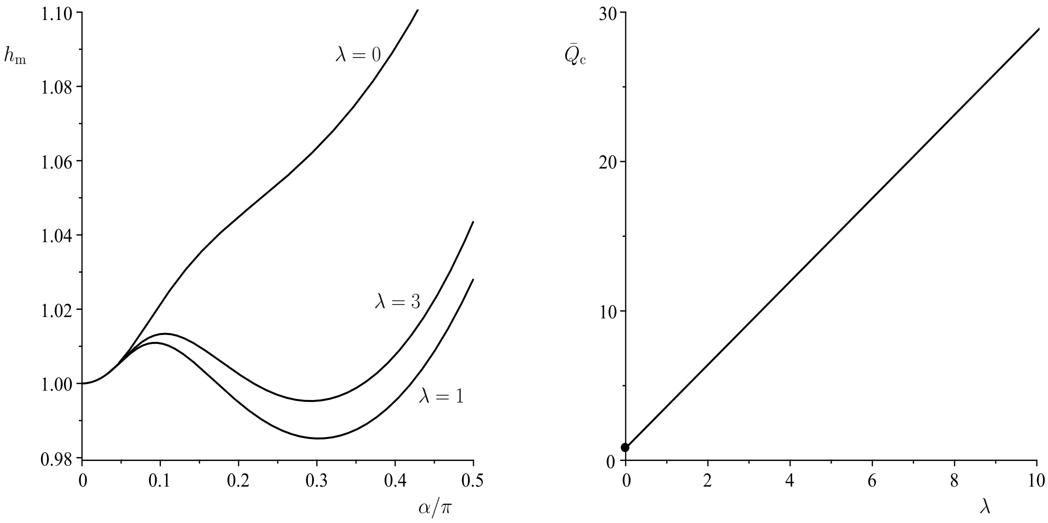

(a) (b)

Figure 2.14: Plots of (a) the maximum thickness $h_{\rm m}$ given by (2.34) as functions of the scaled angle α/π for a rivulet with constant contact angle $\beta = \bar{\beta} = 1$ for $\lambda = 0$ when $\bar{Q} = 1 > \bar{Q}_{\rm c} \simeq 0.817$, $\lambda = 1$ when $\bar{Q} = 3 < \bar{Q}_{\rm c} \simeq 3.614$ and $\lambda = 3$ when $\bar{Q} = 8 < \bar{Q}_{\rm c} \simeq 9.183$ and (b) the critical flux $\bar{Q}_{\rm c}$ as a function of λ. The dot (●) denotes the minimum value $\bar{Q}_{\rm c} \simeq 0.817$ at $\lambda = 0$.

such that if $\bar{Q} < \bar{Q}_c$ then $h_{\rm m}$ has two stationary points, and increases from $h_{\rm m} = 1$ at $\alpha = 0$ to a maximum in $0 < \alpha < \pi/2$, decreases to a minimum also in $0 < \alpha < \pi/2$, and then increases monotonically to ∞ as $\alpha \to \pi^-$, whereas if $\bar{Q} \geq \bar{Q}_c$ then $h_{\rm m}$ has no stationary points, and increases monotonically from $h_{\rm m} = 1$ at $\alpha = 0$ to $h_{\rm m} \to \infty$ as $\alpha \to \pi^-$. Figure 2.14(a) shows plots of the maximum thickness $h_{\rm m}$ given by (2.34) as a function of the scaled angle α/π for a rivulet with constant contact angle $\beta = \bar{\beta} = 1$ for two cases with $\bar{Q} = 3 < \bar{Q}_{\rm c}(1) \simeq 3.614$ and $\bar{Q} = 8 < \bar{Q}_{\rm c}(3) \simeq 9.183$, so that $h_{\rm m}$ has a local maximum and minimum, and for the case $\bar{Q} = 1 > \bar{Q}_{\rm c}(0) \simeq 0.817$ at which $h_{\rm m}$ has no stationary points. Figure 2.14(b) shows a plot of the critical flux $\bar{Q}_{\rm c}$ as function of λ and the dot denotes the minimum value $\bar{Q}_{\rm c} \simeq 0.817$ at $\lambda = 0$. In particular, Figure 2.14(b) shows that $\bar{Q}_{\rm c}$ is a nearly-linearly increasing function of λ for the range of values of λ shown.

Figure 2.12(a) shows that the semi-width a has a single minimum, denoted by $a = a_{\rm min}$ and occurring at $\alpha = \alpha_{\rm min}$. Therefore, in Figure 2.15 we show plots of $\alpha_{\rm min}/\pi$ and $a_{\rm min}$ plotted as functions of the slip length λ for a rivulet with constant contact

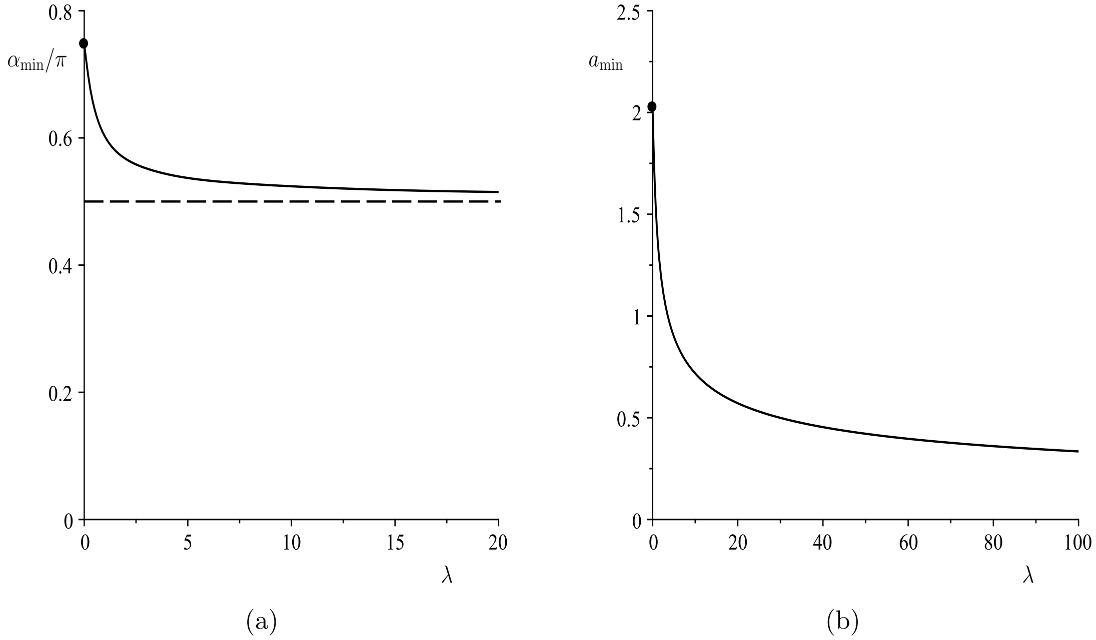

(a) (b)

Figure 2.15: Plots of (a) $\alpha_{\min}/\pi$ and (b) $a_{\min}$ as functions of the slip length λ for a rivulet with constant contact angle $\beta = \bar{\beta} = 1$ when $\bar{Q} = 1$. The dots (●) indicate the corresponding values of (a) $\alpha_{\min}/\pi \simeq 0.7474$ and (b) $a_{\min} \simeq 2.0252$ in the special case $\lambda = 0$, and the dashed line in (a) shows the corresponding value of $\alpha_{\min}/\pi \simeq 0.5$ in the limit $\lambda \to \infty$.

angle $\beta = \bar{\beta} = 1$ when $\bar{Q} = 1$. The dots indicate the corresponding values of $\alpha_{\min}/\pi$ and $a_{\min}$ in the special case $\lambda = 0$, and the dashed line in Figure 2.15(a) shows the corresponding value of $\alpha_{\min}/\pi$ in the limit $\lambda \to \infty$. In particular, Figure 2.15 illustrates that both $\alpha_{\min}/\pi$ and $a_{\min}$ are monotonically decreasing functions of λ, satisfying

$$\alpha_{\min} \sim \alpha_0 + \frac{9\lambda}{2\bar{\beta}} \frac{j(x)x}{s(x)} \sqrt{\frac{2f(x)}{f'(x)x - 4f(x)}} \to {\alpha_0}^{+} \tag{2.93}$$

and

$$a_{\min} \sim a_0 - \frac{9}{\bar{\beta}} \frac{g(x)}{f'(x)} \lambda \to {a_0}^{+} \tag{2.94}$$

in the limit of weak slip, $\lambda \to 0^{+}$, where $x = m(\alpha_0)a(\alpha_0)$ and

$$\alpha_0 = \pi - \arcsin \sqrt{\frac{2f(x)}{f'(x)x - 2f(x)}}, \tag{2.95}$$

$$a_0 = x\left(\frac{f'(x)x - 2f(x)}{f'(x)x - 4f(x)}\right)^{\frac{1}{4}}, \tag{2.96}$$

$$j(x) = \frac{g'(x)f'(x) - g(x)f''(x)}{\left[f'(x)\right]^2}, \tag{2.97}$$

$$s(x) = \frac{1}{2m_0}\frac{f(x)}{f'(x)}\left[3\frac{\left(f'(x)x - 2f(x)\right)^2}{f(x)\left(f'(x)x - 4f(x)\right)} - x^2\frac{f''(x)}{f'(x)x - 4f(x)} - 1\right], \tag{2.98}$$

and

$$\alpha_{\mathrm{min}} \sim \frac{\pi}{2} + \frac{1}{7}\left(\frac{15\bar{Q}}{4\bar{\beta}^2}\right)^{\frac{2}{3}}\left(\frac{1}{\lambda}\right)^{\frac{2}{3}} \to \frac{\pi^{+}}{2} \tag{2.99}$$

and

$$a_{\mathrm{min}} \sim \left(\frac{15\bar{Q}}{4\bar{\beta}^2}\right)^{\frac{1}{3}}\left(\frac{1}{\lambda}\right)^{\frac{1}{3}} - \frac{1}{21}\left(\bar{\beta} + \frac{15\bar{Q}}{56\bar{\beta}^2}\right)\left(\frac{15\bar{Q}}{4\bar{\beta}^2}\right)^{\frac{2}{3}}\left(\frac{1}{\lambda}\right)^{\frac{5}{3}} \to 0^{+} \tag{2.100}$$

in the limit of strong slip, $\lambda \to \infty$.

Figure 2.12(b) shows that the maximum thickness h_{m} has a single minimum, denoted by $h_{\mathrm{m}} = h_{\mathrm{m(min)}}$ and occurring at $\alpha = \alpha_{\mathrm{min}}$. Therefore, in Figure 2.16 we show plots α_{min} and $h_{\mathrm{m(min)}}$ plotted as functions of the slip length λ for a rivulet with constant contact angle $\beta = \bar{\beta} = 1$ when $\bar{Q} = 1$. The dot indicates the corresponding value of $h_{\mathrm{m(min)}}$ in the special case $\lambda = 0$, and the dashed line in Figure 2.16(a) shows the corresponding value of α_{min} in the limit $\lambda \to \infty$. In particular, Figure 2.16 illustrates that α_{min} is an increasing function of λ, while $h_{\mathrm{m(min)}}$ is monotonically decreasing function of λ, satisfying

$$\alpha_{\mathrm{min}} \sim \alpha_0 - \frac{s_2\left(\alpha_0\right)}{s_1'\left(\alpha_0\right)}\lambda \to {\alpha_0}^{+} \tag{2.101}$$

and

$$h_{\mathrm{m(min)}} \sim \frac{\beta}{m_0}h(x) - 9\frac{g(x)}{f'(x)}h'(x)\lambda \to \left.\frac{\beta}{m_0}h(x)\right.^{+} \tag{2.102}$$

in the limit of weak slip, $\lambda \to 0^{+}$, where $x = m_0 a_0$, $h(x) = \tanh(x/2)$ and

$$\alpha_{\mathrm{min}} \sim \frac{\pi}{2} - \frac{3}{112}\left(\frac{30\bar{Q}}{\bar{\beta}^2}\right)^{\frac{2}{3}}\left(\frac{1}{\lambda}\right)^{\frac{2}{3}} \to \frac{\pi^{-}}{2} \tag{2.103}$$

and

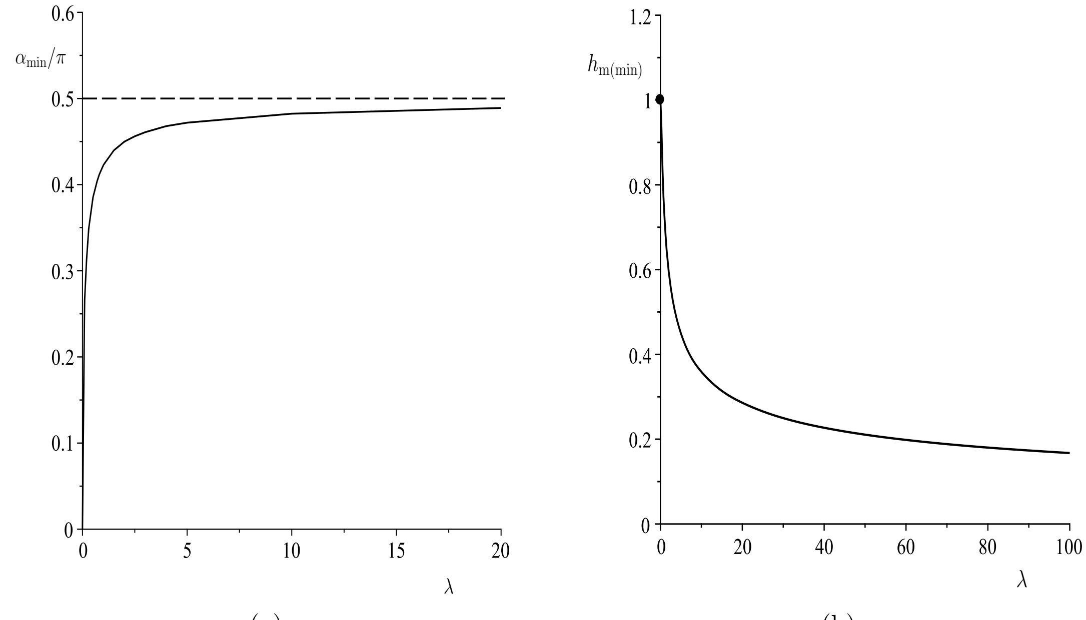

(a) (b)

Figure 2.16: Plots of (a) $\alpha_{\min}/\pi$ and (b) $h_{\mathrm{m(min)}}$ as functions of the slip length λ for a rivulet with constant contact angle $\beta = \bar{\beta} = 1$ when $\bar{Q} = 1$. The dashed line in (a) shows the corresponding value of $\alpha_{\min}/\pi \simeq 0.5$ in the limit $\lambda \to \infty$, and the dot (●) in (b) indicates the corresponding value of $h_{\mathrm{m(min)}} = 1$ in the special case $\lambda = 0$.

$$h_{\mathrm{m(min)}} \sim \frac{1}{2}\left(\frac{15\bar{\beta}\bar{Q}}{4}\right)^{\frac{1}{3}}\left(\frac{1}{\lambda}\right)^{\frac{1}{3}} \to 0^{+} \tag{2.104}$$

in the limit of strong slip, $\lambda \to \infty$, and

$$\alpha_0 = \sin^{-1}\sqrt{\frac{2h'(x)f(x)}{h(x)f'(x) - 2h'(x)f(x)}}, \tag{2.105}$$

$$s_1\left(\alpha_0\right) = \beta h\left(x\right)\frac{\tan\alpha_0}{2m_0} - \beta h'\left(x\right)\frac{f\left(x\right)}{m_0 f'\left(x\right)}[\cot\alpha_0 + 2\tan\alpha_0], \tag{2.106}$$

and

$$s_2\left(\alpha_0\right) = 9\left[\frac{g'(x)}{f'(x)}h'(x) - \frac{g(x)}{[f'(x)]^2}f''(x)h'(x) \ + \frac{g(x)}{f'(x)}h''(x)\right]\frac{\tan\alpha_0}{2}\frac{h(x)}{h'(x)} \tag{2.107}$$

(see Appendix D for details of the derivation of this solution).

2.5.1 The limit of weak slip ($\lambda \to 0^+$)

In the limit of weak slip, $\lambda \to 0^+$, the rivulet approaches its finite semi-width and finite maximum thickness according to

$$a = a_0 - \frac{9g(ma_0)}{\bar{\beta} f'(ma_0)}\lambda + O\left(\lambda^2\right) \to a_0^- \quad \text{and} \quad h_{\mathrm{m}} \sim \frac{\bar{\beta}}{m}\tanh\left(\frac{ma_0}{2}\right) = O(1) \qquad (2.108)$$

for $0 \leq \alpha < \pi/2$,

$$a = \left(\frac{105\bar{Q}}{4\bar{\beta}^3}\right)^{\frac{1}{4}} - \frac{7\lambda}{4\bar{\beta}} + O\left(\lambda^2\right) \to \left(\frac{105\bar{Q}}{4\bar{\beta}^3}\right)^{\frac{1}{4}-} \qquad (2.109)$$

and

$$h_{\mathrm{m}} = \left(\frac{105\bar{Q}\bar{\beta}}{64}\right)^{\frac{1}{4}} - \frac{7\lambda}{8} + O\left(\lambda^2\right) \to \left(\frac{105\bar{Q}\bar{\beta}}{64}\right)^{\frac{1}{4}-} \qquad (2.110)$$

for $\alpha = \pi/2$, and

$$a = a_0 - \frac{9g(ma_0)}{\bar{\beta} f'(ma_0)}\lambda + O\left(\lambda^2\right) \to a_0^- \quad \text{and} \quad h_{\mathrm{m}} \sim \frac{\bar{\beta}}{m}\tan\left(\frac{ma_0}{2}\right) = O(1) \qquad (2.111)$$

for $\pi/2 < \alpha \leq \pi$, where a_0 is given by

$$a_0 = \frac{1}{m} f^{-1}\left(\frac{9Qm^4}{\beta^3 \sin\alpha}\right) \qquad (2.112)$$

where f^{-1} is the inverse function for the function f.

2.5.2 The limit of strong slip ($\lambda \to \infty$)

In the limit of strong slip, $\lambda \to \infty$, the rivulet becomes narrow and shallow according to

$$a \sim \left(\frac{15\bar{Q}}{4\bar{\beta}^2 \lambda \sin\alpha}\right)^{\frac{1}{3}} \to 0^+ \quad \text{and} \quad h_{\mathrm{m}} \sim \left(\frac{15\bar{\beta}\bar{Q}}{32\lambda \sin\alpha}\right)^{\frac{1}{3}} \to 0^+ \qquad (2.113)$$

for all $0 \leq \alpha \leq \pi$.

2.5.3 The limit of small flux ($\bar{Q} \to 0^+$)

In the limit of small flux, $\bar{Q} \to 0^+$, the rivulet becomes narrow and shallow according to

$$a = \left(\frac{15\bar{Q}}{4\lambda\bar{\beta}^2 \sin\alpha}\right)^{\frac{1}{3}} - \frac{\bar{\beta}}{21\lambda}\left(\frac{15\bar{Q}}{4\lambda\bar{\beta}^2 \sin\alpha}\right)^{\frac{2}{3}} + O\left(\bar{Q}\right) \to 0^+ \tag{2.114}$$

and

$$h_{\mathrm{m}} \sim \left(\frac{15\bar{Q}\bar{\beta}}{32\lambda \sin\alpha}\right)^{\frac{1}{3}} \to 0^+ \tag{2.115}$$

for all $0 \le \alpha \le \pi$.

2.5.4 The limit of large flux ($\bar{Q} \to \infty$)

In the limit of large flux, $\bar{Q} \to \infty$, the rivulet becomes wide with finite thickness according to

$$a \sim \frac{3\bar{Q}m^3}{2\bar{\beta}^2 \sin\alpha\left(\bar{\beta} + 3\lambda m\right)} \to \infty \ \text{ and } h_{\mathrm{m}} \sim \frac{\bar{\beta}}{m}\tanh\left(\frac{3\bar{Q}m^4}{4\bar{\beta}^2 \sin\alpha\left(\bar{\beta} + 3\lambda m\right)}\right) \to \frac{\bar{\beta}}{m}^{-} = O(1) \tag{2.116}$$

for $0 \le \alpha < \pi/2$, wide and deep according to

$$a = \left(\frac{105\bar{Q}}{4\bar{\beta}^3}\right)^{\frac{1}{4}} - \frac{7\lambda}{4\bar{\beta}} + O\left(\left(\frac{1}{\bar{Q}}\right)^{\frac{1}{4}}\right) \to \infty \tag{2.117}$$

and

$$h_{\mathrm{m}} = \left(\frac{105\bar{Q}\bar{\beta}}{64}\right)^{\frac{1}{4}} - \frac{7\lambda}{8} + O\left(\left(\frac{1}{\bar{Q}}\right)^{\frac{1}{4}}\right) \to \infty \tag{2.118}$$

at $\alpha = \pi/2$, and deep with finite width according to

$$a = \frac{\pi}{m} - \left(\frac{5\pi\bar{\beta}^3 \sin\alpha}{3m^7\bar{Q}}\right)^{\frac{1}{3}} + O\left(\left(\frac{1}{\bar{Q}}\right)^{\frac{2}{3}}\right) \to \frac{\pi}{m}^{-} = O(1) \ \text{ and} \tag{2.119}$$

and

$$h_{\mathrm{m}} \sim \left(\frac{24\bar{Q}m}{5\pi \sin\alpha}\right)^{\frac{1}{3}} \to \infty \tag{2.120}$$

for $\pi/2 < \alpha \le \pi$.

2.6 Behaviour of a Rivulet with Greenspan Slip

In this section we consider the possibility of there being qualitative changes in the rivulet's behavior when using a slip condition different to that used in this chapter (*i.e.* the Navier slip condition). In particular, we use the Greenspan slip condition introduced by Greenspan [39] in which the constant Navier slip length λ is replaced with the non-constant Greenspan slip length, $\lambda = \lambda_{\mathrm{G}}/h$, where $\lambda_{\mathrm{G}} > 0$.

By analysing this problem with Greenspan slip in the same way as we did for Navier slip, we obtain the corresponding expressions for the velocity in (2.16) and the local flux in (2.17), namely

$$u = \frac{\sin\alpha}{2}\left[2\left(hz + \lambda_{\mathrm{G}}\right) - z^2\right] \tag{2.121}$$

and

$$\bar{u} = \frac{\sin\alpha}{3} h\left(h^2 + 3\lambda_{\mathrm{G}}\right), \tag{2.122}$$

respectively, and hence the volume fluxes in (2.34) and (2.18) become

$$Q = \frac{\beta^3\sin\alpha}{9m^4} f(ma) + \frac{\lambda_{\mathrm{G}}\beta\sin\alpha}{m^2} g_{\mathrm{G}}(ma) \tag{2.123}$$

and

$$Q = \frac{\pi\sin\alpha}{24m} h_{\mathrm{m}}\left(5h_{\mathrm{m}}^2 + 24\lambda_{\mathrm{G}}\right), \tag{2.124}$$

respectively, where the function $g_{\mathrm{G}}(ma)$ is given by

$$g_{\mathrm{G}}(ma) = \begin{cases} 2(ma\coth ma - 1) & \text{for } 0 \le \alpha < \dfrac{\pi}{2}, \\ \dfrac{2}{3}(ma)^2 & \text{for } \alpha = \dfrac{\pi}{2}, \\ 2(1 - ma\cot ma) & \text{for } \dfrac{\pi}{2} < \alpha \le \pi. \end{cases} \tag{2.125}$$

Similar to the analysis we presented in Section 2.2, we show that for $0 \le \alpha < \pi/2$ both g and g_{G} behave qualitatively similarly as both are positive and monotonically increasing functions from zero at $ma = 0$ to infinity as $ma \to \infty$, while their derivatives g' and g'_{G} are also positive and monotonically increasing functions from zero at $ma = 0$

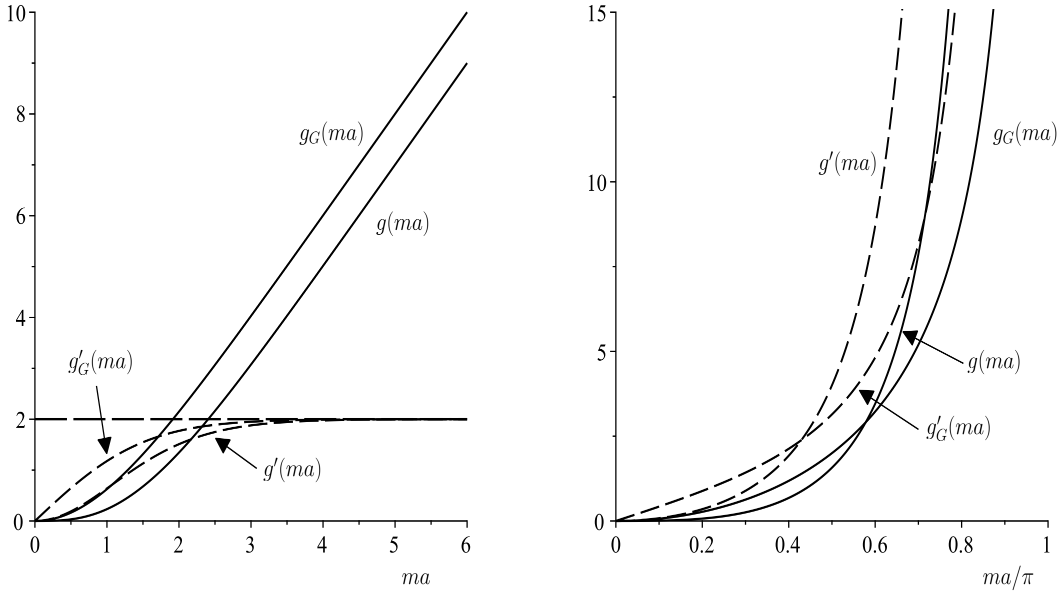

(a) (b)

Figure 2.17: Plots of g and g_{G} (solid lines), defined by (2.36) and (2.125) respectively, together with their derivatives g' and g'_{G} (dashed lines) as (a) functions of ma for $0 \leq \alpha < \pi/2$ when $0 \leq ma < \infty$, and (b) functions of ma/π for $\pi/2 < \alpha \leq \pi$ when $0 \leq ma < \pi$. The horizontal dashed lines in (a) show the constant asymptotic values for g' and g'_{G} in the limit $ma \to \infty$.

to 2 as $ma \to \infty$. Figure 2.17(a) shows plots of g, g_{G}, g', and g'_{G} as functions of ma for $0 \leq \alpha < \pi/2$. For $\pi/2 < \alpha \leq \pi$ both g and g_{G} and their derivatives g' and g'_{G} are positive and monotonically increasing functions from zero at $ma = 0$ to infinity as $ma \to \pi^-$. Figure 2.4(b) shows plots of g, g_{G}, g', and g'_{G} as functions of ma/π for $\pi/2 < \alpha \leq \pi$.

In the special case of a perfectly wetting fluid, $\beta = 0$, Setting $Q = \bar{Q}$ (where Q is given by (2.124)) yields a cubic equation for h_{m}, namely

$$h_{\mathrm{m}}^3 + \frac{24\lambda_{\mathrm{G}}}{5} h_{\mathrm{m}} - \frac{24\bar{Q}m}{5\pi\sin\alpha} = 0. \tag{2.126}$$

In the special case of zero Greenspan slip length, $\lambda_{\mathrm{G}} = 0$, we recover the solution for a rivulet of perfectly wetting fluid given in (1.22), while in the general case, $\lambda_{\mathrm{G}} > 0$, the real solution of (2.126) is given by

$$h_{\mathrm{m}} = \frac{\pi \sin\alpha}{A_1^{\frac{1}{3}}} \left(\frac{A_1^{\frac{2}{3}}}{5\pi^2 \sin^2\alpha} - 8\lambda_{\mathrm{G}} \right), \tag{2.127}$$

where

$$A_1 = \left(20\sqrt{5}\sqrt{32{\lambda_{\mathrm{G}}}^3\pi^2\sin^2\alpha + 45\bar{Q}^2 m^2} + 300\bar{Q}m \right) \pi^2 \sin^2\alpha. \tag{2.128}$$

2.6.1 The case of a rivulet with constant width $a = \bar{a}$ (> 0)

Similar to the analysis we performed in Section 2.4, we set $Q = \bar{Q}$ with Q given by (2.123) and $a = \bar{a}$, then β can be determined from the cubic equation for β, namely

$$\beta^3 + \frac{9\lambda_{\mathrm{G}} m^2 g_{\mathrm{G}}(m\bar{a})}{f(m\bar{a})}\beta - \frac{9\bar{Q}m^4}{f(m\bar{a})\sin\alpha} = 0. \tag{2.129}$$

Setting $\lambda_{\mathrm{G}} = 0$ in equation (2.129) recovers the solution for β given in (2.45) and the maximum thickness h_{m} is given by (2.33) with β given by (2.45).

In the general case, $\lambda_{\mathrm{G}} > 0$, the real solution of (2.129) for the contact angle β is

$$\beta = \frac{2\sin\alpha}{A_2^{\frac{1}{3}}} \left[\frac{A_2^{\frac{2}{3}}}{4f(m\bar{a})\sin^2\alpha} - 3\lambda_{\mathrm{G}} g_{\mathrm{G}}(m\bar{a}) \right], \tag{2.130}$$

where

$$A_2 = \left[12\sqrt{3}\sqrt{\frac{4g_{\mathrm{G}}(m\bar{a})^3{\lambda_{\mathrm{G}}}^3\sin^2\alpha + 3\bar{Q}^2 m^2 f(m\bar{a})}{f(m\bar{a})}} + 36\bar{Q}m \right] f(m\bar{a})^2 \sin^2\alpha, \tag{2.131}$$

where the corresponding solution for h_{m} is given by (2.33) with β given by (2.130).

2.6.2 The limit of strong Greenspan slip ($\lambda_{\mathrm{G}} \to \infty$)

In the limit of strong Greenspan slip length, $\lambda_{\mathrm{G}} \to \infty$, a narrow rivulet becomes shallow according to

$$\beta \sim \frac{\bar{Q}m^2}{\lambda_{\mathrm{G}} g_{\mathrm{G}}(m\bar{a})\sin\alpha} \to 0^+ \quad \text{and} \quad h_{\mathrm{m}} \sim \frac{\bar{Q}m}{\lambda_{\mathrm{G}} g_{\mathrm{G}}(m\bar{a})\sin\alpha}\tanh\left(\frac{m\bar{a}}{2}\right) \to 0^+ \tag{2.132}$$

while for a wide rivulet, the rivulet becomes shallow according to

$$\beta = 0 \quad \text{and} \quad h_{\mathrm{m}} \sim \frac{\bar{Q}m}{\pi\lambda_{\mathrm{G}}\sin\alpha} \to 0^+. \tag{2.133}$$

2.6.3 The case of a rivulet with constant contact angle $\beta = \bar{\beta}$ (> 0)

If we set $Q = \bar{Q}$ with Q given by (2.123) and $\beta = \bar{\beta}$ (> 0), we get a transcendental equation for a, namely

$$f(ma) + \frac{9\lambda_{\mathrm{G}} m^2}{\bar{\beta}^2} g_{\mathrm{G}}(ma) - \frac{9\bar{Q}m^4}{\bar{\beta}^3\sin\alpha} = 0, \tag{2.134}$$

which, in general, can only be solved numerically.

2.6.4 The limit of strong Greenspan slip $(\lambda_{\mathrm{G}} \to \infty)$

In the limit of strong Greenspan slip length, $\lambda_{\mathrm{G}} \to \infty$, the rivulet becomes narrow and shallow according to

$$a \sim \left(\frac{3\bar{Q}}{2\bar{\beta}\lambda_{\mathrm{G}}\sin\alpha}\right)^{\frac{1}{2}} \to 0^+ \quad \text{and} \quad h_{\mathrm{m}} \sim \left(\frac{3\bar{\beta}\bar{Q}}{8\lambda_{\mathrm{G}}\sin\alpha}\right)^{\frac{1}{2}} \to 0^+ \tag{2.135}$$

for all $0 \le \alpha \le \pi$.

2.7 Conclusions

In this chapter we investigated the locally unidirectional flow of a rivulet with positive prescribed flux $Q = \bar{Q} > 0$ on an inclined slippery locally planar substrate, subject to a Navier slip boundary condition. We considered both a rivulet with constant contact angle $\beta = \bar{\beta} > 0$ but slowly varying semi-width $a = a(\alpha)$ and a rivulet with constant semi-width $a = \bar{a}$ but slowly varying contact angle $\beta = \beta(\alpha)$, and showed that they have qualitatively different behaviour. In particular, we determined the effect that varying the slip length λ has on the rivulet and showed that features of the rivulet such as the shape and size of the rivulet depend strongly on the value of λ.

In Section 2.4 we showed that, while a narrow rivulet with constant semi-width $a = \bar{a} \le \pi$ can run from $\alpha = 0$ to $\alpha = \pi$, a wide rivulet with constant semi-width $a = \bar{a} > \pi$ can run from $\alpha = 0$ only to a critical angle $\alpha = \alpha_{\mathrm{c}}$, where its contact angle becomes zero. In particular, we showed that α_{c} is independent of λ. More fundamentally, Figure 2.7 shows that for any given value of α there can be a rivulet solutions for all values of $\lambda \ge 0$, while Figure 2.10 shows that there are no physically realisable rivulet solutions with $a = \bar{a} = 5$ $(> \pi)$ for all values of $\lambda \ge 0$ in the interval $\alpha_{\mathrm{c}} < \alpha \le \pi$. In this section the behaviour of a rivulet with a constant semi-width in the case of zero slip length is qualitatively different to those in the case of positive slip length. In particular, in the limit of strong slip, $\lambda \to \infty$, the rivulet becomes shallow like $O\left(\lambda^{-1/2}\right)$, while in the limit of large flux, $\bar{Q} \to \infty$, the rivulet becomes deep like $O\left(\bar{Q}^{1/3}\right)$.

In Section 2.5 we showed that a rivulet with constant contact angle $\beta = \bar{\beta} > 0$ can run from $\alpha = 0$ to $\alpha = \pi$. In addition, we showed that in the limit of weak slip, $\lambda \to 0^{+}$, the rivulet approaches its finite semi-width and maximum thickness in the case $\lambda = 0$, while in the limit of strong slip, $\lambda \to \infty$, the rivulet becomes narrow like $O\left(\lambda^{-1/3}\right)$ and shallow like $O\left(\lambda^{-1/3}\right)$. Moreover, the maximum thickness h_{m} of the rivulet with $\lambda > 0$ is qualitatively different for a rivulet with zero slip length. In particular, as Figures 2.12(b) and 2.16 illustrate, for $\lambda > 0$ the rivulet maximum thickness h_{m} has a single minimum value which does not exist for the case of $\lambda = 0$.

In Section 2.6 we anticipated that using other slip conditions would not lead to significant qualitative changes in the behavior of the rivulet. In particular, we used the Greenspan slip condition instead of the Navier slip condition and showed that in the limit of strong Greenspan slip, $\lambda_{\mathrm{G}} \to \infty$, the rivulet behave qualitatively similarly to that in the limit of strong Navier slip, $\lambda \to \infty$, described in Subsections 2.4.4 and 2.5.2 with $O\left(\lambda^{-1/2}\right)$ replaced by $O({\lambda_{\mathrm{G}}}^{-1})$ for a rivulet with constant width, and with $O(\lambda^{-1/3})$ replaced by $O({\lambda_{\mathrm{G}}}^{-1/2})$, for a rivulet with positive constant contact angle.

Chapter 3

Rivulet Flow Over and Through a Permeable Membrane

In this chapter we formulate and analyse a mathematical model for the steady gravity-driven flow of a rivulet of fluid over and through a permeable membrane. In particular, we show how the length of the rivulet on the permeable part of the membrane depends on the physical properties of the system, such as the angle of inclination of the membrane and the rivulet's semi-width and contact angle.

3.1 Problem Formulation

3.1.1 Problem description

Consider the steady three-dimensional gravity-driven flow of a symmetric rivulet of an incompressible Newtonian fluid (similar to that analysed in Sections 1.4 and 2.1) over and through a permeable membrane of uniform thickness H', inclined at an angle α $(0 \leq \alpha \leq \pi)$ to the horizontal. Referred to Cartesian coordinates $Ox'y'z'$ with the x' axis down the line of greatest slope, the y' axis horizontal, and the z' axis normal to the substrate $z' = 0$, the membrane at $z' = 0$ is impermeable for $x' \leq 0$ and is permeable with uniform permeability k' for $x' > 0$, as sketched in Figure 3.1. In $x' \leq 0$, the rivulet is uniform with constant volume flux $\bar{Q}' > 0$, constant contact angle

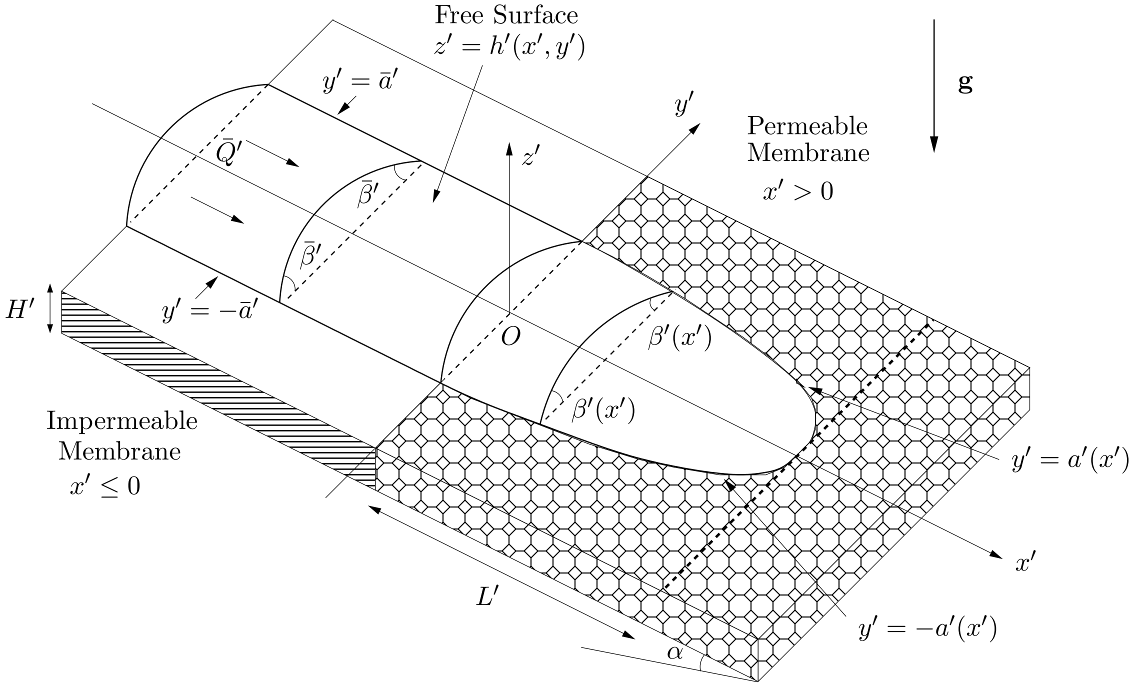

Figure 3.1: Geometry of the steady gravity-driven flow of a rivulet over and through a planar membrane of constant thickness H' which is impermeable for $x' \leq 0$, but permeable with permeability k' for $x' > 0$, inclined at an angle α $(0 \leq \alpha \leq \pi)$ to the horizontal.

$\bar{\beta}' > 0$, and constant semi-width $\bar{a}' > 0$. The fluid is assumed to have constant density ρ, viscosity μ, and coefficient of surface tension γ. The velocity $\mathbf{u}' = (u', v', w')$ and pressure $p'(x', y', z')$ of the fluid are governed by the mass conservation and Navier–Stokes equations (1.1) and (1.2), respectively. The Darcy velocity (*i.e.* the volume flux of fluid per unit area) $\mathbf{U}' = (U', V', W')$ and the pressure $P'(x', y', z')$ within the permeable part of the membrane both satisfy the mass conservation equation

$$\nabla' \cdot \mathbf{U}' = 0, \tag{3.1}$$

and Darcy's law

$$\mathbf{U}' = -\frac{k'}{\mu}\left(\nabla' P' - \rho \mathbf{g}\right), \tag{3.2}$$

where $\mathbf{g} = (g\sin\alpha, 0, -g\cos\alpha)$ denotes acceleration due to gravity. Combining (3.1) and (3.2) shows that P' satisfies Laplace's equation, *i.e.*

$$\nabla'^2 P' = 0. \tag{3.3}$$

The free surface profile is denoted by $z' = h'(x', y')$, so that $h'(x', y')$ is the thickness of the rivulet which satisfies $h' = 0$ when $x' = L'$, where L' is the length of the rivulet on the permeable membrane over which the fluid is completely absorbed. For $0 \leq x' \leq L'$, the contact angle of the rivulet is denoted by $\beta'(x')$ and the semi-width by $a'(x')$. The rivulet is continuous as it passes from the impermeable to the permeable part of the membrane, and so, in particular, Q', a' and β' take the initial values $\bar{Q}'$, $\bar{a}'$ and $\bar{\beta}'$, respectively, at $x' = 0$. We assume that once the fluid from the rivulet has passed through the membrane it plays no further role in the problem. Another assumption would be necessary to describe the situation in which some or all of the fluid adheres to the bottom surface of the membrane in the form of droplets and/or a new rivulet. However, in the present work we restrict our attention to the simplest case in which there is no fluid on the bottom surface of the membrane.

We consider the flow of a thin rivulet, for which the length scale in the z'-direction (denoted by $\delta_R \ell$) is much smaller than the length scale in the y'-direction (denoted by ℓ), which in turn is much smaller than the length scale in the x'-direction (denoted by ℓ/ϵ) *i.e.* $\delta_R \ell \ll \ell \ll \ell/\epsilon$, where δ_R ($\ll 1$) is the transverse aspect ratio of the rivulet and ϵ ($\ll 1$) is the longitudinal aspect ratio of the rivulet, and satisfy $\epsilon \ll \delta_R$. We also assume that $H' \ll h'$, so that $\delta_M \ll \delta_R$, *i.e.* that the membrane is much thinner than the rivulet, where δ_M ($\ll 1$) is the transverse aspect ratio of the membrane, and hence we can neglect the effect of gravity within the membrane. Note that the closely related situation in which the rivulet and the membrane are thin but the thickness of the membrane is comparable to that of the rivulet, *i.e.* when $\delta_M \sim \delta_R \ll 1$, in which gravitational effects will play a more significant role within the membrane, could be analysed using the same approach as that described in the present work. However, in the present work we restrict our attention to the simplest case in which the thickness of the membrane is much thinner than the rivulet.

3.1.2 Lubrication approximation

We non-dimensionalise and scale the variables describing the flow of the rivulet by writing:

$$x' = \frac{\ell}{\epsilon}x, \quad L' = \frac{\ell}{\epsilon}L, \quad y' = \ell y, \quad z' = \delta_R \ell z, \quad h' = \delta_R \ell h, \quad a' = \ell a, \quad \beta' = \delta_R \beta,$$
$$u' = \frac{\delta_R^2 \rho g \ell^2}{\mu}u, \quad v' = \frac{\epsilon \delta_R^2 \rho g \ell^2}{\mu}v, \quad w' = \frac{\epsilon \delta_R^3 \rho g \ell^2}{\mu}w, \quad Q' = \frac{\delta_R^3 \rho g \ell^4}{\mu'}Q, \tag{3.4}$$
$$p' = p_a + \delta_R \rho g \ell p,$$

and the variables describing the flow in the membrane by writing:

$$z' = \delta_M \ell Z, \quad H' = \delta_M \ell H, \quad k' = \epsilon \delta_R^2 \delta_M \ell^2 k,$$
$$U' = \frac{\epsilon \delta_R^2 \delta_M \rho g \ell^2}{\mu}U, \quad V' = \frac{\epsilon \delta_R^3 \delta_M \rho g \ell^2}{\mu}V, \quad W' = \frac{\epsilon \delta_R^3 \rho g \ell^2}{\mu}W, \tag{3.5}$$
$$P' = p_a + \delta_R \rho g \ell P,$$

where p_a denotes the constant atmospheric pressure and g denotes the magnitude of acceleration due to gravity. Note that while the assumption that the rivulet is thin requires that the unscaled contact angle $\beta' \ll 1$ must be small, the scaled contact angle $\beta (> 0)$ can take any positive value.

Furthermore, we may choose

$$\delta_R = \bar{\beta}', \quad \delta_M = \frac{H'}{\ell} \quad \text{and} \quad \epsilon = \frac{k'}{\delta_R^2 \delta_M \ell^2} = \frac{k'}{\bar{\beta}'^2 \ell H'}, \tag{3.6}$$

so that $\bar{\beta} = 1$, $H = 1$ and $k = 1$ without loss of generality. However, to keep the presentation as general as possible, we leave δ_R, δ_M and ϵ unspecified and retain $\bar{\beta}$, H and k in all of the analytical expressions for clarity.

With these scalings, the mass conservation and Navier–Stokes equations (1.1) and (1.2) become

$$u_x + v_y + w_z = 0, \tag{3.7}$$

$$Re^*(uu_x + vu_y + wu_z) = -\epsilon\delta_R p_x + \epsilon^2\delta_R^2 u_{xx} + \delta_R^2 u_{yy} + u_{zz} + \sin\alpha, \tag{3.8}$$

$$\epsilon Re^*(uv_x + vv_y + wv_z) = -\delta_R p_y + \epsilon(\epsilon^2\delta_R^2 v_{xx} + \delta_R^2 v_{yy} + v_{zz}), \tag{3.9}$$

$$\epsilon\delta_R Re^*(uw_x + vw_y + ww_z) = -p_z + \epsilon\delta_R(\epsilon^2\delta_R^2 w_{xx} + \delta_R^2 w_{yy} + w_{zz}) - \cos\alpha, \tag{3.10}$$

where $Re^* = \epsilon\delta_R^4\rho^2 g\ell^3/\mu^2$ is a reduced Reynolds number.

To obtain the lubrication equations for the rivulet, we assume that $Re^* \ll 1$, so that at leading order in δ_R and ϵ, equations (3.7)−(3.10) reduce to the well-known lubrication equations,

$$u_x + v_y + w_z = 0, \tag{3.11}$$

$$u_{zz} + \sin\alpha = 0, \tag{3.12}$$

$$-\delta_R p_y + \epsilon v_{zz} = 0, \tag{3.13}$$

$$-p_z - \cos\alpha = 0. \tag{3.14}$$

Next we will discuss the boundary conditions satisfied by these variables.

3.1.3 Boundary conditions

Depending on the nature of the membrane, a variety of boundary conditions, such as the slip condition discussed in Section 1.5 and used in Chapter 2 or the Beavers-Joseph condition described in Section 1.6, may be appropriate. However, for simplicity we restrict our attention to the simplest case of no flow in the x- and y-directions on the top surface of both the permeable and the impermeable parts of the membrane. In particular, the no-slip condition, relative to the fluid at the interface between the fluid layer and both the permeable and impermeable parts of the membrane, $z = 0$, is

$$u = 0 \quad \text{and} \quad v = 0 \quad \text{on} \quad z = 0. \tag{3.15}$$

The no-penetration condition at the impermeable part of the substrate is

$$w = 0 \quad \text{on} \quad z = 0 \quad \text{for} \quad x \leq 0. \tag{3.16}$$

On the permeable part of the membrane, we impose continuity of both pressure and normal velocity on $Z = 0$ and we impose continuity of pressure on the bottom surface of the membrane, $Z = -H$, *i.e.*

$$P = p \quad \text{and} \quad W = w \quad \text{on} \quad Z = 0, \tag{3.17}$$

$$P = 0 \quad \text{on} \quad Z = -H. \tag{3.18}$$

Note that in dimensionless variables, and by neglecting the effect of gravity since $\delta_M \ll \delta_R$ as previously mentioned, Darcy's law (3.2) and Laplace's equation (3.3) become

$$\mathbf{U} = (U, V, W) = -k \left(\epsilon \delta_R \frac{\partial P}{\partial X}, \frac{\partial P}{\partial Y}, \frac{\partial P}{\partial Z} \right), \tag{3.19}$$

$$\frac{\partial^2 P}{\partial Z^2} = 0. \tag{3.20}$$

Solving equation (3.20) subject to the boundary conditions (3.17) and (3.18) shows that

$$P = p(x, y, 0) \left(1 + \frac{Z}{H} \right). \tag{3.21}$$

Thus the Darcy velocity is given by $\mathbf{U} = (0, 0, W)$, where

$$W = -k \frac{\partial P}{\partial Z} = -\zeta p(x, y, 0), \tag{3.22}$$

where $\zeta = k/H$ is a non-dimensional membrane permeability. Therefore, the appropriate penetration condition on the permeable part of the substrate is

$$W = w = -\zeta p \quad \text{on} \quad z = 0. \tag{3.23}$$

There are two boundary conditions at the free surface $z = h(x, y)$. The first boundary condition is the kinematic condition

$$\frac{\mathrm{D}}{\mathrm{D}t}(z - h(x,y)) = 0 \quad \text{on} \quad z = h, \tag{3.24}$$

where $\mathrm{D}/\mathrm{D}t = \partial/\partial t + \mathbf{u}\cdot\nabla$ denotes the material time derivative. Hence for steady flow the kinematic boundary condition becomes

$$w = u\frac{\partial h}{\partial x} + v\frac{\partial h}{\partial y} \qquad \text{on} \quad z = h, \tag{3.25}$$

The second boundary condition is the continuity of stress condition

$$[\underline{\underline{\sigma}}\cdot\mathbf{n}]_1^2 = K\gamma\,\mathbf{n} \qquad \text{on} \quad z = h, \tag{3.26}$$

where, as described previously in Section 1.4, $\underline{\underline{\sigma}} = -p\mathbf{I} + \mu[\nabla\mathbf{u} + (\nabla\mathbf{u})^{\mathrm{T}}]$ is the stress tensor, $\mathbf{I}$ is the unit tensor, K is the mean curvature of the free surface, $\mathbf{n}$ is the unit vector normal to the free surface, and $[\phi]_1^2$ denotes the jump in the quantity ϕ going from region 1 just below the free surface to region 2 just above the free surface. At the free surface $z = h(x,y)$ the unit normal vector, the tangent vector in the x-direction, the tangent vector in the y-direction, and the curvature of the free surface are given by

$$\mathbf{n} = \frac{(-\epsilon\delta_R h_x, -\delta_R h_y, 1)}{(1 + \epsilon^2\delta_R^2 h_x^2 + \delta_R^2 h_y^2)^{1/2}}, \tag{3.27}$$

$$\mathbf{t}_x = \frac{(1, 0, \epsilon\delta_R h_x)}{(1 + \epsilon^2\delta_R^2 h_x^2)^{1/2}}, \tag{3.28}$$

$$\mathbf{t}_y = \frac{(0, 1, \delta_R h_y)}{(1 + \delta_R^2 h_y^2)^{1/2}}, \tag{3.29}$$

$$K = \frac{-(\epsilon^2\delta_R/\ell)h_{xx}(1 + \delta_R^2 h_y^2) - (\delta_R/\ell)h_{yy}(1 + \epsilon^2\delta_R^2 h_x^2) + 2(\epsilon^2\delta_R^3/\ell)h_x h_y h_{xy}}{(1 + \epsilon^2\delta_R^2 h_x^2 + \delta_R^2 h_y^2)^{3/2}}, \tag{3.30}$$

respectively. The normal and tangential components of (3.26) are

$$\mathbf{n}\cdot\underline{\underline{\sigma}}\cdot\mathbf{n} = K\gamma, \tag{3.31}$$

$$\mathbf{t}_x\cdot\underline{\underline{\sigma}}\cdot\mathbf{n} = 0, \tag{3.32}$$

$$\mathbf{t}_y\cdot\underline{\underline{\sigma}}\cdot\mathbf{n} = 0. \tag{3.33}$$

From equations (3.31), (3.32) and (3.33) we can obtain three scalar expressions for the normal and tangential stress balances, namely

$$\begin{aligned}-p&+\frac{2}{1+\epsilon^2\delta_R^2h_x^2+\delta_R^2h_y^2}[\epsilon^3\delta_R^3u_xh_x^2+\epsilon\delta_R^3v_yh_y^2+\epsilon\delta_R^3h_xh_y(u_y+\epsilon^2v_x)\\&\qquad-\epsilon\delta_Rh_x(u_z+\epsilon^2\delta_R^2w_x)-\delta_Rh_y(\epsilon v_z+\epsilon\delta_R^2w_y)+\epsilon\delta_Rw_z]\\&\qquad=\frac{C_\mathrm{a}^{-1}[-(\epsilon^2h_{xx}+h_{yy})-\epsilon^2\delta_R^2(h_{xx}h_y^2+h_{yy}h_x^2)+2\epsilon^2\delta_R^2h_xh_yh_{xy}]}{(1+\epsilon^2\delta_R^2h_x^2+\delta_R^2h_y^2)^{3/2}},\end{aligned}\tag{3.34}$$

$$\begin{aligned}2\epsilon^2\delta_R^2h_x(w_z-u_x)-\delta_R^2h_y(u_y+\epsilon^2v_x)+(u_z+\epsilon^2\delta_R^2w_x)-\epsilon^2\delta_R^2h_x^2(u_z+\epsilon^2\delta_R^2w_x)\\-\epsilon^2\delta_R^2h_yh_x(v_z+\delta_R^2w_y)=0,\end{aligned}\tag{3.35}$$

$$\begin{aligned}-\delta_R^2h_x(u_y+\epsilon^2v_x)-2\delta_R^2h_y(v_y-w_z)+(v_z+\delta_R^2w_y)+\delta_R^2h_yh_x(u_z+\epsilon^2\delta_R^2w_x)\\-\delta_R^2h_y^2(v_z+\delta_R^2w_y)=0,\end{aligned}\tag{3.36}$$

where $C_\mathrm{a}=\rho g\ell^2/\gamma$ is the appropriate capillary number. At leading order in δ_R and ϵ the normal and tangential stress-balances at the free surface $z=h(x,y)$ given by (3.34), (3.35) and (3.36) reduce to

$$p = -C_\mathrm{a}^{-1}h_{yy},\tag{3.37}$$

$$u_z = v_z = 0.\tag{3.38}$$

The condition of zero thickness at the contact-lines $y=\pm a$ is

$$h=0,\tag{3.39}$$

and the contact angle condition at the contact-lines $y=\pm a$ is

$$h_y=\mp\beta.\tag{3.40}$$

We define ℓ to be the capillary length $(\gamma/\rho g)^{1/2}$ so that $C_{\mathrm{a}} = 1$.

Solving equations (3.11)−(3.14) subject to the boundary conditions (3.15), (3.22), (3.37) and (3.38) gives

$$u = \frac{\sin\alpha}{2}(2hz - z^2), \tag{3.41}$$

$$v = \frac{\delta_R p_y}{2\epsilon}(z^2 - 2hz), \tag{3.42}$$

$$p = (h - z)\cos\alpha - h_{yy}, \tag{3.43}$$

$$w = -\frac{\sin\alpha}{2}h_x z^2 + \frac{\delta_R z^2}{2\epsilon}\big(p_{yy}h + p_y h_y - \frac{z}{3}p_{yy}\big) - \zeta(h\cos\alpha - h_{yy}). \tag{3.44}$$

An expression for $w(x, y, h)$ can be obtained by integrating the continuity equation (3.11), from $z = 0$ to $z = h$ subject to the boundary condition (3.23),

$$w(x,y,h) = -\zeta(h\cos\alpha - h_{yy}) - \frac{\partial}{\partial x}\int_0^h u\,\mathrm{d}z + u(x,y,h)\,\frac{\partial h}{\partial x} - \frac{\partial}{\partial y}\int_0^h v\,\mathrm{d}z + v(x,y,h)\,\frac{\partial h}{\partial y}. \tag{3.45}$$

Substituting the expression for $w(x, y, h)$ given in (3.45) into the kinematic condition (3.25) yields

$$\frac{\partial}{\partial x}\int_0^h u\,\mathrm{d}z + \frac{\partial}{\partial y}\int_0^h v\,\mathrm{d}z = -\zeta(h\cos\alpha - h_{yy}). \tag{3.46}$$

Substituting the solutions for u and v given by (3.41) and (3.42) into (3.46) gives the governing equation for h, namely

$$\frac{\sin\alpha}{3}h_x^3 - \frac{\delta_R h^3}{3\epsilon}(h\cos\alpha - h_{yy})_{yy} - \frac{\delta_R}{3\epsilon}(h^3)_y(h\cos\alpha - h_{yy})_y = -\zeta(h\cos\alpha - h_{yy}). \tag{3.47}$$

Note that, like Paterson et al. [83], we are considering the case $\epsilon \ll \delta_R$, so that (3.13) becomes $p_y = 0$, and hence from (3.47) h satisfies

$$\Big[h^3\,(h\cos\alpha - h_{yy})_y\Big]_y = 0, \tag{3.48}$$

so that

$$h^3(h\cos\alpha - h_{yy})_y = C, \tag{3.49}$$

and because of the boundary conditions the constant is zero and then we can divide by

h^3 to obtain

$$(h\cos\alpha - h_{yy})_y = 0. \tag{3.50}$$

We solve (3.50) subject to (3.39) and (3.40) to recover the free surface shape obtained by Duffy and Moffatt [31], as discussed in Section 1.4, namely

$$h = \beta \times \begin{cases} \dfrac{\cosh ma - \cosh my}{m \sinh ma} & \text{for } 0 \le \alpha < \dfrac{\pi}{2}, \\ \dfrac{a^2 - y^2}{2a} & \text{for } \alpha = \dfrac{\pi}{2}, \\ \dfrac{\cos my - \cos ma}{m \sin ma} & \text{for } \dfrac{\pi}{2} < \alpha \le \pi, \end{cases} \tag{3.51}$$

and so, in particular, the maximum thickness of rivulet, $h_m(x) = h(x, 0)$, is given by

$$h_m = \beta \times \begin{cases} \dfrac{1}{m} \tanh\left(\dfrac{ma}{2}\right) & \text{for } 0 \le \alpha < \dfrac{\pi}{2}, \\ \dfrac{a}{2} & \text{for } \alpha = \dfrac{\pi}{2}, \\ \dfrac{1}{m} \tan\left(\dfrac{ma}{2}\right) & \text{for } \dfrac{\pi}{2} < \alpha \le \pi, \end{cases} \tag{3.52}$$

where we have defined $m = |\cos\alpha|^{1/2}$.

3.1.4 Solution on the impermeable part of the membrane

On the impermeable part of the membrane, *i.e.* in $x \le 0$, the volume flux along the rivulet is given by

$$Q = 2\int_0^a \int_0^h u \,\mathrm{d}z\,\mathrm{d}y = \frac{\beta^3 \sin\alpha}{9m^4} f(ma), \tag{3.53}$$

where the function $f(ma)$, as described in Section 1.4 and Chapter 2, is given by

$$f(ma) = \begin{cases} 15ma\coth^3 ma - 15\coth^2 ma - 9ma\coth ma + 4 & \text{for } 0 \le \alpha < \dfrac{\pi}{2}, \\ \dfrac{12}{35}(ma)^4 & \text{for } \alpha = \dfrac{\pi}{2}, \\ -15ma\cot^3 ma + 15\cot^2 ma - 9ma\cot ma + 4 & \text{for } \dfrac{\pi}{2} < \alpha \le \pi. \end{cases} \tag{3.54}$$

As described in Section 1.4, in the special case of zero contact angle $\beta = 0$, Wilson and Duffy [120] showed that there is no rivulet solution for $0 \le \alpha \le \pi/2$ but for

$\pi/2 < \alpha \leq \pi$ there are infinitely many solutions given by

$$a = \frac{n\pi}{m}, \qquad h = \frac{h_m}{2}(1 - (-1)^n \cos my), \tag{3.55}$$

for $n = 1, 2, 3, ...$, and the maximum thickness of the rivulet h_m is given by

$$h_m = \left(\frac{24m\bar{Q}}{5n\pi \sin\alpha} \right)^{\frac{1}{3}}. \tag{3.56}$$

3.1.5 Solution on the permeable part of the membrane

On the permeable part of the membrane, by the global conservation of mass, the volume flux along the rivulet is equal to the sum of the volume flux along the rivulet at $x = 0$, namely $\bar{Q}$, and the (negative) volume flux lost through the membrane between $x = 0$ and the location x, namely

$$Q = \bar{Q} + \int_0^x \int_{-a(\tilde{x})}^{a(\tilde{x})} w(\tilde{x}, y, 0)\,\mathrm{d}y\,\mathrm{d}\tilde{x}. \tag{3.57}$$

Substituting the solution for p given in (3.43) into the condition of continuity of flux through the base of the rivulet (3.23) yields

$$w(x, y, 0) = -\zeta p(x, y, 0) = -\zeta\,(h\cos\alpha - h_{yy}) \quad \text{for} \quad x > 0, \tag{3.58}$$

hence, substituting (3.53) and (3.58) into (3.57) yields

$$\frac{2}{3}\int_0^{a(x)} h^3 \sin\alpha\,\mathrm{d}y = \bar{Q} - 2\zeta \int_0^x \int_0^{a(\tilde{x})} (h\cos\alpha - h_{yy})\,\mathrm{d}y\,\mathrm{d}\tilde{x}. \tag{3.59}$$

Substituting the solutions for h given in equation (3.51) into (3.59) leads to a key equation describing the behaviour of the rivulet on which all of the subsequent analysis is based, namely

$$\frac{\beta^3 \sin\alpha}{9m^4} f(ma) = \bar{Q} - 2\zeta \int_0^x \beta g(ma)\,\mathrm{d}\tilde{x}, \tag{3.60}$$

where the function $g(ma)$ is given by

$$g(ma) = \begin{cases} ma \coth ma & \text{for } 0 \leq \alpha < \dfrac{\pi}{2}, \\ 1 & \text{for } \alpha = \dfrac{\pi}{2}, \\ ma \cot ma & \text{for } \dfrac{\pi}{2} < \alpha \leq \pi. \end{cases} \tag{3.61}$$

Note that for sessile and vertical rivulets (*i.e.* for $0 \leq \alpha \leq \pi/2$) the pressure at the base of the rivulet, $\beta g(ma)/a$, is always positive, which always drives fluid out of the base of the rivulet and through the membrane. However, for a pendant rivulet (*i.e.* for $\pi/2 < \alpha \leq \pi$), there are three cases for the pressure at the base of the rivulet, *i.e.* positive, zero and negative. First case is when $a < a_{\mathrm{crit}}$, where $a_{\mathrm{crit}} = \pi/(2m)$, and in this case the pressure is positive which drives fluid out of the base of the rivulet and through the membrane. Second case is when $a = a_{\mathrm{crit}}$, and in this case the pressure at the base of the rivulet is precisely zero, and hence no fluid flows either out of or into the rivulet, and so the rivulet is infinitely long and remains uniform with constant semi-width $a = \bar{a}$ and constant contact angle $\beta = \bar{\beta}$ at all stations $x > 0$. The third case is when $a > a_{\mathrm{crit}}$, and in this case the pressure at the base of the rivulet is negative, which would draw fluid through the membrane and into the base of the rivulet. However, since, as previously noted, in the present work we assume that there is no fluid on the bottom surface of the membrane, this is impossible and so there is no physically realisable rivulet solution in this case. Hence, since $a \leq \bar{a}$ at all stations $x > 0$, there are sessile and vertical rivulet solutions for all values of $\bar{a}$, whereas there is a pendant rivulet solution only for $\bar{a} < a_{\mathrm{crit}}$. Note also that on the permeable membrane, there is no solution corresponding to a rivulet with zero contact angle, $\beta = 0$, as we have on the impermeable membrane given by (3.55) and (3.56), since such a rivulet is possible only for $\pi/2 < \alpha \leq \pi$ and has semi-width $a = \pi/m = 2a_{\mathrm{crit}}$, regardless of the value of $\bar{Q}$.

3.2 A Rivulet with Constant Semi-Width ($a \equiv \bar{a}$)

In this section we consider the case of a rivulet with constant semi-width. Setting $a = \bar{a}$ and differentiating (3.60) with respect to x yields the first-order ordinary differential equation for $\beta = \beta(x)$ ($\leq \bar{\beta}$) in $0 < x \leq L$, namely

$$\frac{\mathrm{d}\left(\beta^2\right)}{\mathrm{d}x} = -\frac{12\zeta m^4 g(m\bar{a})}{\sin\alpha f(m\bar{a})}, \tag{3.62}$$

which can be solved subject to the condition that $\beta(0) = \bar{\beta}$, to yield the explicit solution for β,

$$\beta = \bar{\beta}\left(1 - \frac{12\,\zeta\, m^4 g(m\bar{a})}{\bar{\beta}^2 \sin\alpha f(m\bar{a})} x\right)^{1/2}, \tag{3.63}$$

and hence, setting $\beta(L) = 0$, the length of the rivulet on the permeable membrane is given explicitly by

$$L = \frac{\bar{\beta}^2 \sin\alpha f(m\bar{a})}{12\,\zeta\, m^4 g(m\bar{a})}. \tag{3.64}$$

Note that, in the special case of a vertical rivulet, (3.63) and (3.64) reduce to simply

$$\beta = \bar{\beta}\left(1 - \frac{35\zeta}{\bar{\beta}^2 \bar{a}^4} x\right)^{1/2}, \quad L = \frac{\bar{\beta}^2 \bar{a}^4}{35\zeta}. \tag{3.65}$$

Inspection of the solution for L given by (3.64), shows that L is finite unless $g(m\bar{a}) = 0$, and so for a narrow rivulet with constant width $0 < \bar{a} < \pi/2$, there is a rivulet solution which has a finite length for all $0 \leq \alpha \leq \pi$, but for a wide rivulet with constant width $\bar{a} \geq \pi/2$, there exists a critical value of $\alpha = \alpha_{\mathrm{crit}}$ ($\pi/2 < \alpha_{\mathrm{crit}} \leq \pi$) such that there is a rivulet solution only for $0 \leq \alpha \leq \alpha_{\mathrm{crit}}$, which has a length that tends to infinity at α_{crit} and above which there is no physically realisable solution. The critical value α_{crit} is obtained by solving the equation $m\bar{a} = \pi/2$ for α to obtain

$$\alpha_{\mathrm{crit}} = \cos^{-1}\left(-\frac{\pi^2}{4\bar{a}^2}\right) \quad \text{for} \quad \bar{a} \geq \frac{\pi}{2}. \tag{3.66}$$

In what follows we describe the behaviour of both narrow and wide rivulets, and,

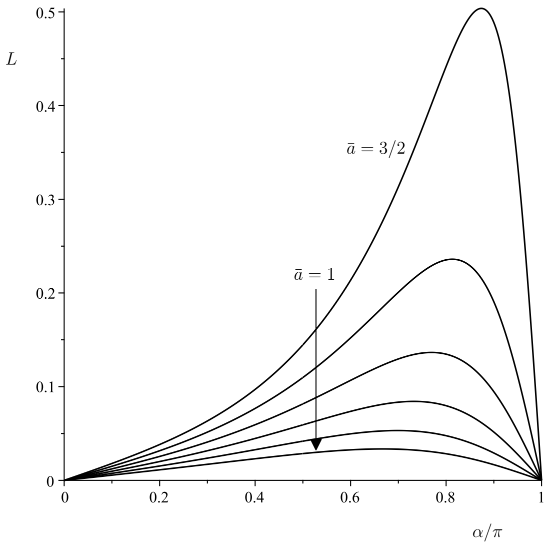

Figure 3.2: The length L of a rivulet with constant semi-width $a \equiv \bar{a}$ given by (3.64) plotted as a function of α/π for a narrow rivulet with $\bar{a} = 1, 1.1, 1.2, 1.3, 1.4, 1.5$ $(< \pi/2)$, initial contact angle $\bar{\beta} = 1$ and permeability constant $\zeta = 1$.

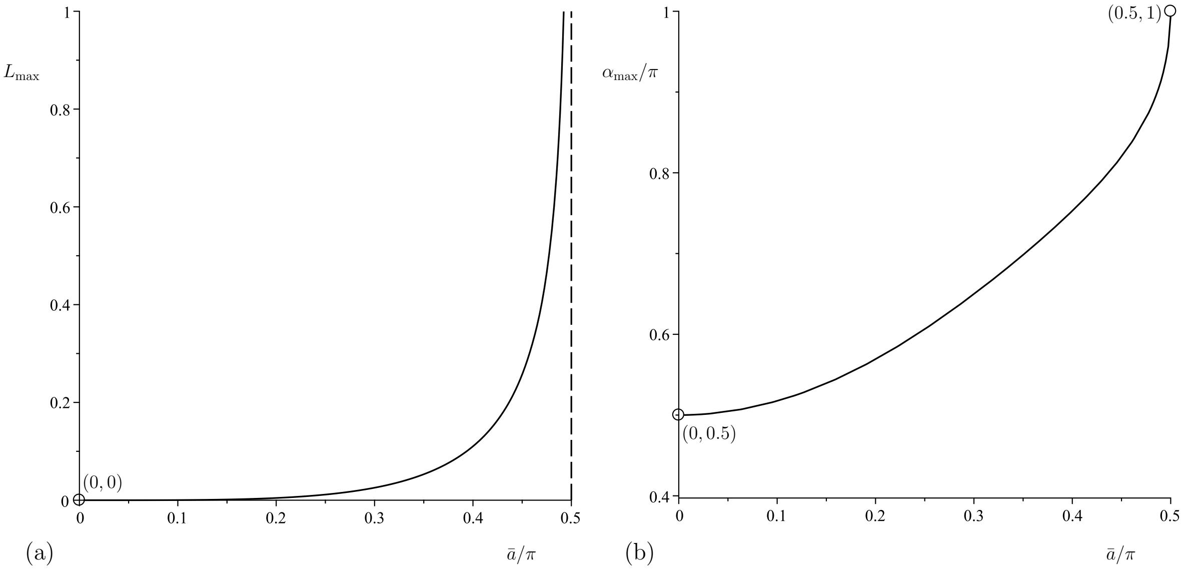

Figure 3.3: (a) $L_{\max}$ and (b) $\alpha_{\max}/\pi$ for a narrow rivulet with constant semi-width $a \equiv \bar{a}$ plotted as functions of $\bar{a}/\pi$ with initial contact angle $\bar{\beta} = 1$ and permeability constant $\zeta = 1$. The dashed line in part (a) denotes the vertical asymptote of $L_{\max}$ at $\bar{a} = \pi/2$.

in particular, their lengths L as a function of the scaled angle α/π, including sessile ($0 \leq \alpha < \pi/2$), vertical ($\alpha = \pi/2$), and pendant ($\pi/2 < \alpha \leq \pi$) rivulets.

3.2.1 A narrow rivulet with $0 < \bar{a} < \pi/2$

Figure 3.2 shows plots of L as a function of the scaled angle α/π for a narrow rivulet with constant semi-width $0 < \bar{a} < \pi/2$. Such rivulets exist and have a finite length for all $0 \leq \alpha \leq \pi$ which satisfies $L \to 0^+$ as $\alpha \to 0^+$ and $\alpha \to \pi^-$. Specifically, Figure 3.2 shows that for larger values of α the length of a narrow rivulet increases to a global maximum value $L = L_{\mathrm{max}}$ at $\alpha = \alpha_{\mathrm{max}}$ ($\pi/2 < \alpha_{\mathrm{max}} < \pi$) and then becomes short again.

Specifically, the asymptotic behaviour of L is

$$L \sim \frac{\bar{\beta}^2 f(\bar{a})}{12\zeta g(\bar{a})}\alpha \to 0^+ \tag{3.67}$$

as $\alpha \to 0^+$,

$$L = \frac{\bar{\beta}^2 \bar{a}^4}{35\zeta} + O\left(\alpha - \frac{\pi}{2}\right) \to \frac{\bar{\beta}^2 \bar{a}^4}{35\zeta} \tag{3.68}$$

as $\alpha \to \dfrac{\pi}{2}$, and

$$L \sim \frac{\bar{\beta}^2 f(\bar{a})}{12\zeta g(\bar{a})}(\pi - \alpha) \to 0^+ \tag{3.69}$$

as $\alpha \to \pi^-$.

Figure 3.3 shows (a) L_{max} and (b) $\alpha_{\mathrm{max}}/\pi$ for a narrow rivulet plotted as functions of $\bar{a}/\pi$, and, in particular, confirms that L_{max} and α_{max} are monotonically increasing functions of $\bar{a}$, and shows that L_{max} and α_{max} increase from $L_{\mathrm{max}} \to 0^+$ and $\alpha_{\mathrm{max}} = (\pi/2)^+$ as $\bar{a} \to 0^+$ to $L_{\mathrm{max}} \to \infty$ and $\alpha_{\mathrm{max}} \to \pi^-$ as $\bar{a} \to (\pi/2)^-$.

3.2.2 A wide rivulet with $\bar{a} \geq \pi/2$

Figure 3.4 shows plots of L as a function of the scaled angle α/π for a wide rivulet with constant semi-width $\bar{a} \geq \pi/2$. Such rivulets only exist and have a finite length for $0 \leq \alpha < \alpha_{\mathrm{crit}}$ with $L \to 0^+$ as $\alpha \to 0^+$ and $L \to \infty$ as $\alpha \to {\alpha_{\mathrm{crit}}}^-$, where α_{crit} ($\pi/2 < \alpha_{\mathrm{crit}} \leq \pi$) is given by (3.66). Specifically, Figure 3.4 shows that the length of a

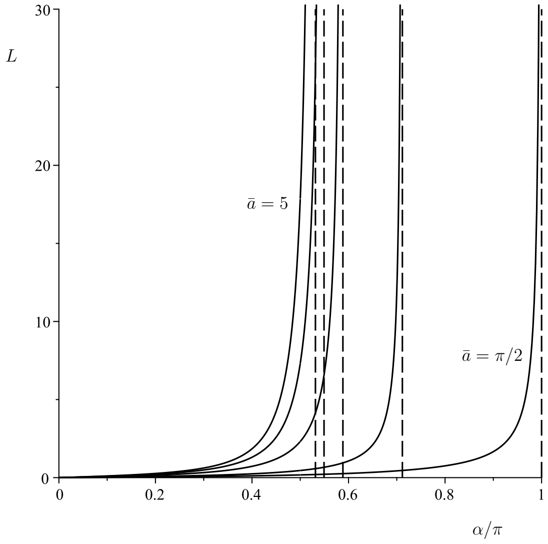

Figure 3.4: The length L of a rivulet with constant semi-width $a \equiv \bar{a}$ given by (3.64) plotted as a function of α/π for a wide rivulets with $\bar{a} = \pi/2, 2, 3, 4, 5$ $(\geq \pi/2)$, initial contact angle $\bar{\beta} = 1$ and permeability constant $\zeta = 1$. The dashed lines denote the vertical asymptotes of L at $\alpha = \alpha_{\rm crit}$.

wide rivulet always increases with α, and wide rivulets become infinitely long.

Specifically, the asymptotic behaviour of L is

$$L \sim \frac{\bar{\beta}^2 f(\bar{a})}{12\zeta g(\bar{a})}\alpha \to 0^+ \tag{3.70}$$

as $\alpha \to 0^+$,

$$L = \frac{\bar{\beta}^2 \bar{a}^4}{35\zeta} + O\big(\alpha - \frac{\pi}{2}\big) \to \frac{\bar{\beta}^2 \bar{a}^4}{35\zeta} \tag{3.71}$$

as $\alpha \to \dfrac{\pi}{2}$, and

$$L \sim \frac{32\bar{\beta}^2 \bar{a}^2}{3\zeta\pi^4}(\alpha_{\rm crit} - \alpha)^{-1} \to \infty \tag{3.72}$$

as $\alpha \to {\alpha_{\rm crit}}^-$.

3.2.3 Behaviour of the rivulet length L as a function of $\bar{a}$

Figure 3.5 shows a plot of L as a function of $\bar{a}$ for a sessile rivulets with a range of values of α $(< \pi/2)$. In particular, Figure 3.5 shows that the length of a sessile rivulet always increases with $\bar{a}$ towards a constant value. In this case the length of the rivulet is always finite and satisfies $L \to 0^+$ as $\bar{a} \to 0^+$ and $L \to \text{constant}^-$ as $\bar{a} \to \infty$.

Specifically, the asymptotic behaviour of L is

$$L = \frac{\bar{\beta}^2 \sin\alpha}{35\zeta}\,\bar{a}^4 + O\left(\bar{a}^6\right) \to 0^+ \tag{3.73}$$

as $\bar{a} \to 0^+$, and

$$L = \frac{\bar{\beta}^2 \sin\alpha}{2\zeta m^4} + O\left(\frac{1}{\bar{a}}\right) \to \left(\frac{\bar{\beta}^2 \sin\alpha}{2\zeta m^4}\right)^- \tag{3.74}$$

as $\bar{a} \to \infty$.

Note that the asymptotic behaviour of L as $\bar{a} \to \infty$ given by (3.74) provides the expression for the length of an infinitely-wide sessile sheet flowing over and through a permeable membrane, namely

$$L = \frac{\bar{\beta}^2 \sin\alpha}{2\zeta m^4} = \frac{\bar{h}_{\mathrm{m}}^2 \tan\alpha}{2\zeta}, \tag{3.75}$$

where $\bar{h}_{\mathrm{m}} = \bar{\beta}/m$ is the initial thickness of the sheet, which is in agreement with the corresponding expression given by Davis and Hocking [29] provided that their erroneous scaling of the membrane permeability is corrected as described in Appendix E.

Figure 3.6 shows plots of L as a function of $\bar{a}$ for a vertical and pendant rivulets with a range of values of α $(\geq \pi/2)$. Figure 3.6 shows that in the special case $\alpha = \pi/2$ the rivulet exists for all $\bar{a} > 0$ and satisfies $L \to 0^+$ as $\bar{a} \to 0^+$ and $L \to \infty$ as $\bar{a} \to \infty$. Specifically on the other hand, Figure 3.6 shows that when $\pi/2 < \alpha \leq \pi$ there is a critical value of $\bar{a} = \bar{a}_{\mathrm{crit}}$ at which the length of the rivulet tends to infinity and above which there is no physically realisable solution. The critical value $\bar{a}_{\mathrm{crit}}$ is obtained by solving the equation $ma = \pi/2$ for a to obtain

$$a_{\mathrm{crit}} = \frac{\pi}{2m} \quad \text{for} \quad \frac{\pi}{2} < \alpha \leq \pi. \tag{3.76}$$

When $\alpha = \pi/2$ the asymptotic behaviour of L is

$$L \sim \frac{\bar{\beta}^2}{35\zeta}\bar{a}^4 \to 0^+ \tag{3.77}$$

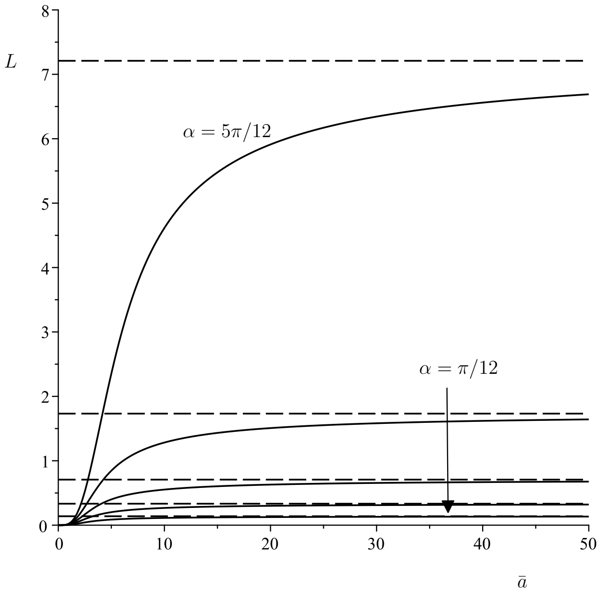

Figure 3.5: The length L of a rivulet with constant semi-width $a \equiv \bar{a}$ given by (3.64) plotted as a function of $\bar{a}$ for a sessile rivulets with $\alpha = \pi/12, \pi/6, \pi/4, \pi/3, 5\pi/12$ ($< \pi/2$), initial contact angle $\bar{\beta} = 1$ and permeability constant $\zeta = 1$. The dashed lines denote the asymptotic values of L as $\bar{a} \to \infty$.

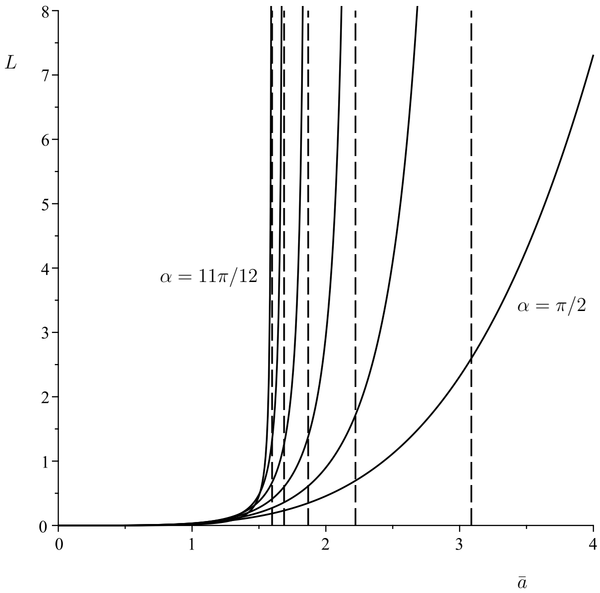

Figure 3.6: The length L of a rivulet with constant semi-width $a \equiv \bar{a}$ given by (3.64) plotted as a function of $\bar{a}$ for a vertical and pendant rivulets with $\alpha = \pi/2, 7\pi/12, 2\pi/3, 3\pi/4, 5\pi/6, 11\pi/12$ ($\geq \pi/2$). The dashed lines denote the vertical asymptotes of L at $\bar{a} = a_{\text{crit}}$ above which rivulet solutions do not exist.

as $\bar{a} \to 0^+$, and

$$L \sim \frac{\bar{\beta}^2}{35\zeta}\bar{a}^4 \to \infty \tag{3.78}$$

as $\bar{a} \to \infty$.

On the other hand, when $\pi/2 < \alpha \leq \pi$ the asymptotic behaviour of L is

$$L = \frac{\bar{\beta}^2 \sin\alpha}{35\zeta}\,\bar{a}^4 + O\left(\bar{a}^6\right) \to 0^+ \tag{3.79}$$

as $\bar{a} \to 0^+$, and

$$L \sim \frac{2\bar{\beta}^2 \sin\alpha}{3\zeta\pi m^5}\,(a_{\text{crit}} - \bar{a})^{-1} \to \infty \tag{3.80}$$

as $\bar{a} \to {a_{\text{crit}}}^-$.

3.2.4 Behaviour of the rivulet length L as a function of $\bar{\beta}$

Figures 3.7 and 3.8 show plots of L as a function of $\bar{\beta}$ for a rivulet on a substrate with angle $0 < \alpha \leq \pi$ for the cases $\bar{a} = 1$ $(< \pi/2)$ and $\bar{a} = 2$ $(\geq \pi/2)$, respectively. In particular, Figure 3.7 shows that, for different values of α, a rivulet exists for all $\bar{\beta} > 0$ and satisfies $L \to 0^+$ as $\bar{\beta} \to 0^+$ and $L \to \infty$ as $\bar{\beta} \to \infty$. Note that the length of the rivulet increases as we increase $\bar{\beta}$ for $0 \leq \alpha \leq \alpha_{\text{max}} = 2.095$ then the length decreases until it reaches zero, this behaviour is consistent with the results shown previously in Figure 3.2. On the other hand, Figure 3.8 shows that for $0 \leq \alpha \leq \alpha_{\text{crit}}$ the length of the rivulet always increases with $\bar{\beta}$ and satisfies $L \to 0^+$ as $\bar{\beta} \to 0^+$ and $L \to \infty$ as $\bar{\beta} \to \infty$.

Specifically, the asymptotic behaviour of L is

$$L \sim \frac{\sin\alpha f(m\bar{a})}{12\zeta m^4 g(m\bar{a})}\bar{\beta}^2 \to 0^+ \tag{3.81}$$

as $\bar{\beta} \to 0^+$, and

$$L \sim \frac{\sin\alpha f(m\bar{a})}{12\zeta m^4 g(m\bar{a})}\bar{\beta}^2 \to \infty \tag{3.82}$$

as $\bar{\beta} \to \infty$.

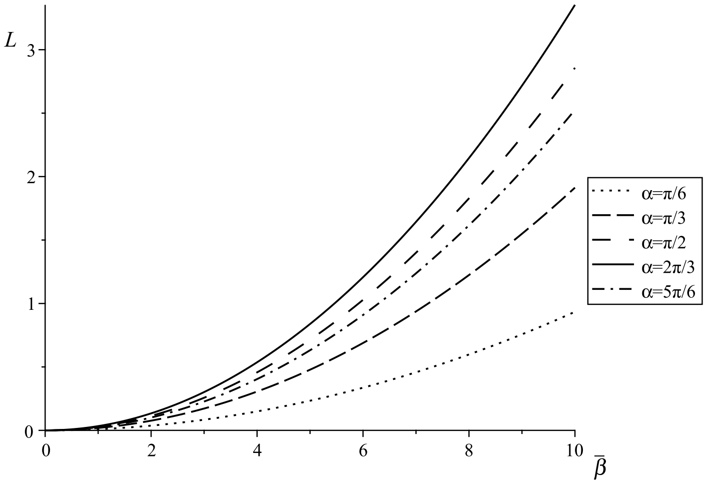

Figure 3.7: The length L of a rivulet with constant semi-width $a \equiv \bar{a}$ given by (3.64) plotted as a function of $\bar{\beta}$ for $\bar{a} = 1$ with $\alpha = \pi/6, \pi/3, \pi/2, 2\pi/3, 5\pi/6$ and permeability constant $\zeta = 1$.

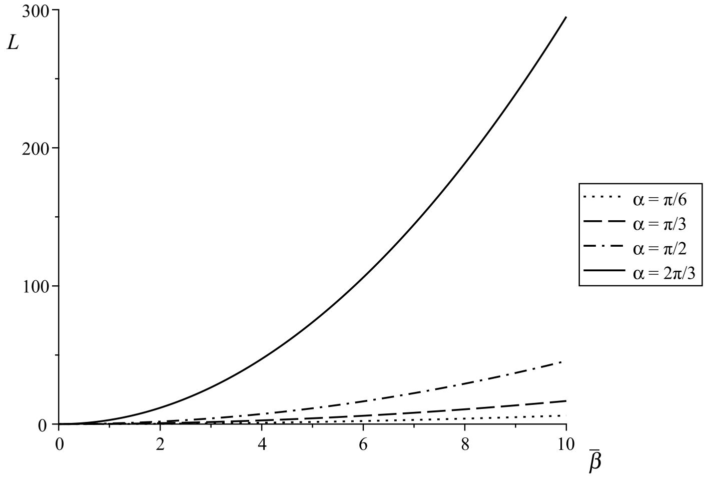

Figure 3.8: The length L of a rivulet with constant semi-width $a \equiv \bar{a}$ given by (3.64) plotted as a function of $\bar{\beta}$ for $\bar{a} = 2$ with $\alpha = \pi/6, \pi/3, \pi/2, 2\pi/3$ and permeability constant $\zeta = 1$.

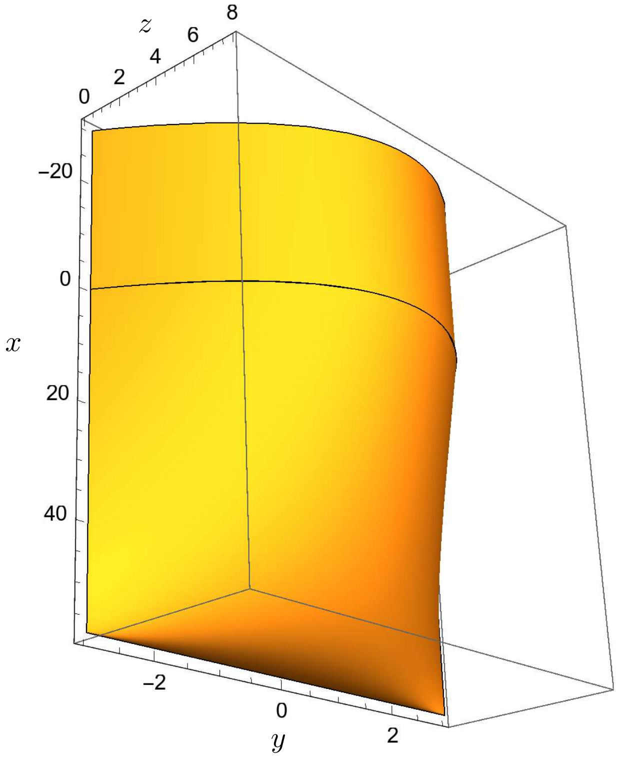

Figure 3.9: The three-dimensional shape of the free surface of a vertical rivulet with constant semi-width $a \equiv \bar{a} = 3$, initial contact angle $\bar{\beta} = 5$, permeability constant $\zeta = 1$, and length $L = \bar{\beta}^2\bar{a}^4/(35\zeta) = 2025/35 \simeq 57.8571$.

3.2.5 Rivulet shape

Figure 3.9 shows a typical example of the three-dimensional shape of the free surface of a vertical rivulet, and Figure 3.10 shows plots of the contact angle β as a function of x for a sessile and pendant rivulets and for a range of values of $\bar{a}$.

Specifically, the asymptotic behaviour of β is

$$\beta = \bar{\beta} - \frac{6\zeta m^4 g(m\bar{a})}{\bar{\beta}\sin\alpha f(m\bar{a})}x + O\left(x^2\right) \to \bar{\beta}^- \tag{3.83}$$

as $x \to 0^+$, and

$$\beta \sim \bar{\beta}\left(1 - \frac{12\,\zeta\, m^4 g(m\bar{a})}{\bar{\beta}^2\sin\alpha f(m\bar{a})}x\right)^{1/2} \to 0^+ \tag{3.84}$$

as $x \to L^-$, where L is given by (3.64).

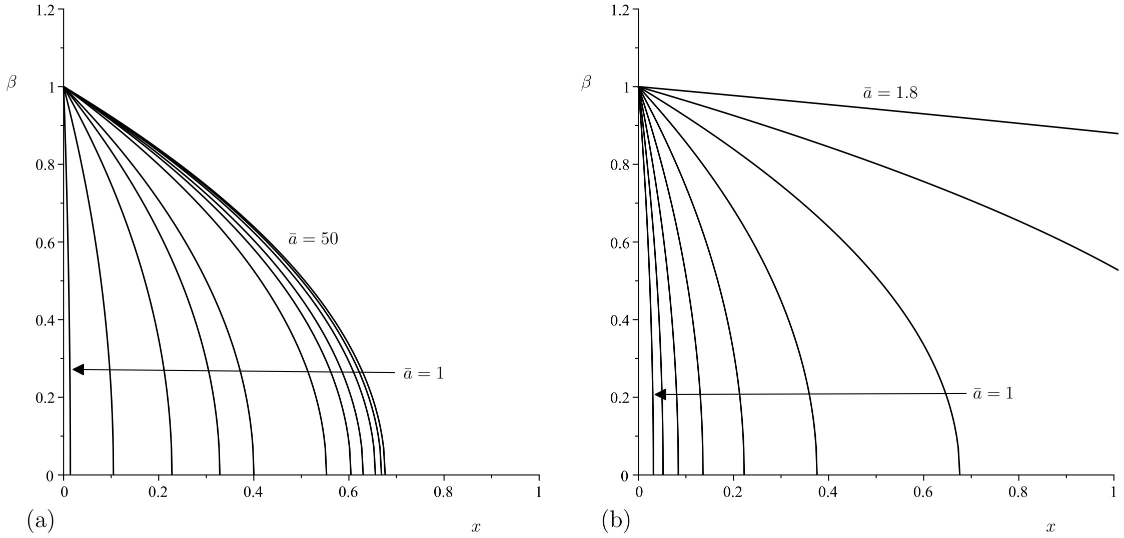

Figure 3.10: The contact angle β of a rivulet with constant semi-width $a \equiv \bar{a}$ given by (3.63) plotted as a function of x with initial contact angle $\bar{\beta} = 1$ and permeability constant $\zeta = 1$ for (a) a sessile rivulet with $\alpha = \pi/4$ for $\bar{a} = 1, 2, 3, 4, 5, 10, 15, 20, 30, 40, 50$, and (b) a pendant rivulet with $\alpha = 3\pi/4$ for $\bar{a} = 1, 1.1, 1.2, \ldots, 1.8$ ($< a_{\text{crit}} \simeq 1.8680$).

3.3 A Rivulet with Constant Contact Angle ($\beta \equiv \bar{\beta}$)

In this section we consider the case of a rivulet with constant contact angle. Setting $\beta = \bar{\beta}$ and differentiating (3.60) with respect to x yields a non-linear ordinary differential equation for $a = a(x)$ ($\leq \bar{a}$) in $0 < x \leq L$, namely

$$\frac{\mathrm{d}a}{\mathrm{d}x} = -\frac{18\zeta m^4 g(ma)}{\bar{\beta}^2 \sin\alpha\, q(ma)}, \tag{3.85}$$

where

$$q(ma) = \begin{cases} -45m^2 a \coth^4 ma + 54m^2 a \coth^2 ma + 45m \coth^3 ma - 9m^2 a - 39m \coth ma \\ \qquad\qquad\qquad\qquad\qquad\qquad\qquad\qquad \text{for } \ 0 \leq \alpha < \dfrac{\pi}{2}, \\ \dfrac{48}{35} m^4 a^3 \qquad\qquad\qquad\qquad\qquad\qquad\quad \text{for } \ \alpha = \dfrac{\pi}{2}, \\ 45m^2 a \cot^4 ma + 54m^2 a \cot^2 ma - 45m \cot^3 ma + 9m^2 a - 39m \cot ma \\ \qquad\qquad\qquad\qquad\qquad\qquad\qquad\qquad \text{for } \ \dfrac{\pi}{2} < \alpha \leq \pi. \end{cases} \tag{3.86}$$

For $\alpha = \pi/2$, equation (3.85) can be solved subject to the condition that $a(0) = \bar{a}$ to yield the exact solution for a,

$$a = \bar{a}\left(1 - \frac{105\,\zeta}{2\bar{\beta}^2\bar{a}^4}x\right)^{1/4}, \tag{3.87}$$

and hence, setting $a(L) = 0$, the length of the rivulet on the permeable membrane is given explicitly by

$$L = \frac{2\bar{\beta}^2\bar{a}^4}{105\,\zeta}, \tag{3.88}$$

while for $0 \leq \alpha < \pi/2$ and $\pi/2 < \alpha \leq \pi$ it is necessary to solve equation (3.85) numerically using a standard software package such as Maple. As we did in the constant semi-width case, we will describe the behaviour of sessile, vertical and pendant rivulets, and, in particular, describe their lengths L as a function of the scaled angle of inclination α/π.

In order to study the asymptotic behaviour of the length of the rivulet L, it is more convenient to consider x as a function of a, and we write (3.85) in terms of $x = x(a)$ to give

$$\frac{\mathrm{d}x}{\mathrm{d}a} = -\frac{\bar{\beta}^2 \sin\alpha\, q(ma)}{18\zeta m^4\, g(ma)}, \tag{3.89}$$

subject to

$$x(0) = L \quad \text{and} \quad x(\bar{a}) = 0. \tag{3.90}$$

3.3.1 A narrow rivulet with $0 < \bar{a} \leq \pi/2$

Figure 3.11 shows plots of L as a function of the scaled angle α/π for a narrow rivulet with constant contact angle $\beta = \bar{\beta}$ and for a range of values of $\bar{a}$ ($\bar{a} < \pi/2$). Such rivulets exist and have a finite length for all $0 \leq \alpha \leq \pi$. The length of the rivulet satisfies $L \to 0^+$ as $\alpha \to 0^+$ and $\alpha \to \pi^-$. In particular, Figure 3.11 shows that the length of a narrow rivulet increases to a global maximum value $L = L_{\max}$ at $\alpha = \alpha_{\max}$ and then becomes short again. Figure 3.12 shows (a) $L_{\max}$ and (b) $\alpha_{\max}/\pi$ for a narrow rivulet, plotted as functions of $\bar{a}/\pi$, and, in particular, confirms that $L_{\max}$ and $\alpha_{\max}$ are monotonically increasing functions of $\bar{a}$, and shows that $L_{\max}$ and

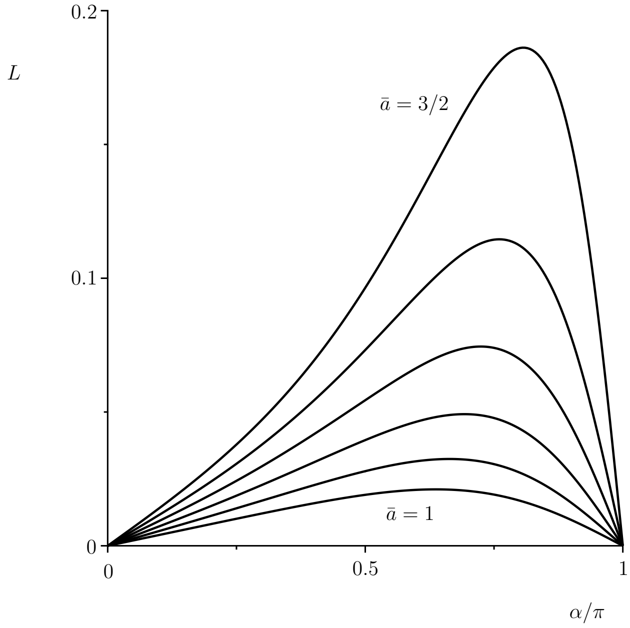

Figure 3.11: The length L of a rivulet with constant contact angle $\bar{\beta} = 1$ given by (3.85) plotted as a function of α/π for a narrow rivulet with initial semi-width $\bar{a} = 1, 1.1, 1.2, 1.3, 1.4, 1.5$ $(< \pi/2)$ and permeability constant $\zeta = 1$.

$\alpha_{\max}$ increase from $L_{\max} \to 0^+$ and $\alpha_{\max} = (\pi/2)^+$ as $\bar{a} \to 0^+$ to $L_{\max} = 0.2998$ and $\alpha_{\max} \simeq 0.8750\pi \simeq 2.7488$ when $\bar{a} = \pi/2$.

To study the behaviour of L as $\alpha \to 0^+$, we substitute (3.61) and (3.86) into (3.89) to get

$$\frac{\mathrm{d}x}{\mathrm{d}a} = -\frac{\bar{\beta}^2 \sin\alpha \left(-45m^2 a \coth^4 ma + 54m^2 a \coth^2 ma + 45m \coth^3 ma - 9m^2 a - 39m \coth ma\right)}{18\zeta m^5 a \coth ma}. \tag{3.91}$$

We expand the right-hand side of equation (3.91) as a Taylor series in powers of α. Then (3.91) becomes

$$\frac{\mathrm{d}x}{\mathrm{d}a} = f_1(a)\alpha + O\left(\alpha^3\right), \tag{3.92}$$

where

$$f_1(a) = -\frac{\bar{\beta}^2 \left(6\cosh^3 a \sinh a - 36a\, \cosh^2 a + 39\, \cosh a \sinh a - 9\, a\right)}{18\zeta a\, \sinh^3 a \cosh a}. \tag{3.93}$$

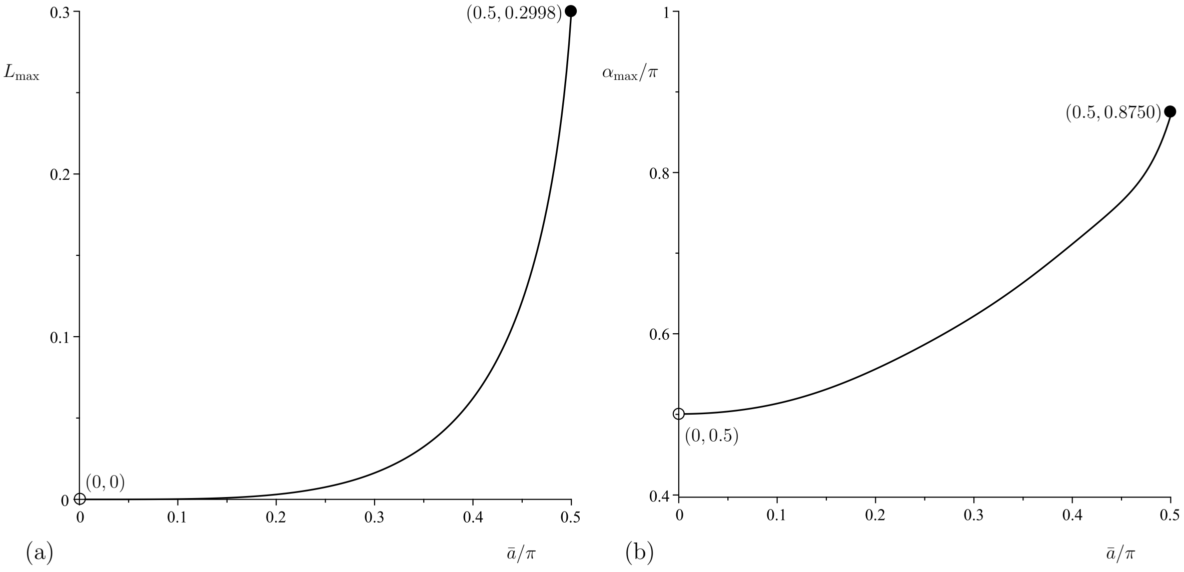

Figure 3.12: (a) $L_{\max}$ and (b) $\alpha_{\max}/\pi$ for a narrow rivulet with constant contact angle $\bar{\beta} = 1$ plotted as functions of $\bar{a}/\pi$ with permeability constant $\zeta = 1$.

Integrating equation (3.92) with respect to a, and taking into account that $x(\bar{a}) = 0$, we get

$$L = x(0) = F(\bar{a})\alpha + O\left(\alpha^3\right), \tag{3.94}$$

where

$$F(\bar{a}) = \int_{\bar{a}}^{0} f_1(a) \, \mathrm{d}a \tag{3.95}$$

As a result, the asymptotic behaviour of L is

$$L = F(\bar{a})\alpha + O(\alpha^3) \to 0^+ \tag{3.96}$$

as $\alpha \to 0^+$.

For the behaviour of L as $\alpha \to \pi/2^-$, we expand the right-hand side of equation (3.91) as a Taylor series in powers of $\pi/2 - \alpha$. Then (3.91) becomes

$$\frac{\mathrm{d}x}{\mathrm{d}a} = g_1(a) + g_2(a)\left(\frac{\pi}{2} - \alpha\right) + O\left(\left(\frac{\pi}{2} - \alpha\right)^2\right), \tag{3.97}$$

where

$$g_1(a) = -\frac{8\,\bar{\beta}^2 a^3}{105\,\zeta}, \tag{3.98}$$

$$g_2(a) = \frac{16\,\bar{\beta}^2 a^5}{315\,\zeta}. \tag{3.99}$$

Integrating equation (3.97) with respect to a, and taking into account that $x(\bar{a}) = 0$, we get

$$L = x(0) = B_1 + B_2\left(\frac{\pi}{2} - \alpha\right) + O\left(\left(\frac{\pi}{2} - \alpha\right)^2\right), \tag{3.100}$$

where

$$B_1 = \int_{\bar{a}}^{0} g_1(a)\ \mathrm{d}a = \frac{2\,\bar{\beta}^2 \bar{a}^4}{105\,\zeta}, \tag{3.101}$$

$$B_2 = \int_{\bar{a}}^{0} g_2(a)\ \mathrm{d}a = -\frac{8\,\bar{\beta}^2 \bar{a}^6}{945\,\zeta}. \tag{3.102}$$

As a result, the asymptotic behaviour of L is

$$L = \frac{2\,\bar{\beta}^2 \bar{a}^4}{105\zeta} + O\left(\frac{\pi}{2} - \alpha\right) \to \left(\frac{2\beta^2 \bar{a}^4}{105}\right)^- \tag{3.103}$$

as $\alpha \to (\pi/2)^-$.

For the behaviour of L as $\alpha \to \pi^-$, we substitute (3.61) and (3.86) into (3.89) to get

$$\frac{\mathrm{d}x}{\mathrm{d}a} = -\frac{\bar{\beta}^2 \sin\alpha \left(45m^2 a\cot^4 ma + 54m^2 a\cot^2 ma - 45m\cot^3 ma + 9m^2 a - 39m\cot ma\right)}{18\zeta m^5 a\cot ma}. \tag{3.104}$$

We expand the right-hand side of equation (3.104) as a Taylor series in powers of $\pi - \alpha$. Then (3.104) becomes

$$\frac{\mathrm{d}x}{\mathrm{d}a} = m_1(a)\,(\pi - \alpha) + O\left((\pi - \alpha)^3\right) \tag{3.105}$$

where

$$m_1(a) = -\frac{\bar{\beta}^2 \left(-6\cos^3 a \sin a + 36a\ \cos^2 a - 39\ \cos a \sin a + 9a\right)}{18\zeta a\ \sin^3 a \cos a}. \tag{3.106}$$

Integrating equation (3.105) with respect to a, and taking into account that $x(\bar{a}) = 0$, we get

$$L = x(0) = M(\bar{a})\,(\pi - \alpha) + O\left((\pi - \alpha)^3\right), \tag{3.107}$$

where

$$M(\bar{a}) = \int_{\bar{a}}^{0} m(a)\ \mathrm{d}a \tag{3.108}$$

As a result, the asymptotic behaviour of L is

$$L = M(\bar{a})\,(\pi - \alpha) + O\left((\pi - \alpha)^3\right) \to 0^+ \tag{3.109}$$

as $\alpha \to \pi^-$.

3.3.2 A wide rivulet with $\bar{a} > \pi/2$

For a wide rivulet with constant contact angle when $\bar{a} > \pi/2$ there is a critical value of $\alpha = \alpha_{\text{crit}}$ ($\pi/2 < \alpha_{\text{crit}} \le \pi$) given by equation (3.66), at which the length of the rivulet tends to infinity and above which there is no physically realisable solution (*i.e.* $L < 0$). In Figure 3.13, unlike in the case described in Subsection 3.2, when $\pi/2 < \bar{a} < a_{\max}$ the length of the rivulet has a local maximum and local minimum, where $a_{\max} \simeq 0.5024\pi \simeq 1.5785$ (see Figure 3.13(a)). Figure 3.13 shows plots of L as a function of the scaled angle α/π for a rivulet with constant contact angle $\bar{\beta}$ for (a) $\pi/2 < \bar{a} < a_{\max}$, (b) $\bar{a} = a_{\max}$ and (c) $\bar{a} > a_{\max}$. Such rivulets only exist and have a finite length for $0 \le \alpha < \alpha_{\text{crit}}$ with $L \to 0^+$ as $\alpha \to 0^+$ and $L \to \infty$ as $\alpha \to {\alpha_{\text{crit}}}^-$. At the value $a_{\max}$, the local maximum and minimum will coincide, as seen in Figure 3.13(b). In Figure 3.13(c), for all $\bar{a} > a_{\max}$ the length of the rivulet is a monotonically increasing function of α. Figure 3.14 shows that the qualitative behaviour of the length of a wide rivulet with constant contact angle depends on the value of $\bar{a}$ as illustrated in Figure 3.13. Figure 3.15 shows (a) $L_{\max}$ and $L_{\min}$ and (b) $\alpha_{\max}/\pi$ and $\alpha_{\min}/\pi$ for a wide rivulet

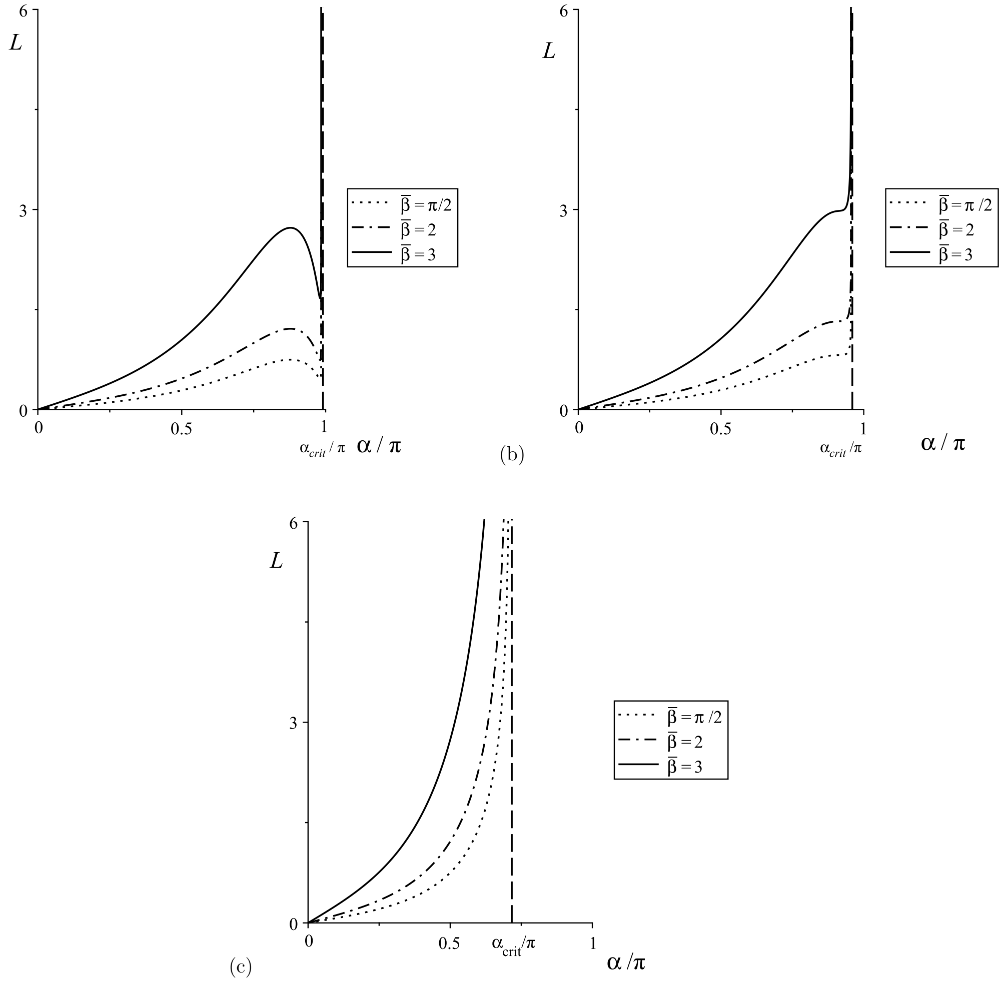

(a) (b) (c)

Figure 3.13: Plots of L as a function of α/π for a rivulet with constant contact angle $\bar{\beta} = \pi/2, 2, 3$ for initial semi-width (a) $\bar{a} = \pi/2 + 10^{-3}$ ($< a_{\max}$), (b) $\bar{a} = a_{\max}$, (c) $\bar{a} = 2$ ($> a_{\max}$) with permeability constant $\zeta = 1$. The vertical dashed lines represent the critical value α_{crit} given by (3.66).

plotted as functions of $\bar{a}/\pi$, and, in particular, confirms that $L_{\max}$, $L_{\min}$ and $\alpha_{\max}$ are monotonically increasing functions of $\bar{a}$ and that $\alpha_{\min}$ is a monotonically decreasing function of $\bar{a}$, and shows that $L_{\max} = L_{\min} \simeq 0.3289$, $\alpha_{\max} = \alpha_{\min} \simeq 0.9150\pi \simeq 2.8746$ when $\bar{a} = a_{\max}$.

The behaviour of L as $\alpha \to 0^+$ and $\alpha \to \pi/2^-$ when $\bar{a} > \pi/2$ is rather similar to those described in the previous Subsection 3.3.1.

For the behaviour of L as $\alpha \to {\alpha_{\text{crit}}}^-$, the differential equation describing the func-

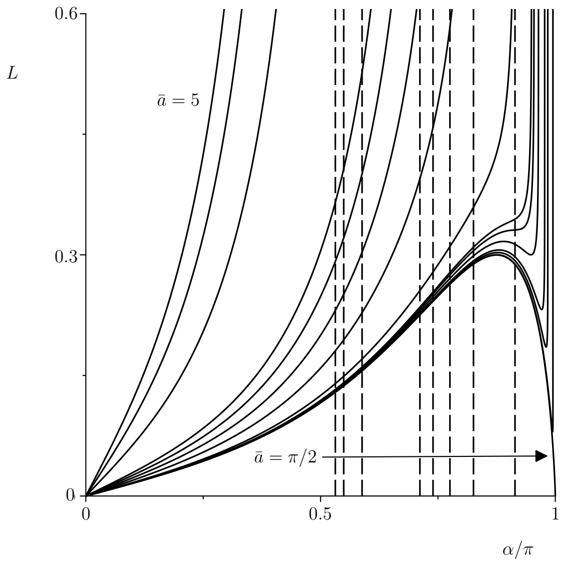

Figure 3.14: The length L of a rivulet with constant contact angle $\bar{\beta} = 1$ given by (3.85) plotted as a function of α/π for a wide rivulets with initial semi-width $\bar{a} = \pi/2, 1.571, 1.572, 1.573, 1.576, 1.579, 1.6, 1.7, 1.8, 1.9, 2, 3, 4, 5$ ($\geq \pi/2$) and permeability constant $\zeta = 1$. The dashed lines denote the vertical asymptotes of L at $\alpha = \alpha_{\mathrm{crit}}$ for $\bar{a} = 1.6, ..., 5$ (the vertical asymptotes for $\bar{a} = \pi/2, ..., 1.58$ having been omitted for clarity).

tion $x(a)$ is given by (3.104). We expand the right-hand side of equation (3.104) as a Taylor series in powers of $\alpha_{\mathrm{crit}} - \alpha$. Then (3.104) becomes

$$\frac{\mathrm{d}x}{\mathrm{d}a} = b_1(a)\,(\alpha_{\mathrm{crit}} - \alpha)^{-1} + O(1), \tag{3.110}$$

where

$$b_1(a) = -\frac{4a\bar{\beta}^2}{\zeta\pi^2}. \tag{3.111}$$

Integrating equation (3.110) with respect to a, and taking into account that $x(\bar{a}) = 0$, we get

$$L = x(0) = E_1\,(\alpha_{\mathrm{crit}} - \alpha)^{-1} + O\,(1)\,, \tag{3.112}$$

where

$$E_1 = \int_{\bar{a}}^{0} b_1(a)\;\mathrm{d}a = \frac{2\bar{a}^2\bar{\beta}^2}{\zeta\,\pi^2}. \tag{3.113}$$

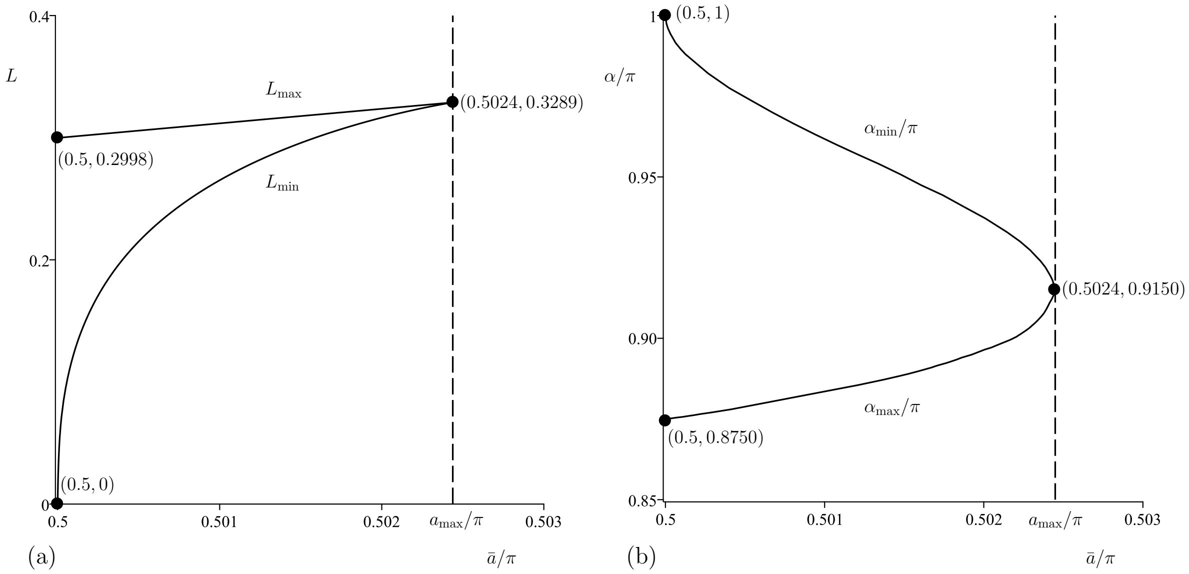

Figure 3.15: (a) $L_{\max}$ and $L_{\min}$ and (b) $\alpha_{\max}/\pi$ and $\alpha_{\min}/\pi$ for a wide rivulet with constant contact angle $\bar{\beta} = 1$ plotted as functions of $\bar{a}/\pi$ with permeability constant $\zeta = 1$.

As a result, the asymptotic behaviour of L is

$$L = \frac{2\bar{a}^2\bar{\beta}^2}{\zeta\,\pi^2}\left(\alpha_{\mathrm{crit}} - \alpha\right)^{-1} + O\left(1\right) \to \infty \tag{3.114}$$

as $\alpha \to {\alpha_{\mathrm{crit}}}^{-}$.

3.3.3 Behaviour of the rivulet length L as a function of $\bar{a}$

Figure 3.16 shows a plot of L as a function of $\bar{a}$ for a sessile rivulet with a range of values of α. In this case the length of the rivulet becomes short and always increases with $\bar{a}$ according to $L \to 0^+$ as $\bar{a} \to 0^+$ and $L \to \infty$ as $\bar{a} \to \infty$, respectively.

To study the behaviour of L as $\bar{a} \to 0^+$, we expand the right-hand side of equation (3.91) as a Taylor series in powers of a. Then (3.91) becomes

$$\frac{\mathrm{d}x}{\mathrm{d}a} = c_1(\alpha)a^3 + c_2(\alpha)a^5 + O\left(a^7\right), \tag{3.115}$$

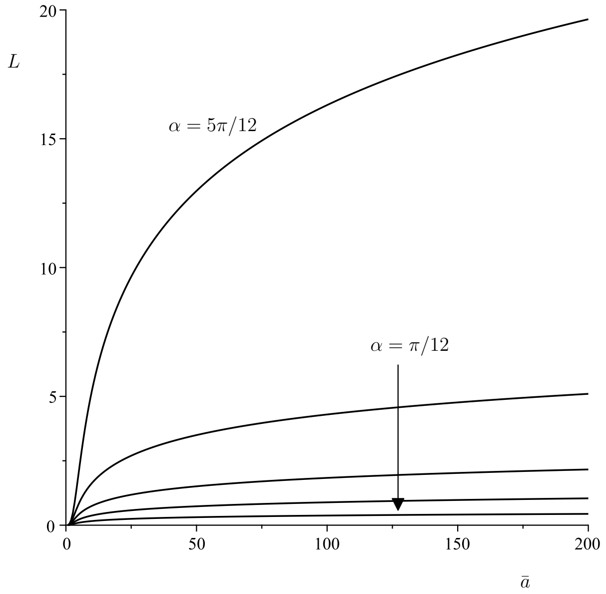

Figure 3.16: The length L of a rivulet with constant contact angle $\bar{\beta} = 1$ given by (3.85) plotted as a function of $\bar{a}$ for $\alpha = \pi/12, \pi/6, \pi/4, \pi/3, 5\pi/12$ ($< \pi/2$) with permeability constant $\zeta = 1$.

where

$$c_1(\alpha) = -\frac{8\bar{\beta}^2 \sin\alpha}{105\,\zeta}, \tag{3.116}$$

$$c_2(\alpha) = \frac{16m^2\bar{\beta}^2 \sin\alpha}{315\,\zeta}. \tag{3.117}$$

Integrating equation (3.115) with respect to a, and taking into account that $x(\bar{a}) = 0$, we get

$$L = x(0) = \frac{2\bar{\beta}^2 \sin\alpha}{105\,\zeta}\bar{a}^4 - \frac{8m^2\bar{\beta}^2 \sin\alpha}{945\,\zeta}\bar{a}^6 + O\left(\bar{a}^8\right). \tag{3.118}$$

As a result, the asymptotic behaviour of L is

$$L = \frac{2\bar{\beta}^2 \sin\alpha}{105\zeta}\,\bar{a}^4 + O\left(\bar{a}^6\right) \to 0^+ \tag{3.119}$$

as $\bar{a} \to 0^+$.

Figure 3.16 indicates that as $\bar{a} \to \infty$, $L \sim O\left(\log(\bar{a})\right)$. While proving rigorously that this is the case needs an involved matched asymptotics argument, which we do not provide, we can argue heuristically as follows:

For large $\bar{a}$,

$$\frac{dx}{da} \sim -\frac{\bar{\beta}^2 \sin\alpha}{3\zeta m^4}\frac{1}{a} + O(e^{-2ma}). \tag{3.120}$$

Hence it is reasonable to suggest, by integrating, that

$$x(\bar{a}) - x(0) \sim -\frac{\bar{\beta}^2 \sin\alpha}{3\zeta m^4}\log(\bar{a}) + O\left(\log(\bar{a})\right), \tag{3.121}$$

so that

$$L \sim \frac{\bar{\beta}^2 \sin\alpha}{3\zeta m^4}\log(\bar{a}). \tag{3.122}$$

as $\bar{a} \to \infty$.

Figure 3.17 shows plots of L as a function of $\bar{a}$ for vertical and pendant rivulets with angle $\pi/2 \le \alpha \le \pi$. Figure 3.17 shows that in the special case $\alpha = \pi/2$ (*i.e.* a rivulet on a vertical substrate) the rivulet exists for all $\bar{a} > 0$ and satisfies $L \to 0^+$ as $\bar{a} \to 0^+$ and $L \to \infty$ as $\bar{a} \to \infty$. On the other hand, Figure 3.17 shows that when $\pi/2 < \alpha \le \pi$ there is a critical value of $\bar{a} = \bar{a}_{\text{crit}}$ given by (3.76) at which the length of the rivulet tends to infinity and above which there is no physically realisable solution.

When $\alpha = \pi/2$, we see from equation (3.88) that

$$L \sim \frac{2\bar{\beta}^2}{105\zeta}\bar{a}^4 \to 0^+ \tag{3.123}$$

as $\bar{a} \to 0^+$, and

$$L \sim \frac{2\bar{\beta}^2}{105\zeta}\bar{a}^4 \to \infty \tag{3.124}$$

as $\bar{a} \to \infty$.

On the other hand, when $\pi/2 < \alpha \le \pi$, we expand the right-hand side of equation (3.104) as a Taylor series in powers of a. Then (3.104) becomes

$$\frac{\mathrm{d}x}{\mathrm{d}a} = k_1(\alpha)a^3 + k_2(\alpha)a^5 + O\left(a^7\right), \tag{3.125}$$

where

$$k_1(\alpha) = -\frac{8\bar{\beta}^2 \sin\alpha}{105\,\zeta}, \tag{3.126}$$

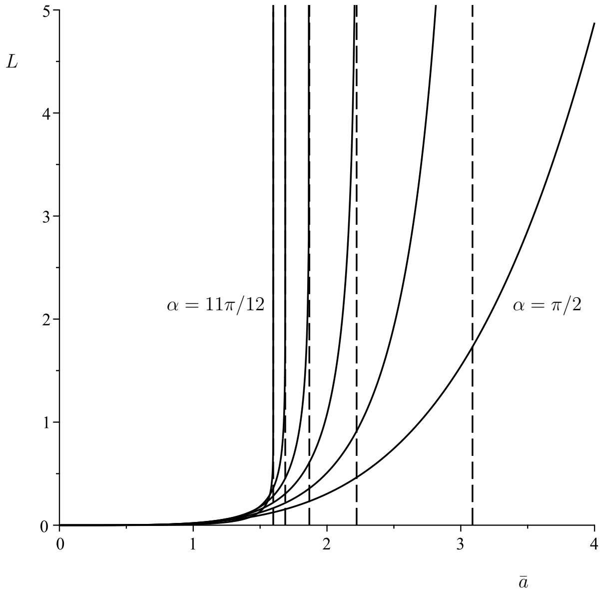

Figure 3.17: The length L of a rivulet with constant contact angle $\bar{\beta} = 1$ given by (3.85) plotted as a function of $\bar{a}$ for a vertical and pendant rivulets with $\alpha = \pi/2, 7\pi/12, 2\pi/3, 3\pi/4, 5\pi/6, 11\pi/12$ ($\geq \pi/2$) with permeability constant $\zeta = 1$. The dashed denote the vertical asymptotes of L at $\bar{a} = a_{\text{crit}}$ for pendant rivulets.

$$k_2(\alpha) = -\frac{16m^2\bar{\beta}^2 \sin\alpha}{315\,\zeta}. \tag{3.127}$$

Integrating equation (3.125) with respect to a, and taking into account that $x(\bar{a}) = 0$, we get

$$L = x(0) = \frac{2\bar{\beta}^2 \sin\alpha}{105\,\zeta}\bar{a}^4 + \frac{8m^2\bar{\beta}^2 \sin\alpha}{945\,\zeta}\bar{a}^6 + O\left(\bar{a}^8\right). \tag{3.128}$$

Specifically, the asymptotic behaviour of L is

$$L = \frac{2\bar{\beta}^2 \sin\alpha}{105\zeta}\,\bar{a}^4 + O\left(\bar{a}^6\right) \to 0^+ \tag{3.129}$$

as $\bar{a} \to 0^+$.

For $\bar{a} \to a_{\text{crit}}^-$, we expand the right-hand side of equation (3.104) as a Taylor series in powers of $a_{\text{crit}} - a$. Then (3.104) becomes

$$\frac{\mathrm{d}x}{\mathrm{d}a} = -\frac{\bar{\beta}^2 \sin\alpha}{2\zeta m^4}\left(a_{\text{crit}} - a\right)^{-1} + \frac{13\bar{\beta}^2 \sin\alpha}{3\zeta\pi m^3} + O\left(a_{\text{crit}} - a\right). \tag{3.130}$$

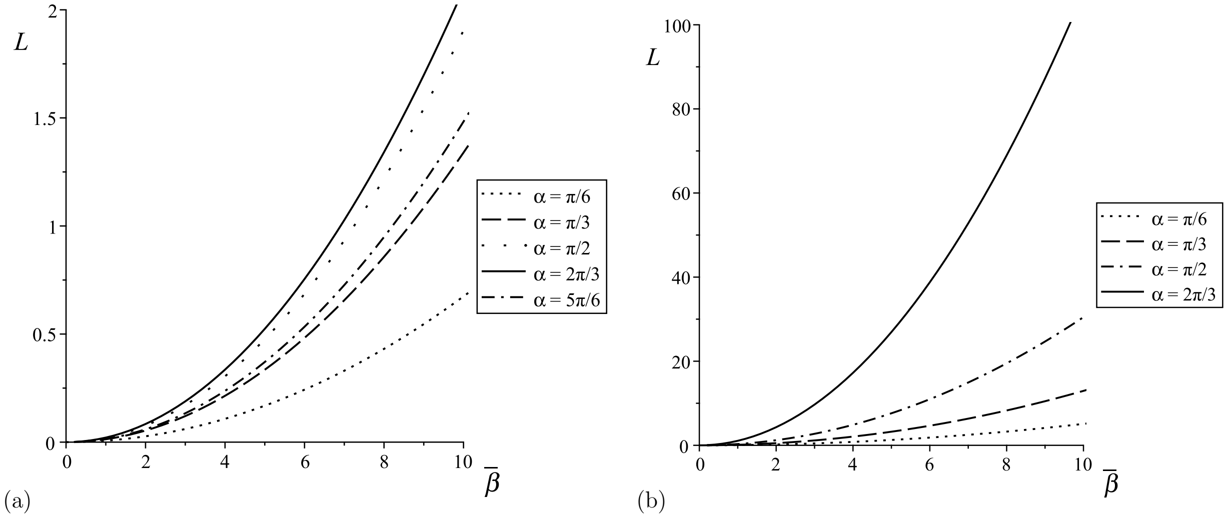

Figure 3.18: Plots of L as a function of the contact angle $\bar{\beta}$ for a rivulet with constant contact angle for (a) $\bar{a} = 1$, $\alpha = \pi/6, ..., 5\pi/6$ and (b) $\bar{a} = 2$, $\alpha = \pi/6, ..., 2\pi/3$.

Integrating equation (3.130) with respect to a, and taking into account that $x(\bar{a}) = 0$, we get the asymptotic behaviour of L as

$$L \sim -\frac{\bar{\beta}^2 \sin\alpha}{2\zeta m^4} \log\left(a_{\mathrm{crit}} - \bar{a}\right) \to \infty \quad \text{as} \quad \bar{a} \to a_{\mathrm{crit}}^-. \tag{3.131}$$

3.3.4 Behaviour of the rivulet length L as a function of $\bar{\beta}$

Figure 3.18 shows plots of L as a function of $\bar{\beta}$ for a rivulet with angle $0 < \alpha \leq \pi$ for (a) $\bar{a} = 1$ $(< \pi/2)$ and (b) $\bar{a} = 2$ $(\geq \pi/2)$. Figure 3.18(a) shows that, for different values of α, the rivulet exists for all $\bar{\beta} > 0$ and satisfies $L \to 0^+$ as $\bar{\beta} \to 0^+$ and $L \to \infty$ as $\bar{\beta} \to \infty$. Note that for a fixed value of $\bar{\beta}$ the length of the rivulet increases as α increases for $0 \leq \alpha \leq \alpha_{\mathrm{max}}$. However, for $\alpha > \alpha_{\mathrm{max}}$ the length of the rivulet decreases until it reaches zero, this behaviour is consistent with the results shown previously in Figure 3.11. On the other hand, Figure 3.18(b) shows that for $0 \leq \alpha \leq \alpha_{\mathrm{crit}}$ the length of the rivulet exists for all $\bar{\beta} > 0$ and satisfies $L \to 0^+$ as $\bar{\beta} \to 0^+$ and $L \to \infty$ as $\bar{\beta} \to \infty$.

To study the behaviour of L as $\bar{\beta} \to 0^+$, we integrate equation (3.89) with respect to a, and taking into account that $x(\bar{a}) = 0$, we get

$$L = x(0) = \frac{\sin\alpha\, G(m\bar{a})}{18\zeta\, m^4}\bar{\beta}^2, \tag{3.132}$$

where

$$G(m\bar{a}) = \int_{\bar{a}}^{0} \frac{q(ma)}{g(ma)}\, \mathrm{d}a. \tag{3.133}$$

Specifically, the asymptotic behaviour of L is

$$L \sim \frac{\sin\alpha\, G(m\bar{a})}{18\zeta\, m^4}\bar{\beta}^2 \to 0^+ \tag{3.134}$$

as $\bar{\beta} \to 0^+$, and

$$L \sim \frac{\sin\alpha\, G(m\bar{a})}{18\zeta\, m^4}\bar{\beta}^2 \to \infty \quad \text{as} \quad \bar{\beta} \to \infty. \tag{3.135}$$

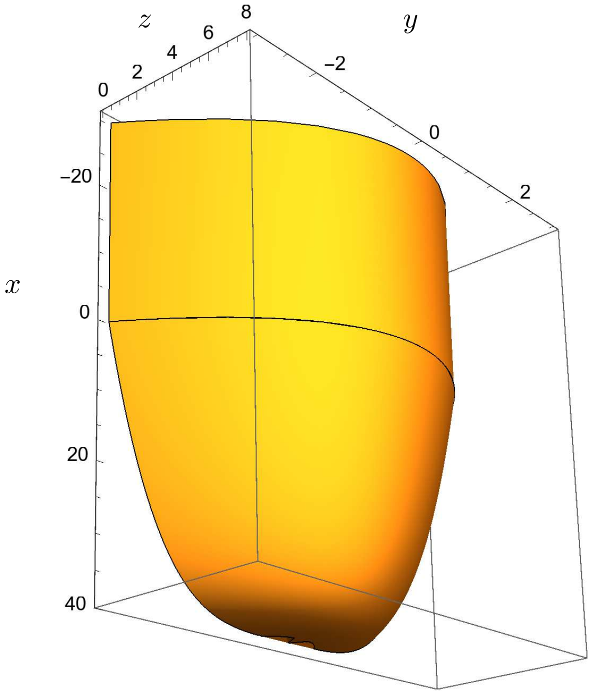

Figure 3.19: The three-dimensional shape of the free surface of a vertical rivulet with constant contact angle $\bar{\beta} = 5$, initial semi-width $\bar{a} = 3$, permeability constant $\zeta = 1$ and length $L = 2\bar{\beta}^2\bar{a}^4/(105\zeta) = 4050/105 \simeq 38.5714$.

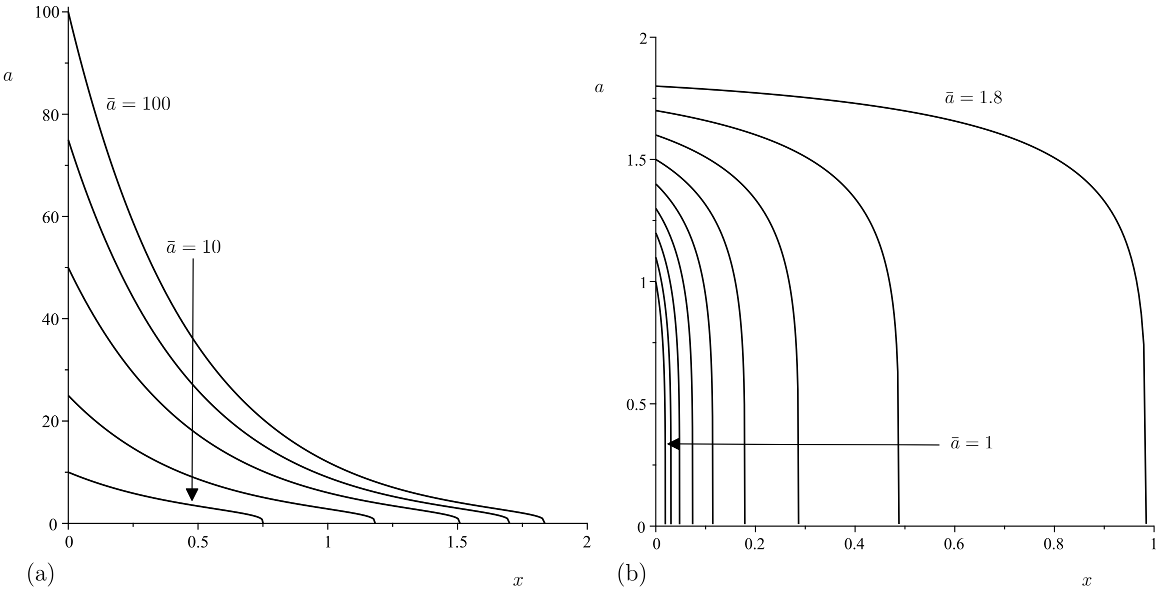

Figure 3.20: The semi-width a of a rivulet with constant contact angle $\bar{\beta} = 1$ given by (3.85) plotted as a function of x with permeability constant $\zeta = 1$ for (a) a sessile rivulet with $\alpha = \pi/4$ for $\bar{a} = 10, 25, 50, 75, 100$, and (b) a pendant rivulet with $\alpha = 3\pi/4$ for $\bar{a} = 1, 1.1, 1.2, \ldots, 1.8$ ($< a_{\mathrm{crit}} \simeq 1.8680$).

3.3.5 Rivulet shape

Figure 3.19 shows a typical example of the three-dimensional shape of the free surface of a vertical rivulet, and Figure 3.20 shows plots of the semi-width a as a function of x for a sessile and pendant rivulets and for a range of values of $\bar{a}$.

To study the behaviour of the width a as $x \to 0^+$ and as $x \to L^-$ in the special case of a vertical rivulet, we expand the right-hand side of equation (3.87) as a Taylor series in powers of x. Then specifically, the asymptotic behaviour of $a(x)$ is given by

$$a = \bar{a} - \frac{105\,\zeta}{8\,\bar{a}^3\bar{\beta}^2}x + O\left(x^2\right) \to \bar{a} \qquad (3.136)$$

as $x \to 0^+$.

For $x \to L^-$, we expand the right-hand side of equation (3.87) as a Taylor series in powers of $L - x$. Then specifically, the asymptotic behaviour of a is

$$a \sim \left[\frac{105\,\zeta}{2\,\bar{\beta}^2}(L - x)\right]^{1/4} \to 0^+ \quad \text{as} \quad x \to L^-. \qquad (3.137)$$

3.4 Conclusions

In this chapter we used lubrication theory to obtain and analyse the solution for the steady gravity-driven flow of a thin rivulet over and through an inclined permeable membrane.

In Section 3.2 we described the flow of a rivulet with constant semi-width but decreasing contact angle. In particular, we obtained the exact solutions for both the contact angle and the length of the rivulet on the permeable part of the membrane by solving a first order ordinary differential equation given by (3.62). We found that the behaviour of the length L of a rivulet with constant semi-width ($a \equiv \bar{a}$) on the permeable part of the membrane depends on the value of $\bar{a}$. In particular, while a narrow rivulet with constant semi-width $0 < \bar{a} < \pi/2$ has always a finite length for all $0 \leq \alpha \leq \pi$, a wide rivulet with constant semi-width $\bar{a} \geq \pi/2$ only exists and has a finite length for $0 \leq \alpha < \alpha_{\mathrm{crit}}$, where the critical angle α_{crit} is given by (3.66).

In Section 3.3 we described the flow of a rivulet with constant contact angle but decreasing contact width. In particular, we obtained the exact solutions for both the contact angle and the length of the rivulet on the porous membrane just for the case $\alpha = \pi/2$, while in the cases of rivulets with $0 \leq \alpha < \pi/2$ and $\pi/2 < \alpha \leq \pi$, we solved a non-linear ordinary differential equation given by (3.85) numerically and analysed the behaviour of the length of the rivulet. Similar to that in the case of a rivulet with constant semi-width, we found that a narrow rivulet with constant contact angle $\beta \equiv \bar{\beta}$ when $0 < \bar{a} \leq \pi/2$ exists and has a finite length for all $0 \leq \alpha \leq \pi$, while a wide rivulet with constant contact angle when $\bar{a} > \pi/2$ only has a finite length for $0 \leq \alpha < \alpha_{\mathrm{crit}}$ but, unlike the case for a rivulet with constant semi-width $\bar{a} \geq \pi/2$, the length of the rivulet has both a local maximum and local minimum. Specifically, the length of the rivulet increases to a local maximum value $L = L_{\mathrm{max}}$ at $\alpha = \alpha_{\mathrm{max}}$ and then decreases to a local minimum value $L = L_{\mathrm{min}}$ at $\alpha = \alpha_{\mathrm{min}}$ ($\pi/2 < \alpha_{\mathrm{max}} < \alpha_{\mathrm{min}} < \alpha_{\mathrm{crit}}$) before increasing again and becoming infinitely long, as shown in Figure 3.14.

Chapter 4

Patterns Formed in a Thin Film with Spatially Homogeneous and Non-Homogeneous Derjaguin Disjoining Pressure

In this chapter we consider patterns formed in a two-dimensional thin film on a planar substrate with a Derjaguin disjoining pressure and periodic wettability stripes. We revisit the work of Honisch et al. [46], as discussed in Section 1.7, and we rigorously clarify some of their numerical results. In particular, we examine steady-state solutions of a one-dimensional thin-film equation with spatially homogeneous and non-homogeneous Derjaguin disjoining pressure. For the case of constant wettability, we elucidate the change in the global structure of branches of steady-state solutions as the average film thickness and the domain size are varied. We discuss admissible forms of spatially non-homogeneous disjoining pressure, and clarify the dependence of the steady-state solutions on the wettability contrast in the case of a periodically patterned substrate.

4.1 Problem Statement

Denoting the height of the thin liquid film by $z = h(x, y, t)$, where (x, y, z) are the usual Cartesian coordinates and t is time, Honisch et al. [46] considered the thin-film equation

$$h_t = \nabla \cdot \{Q(h)\nabla P(h, x, y)\}, \qquad t > 0, \qquad (x, y) \in \mathbb{R}^2, \tag{4.1}$$

where $Q(h) = h^3/(3\eta)$ is the mobility coefficient, with η being the dynamic viscosity and the generalized pressure $P(h, x, y)$ given by

$$P(h, x, y) = -\gamma \Delta h - \Pi(h, x, y),$$

where γ is the surface tension. Here we follow [46] in taking the Derjaguin disjoining pressure $\Pi(h, x, y)$ in the spatially homogeneous case to be of the form

$$\Pi(h, x, y) = -\frac{A}{h^3} + \frac{B}{h^6} \tag{4.2}$$

suggested, for example, by Pismen [86]. Here A and B are positive parameters that measure the relative contributions of the short-range (h^{-6} term) and long-range (h^{-3} term) forces, as discussed in Section 1.8. However, we will see that both of these constants can be scaled out of the mathematical problem.

In the case where the substrate is taken to be non-homogeneous, we can modify (4.2) by assuming that the Derjaguin pressure term Π changes periodically in the x-direction, with period L. The appropriate forms of Π in the non-homogeneous case are discussed in Section 4.5.

In order to better understand solutions of (4.1), we study its one-dimensional, *i.e.* y-independent, version,

$$h_t = \left(Q(h)P(h, x)_x\right)_x, \quad 0 < x < L. \tag{4.3}$$

We start by characterising steady-state solutions of (4.3), subject to periodic boundary conditions at $x = 0$ and $x = L$. In other words, we seek solutions $h(x)$ of (4.3) satisfying, in dimensional variables, the following non-local boundary value problem, namely

$$\gamma h_{xx} + \frac{B}{h^6} - \frac{A}{h^3} - \frac{1}{L}\int_0^L \left[\frac{B}{h^6} - \frac{A}{h^3}\right] \mathrm{d}x = 0, \quad 0 < x < L, \tag{4.4}$$

subject to the constraint

$$\frac{1}{L}\int_0^L h(x)\,\mathrm{d}x = h^*, \tag{4.5}$$

where the constant h^* (> 0) denotes the (scaled) average film thickness, and the periodic boundary conditions

$$h(0) = h(L), \quad h_x(0) = h_x(L). \tag{4.6}$$

Note that to obtain (4.4) we set $h_t = 0$ in (4.3), and integrated twice with respect to x. The first integration yields

$$0 = -\gamma h_{xxx} - \Pi(h,x)_x + \frac{C_0}{Q(h)}, \tag{4.7}$$

where C_0 is a constant of integration. Here we are either considering $P(h,x)$ periodic in x or independent of x. Hence by periodicity of h, in both cases

$$h_{xx}(0) = h_{xx}(L), \quad P(h(0),0) = P(h(L),L). \tag{4.8}$$

Therefore noting that $Q(h) > 0$, we integrate (4.7) between 0 and L and used (4.8) to obtain

$$\int_0^L \frac{C_0}{Q(h)}\,\mathrm{d}x = 0, \tag{4.9}$$

and from that it follows that C_0 is zero. The second integration yields

$$C_1 = -\gamma h_{xx} - \Pi(h,x). \tag{4.10}$$

In order to determine the value of C_1, we integrated (4.10) from $x = 0$ to $x = L$ and used (4.6) to obtain

$$C_1 = -\frac{1}{L}\int_0^L \Pi(h,x)\,\mathrm{d}x. \tag{4.11}$$

Now we non-dimensionalise. Setting

$$H = \left(\frac{B}{A}\right)^{1/3}, \quad h = H\tilde{h}, \quad \text{and } x = L\tilde{x},$$

in (4.4) and removing the tildes, we obtain

$$\epsilon^2 h_{xx} + f(h) - \int_0^1 f(h)\,\mathrm{d}x = 0, \quad 0 < x < 1, \tag{4.12}$$

where

$$f(h) = \frac{1}{h^6} - \frac{1}{h^3} \tag{4.13}$$

and

$$\epsilon^2 = \frac{\gamma B^{4/3}}{L^2 A^{7/3}}, \tag{4.14}$$

subject to the periodic boundary conditions

$$h(0) = h(1), \quad h_x(0) = h_x(1), \tag{4.15}$$

and the volume constraint

$$\int_0^1 h(x)\,\mathrm{d}x = \bar{h} := \frac{h^* A^{1/3}}{B^{1/3}}. \tag{4.16}$$

Note that the problem (4.12)–(4.16) is very similar to the corresponding stationary problem for the Cahn–Hilliard equation, considered as a bifurcation problem in the parameters $\bar{h}$ and ϵ by Eilbeck et al. [33]. The boundary conditions considered in that work were the physically natural double Neumann conditions. The periodic boundary conditions (4.15) in the present problem slightly change the analysis, but our general approach in characterising different bifurcation regimes still follows that of Eilbeck et al. [33], though the correct interpretation of the limit as $\epsilon \to 0^+$ is that now we let the surface tension γ go to zero. In particular, we perform a Liapunov–Schmidt reduction to determine the local behaviour close to bifurcation points and then use AUTO (in the present work we use the AUTO-07p version [30]) to explore the global structure of branches of steady-state solutions, both for the spatially homogeneous case and for the spatially non-homogeneous case in the case of an x-periodically patterned substrate.

We first investigate the homogeneous case, and having elucidated the structure of the bifurcations of non-trivial solutions from the constant solution $h = \bar{h}$ in that case in Sections 4.3 and 4.4, we study forced rotational ($O(2)$) symmetry breaking in the non-homogeneous case in Section 4.5. We concentrate on the simplest steady-state solutions of (4.12)–(4.16), as by a result of Laugesen and Pugh [58, Theorem 1] only such solutions, that is, constant solutions and those having only one extremum point, are linearly stable in the homogeneous case.

4.2 Liapunov–Schmidt Reduction Method

In this section we introduce the Liapunov–Schmidt reduction method, as described by Golubitsky and Schaeffer in [38], which can be used to classify the local structure and nature of the bifurcations for solutions to equation (4.12).

Many problems in applied mathematics which exhibit multiple steady-state solutions can be reduced to a single equation of the form $g(x, \lambda) = 0$ by a process called the Liapunov–Schmidt reduction, where $g : \mathbb{R} \times \mathbb{R} \to \mathbb{R}$. The reduction starts by writing the boundary problem in an abstract form

$$G(u, \lambda) = 0, \tag{4.17}$$

where the unknown u is the state variable and λ is the bifurcation parameter. We assume that $G : X \times \mathbb{R} \to Y$ is a smooth mapping between the Banach spaces X and Y, such that

$$G(0, \lambda) = 0 \quad \text{for all } \lambda \in \mathbb{R}. \tag{4.18}$$

We use the Liapunov–Schmidt reduction to reduce the study of steady-state solutions of (4.17) to the study of the zeros of a single algebraic equation $g(x, \lambda) = 0$.

In order to investigate possible multiplicity of solutions to (4.17), we study the linearisation $(dG)_{u,\lambda}$ of G. The linearisation of G applied to $v \in X$ is given by

$$(dG)_{u,\lambda} \cdot v = \lim_{\tau \to 0} \frac{G(u + \tau v, \lambda) - G(u)}{\tau}, \tag{4.19}$$

and we let S be $(dG)_{0,\lambda_i} = G_u\,(0, \lambda_i)$ where the values λ_i are points of bifurcation from the trivial solution $u = 0$ for $i = 1, ..., n$. We assume that $S : X \to Y$ is a Fredholm operator of index zero, meaning that $\dim\ker S < \infty$, $\operatorname{range} S$ is closed and $\dim\ker S = \operatorname{codim}\operatorname{range} S$. Following Golubitsky and Schaeffer [38], the derivation of the reduced equation g can then be divided into the following five steps:

Step 1: Decompose the spaces X and Y into

$$\begin{aligned} &\text{(a)} \quad & X &= \ker S \oplus M, & \qquad (4.20)\\ &\text{(b)} \quad & Y &= \operatorname{range} S \oplus N, & \qquad (4.21) \end{aligned}$$

where $M = (\ker S)^{\perp}$ and $N = (\operatorname{range} S)^{\perp}$.

Step 2: Split the equation $G(u, \lambda) = 0$ into an equivalent pair of equations

$$EG(u, \lambda) = 0, \tag{4.22}$$

$$(I - E)G(u, \lambda) = 0, \tag{4.23}$$

where $E : Y \to \operatorname{range} S$ denotes the projection of Y onto $\operatorname{range} S$.

Step 3: Use the equation (4.20) to write $u = v + w$, where $v \in \ker S$, $w \in M$. Then solve (4.22) for w as a function of λ and v by the implicit function theorem. This leads to a function $W : \ker S \times \mathbb{R} \to M$ such that

$$EG(v + W(v, \lambda), \lambda) = 0. \tag{4.24}$$

Step 4: Define $\phi : \ker S \times \mathbb{R} \to N$ by

$$\phi(v, \lambda) = (I - E)G(v + W(v, \lambda), \lambda). \tag{4.25}$$

Step 5: Choose a basis $v_1, v_2, ..., v_n \in \ker S$ and a basis $v_1^*, v_2^*, ..., v_n^* \in N$ and define $g : \mathbb{R}^n \times \mathbb{R} \to \mathbb{R}^n$ by

$$g_i(x, \lambda) = \langle v_i^*, \phi\left(x_1 v_1 + ... + x_n v_n, \lambda\right)\rangle, \quad i = 1, ..., n, \tag{4.26}$$

in which Y is now equipped with the L^2-inner product denoted by $\langle \cdot, \cdot \rangle$. Note that since $v_i^* \in N$ and for any vector $V \in Y$, $EV \in \operatorname{range} S$, so $\langle v_i^*, EV\rangle = 0$. Hence

$$\langle v_i^*, (I - E)V\rangle = \langle v_i^*, V\rangle. \tag{4.27}$$

Note also that if we substitute the definition of ϕ in (4.25) into (4.26), the projection $I - E$ drops out as a result of equation (4.27) and we obtain the following reduced function:

$$g_i(x, \lambda) = \left\langle v_i^*, G\left(\sum_{i=1}^n x_i v_i + W\left(\sum_{i=1}^n x_i v_i, \lambda\right), \lambda\right)\right\rangle. \tag{4.28}$$

Therefore we have from Golubitsky and Schaeffer [38, Proposition 1.5] that the solutions of (4.17) are locally in one-to-one correspondence with solutions of $g_i(x, \lambda) = 0$, $i = 1, 2, ..., n$. where g_i is defined by (4.26).

The partial derivatives of the function g_i at a bifurcation point $(0, \lambda_i)$ can be computed with the use of the following chain rule:

$$\begin{aligned} &\frac{\partial}{\partial x}\left\{(d^r G)_{u,\lambda}(z_1, \ldots, z_r)\right\} \\ &\quad = \left(d^{r+1}G\right)_{u,\lambda}\left(\frac{\partial u}{\partial y}, z_1, \ldots, z_r\right) + \sum_{i=1}^r (d^r G)_{u,\lambda}\left(z_1, \ldots, \frac{\partial z_i}{\partial y}, \ldots, z_r\right), \end{aligned} \tag{4.29}$$

where $r \in \mathbb{N}$ is fixed and $(d^r G)_{u,\lambda}$ is a symmetric, multilinear function of r arguments given by

$$(d^r G)_{u,\lambda}(z_1, \cdots, z_r) = \left.\frac{\partial^r}{\partial t_1 \cdots \partial t_r} G\left(u + t_1 z_1 + \cdots + t_r z_r, \lambda\right)\right|_{t_1 = \cdots = t_r = 0}. \tag{4.30}$$

The derivatives of the reduced function (4.28) as shown in [38, Equation 1.14] are given by

$$\begin{aligned}
\frac{\partial g_i}{\partial x_i} &= \left\langle v_i^*, dG\left(v_i\right)\right\rangle , \\
\frac{\partial^2 g_i}{\partial x_j \partial x_k} &= \left\langle v_i^*, d^2 G\left(v_j, v_k\right)\right\rangle , \\
\frac{\partial^3 g_i}{\partial x_j \partial x_k \partial x_l} &= \left\langle v_i^*, V\right\rangle , \\
\frac{\partial g_i}{\partial \lambda_l} &= \left\langle v_i^*, G_{\lambda_l}\right\rangle , \\
\frac{\partial^2 g_i}{\partial x_j \partial \lambda_l} &= \left\langle v_i^*, \left(dG_{\lambda_l}\right) \cdot v_j - d^2 G\left(v_j, L^{-1} E G_{\lambda_l}\right)\right\rangle ,
\end{aligned} \tag{4.31}$$

where

$$\begin{aligned}
V &= d^3 G\left(v_j, v_k, v_l\right) - d^2 G\left(v_j, w_{lk}\right) - d^2 G\left(v_k, w_{lj}\right) - d^2 G\left(v_l, w_{kj}\right) , \text{ and} \\
w_{st} &= L^{-1} E d^2 G\left(v_s, v_t\right) .
\end{aligned}$$

By using Liapunov–Schmidt reduction, we are mainly interested in the local bifurcation structure of our problem and how it depends on the the average film thickness, which we are going to demonstrate in the following three Sections 4.3–4.5.

4.3 Liapunov–Schmidt Reduction in the Spatially Homogeneous Case

We start by performing an analysis of the dependence of the global structure of branches of steady-state solutions of the problem in the spatially homogeneous case, given by (4.12)–(4.16) on the parameters $\bar{h}$ and ϵ. To do this, we use the Liapunov–Schmidt reduction, as described in Section 4.2.

In what follows, we do not indicate explicitly the dependence of the operators on the parameters $\bar{h}$ and ϵ, and all of the calculations are performed for a fixed value of $\bar{h}$ and close to a bifurcation point $\epsilon = \epsilon_k$ for $k = 1, 2, 3, \ldots$ defined below.

In order to set up the Liapunov–Schmidt reduction for (4.12) we set $v = h - \bar{h}$, so that $v = v(x)$ has zero mean, and rewrite (4.12) as

$$G(v) = 0,$$

where

$$G(v) = \epsilon^2 v_{xx} + f(v + \bar{h}) - \int_0^1 f(v(x) + \bar{h})\,\mathrm{d}x.$$

If we set

$$H = \left\{ w \in C(0,1) \,:\, \int_0^1 w(x)\,\mathrm{d}x = 0 \right\},$$

where G is an operator from $D(G) \subset H \to H$, then $D(G)$ is given by

$$D(G) = \left\{ v \in C^2(0,1) \,:\, v(0) = v(1),\, v_x(0) = v_x(1),\, \int_0^1 v(x)\,\mathrm{d}x = 0 \right\}.$$

The linearisation of G at v applied to w is defined by

$$dG(v)w = \lim_{\tau \to 0} \frac{G(v + \tau w) - G(v)}{\tau}.$$

We denote $dG(0)$ by S, so that S applied to w is given by

$$Sw = \epsilon^2 w_{xx} + f'(\bar{h})w. \tag{4.32}$$

To locate bifurcation points, we have to find the nontrivial solutions of the equation $Sw = 0$, subject to

$$w(0) = w(1), \qquad w_x(0) = w_x(1). \tag{4.33}$$

The kernel of S is non-empty and two dimensional when

$$\epsilon = \epsilon_k = \frac{\sqrt{f'(\bar{h})}}{2k\pi} \quad \text{for} \quad k = 1, 2, 3, \ldots, \tag{4.34}$$

and is spanned by $\cos(2k\pi x)$ and $\sin(2k\pi x)$. That these values of ϵ correspond to bifurcation points follows from two theorems of Vanderbauwhede [112, Theorems 2 and 3].

In the neighbourhood of a bifurcation point $(\epsilon_k, 0)$ in (ϵ, v) space, solutions of

$G(v) = 0$ on H are in one-to-one correspondence with solutions of the reduced system of equations on $\mathbb{R}^2$,

$$g_1(x, y, \epsilon) = 0, \quad g_2(x, y, \epsilon) = 0, \tag{4.35}$$

for some functions g_1 and g_2 to be obtained through the Liapunov–Schmidt reduction [38].

In accordance with Section 4.2, we decompose $D(G)$ and H as follows:

$$D(G) = \ker S \oplus M$$

and

$$H = N \oplus \operatorname{range} S.$$

Since S is self-adjoint with respect to the L^2-inner product denoted by $\langle \cdot, \cdot \rangle$, we can choose

$$M = N = \operatorname{span}\left\{\cos(2kx), \sin(2kx)\right\},$$

and denote the above basis for M by $\{w_1, w_2\}$ and for N by $\{w_1^*, w_2^*\}$. We also denote the projection of H onto $\operatorname{range} S$ by E.

Since the present problem is invariant with respect to the group $O(2)$, the functions g_1 and g_2 must have the form

$$g_1(x, y, \epsilon) = xp(x^2 + y^2, \epsilon), \quad g_2(x, y, \epsilon) = yp(x^2 + y^2, \epsilon), \tag{4.36}$$

for some function $p(\cdot, \cdot)$ [22], which means that, in order to determine the bifurcation structure, the only derivatives given in (4.31) that need to be computed are $g_{1,x\epsilon}$ and $g_{1,xxx}$, as these immediately give $g_{2,y\epsilon}$ and $g_{2,yyy}$ and all of the other second and third partial derivatives of g_1 and g_2 are identically zero.

We set $v = 0$ and choose

$$w_1 = w_1^* = \cos(2k\pi x),$$

where $w_1 \in \ker S$ and $w_1^* \in (\text{range } S)^\perp$. Therefore, from (4.31) we have

$$\begin{aligned} d^2G(z_1, z_2) &= \left.\frac{\partial^2}{\partial t_1 \partial t_2} G(t_1 z_1 + t_2 z_2)\right|_{t_1=t_2=0} \\ &= \frac{\partial^2}{\partial t_1 \partial t_2} \Big[\epsilon_k (t_1 z_{1,xx} + t_2 z_{2,xx}) + f(t_1 z_1 + t_2 z_2 + \bar{h}) \\ &- \left.\int_0^1 f(t_1 z_1 + t_2 z_2 + \bar{h})\, \mathrm{d}x \Big]\right|_{t_1=t_2=0} \\ &= f''(\bar{h}) z_1 z_2 - \int_0^1 f''(\bar{h}) z_1 z_2 \, \mathrm{d}x, \end{aligned}$$

and so

$$\begin{aligned} d^2G(\cos(2k\pi x), \cos(2k\pi x)) &= f''(\bar{h}) \cos^2(2k\pi x) - \int_0^1 f''(\bar{h}) \cos^2(2k\pi x)\, \mathrm{d}x \\ &= f''(\bar{h}) \cos^2(2k\pi x) - \frac{1}{2} f''(\bar{h}). \end{aligned}$$

Since $E : H \to \text{range}\, S$ is the projection of H onto the range of S, we have

$$E\left[\left(d^2G\right)(w_1, w_1)\right] = \left(d^2G\right)(w_1, w_1),$$

and we consider

$$\begin{aligned} &S^{-1} E\left[\left(d^2G\right)(w_1, w_1)\right] = S^{-1}\left(d^2G\right)(w_1, w_1) = R(x) \\ &\Rightarrow \left(d^2G\right)(w_1, w_1) = SR(x). \end{aligned}$$

To obtain $S^{-1}E[d^2G(w_1, w_1)]$, which we denote by $R(x)$, so that $SR = E[d^2G(w_1, w_1)]$, we use the definition of ϵ_k given in (4.34) and solve the second order ordinary differential equation satisfied by $R(x)$,

$$R_{xx} + 4k^2\pi^2 R = 4k^2\pi^2 \frac{f''(\bar{h})}{f'(\bar{h})} \cos^2(2k\pi x) - 2k^2\pi^2 \frac{f''(\bar{h})}{f'(\bar{h})},$$

subject to

$$R(0) = R(1) \quad \text{and} \quad R_x(0) = R_x(1),$$

which has the solution

$$R(x) = S^{-1}E[d^2G(w_1, w_1)] = -\frac{1}{6}\frac{f''(\bar{h})}{f'(\bar{h})}\cos(4k\pi x),$$

and hence

$$\begin{aligned} d^2G(w_1, S^{-1}E[d^2G(w_1, w_1)]) &= d^2G\left(\cos(2k\pi x), -\frac{1}{6}\frac{f''(\bar{h})}{f'(\bar{h})}\cos(4k\pi x)\right) \\ &= f''(\bar{h})\cos(2k\pi x)\left(-\frac{1}{6}\frac{f''(\bar{h})}{f'(\bar{h})}\cos(4k\pi x)\right) \\ &\quad -\int_0^1 f''(\bar{h})\cos(2k\pi x)\left(-\frac{1}{6}\frac{f''(\bar{h})}{f'(\bar{h})}\cos(4k\pi x)\right)\mathrm{d}x \\ &= -\frac{1}{6}\frac{[f''(\bar{h})]^2}{f'(\bar{h})}\cos(2k\pi x)\cos(4k\pi x). \end{aligned} \tag{4.37}$$

In addition, from (4.30) we have

$$\begin{aligned} d^3G(z_1, z_2, z_3) &= \left.\frac{\partial^3}{\partial t_1 \partial t_2 \partial t_3} G(t_1 z_1 + t_2 z_2 + t_3 z_3)\right|_{t_1=t_2=t_3=0} \\ &= f'''(\bar{h}) z_1 z_2 z_3 - \int_0^1 f'''(\bar{h}) z_1 z_2 z_3 \, \mathrm{d}x, \end{aligned}$$

and therefore,

$$\begin{aligned} d^3G(\cos(2k\pi x), \cos(2k\pi x), \cos(2k\pi x)) &= f'''(\bar{h})\cos^3(2k\pi x) - \int_0^1 f'''(\bar{h})\cos^3(2k\pi x)\,\mathrm{d}x \\ &= f'''(\bar{h})\cos^3(2k\pi x). \end{aligned} \tag{4.38}$$

Therefore, from (4.31), (4.37) and (4.38) we obtain

$$\begin{aligned} g_{1,xxx} &= \langle w_1^*, d^3G(w_1, w_1, w_1) - 3d^2G(w_1, S^{-1}E[d^2G(w_1, w_1)])\rangle \\ &= \int_0^1 \cos(2k\pi x)\left[f'''(\bar{h})\cos^3(2k\pi x) - 3\left(-\frac{1}{6}\frac{[f''(\bar{h})]^2}{f'(\bar{h})}\cos(2k\pi x)\cos(4k\pi x)\right)\right]\mathrm{d}x \\ &= \frac{3}{8}f'''(\bar{h}) + \frac{1}{8}\frac{[f''(\bar{h})]^2}{f'(\bar{h})}. \end{aligned} \tag{4.39}$$

In addition, $G_\epsilon(v) = v_{xx}$, so that $G_\epsilon(0) = 0$ at $v = 0$, and hence we have

$$d^2G(w_k, S^{-1}EG_\epsilon(0)) = 0.$$

Furthermore, since $dG_\epsilon(w) = w_{xx}$, from (4.31) we obtain

$$\begin{aligned} g_{1,x\epsilon} &= \langle w_1^*, dG_\epsilon(w_1) - d^2G(w_1, S^{-1}EG_\epsilon(0))\rangle \\ &= \int_0^1 \cos(2k\pi x)\left(-4\pi^2k^2\cos(2k\pi x)\right)\,\mathrm{d}x \\ &= -2k^2\pi^2. \end{aligned} \tag{4.40}$$

Referring to (4.36) and the argument following that equation, the above analysis shows that as long as $f'(\bar{h}) > 0$ at $\epsilon = \epsilon_k$ a circle of equilibria bifurcates from the constant solution $h \equiv \bar{h}$. The direction of bifurcation is locally determined by the sign of $g_{1,xxx}$ given by (4.39). Hence, using $1/\epsilon$ as the bifurcation parameter, the bifurcation of nontrivial equilibria is supercritical if $g_{1,xxx}$ is negative and subcritical if it is positive.

By finding the values of $\bar{h}$ where $g_{1,xxx}$ given by (4.39) with $f(h)$ given by (4.13) is zero, we finally obtain the following proposition:

Proposition 1. *Bifurcations of nontrivial solutions from the constant solution* $h = \bar{h}$ *of the problem* (4.12)–(4.16) *are supercritical if* $1.289 < \bar{h} < 1.747$ *and subcritical if* $1.259 < \bar{h} < 1.289$ *or if* $\bar{h} > 1.747$.

Proof. The constant solution $h \equiv \bar{h}$ will lose stability as ϵ is decreased only if $f'(\bar{h}) > 0$. *i.e.* if $-6/\bar{h}^7 + 3/\bar{h}^4 > 0$, for $\bar{h} > 2^{1/3} \approx 1.259$. From (4.39) we have that

$$g_{1,xxx} = \frac{57\bar{h}^6 - 426\bar{h}^3 + 651}{2\bar{h}^9(\bar{h}^3 - 2)},$$

so that $g_{1,xxx} < 0$ if $\bar{h} \in (1.289, 1.747)$ giving the result. □

For $\bar{h} \leqslant 2^{1/3}$ there are no bifurcations from the constant solution $h = \bar{h}$. Furthermore, we have the following proposition:

Proposition 2. *The problem* (4.12)–(4.16) *has no nontrivial solutions when* $\bar{h} \leq 1$.

Proof. Assume that such a nontrivial solution exists. Then, since $\bar{h} \leq 1$, its global minimum, achieved at some point $x_0 \in (0,1)$, must be less than 1. (We may take the point x_0 to be an interior point by translation invariance.) But then

$$\epsilon^2 h_{xx}(x_0) = \int_0^1 f(h)\,\mathrm{d}x - f(h(x_0)) < 0,$$

so the point x_0 cannot be a minimum. ☐

4.4 Two–Parameter Continuation of Solutions in the Spatially Homogeneous Case

To describe the change in the global structure of branches of steady-state solutions of the problem (4.12)–(4.16) as $\bar{h}$ and ϵ are varied, we use AUTO [30] and our results are summarised in Figure 4.1.

As Figure 4.1 shows, a curve of saddle-node (SN) bifurcations which originates from $\bar{h} \approx 1.289$ at $1/\epsilon \approx 23.432$ satisfies $\bar{h} \to 1^+$ as $1/\epsilon \to \infty$, while a curve of SN bifurcations which originates from $\bar{h} \approx 1.747$, $1/\epsilon \approx 13.998$ satisfies $\bar{h} \to \infty$ as $1/\epsilon \to \infty$.

Figure 4.1 identifies three different bifurcation regimes, denoted by I, II and III, with differing bifurcation behaviour occurring in the different regimes, namely (using the terminology of [33] in the context of the Cahn–Hilliard equation):

- a “nucleation” regime for $1 < \bar{h} < 2^{1/3} \approx 1.259$ (Regime I),
- a “metastable” regime for $2^{1/3} < \bar{h} < 1.289$ and $\bar{h} > 1.747$ (Regime II), and
- an “unstable” regime for $1.289 < \bar{h} < 1.747$ (Regime III).

In Regime I, the constant solution $h(x) \equiv \bar{h}$ is linearly stable, which follows from analysing the spectrum of the operator S for $f'(\bar{h}) < 0$ in (4.32) and (4.33), but under sufficiently large perturbations, the system will evolve to a non-constant steady-state solution. See Laugesen and Pugh [58] for an extensive discussion of the stability analysis of steady-state solutions to thin-film equations.

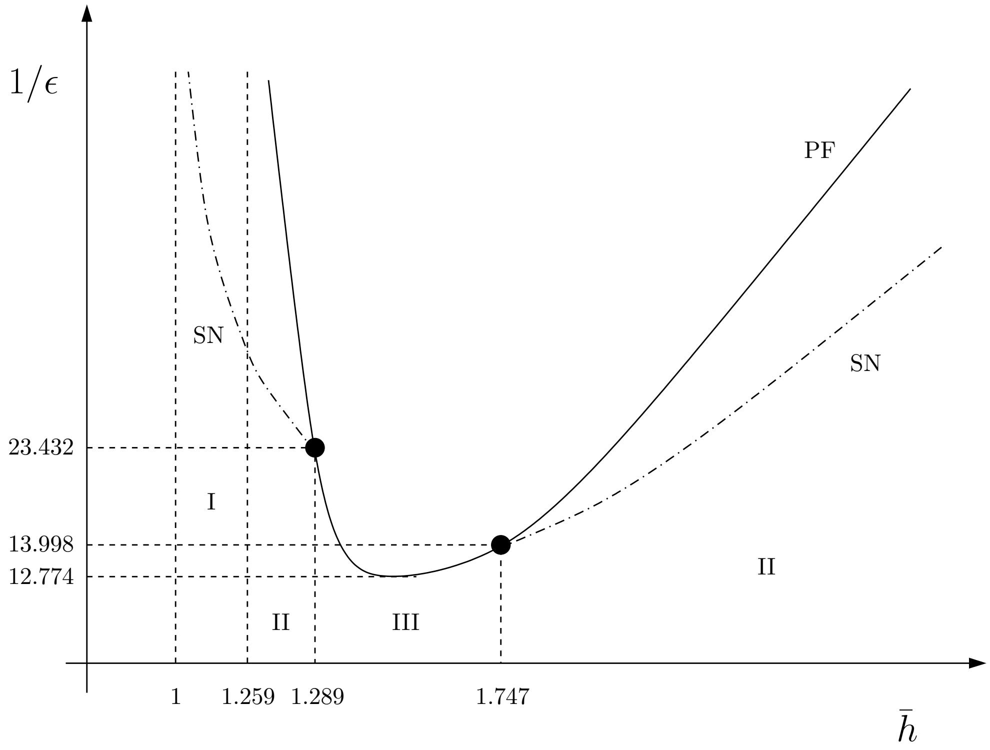

Figure 4.1: The global structure of branches of steady-state solutions with a unique maximum, including both saddle-node (SN) (shown with dash-dotted curves) and pitchfork (PF) bifurcation branches (shown with solid curves). The nucleation regime $1 < \bar{h} < 2^{1/3} \approx 1.259$ (Regime I), the metastable regime $2^{1/3} < \bar{h} < 1.289$ and $\bar{h} > 1.747$ (Regime II), and the unstable regime $1.289 < \bar{h} < 1.747$ (Regime III) are also indicated.

In Regime II, as ϵ is decreased, the constant solution $h(x) \equiv \bar{h}$ loses stability through a subcritical bifurcation.

In Regime III, as ϵ is decreased, the constant solution $h(x) \equiv \bar{h}$ loses stability through a supercritical bifurcation.

4.5 The Spatially Non-Homogeneous Case

As discussed in Section 1.8, Honisch et al. [46] chose the Derjaguin disjoining pressure $\Pi(h, x, y)$ to be of the form

$$\Pi(h, x, y) = \left(\frac{1}{h^6} - \frac{1}{h^3}\right)(1 + \rho\, G(x, y)), \tag{4.41}$$

where the function $G(x, y)$ models the non-homogeneity of the substrate and the parameter ρ, which can be either positive or negative, is called the "wettability contrast". Following Honisch et al. [46], in the remainder of the present work, we consider the specific case

$$G(x, y) = \sin(2\pi x) := G(x), \tag{4.42}$$

corresponding to an x-periodically patterned (*i.e.* striped) substrate.

There are, however, some difficulties in accepting (4.41) as a physically realistic form of the disjoining pressure for a non-homogeneous substrate. The problems arise because the two terms in (4.41) represent rather different physical effects. Specifically, since the $1/h^6$ term models the short-range interaction amongst the molecules of the liquid and the $1/h^3$ term models the long-range interaction, assuming that both terms reflect the patterning in the substrate in exactly the same way through their dependence on the same function $G(x, y)$ does not seem very plausible. Moreover, there are other studies which assume that the wettability of the substrate is incorporated in either the short-range interaction term or the long-range interaction term, but not both simultaneously, as discussed in Section 1.8. Hence in what follows we will consider the two cases $\Pi(h, x) = \Pi_{\mathrm{LR}}(h, x)$ and $\Pi(h, x) = \Pi_{\mathrm{SR}}(h, x)$, where LR stands for "long range" and SR stands for "short range", where

$$\Pi_{\mathrm{LR}}(h, x) = \frac{1}{h^6} - \frac{1}{h^3}(1 + \rho G(x)) \tag{4.43}$$

and

$$\Pi_{\mathrm{SR}}(h, x) = \frac{1}{h^6}(1 + \rho G(x)) - \frac{1}{h^3}, \tag{4.44}$$

in both of which $G(x)$ is given by (4.42) and ρ is the wettability contrast.

For small wettability contrast, $|\rho| \ll 1$, we do not expect there to be significant differences between the influence of Π_{LR} or Π_{SR} of the bifurcation diagrams, as these results depend only on the nature of the bifurcation in the homogeneous case $\rho = 0$ and on the symmetry groups under which the equations are invariant. To see this, consider the spatially non-homogeneous version of (4.12); *i.e.* the boundary value problem

$$\epsilon^2 h_{xx} + f(h,x) - \int_0^1 f(h,x)\,\mathrm{d}x = 0, \;\; 0 < x < 1, \tag{4.45}$$

where now

$$f(h,x) = \Pi_{\mathrm{LR}}(h,x) \text{ or } f(h,x) = \Pi_{\mathrm{SR}}(h,x). \tag{4.46}$$

subject to the periodic boundary conditions and the volume constraint,

$$h(0) = h(1), \quad h_x(0) = h_x(1), \text{ and } \int_0^1 h(x)\,\mathrm{d}x = \bar{h}. \tag{4.47}$$

Seeking an asymptotic solution to (4.45)–(4.47) in the form

$$h(x) = \bar{h} + \rho h_1(x) + O(\rho^2)$$

in the limit $\rho \to 0$, by substituting this anzatz into (4.45), we find that in the case of $\Pi_{\mathrm{LR}}(h,x)$, we have

$$h_1(x) = -\frac{\bar{h}^4 \sin(2\pi x)}{4\pi^2 \bar{h}^7 \epsilon^2 - 3\bar{h}^3 + 6}, \tag{4.48}$$

while, in the case of $\Pi_{\mathrm{SR}}(h,x)$, the equivalent result is

$$h_1(x) = \frac{\bar{h} \sin(2\pi x)}{4\pi^2 \bar{h}^7 \epsilon^2 - 3\bar{h}^3 + 6}, \tag{4.49}$$

(see Appendix F for details of the derivation of these two solutions).

For non-zero values of ρ, in both the Π_{LR} and Π_{SR} cases, the changes in the bifurcation diagrams obtained in the homogeneous case ($\rho = 0$) are an example of forced symmetry breaking (see, for example, Chillingworth [20]), which we discuss further in Appendix G. More precisely, we show there that, when $\rho \neq 0$, out of the entire $O(2)$ orbit, only two equilibria are left after symmetry breaking. Note that, in Figure 4.2 and subsequent figures, we use $\|\cdot\|_2$ to denote $L^2([0,1])$ norms.

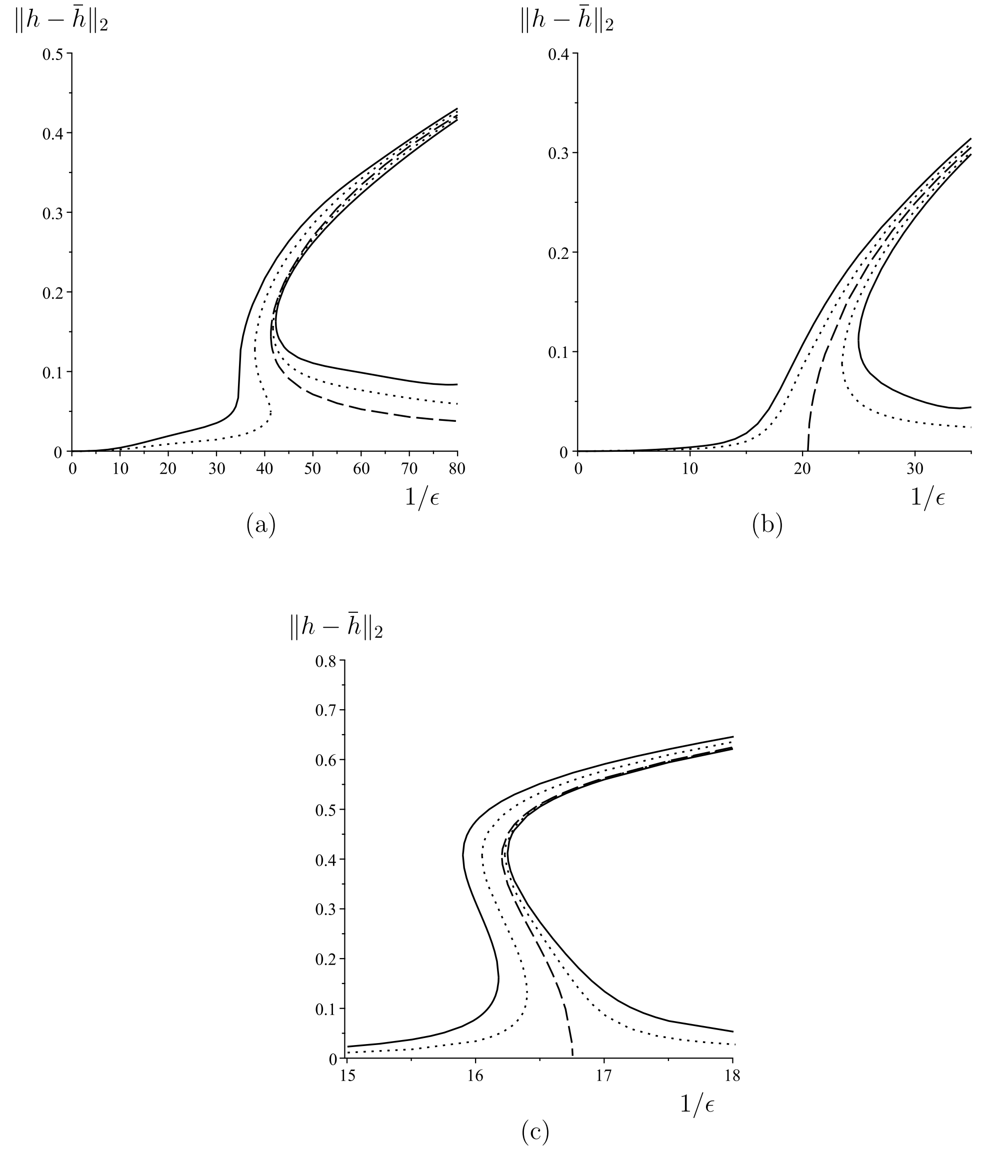

Figure 4.2: Bifurcation diagrams of solutions with a unique maximum, showing $\|h-\bar{h}\|_2$ plotted as a function of $1/\epsilon$ when the disjoining pressure is Π_{LR} for $\rho = 0$ (dashed curves), $\rho = 0.005$ (doted curves) and $\rho = 0.05$ (solid curves) for (a) $\bar{h} = 1.24$, (b) $\bar{h} = 1.3$, and (c) $\bar{h} = 2$, corresponding to Regimes I, III and II, respectively.

Figure 4.2 shows how, for small wettability contrast, $|\rho| \ll 1$, the resulting spatial non-homogeneity introduces imperfections [38] in the bifurcation diagrams of the homogeneous case $\rho = 0$ discussed in Section 4.4. It presents bifurcation diagrams in Regimes I, II and III when the disjoining pressure Π_{LR} is given by (4.43) for a range

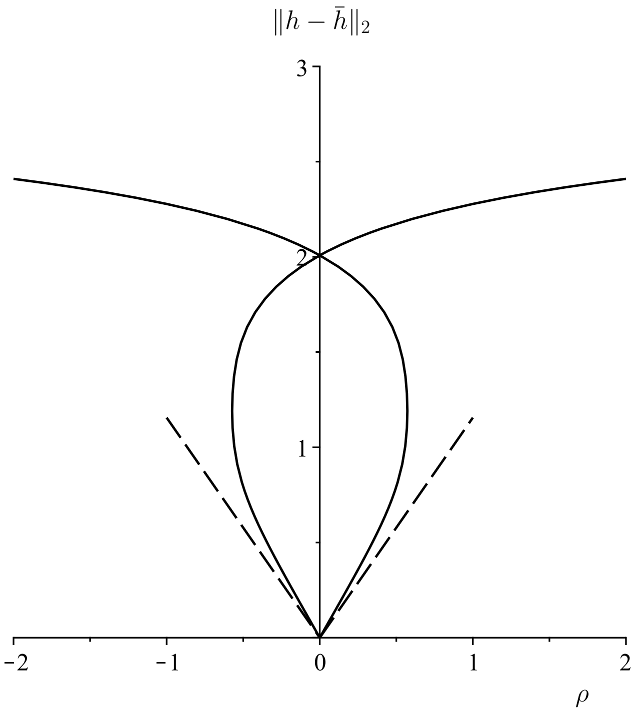

Figure 4.3: Bifurcation diagram for steady-state solutions with a unique maximum showing $\|h - \bar{h}\|_2$ plotted as a function of ρ when the disjoining pressure is Π_{LR}, for $\bar{h} = 3$ and $1/\epsilon = 50$. The leading-order dependence of $\|h - \bar{h}\|_2$ on ρ as $\rho \to 0$, given by (4.48), is shown with dashed lines.

of small values of ρ, together with the corresponding diagrams in the case $\rho = 0$. The corresponding bifurcation diagrams when the disjoining pressure Π_{SR} is given by (4.44) are very similar and hence are not shown here.

For large wettability contrast, specifically for $|\rho| \geq 1$, significant differences between the two forms of the disjoining pressure are to be expected. When using Π_{LR}, one expects global existence of positive solutions for all values of $|\rho|$; see for example Wu and Zheng [123]. On the other hand, when using Π_{SR}, there is the possibility of rupture of the liquid film for $|\rho| \geq 1$; see for example Bertozzi et al. [12] and Wu and Zheng [123], which means in this case we do not expect positive solutions for sufficiently large values of $|\rho|$.

In Figure 4.3, we plot the branches of the positive solutions of (4.45)–(4.47) with a unique maximum when the disjoining pressure is Π_{LR} for $\bar{h} = 3$ and $1/\epsilon = 50$, so

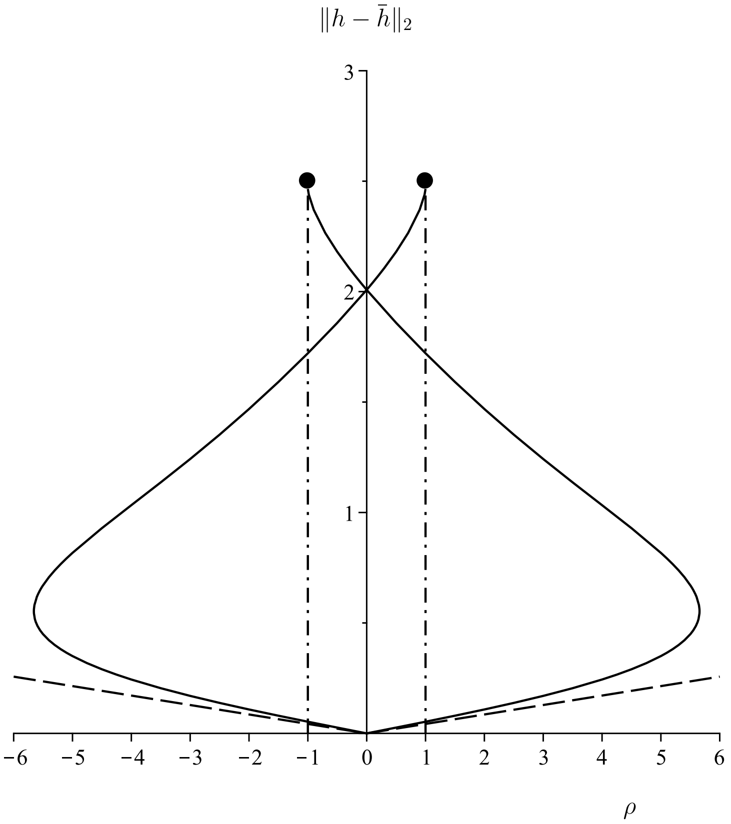

Figure 4.4: Bifurcation diagram for steady-state solutions with a unique maximum showing $\|h-\bar{h}\|_2$ plotted as a function of ρ when the disjoining pressure is Π_{SR}, for $\bar{h}=3$ and $1/\epsilon = 50$. The leading-order dependence of $\|h-\bar{h}\|_2$ on ρ as $\rho \to 0$, computed using (4.49), is shown with dashed lines. Note that the upper branches of solutions cannot be extended beyond $|\rho| = 1$ (indicated by filled circles).

that when $\rho = 0$ we are in Regime II above the curve PF of pitchfork bifurcations from the constant solution (see Figure 4.1). The work of Bertozzi et al. [12] and of Wu and Zheng [123], shows that strictly positive solutions exist for all values of $|\rho|$, beyond the range $[-2,2]$ for which we have we performed the continuation.

Figure 4.4 shows that the situation is different when the disjoining pressure is Π_{SR} (with same $\bar{h}$ and ϵ). At $|\rho| = 1$, one of the branches of smooth solutions disappears due to rupture of the film, so that at some point $x_0 \in [0,1]$, we have $h = 0$ and a strictly positive solution no longer exists, while the other two branches disappear at a saddle node bifurcation at $|\rho| \approx 5.8$. Note that, in Figures 4.3 and 4.4, the non-trivial "solution" on the axis $\rho = 0$ is, in fact, a whole $O(2)$-symmetric orbit of solutions

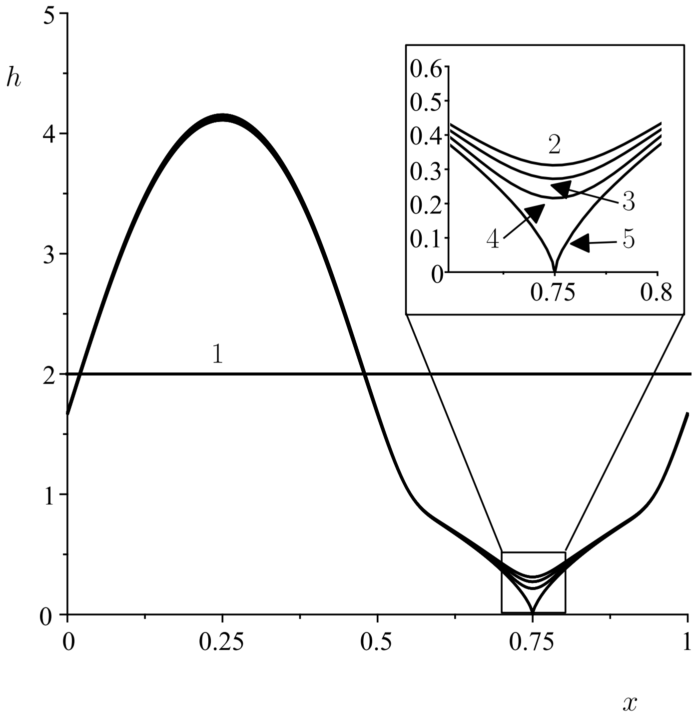

Figure 4.5: Solutions $h(x)$ when the disjoining pressure is Π_{SR} for $\bar{h} = 2$ and $1/\epsilon = 30$ for $\rho = 0$, 0.97, 0.98, 0.99 and 1, denoted by 1, 2, 3, 4 and 5, respectively, showing convergence of strictly positive solutions to a non-strictly positive one as $\rho \to 1^-$.

predicted by the analysis leading to Figure 4.1.

Note that, when the disjoining pressure is Π_{SR}, given by (4.44), we are unable to use AUTO to continue branches of solutions beyond the rupture of the film.

Figure 4.5 shows the film approaching rupture as $\rho \to 1^-$ at the point where the coefficient of the short-range interaction term disappears when $\rho = 1$, *i.e.* when $1 + \sin(2\pi x) = 0$ and hence at $x = 3/4$. These numerical results are consistent with the arguments of Bertozzi et al. [12].

Investigation of the possible leading-order balance in (4.12) when the disjoining pressure is Π_{SR} and $\rho = 1$ in the limit $x \to 3/4$ reveals that $h(x) = O\left((x - 3/4)^{2/3}\right)$; continuing the analysis to higher order yields

$$h = (2\pi^2)^{\frac{1}{3}} \left(x - \frac{3}{4}\right)^{\frac{2}{3}} - \frac{4\left(4\pi^{10}\right)^{1/3}\epsilon^2}{27}\left(x - \frac{3}{4}\right)^{\frac{4}{3}} + O\left(\left(x - \frac{3}{4}\right)^2\right). \qquad (4.50)$$

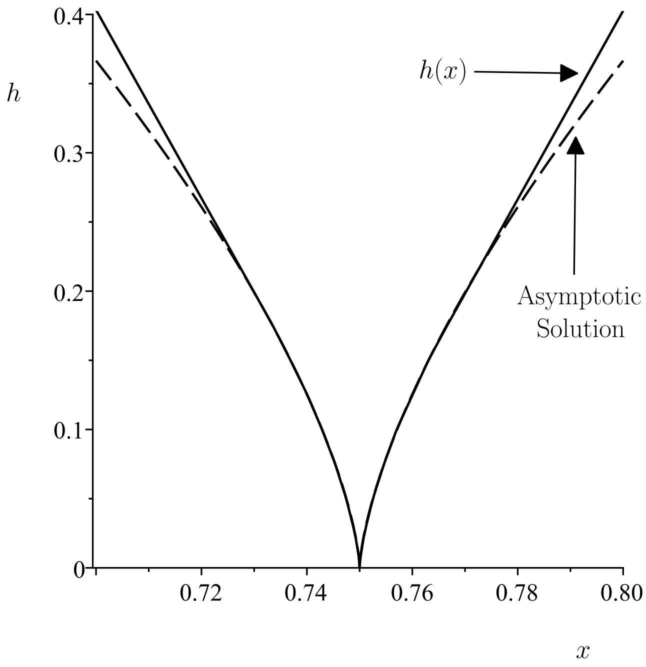

Figure 4.6: Detail near $x = 3/4$ of the solution $h(x)$ shown with solid line when the disjoining pressure is Π_{SR} and $\rho = 1$, and the two-term asymptotic solution given by (4.50) shown with dashed lines for $\bar{h} = 2$ and $\epsilon = 1/30$.

Figure 4.6 shows the detail of the excellent agreement between the solution $h(x)$ when $\rho = 1$ and the two-term asymptotic solution given by (4.50) close to $x = 3/4$.

Finally, Figures 4.7 and 4.8 show the multiplicity of solutions with a unique maximum for the disjoining pressures Π_{LR} and Π_{SR}, respectively, in the $(1/\epsilon, \rho)$-plane in the three regimes shown in Figure 4.1.

In Figure 4.8 the horizontal dashed line at $\rho = 1$ indicates rupture of the film and loss of a smooth strictly positive solution, implying that there are regions in parameter space where no such solutions exist.

In Figure 4.9, we give a detailed interpretation of Figure 4.7(c); a similar interpretation applies to the other parts of Figure 4.7 and Figure 4.8. Each of the curves in Figure 4.7(c) represents a saddle-node bifurcation. Like Figure 4.2(c), Figure 4.9 illustrates the bifurcation diagram of steady-state solutions with $\bar{h} = 2$ (Regime II) for $\rho = 0$ and $\rho = 0.005$. Increasing $1/\epsilon$ leads to a succession of saddle-node bifurcations in which the steady-state solutions change from 1 to 3 to 5 and then back to 3 again.

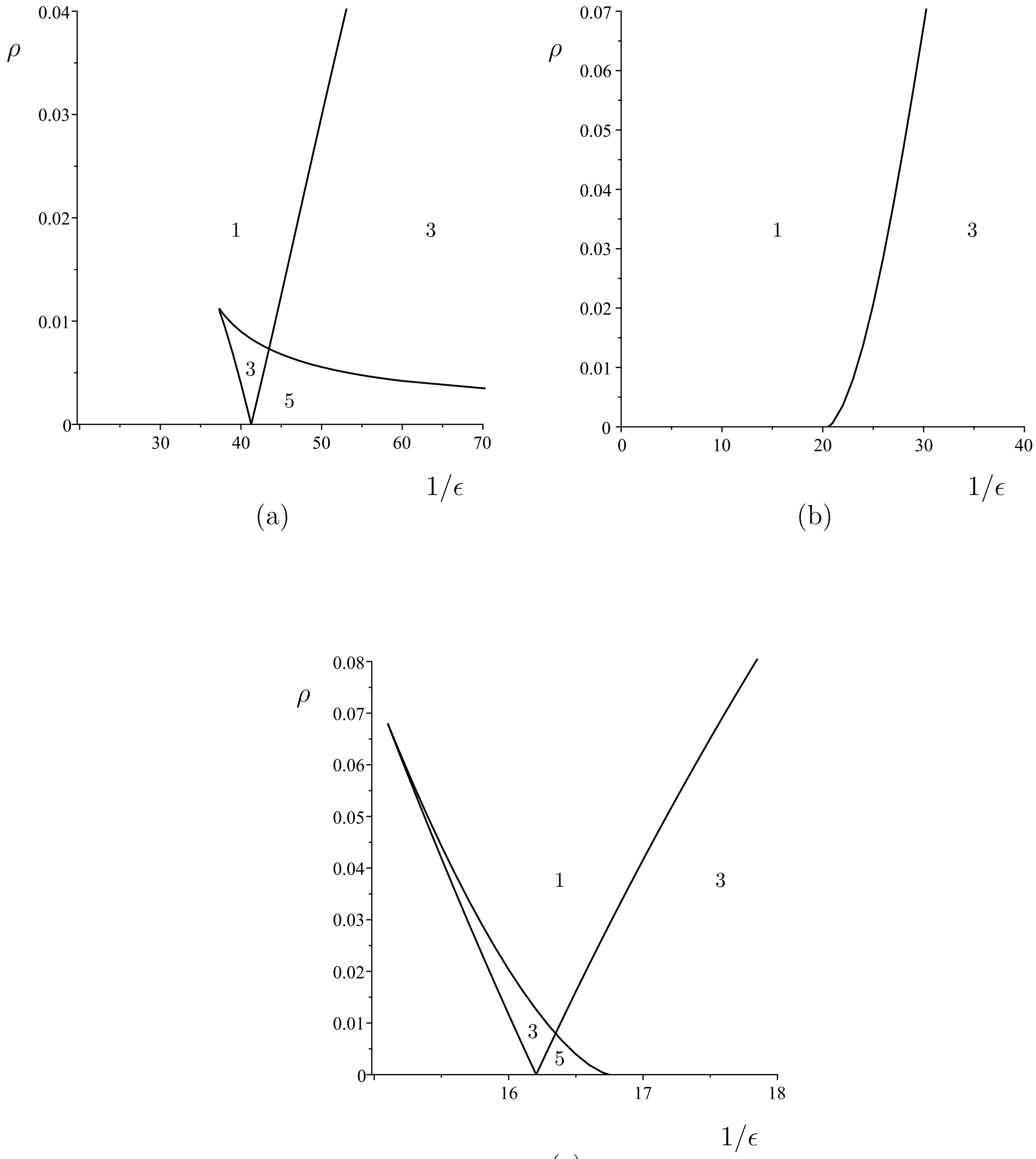

(a) (b)

(c)

Figure 4.7: Multiplicity of strictly positive solutions with a unique maximum in the $(1/\epsilon, \rho)$-plane when the disjoining pressure is Π_{LR} for (a) $\bar{h} = 1.24$ (Regime I), (b) $\bar{h} = 1.3$ (Regime III), and (c) $\bar{h} = 2$ (Regime II).

Figure 4.10, is a plot of the five steady-state solutions with a unique maximum, as shown in Figure 4.9 by (i)-(v).

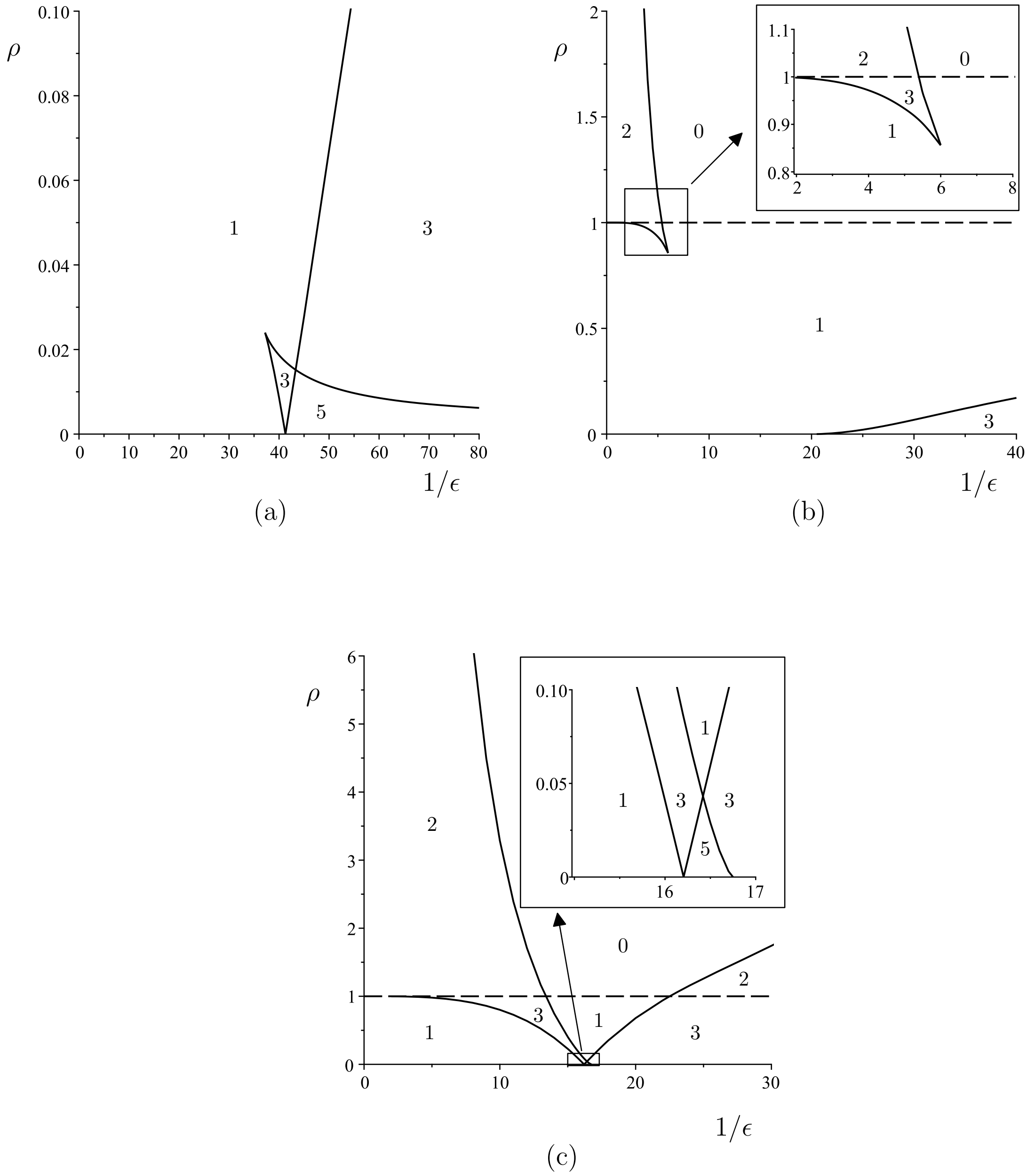

(a) (b) (c)

Figure 4.8: Multiplicity of strictly positive steady state solutions with a unique maximum in the $(1/\epsilon, \rho)$-plane when the disjoining pressure is Π_{SR} for (a) $\bar{h} = 1.24$ (Regime I), (b) $\bar{h} = 1.3$ (Regime III), and (c) $\bar{h} = 2$ (Regime II).

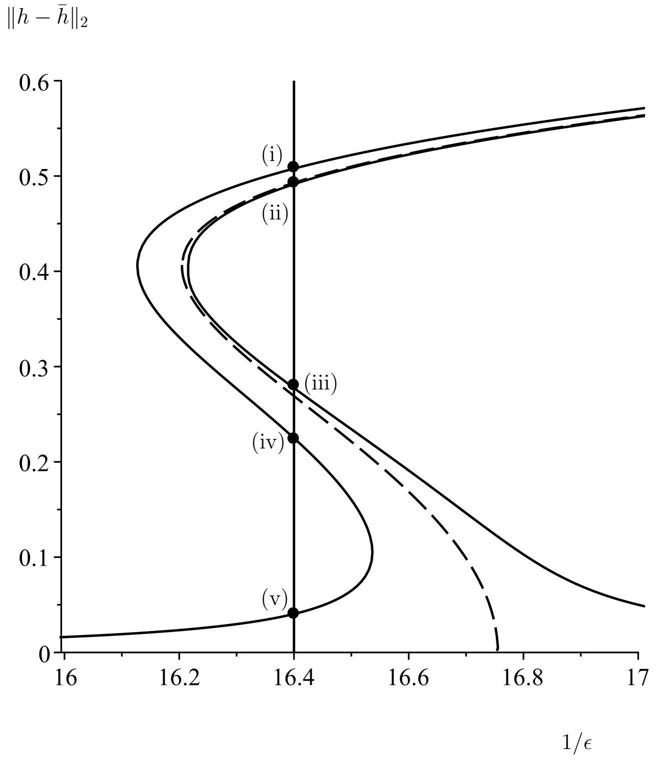

Figure 4.9: Bifurcation diagram of steady-state solutions with $\bar{h} = 2$ (Regime II) for $\rho = 0$ (dashed curves) and $\rho = 0.005$ (solid curves) indicating the different branches of steady-state solutions.

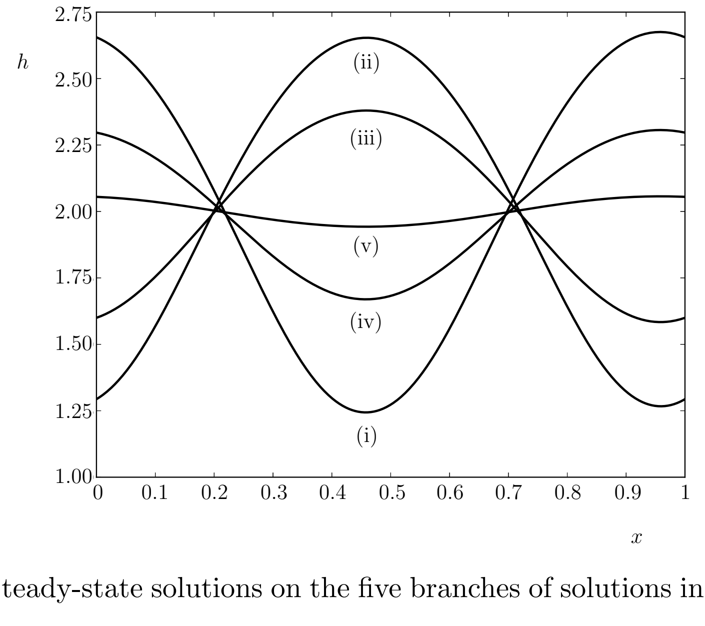

Figure 4.10: Steady-state solutions on the five branches of solutions indicated in Figure 4.9 by (i)-(v).

4.6 Conclusions

In the present chapter we have investigated the steady-state solutions of the thin-film evolution equation (4.1) both in the spatially homogeneous case (4.12)–(4.15) and in the spatially non-homogeneous case for two choices. Notably, these choices of spatially non-homogeneous Derjaguin disjoining pressure are given by (4.43) and (4.44). To this end, we provided a physical motivation for the above choices regarding the disjoining pressure. As we described in Section 4.1, we concentrated on the simplest steady-state solutions of (4.12)–(4.16); in particular, on branches of solutions with a unique maximum.

In the spatially homogeneous case (4.12)–(4.16), we used the Liapunov–Schmidt reduction of an equation invariant under the action of the $O(2)$ symmetry group to obtain local bifurcation results and to determine the dependence of the direction and nature of bifurcation in bifurcation parameter $1/\epsilon$ on the average film thickness $\bar{h}$; our results on the existence of three different bifurcation regimes, (namely nucleation, metastable, and unstable) are summarised in Propositions 1 and 2 and in the phase diagram shown in Figure 4.1, obtained using AUTO.

In the spatially non-homogeneous case (4.45)–(4.47), we clarified the $O(2)$ symmetry breaking phenomenon (see Appendix G) and presented imperfect bifurcation diagrams in Figure 4.2 and global bifurcation diagrams using the wettability contrast ρ as a bifurcation parameter for fixed ϵ and $\bar{h}$ in Figures 4.3 and 4.4.

To assist in more detailed discussion of Figure 4.3, Figure 4.11 adds labels to the various branches of strictly positive steady state solutions that have a unique maximum. These labels are explained below.

The language of global compact attractors [41, 123] can be used to explain our results. In systems such as (4.3), the global compact attractor of the PDE is the union of equilibria and their unstable manifolds. Figures 4.12 and 4.13 illustrate the global

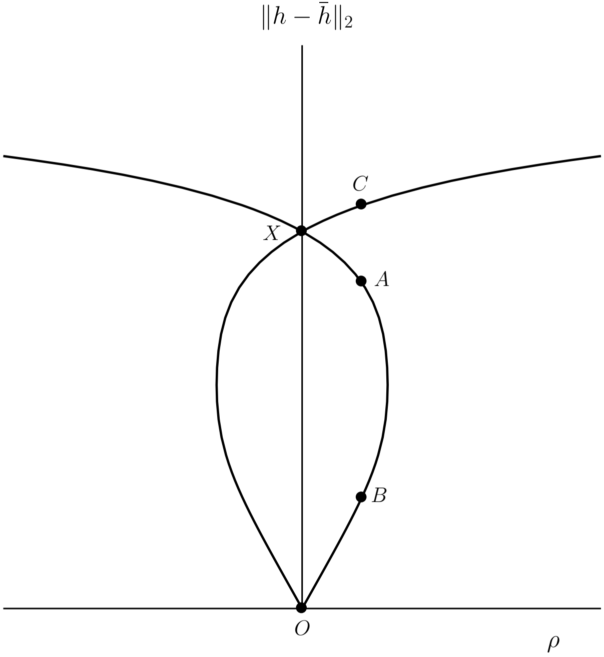

Figure 4.11: Figure 4.3 with the different solution branches labelled.

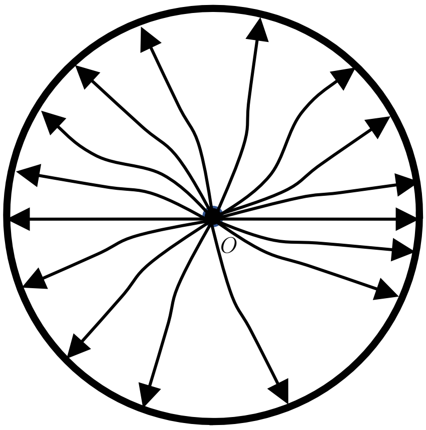

Figure 4.12: Sketch of the global attractor for $\rho = 0$. The thicker circle represents the $O(2)$ orbit of steady-states and O represents the constant solution $h(x) = \bar{h}$.

attractor of (4.3) for $\epsilon = 1/50$ and $\bar{h} = 3$, which are the values that were used to plot Figure 4.3. For these values of the parameters the attractor is two-dimensional and we sketch its projection onto a plane.

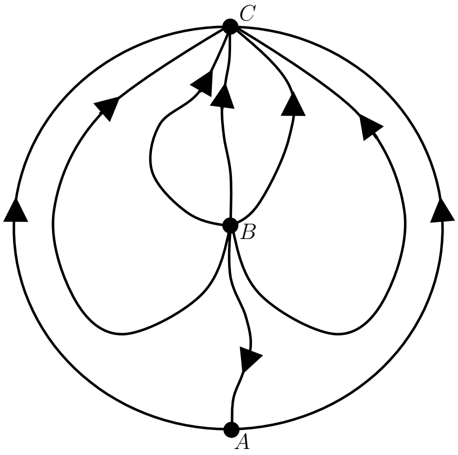

Figure 4.13: Sketch of the global attractor for small non-zero values of $|\rho|$. The points A, B, C correspond to the steady-state solutions labelled in Figure 4.11.

When $\rho = 0$, for $1/\epsilon = 50$, the attractor is two-dimensional; the constant solution $h \equiv \bar{h}$ denoted by O has a two-dimensional unstable manifold and X corresponds to a whole $O(2)$ orbit of steady-state solutions. A sketch of the attractor in this case is shown in Figure 4.12.

When $|\rho|$ takes small positive values, only two steady-state solutions, denoted by A and C remain from the entire $O(2)$ orbit, as discussed in Appendix G, while the constant solution continues to B without change of stability. The resulting two-dimensional attractor is sketched in Figure 4.13.

Increasing $|\rho|$ causes the steady-state solutions A and B to coalesce in a saddle-node bifurcation, so that the attractor degenerates to a single asymptotically stable steady-state solution. It would be interesting to understand why this collision of steady-state solution branches occurs.

We have also explored the geometry of film rupture, which occurs as $\rho \to 1^-$ when the disjoining pressure is given by Π_{SR}. This phenomenon is shown in detail in Figures 4.5 and 4.6.

Finally, Figures 4.7 and 4.8 show the results of a two-parameter continuation study in the $(1/\epsilon, \rho)$ plane, which illustrates how the multiplicity of positive steady-state solutions changes as parameters are varied. Specifically, in the case of Derjaguin pressure

Π_{SR} shown in Figure 4.8, regimes are indicated in parameter space where no such solutions exist. We conjecture that, in such regimes, solving the unsteady problem for any positive initial condition will converge to a weak non-negative steady-state solution of the thin-film equation, with regions where $h(x) = 0$, *i.e.* a steady-state solution with film rupture. A discussion of this kind of non-classical solution of thin-film equations in homogeneous cases is given in the work of Laugesen and Pugh [59].

In the case of disjoining pressure Π_{SR} (4.44), we could not use the AUTO-07p version of AUTO to continue branches of solutions beyond rupture; that is, we could not use AUTO to compute weak non-negative steady-state solutions discussed in the previous paragraph. It would be an interesting project to develop such a capability for this powerful and versatile piece of software.

Figures 4.8(b) and 4.8(c) provide numerical evidence for the existence of a curve of saddle-node bifurcations, converging to the point $(0, 1)$ in the $(1/\epsilon, \rho)$ plane; an explanation for this feature of the global bifurcation diagrams requires further study.

In summary: the primary inspiration for our study came from the work of Honisch et al. [46]. Our study clarifies the mathematical properties of (4.12)–(4.15) and (4.45)–(4.47), giving a better understanding of the structure of bifurcations in Figure 3(a) of that paper for non-zero values of ρ. However, mathematical exploration of many of their other numerical findings has not yet been undertaken; this includes the stability of ridge solutions shown in their Figure 5 in the context of the full two-dimensional problem of a substrate with periodic wettability stripes. Clearly, a lot of work is still needed on heterogeneous substrates with more complex wettability geometry.

Chapter 5

Conclusions and Future Work

5.1 Conclusions

In this thesis, we considered three different but related problems involving thin-film flow over complex surfaces, two problems concerned with rivulet flow down an inclined substrate and one concerning thin-film flow on a heterogeneous substrate.

In Chapter 2, we examined the locally unidirectional flow of a rivulet with prescribed flux $\bar{Q} > 0$ on a slippery substrate inclined at an angle α to the horizontal in two cases. The first case concerned a rivulet with constant semi-width $a = \bar{a}$ (> 0) (*i.e.* pinned contact lines) and a variable contact angle. The second case concerned a rivulet with variable semi-width and a constant non-zero contact angle $\beta = \bar{\beta}$ (≥ 0). In particular, we considered rivulet flow in the azimuthal direction from the top, corresponding to $\alpha = 0$, to the bottom, corresponding to $\alpha = \pi$, of a large horizontal cylinder. The influence of different slip lengths λ upon the flow was determined, and, in particular, we were able to show that the features of the rivulet, including shape and size, were strongly dependent on the value of λ. However, in both cases, we found that for all values of $\lambda > 0$ many of the qualitative features of the rivulet (such as, for example, that a narrow rivulet with constant semi-width $a = \bar{a} \leq \pi$ can run from $\alpha = 0$ to $\alpha = \pi$ and a wide rivulet with constant semi-width $a = \bar{a} > \pi$ can run from $\alpha = 0$, but only to a critical angle $\alpha = \alpha_{\mathrm{c}}$) are the same as in the classical case of no slip, $\lambda = 0$. Furthermore, we observed that α_{c} is independent of λ.

For a rivulet with constant semi-width $a = \bar{a}$ (> 0), we found that, in the limit of strong slip (*i.e.* $\lambda \to \infty$) the rivulet becomes shallow and the velocity becomes large and plug-like, while for a rivulet with positive constant contact angle $\beta = \bar{\beta}$ (> 0), we found that in the same limit the rivulet becomes narrow and shallow and the velocity becomes large and plug-like.

We also considered the effect of a Greenspan (rather than a Navier) slip condition and found that the behaviour of the rivulet is qualitatively (but not quantitatively) similar to the behaviour of the rivulet with the Navier slip condition.

In Chapter 3, we considered the steady gravity-driven flow of a symmetrical rivulet of a Newtonian fluid as it flows over and through an inclined planar membrane inclined at an angle α to the horizontal. In this problem, the membrane consists of two parts: an impermeable part for $x \leq 0$, and a permeable part for $x > 0$. As in Chapter 2, we studied how a rivulet with a prescribed volume flux $\bar{Q}$ (> 0) behaves with either a constant semi-width or with a constant contact angle. We focused on the behaviour of the rivulet on the permeable part of the membrane. In particular, we determined the survival length L of the rivulet on the permeable part.

For a rivulet with constant semi-width $a = \bar{a}$ (> 0), we found exact solutions for both the contact angle and the survival length L of the rivulet. We found that the survival length L of the rivulet depends on the value of $\bar{a}$. When $0 < \bar{a} < \pi/2$, rivulets exist and have a finite survival length for all values of α. On the other hand, when $\bar{a} \geq \pi/2$, there is a critical value of $\alpha = \alpha_{\text{crit}}$ at which the survival length of the rivulet tends to infinity, and for $\alpha > \alpha_{\text{crit}}$ there is no physically realisable solutions because it always predicts that $L < 0$, where α_{crit} ($\pi/2 < \alpha_{\text{crit}} \leq \pi$) is obtained by solving the equation $m\bar{a} = \pi/2$ for α.

For a rivulet with a constant contact angle $\beta = \bar{\beta}$ (≥ 0), we obtained exact solutions for both the contact angle and the survival length of the rivulet only for the special case $\alpha = \pi/2$. For other values of α, a nonlinear ordinary differential equation for $a(x)$ had to be solved numerically. We found that when $0 < \bar{a} \leq \pi/2$, rivulets exist and have a finite survival length L for all values of α. On the other hand, when $\bar{a} > \pi/2$, similar to the case of constant semi-width, there is a critical value of $\alpha = \alpha_{\text{crit}}$ at which the survival length of the rivulet tends to infinity, and for $\alpha > \alpha_{\mathrm{crit}}$ there is no physically realisable solutions. We also found that there exists an interval for the constant semi-width $\bar{a}$ in which the survival length of the rivulet L varies non-monotonically with α, having a local maximum and a local minimum. At a critical value of $\bar{a} = \bar{a}_{\mathrm{crit}}$, the local maximum and minimum coalesce. Above this critical value, the survival length of the rivulet increases monotonically to infinity as $\alpha \to {\alpha_{\mathrm{crit}}}^{-}$.

In Chapter 4, we investigated pattern formation in a thin film on both spatially homogeneous and non-homogeneous planar substrates with a Derjaguin disjoining pressure. In the case of spatially homogeneous substrate we used a Liapunov–Schmidt reduction to show how the local bifurcation structure of the problem is dependent on the average film thickness $\bar{h}$. Using AUTO, we explored the global structure of branches of stationary solutions for both a spatially homogeneous substrate case and a spatially non-homogeneous substrate case.

For the spatially homogeneous case, we showed, in Propositions 2 and 3, the conditions under which supercritical and subcritical bifurcations occur. We also showed that there are no nontrivial solutions when $\bar{h} \leq 1$. We identified three different bifurcation regimes; nucleation, metastable, and unstable regimes, as shown in Figure 4.1.

For the spatially non-homogeneous case, we considered two forms of Derjaguin disjoining pressure and studied the dependence of the stationary solutions on the wettability contrast ρ. When the wettability contrast was small, we found the same imperfections were introduced in the bifurcation diagrams of the homogeneous case for both forms of disjoining pressure. When the wettability contrast was large, we found significant differences between the bifurcation diagrams for the two forms of disjoining pressure. Specifically, for the first form in which we introduced varying wettability properties in the long-range part of the disjoining pressure, we found that positive solutions exist for all values of the wettability contrast. For the second form in which we introduced varying wettability properties in the short-range part of the disjoining pressure, we found that positive solutions do not exist for sufficiently large values of the wettability contrast. This is due to the rupture of the film which is expected since the disjoining pressure of the second form is known to lead to finite-time rupture.

For both cases, we calculated branches of stationary solutions using AUTO. However, for the spatially non-homogeneous case, we were not able to use AUTO to continue generating branches of solutions beyond the rupture of the film. In particular, we could not use AUTO to compute weak non-negative stationary solutions of the thin-film equation having regions in which the steady state is zero (*i.e.* $h(x) = 0$).

5.2 Future Work

As we said at the start of Section 5.1, the work described in this thesis has addressed some problems regarding thin-film flows over complex surfaces. This section discusses some possible directions for future work in this area building on the work presented in this thesis.

In Chapter 2, we considered gravity-driven rivulet flow down an inclined slippery substrate for a rivulet with either constant width or constant contact angle. In particular, we employed the most widely used slip condition, namely the Navier slip condition, and determined the effect that varying the slip length λ has on the rivulet. Even though we also used another slip model, namely the Greenspan slip condition, in which λ is considered as a function of the rivulet thickness h namely $\lambda = \lambda_{\mathrm{G}}/h$, where λ_{G} is a positive constant, it would also be of interest to examine the effects of other slip models and compare it with our analysis. For example, the slip model proposed by Haley and Miksis [42] namely $\lambda = \lambda_{\mathrm{HM}}/h^2$, where λ_{HM} is a positive constant, could be considered.

In Chapter 3, we considered the steady gravity-driven flow of a symmetrical rivulet over and through a permeable membrane. One of the most fundamental assumptions in this analysis is that once the fluid has passed through the membrane, it falls off the lower surface of the membrane and plays no further role in the problem. Future research on this problem should consider what happens if some or all of the fluid adheres to the lower surface of the membrane in the form of a new rivulet, as shown in Figure 5.1, where $h^{+}(x, y)$ and $h^{-}(x, y)$ denote the film thickness above and below the membrane, respectively. In this situation (*i.e.* a rivulet flow below the membrane), the rivulet may become unstable and break up into a number of separate rivulets depending on

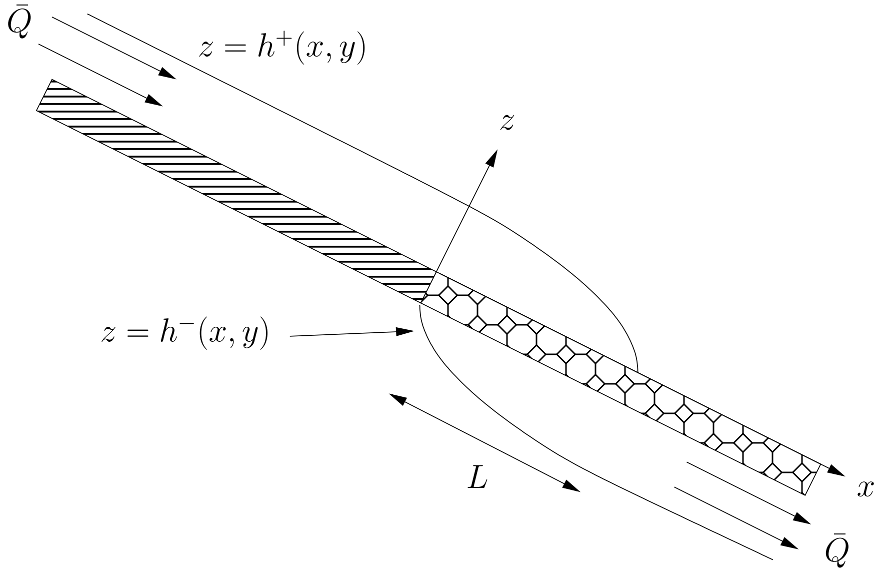

Figure 5.1: Geometry of a rivulet flowing down an inclined planar substrate similar to the problem considered in Chapter 3, where $h^+(x,y)$ and $h^-(x,y)$ denote the film thickness above and below the membrane, respectively. However, in this problem fluid forms a second rivulet on the underside of the membrane after passing through it.

its width and the substrate inclination.

In Chapter 4, we revisited the work of Honisch et al. [46] and we investigated the stationary solutions of a thin-film equation. One possible avenue for future research would be to extend this work by studying a three-dimensional situation in which the height of the thin liquid layer h is dependent upon both the x and the y coordinates. Such a study would help us to understand how ρ and $\bar{h}$ influence the stability of y-independent solutions in the plane and thereby investigate the stability of ridge solutions shown in Figure 5 of Honisch et al. [46].

Future research could also examine the asymptotic structure of the stationary solutions of (4.12)–(4.16) in the limit $\epsilon \to 0$, which corresponds to the limit of weak surface tension. Our numerical calculations using AUTO show that a droplet-like (*i.e.* "hump") solution of this problem, with volume $\bar{h} - 1 > 0$ sitting on an adsorbed film of uniform thickness unity, becomes thinner and taller as $\epsilon \to 0$. Though this limit takes us beyond the domain of validity of the thin film approximation, the challenge is to quantify mathematically this sharpening and thinning process.

Several studies, for example, Oron and Bankoff [79], Amini and Homsy [7] and Ji and Witelski [50] have studied various evaporation models in which the evaporative flux (*i.e.* the mass loss) has various different forms. Another way to expand upon the work presented in Chapter 4 would be to incorporate the effects of evaporation into the thin-film equation (4.1) and then to investigate the bifurcation structure of its steady state solutions. Also, for example, we can investigate the influence of the substrate properties, such as the wettability of the substrate and the stripe widths, on the evaporation rate. Such an analysis would help to improve our fundamental understanding of evaporation on complex surfaces.

Bates and Fife [9] formulated spectral comparison principles, comparing the spctra of linearizations around steady states for the Cahn-Hilliard and nonlocal bistable reaction-diffusion equation. This has relevance to the work described in Chapter 4. The solutions of equations (4.45)–(4.47), the steady-state solutions of the one-dimensional version of the evolution equation (4.1), which is a degenerate quasi-linear fourth-order PDE given by (4.3), namely

$$h_t = (Q(h)P(x,h)_x)_x, \quad 0 < x < L, \tag{5.1}$$

where $Q(h)$ is the mobility coefficient, and $P(x,h)$ is the generalized pressure as discussed in Section 4.1, are be thought of as the steady-state solutions of a much simpler second-order semi-linear non-local equation:

$$h_t = \gamma h_{xx} + \Pi(h,x) - \frac{1}{L}\int_0^L \Pi(h,x)\,\mathrm{d}x, \quad 0 < x < L. \tag{5.2}$$

Thus, it would be interesting to extend the work of Chapter 4 by using the spectral comparison principles of Bates and Fife [9] to discuss the stability of stationary solutions of equation (5.2).

As we mentioned at the end of Section 5.1, we could not use AUTO to compute weak non-negative stationary solutions of the thin-film equation. Therefore, future studies could fruitfully explore this issue further by adding to AUTO the capability to solve for non-negative, non-smooth stationary solutions.

In conclusion, while the work in this thesis gives some new insights into thin-film flow over complex surfaces, there are still many aspects of this fascinating and industrially important area to explore.

Appendix A

Real Solution of Equation (2.19) in the General Case $\lambda \geq 0$

In this Appendix we present the real solution h_{m} of the cubic polynomial equation (2.19), namely

$$h_{\mathrm{m}}^3 + \frac{18\lambda}{5} h_{\mathrm{m}}^2 - \frac{24\bar{Q}m}{5\pi \sin\alpha} = 0, \tag{A.1}$$

in the general case $\lambda \geq 0$.

Given a cubic polynomial of the form

$$f(x) = ax^3 + bx^2 + cx + d, \tag{A.2}$$

and defining the following quantities

$$x_N = -\frac{b}{3a}, \quad y_N = f(x_N), \quad \delta^2 = \frac{b^2 - 3ac}{9a^2}, \quad k = 2a\delta^3, \tag{A.3}$$

Holmes [45] shows that in the case $|y_N/k| > 1$, there is one real root given by

$$x = x_N + 2\delta \cosh\left(\frac{1}{3}\cosh^{-1}\left(-\frac{y_N}{k}\right)\right), \tag{A.4}$$

when

$$\frac{y_N}{k} < -1, \tag{A.5}$$

and

$$x = x_N - 2\delta \cosh\left(\frac{1}{3}\cosh^{-1}\left(\frac{y_N}{k}\right)\right), \tag{A.6}$$

when

$$\frac{y_N}{k} > 1. \tag{A.7}$$

For the case $|y_N/k| \leq 1$, Nickalls [75] showed that there are three real roots given by

$$x_1 = x_N + 2\delta \cos\theta, \tag{A.8}$$

$$x_2 = x_N + 2\delta \cos\left(2\pi/3 + \theta\right), \tag{A.9}$$

$$x_3 = x_N + 2\delta \cos\left(4\pi/3 + \theta\right), \tag{A.10}$$

where

$$\theta = \frac{1}{3}\cos^{-1}\left(-\frac{y_N}{k}\right). \tag{A.11}$$

Following the approach of Holmes [45] and Nickalls [75], we define the following quantities

$$\begin{aligned} a &= 1, \quad b = \frac{18\lambda}{5}, \quad x_N = -\frac{6\lambda}{5}, \\ y_N &= \frac{432}{125}\lambda^3 - \frac{24\bar{Q}m}{5\pi\sin\alpha}, \quad \delta = \frac{6\lambda}{5}, \quad k = \frac{432\lambda^3}{125}, \end{aligned} \tag{A.12}$$

hence when $\bar{Q} > Q^*$ for $\lambda > 0$, we obtain $y_N/k < -1$ and therefore the solution of (A.1) is

$$h_{\mathrm{m}} = \frac{6\lambda}{5}\left\{2\cosh\left[\frac{1}{3}\cosh^{-1}\left(\frac{25\bar{Q}m}{18\pi\lambda^3\sin\alpha} - 1\right)\right] - 1\right\}, \tag{A.13}$$

and that when $0 \leq \bar{Q} \leq Q^*$ for $\lambda > 0$, we have $|y_N/k| \leq 1$ and therefore there is a unique positive solution

$$h_{\mathrm{m}} = \frac{6\lambda}{5}\left\{2\cos\left[\frac{1}{3}\cos^{-1}\left(\frac{25\bar{Q}m}{18\pi\lambda^3\sin\alpha} - 1\right)\right] - 1\right\}. \tag{A.14}$$

Note that in the limit of weak slip, $\lambda \to 0^+$, the leading-order term of equations (A.13) and (A.14) is given by

$$h_{\mathrm{m}} = \left(\frac{24\bar{Q}m}{5\pi\sin\alpha}\right)^{\frac{1}{3}} \tag{A.15}$$

which is exactly the solution in the special case of zero slip length, $\lambda = 0$, given by equation (1.22).

Appendix B

Real Solution of Equation (2.44) in the General Case $\lambda \geq 0$

In this Appendix we follows very similar lines to the derivation in Appendix A and present the real solution β of the cubic polynomial equation (2.44), namely

$$\beta^3 + \frac{9\lambda m g(m\bar{a})}{f(m\bar{a})}\beta^2 - \frac{9\bar{Q}m^4}{f(m\bar{a})\sin\alpha} = 0, \tag{B.1}$$

in the general case $\lambda \geq 0$.

Given a cubic polynomial of the form

$$f(x) = ax^3 + bx^2 + cx + d, \tag{B.2}$$

and defining the following quantities

$$x_N = -\frac{b}{3a}, \quad y_N = f(x_N), \quad \delta^2 = \frac{b^2 - 3ac}{9a^2}, \quad k = 2a\delta^3, \tag{B.3}$$

Holmes [45] shows that in the case $|y_N/k| > 1$, there is one real root given by

$$x = x_N + 2\delta\cosh\left(\frac{1}{3}\cosh^{-1}\left(-\frac{y_N}{k}\right)\right), \tag{B.4}$$

when

$$\frac{y_N}{k} < -1, \tag{B.5}$$

and

$$x = x_N - 2\delta \cosh\left(\frac{1}{3}\cosh^{-1}\left(\frac{y_N}{k}\right)\right), \tag{B.6}$$

when

$$\frac{y_N}{k} > 1. \tag{B.7}$$

For the case $|y_N/k| \leq 1$, Nickalls [75] showed that there are three real roots given by

$$x_1 = x_N + 2\delta \cos\theta, \tag{B.8}$$

$$x_2 = x_N + 2\delta \cos\left(2\pi/3 + \theta\right), \tag{B.9}$$

$$x_3 = x_N + 2\delta \cos\left(4\pi/3 + \theta\right), \tag{B.10}$$

where

$$\theta = \frac{1}{3}\cos^{-1}\left(-\frac{y_N}{k}\right). \tag{B.11}$$

Following the approach of Holmes [45] and Nickalls [75], we define the following quantities

$$\begin{aligned} a = 1, \;\; b = \frac{9\lambda m g(m\bar{a})}{f(m\bar{a})}, \;\; x_N = -\frac{3\lambda m g(m\bar{a})}{f(m\bar{a})}, \\ y_N = \frac{54\lambda^3 m^3 g(m\bar{a})^3}{f(m\bar{a})^3} - \frac{9\bar{Q}m^4}{f(m\bar{a})\sin\alpha}, \;\; \delta = \frac{3\lambda m g(m\bar{a})}{f(m\bar{a})}, \;\; k = \frac{54\lambda^3 m^3 g(m\bar{a})^3}{f(m\bar{a})^3}, \end{aligned} \tag{B.12}$$

hence when $\bar{Q}mf(m\bar{a})^2 > 12\lambda^3 g(m\bar{a})^3 \sin\alpha$ for $\lambda > 0$, we obtain $y_N/k < -1$ and therefore the solution of (B.1) is

$$\beta = \frac{3\lambda\, m g(m\bar{a})}{f(m\bar{a})}\left\{2\cosh\left[\frac{1}{3}\cosh^{-1}\left(\frac{\bar{Q}mf(m\bar{a})^2}{6\lambda^3 g(m\bar{a})^3 \sin\alpha} - 1\right)\right] - 1\right\}. \tag{B.13}$$

Here we did not use (B.6) since (B.7) is not fulfilled. When $0 \leq \bar{Q}mf(m\bar{a})^2 \leq 12\lambda^3 g(m\bar{a})^3 \sin\alpha$ and for $\lambda > 0$, we have $|y_N/k| \leq 1$ and therefore there is a unique positive solution given by

$$\beta = \frac{3\lambda\, mg(m\bar{a})}{f(m\bar{a})}\left\{2\cos\left[\frac{1}{3}\cos^{-1}\left(\frac{\bar{Q}mf(m\bar{a})^2}{6\lambda^3 g(m\bar{a})^3\sin\alpha}-1\right)\right]-1\right\}. \tag{B.14}$$

Note that in the limit of weak slip, $\lambda \to 0^+$, the leading-order term of equations (B.13) and (B.14) is given by

$$\beta = \left(\frac{9\bar{Q}m^4}{f(m\bar{a})\sin\alpha}\right)^{\frac{1}{3}} \tag{B.15}$$

which is exactly the solution in the special case of zero slip length, $\lambda = 0$, given by equation (2.45).

Appendix C

Asymptotic Behaviour of α_{min} and β_{min} in the Limit $\lambda \to \infty$

In this Appendix we determine the asymptotic behaviour of α_{min} and β_{min} shown in Figure 2.9 in Chapter 2 in the limit of a strong slip, $\lambda \to \infty$, for a rivulet with constant semi-width $a = \bar{a}$. Note that a similar procedure can be used to determine the asymptotics behaviour in the limit of a weak slip, $\lambda \to 0^+$.

When $\lambda \to \infty$ we find from (2.34) that $\beta \to 0$. Writing the solution of equation (2.34) in the form of an expansion

$$\beta(\lambda) = \beta_0(\lambda) + \beta_1(\lambda) \tag{C.1}$$

and substituting expansion (C.1) in (2.34), taking only the main terms $\beta_0(\lambda)$, we obtain

$$\beta_0 = \sqrt{\frac{m^3\bar{Q}}{g(m\bar{a})\sin\alpha}\frac{1}{\lambda}} \quad \text{and} \quad \beta_1 = -\frac{\beta_0^2}{18m}\frac{f(m\bar{a})}{g(m\bar{a})}\frac{1}{\lambda}. \tag{C.2}$$

Hence we have

$$\beta = \sqrt{\frac{m^3\bar{Q}}{g(m\bar{a})\sin\alpha}\frac{1}{\lambda}} - \frac{m^2\bar{Q}}{18\sin\alpha}\frac{f(m\bar{a})}{(g(m\bar{a}))^2}\left(\frac{1}{\lambda}\right)^2. \tag{C.3}$$

Let

$$B_1(\alpha) = \sqrt{\frac{m^3\bar{Q}}{g(m\bar{a})\sin\alpha}} \quad \text{and} \quad B_2(\alpha) = -\frac{m^2\bar{Q}}{18\sin\alpha}\frac{f(m\bar{a})}{(g(m\bar{a}))^2}. \tag{C.4}$$

Then

$$\beta = B_1(\alpha)\left(\frac{1}{\lambda}\right)^{\frac{1}{2}} + B_2(\alpha)\left(\frac{1}{\lambda}\right)^{2}. \tag{C.5}$$

To find $\alpha_{\min}$, we write the equation $\beta'(\alpha) = 0$ then

$$\beta'(\alpha) = B_1'(\alpha)\left(\frac{1}{\lambda}\right)^{\frac{1}{2}} + B_2'(\alpha)\left(\frac{1}{\lambda}\right)^{2} = 0, \tag{C.6}$$

where

$$B_1'(\alpha) = \frac{1}{2}\sqrt{\frac{m\bar{Q}}{g(m\bar{a})\sin\alpha}}\left\{\left[3 - \frac{g'(m\bar{a})}{g(m\bar{a})}m\bar{a}\right]m'(\alpha) - m\cot\alpha\right\} \tag{C.7}$$

and

$$\begin{aligned} B_2'(\alpha) = &-\frac{m\bar{Q}}{18(g(m\bar{a}))^2\sin\alpha} \\ &\times\left\{\left(2f(m\bar{a})\left[1 - \frac{g'(m\bar{a})}{g(m\bar{a})}m\bar{a}\right] + f'(m\bar{a})m\bar{a}\right)m'(\alpha) - mf(m\bar{a})\cot\alpha\right\}. \end{aligned} \tag{C.8}$$

We write the solution of equation (C.6) in the form

$$\alpha(\lambda) = \alpha_0(\lambda) + \alpha_1(\lambda). \tag{C.9}$$

Substituting expansion (C.9) in (C.6) and taking the first term $\alpha_0(\lambda)$ and the main terms, we obtain

$$B_1'\left(\alpha_0\right)\left(\frac{1}{\lambda}\right)^{\frac{1}{2}} = 0 \tag{C.10}$$

and hence

$$B_1'\left(\alpha_0\right) = 0. \tag{C.11}$$

Substituting (C.7) in (C.11) and using $m = \sqrt{|\cos\alpha|}$ and $m'(\alpha) = -\sin\alpha/2m$, we get

$$\frac{g'\left(m_0\bar{a}\right)}{g\left(m_0\bar{a}\right)}m_0\bar{a} - 3 = \frac{2m_0^4}{1 - m_0^4}, \tag{C.12}$$

where $m_0 = m(\alpha_0)$. Let $x = m_0\bar{a}$, then

$$\frac{g'(x)}{g(x)}x - 3 = \frac{2x^4}{\bar{a}^4 - x^4} \tag{C.13}$$

and hence

$$\bar{a}^4 = x^4 \frac{g'(x)x - g(x)}{g'(x)x - 3g(x)}. \tag{C.14}$$

Let

$$H(x) = \bar{a} = x\left(\frac{g'(x)x - g(x)}{g'(x)x - 3g(x)}\right)^{\frac{1}{4}} \tag{C.15}$$

then we can write x as

$$x = H^{-1}(\bar{a}) \tag{C.16}$$

where H^{-1} is the inverse function of $H(x)$. Then we have

$$m_0 = \frac{1}{\bar{a}}H^{-1}(\bar{a}) \tag{C.17}$$

and

$$\alpha_0 = \pi - \arccos\left(\frac{1}{\bar{a}^2}\left[H^{-1}(\bar{a})\right]^2\right). \tag{C.18}$$

To find the term $\alpha_1(\lambda)$, we substitute the expansion (C.9) in (C.6) and obtain

$$\alpha_1 = -\frac{B_2'(\alpha_0)}{B_1''(\alpha_0)}\left(\frac{1}{\lambda}\right)^{\frac{3}{2}} \tag{C.19}$$

then we have

$$\alpha_{\min}(\lambda) = \alpha_0 - \frac{B_2'(\alpha_0)}{B_1''(\alpha_0)}\left(\frac{1}{\lambda}\right)^{\frac{3}{2}}. \tag{C.20}$$

To find $\beta_{\min}$, we can write from (C.5) that

$$\beta_{\min} = B_1(\alpha_{\min})\left(\frac{1}{\lambda}\right)^{\frac{1}{2}} + B_2(\alpha_{\min})\left(\frac{1}{\lambda}\right)^2. \tag{C.21}$$

Substituting expansion (C.9) in (C.21), taking into account (C.11) we obtain

$$\beta_{\min} = B_1(\alpha_0)\left(\frac{1}{\lambda}\right)^{\frac{1}{2}} + B_2(\alpha_0)\left(\frac{1}{\lambda}\right)^2 \tag{C.22}$$

and hence

$$\beta_{\min} = \sqrt{\frac{m_0^3 \bar{Q}}{g\left(m_0 \bar{a}\right) \sin \alpha_0}} \left(\frac{1}{\lambda}\right)^{\frac{1}{2}} - \frac{m_0^2 \bar{Q}}{18 \sin \alpha_0} \frac{f\left(m_0 \bar{a}\right)}{\left(g\left(m_0 \bar{a}\right)\right)^2} \left(\frac{1}{\lambda}\right)^2 \tag{C.23}$$

(Note that the root of (C.15) can only be found using a numerical method. Here we used the mathematical software Mathematica and in particular we use the command FindRoot which searches for a numerical root for the equation).

Appendix D

Asymptotic Behaviour of α_{min} and $h_{\mathrm{m(min)}}$ in the Limit $\lambda \to \infty$

In this Appendix we determine the asymptotic behaviour of α_{min} and $h_{\mathrm{m(min)}}$ shown in Figure 2.16 in Chapter 2 in the limit of a strong slip, $\lambda \to \infty$, for a rivulet with constant contact angle $\beta = \bar{\beta}$. Note that the same procedure can be used to determine the asymptotics behaviour in the limit of a weak slip, $\lambda \to 0^+$.

When $\lambda \to \infty$ we find from (2.113) that

$$a = a_0 + a_1 = \left(\frac{15\bar{Q}}{4\bar{\beta}^2 \sin\alpha}\right)^{\frac{1}{3}} \left(\frac{1}{\lambda}\right)^{\frac{1}{3}} \pm \frac{5\bar{Q}m^2}{28\bar{\beta}^2 \sin\alpha}\frac{1}{\lambda}, \tag{D.1}$$

where the upper sign in (D.1) (and in the following formulas) corresponds to case $0 \le \alpha < \pi/2$, and the lower one corresponds to case $\pi/2 < \alpha \le \pi$.

In the limit $ma \to 0^+$, equation (2.33) become

$$h_{\mathrm{m}} = \frac{\bar{\beta}}{m} \times \begin{cases} \dfrac{ma}{2} - \dfrac{(ma)^3}{24} + \dfrac{(ma)^5}{240} + O\left((ma)^7\right) & \text{for} \quad 0 \le \alpha < \dfrac{\pi}{2}, \\ \dfrac{ma}{2} & \text{for} \quad \alpha = \dfrac{\pi}{2}, \\ \dfrac{ma}{2} + \dfrac{(ma)^3}{24} + \dfrac{(ma)^5}{240} + O\left((ma)^7\right) & \text{for} \quad \dfrac{\pi}{2} < \alpha \le \pi. \end{cases} \tag{D.2}$$

Then, using (D.2) the expansion for function h_{m} can be written as

$$h_{\mathrm{m}} = \frac{\beta}{m}\left\{\frac{m}{2}\left(a_0 + a_1 + \cdots\right) \mp \frac{m^3}{24}\left(a_0 + a_1 + \cdots\right)^3 \mp \frac{m^5}{240}\left(a_0 + a_1 + \cdots\right)^5 + \cdots\right\} \tag{D.3}$$

then

$$h_{\mathrm{m}} = \frac{\bar{\beta}}{2}\left\{a_0 + \left(a_1 \mp \frac{m^2}{12}a_0^3\right) + \cdots\right\}. \tag{D.4}$$

Substituting a_0 and a_1 from (D.1) in (D.4), we obtain

$$h_{\mathrm{m}} = \frac{1}{2}\left(\frac{15\bar{\beta}\bar{Q}}{4\sin\alpha}\right)^{\frac{1}{3}}\left(\frac{1}{\lambda}\right)^{\frac{1}{3}} \mp \frac{15\bar{Q}m^2}{224\bar{\beta}\sin\alpha}\frac{1}{\lambda} \mp \frac{1}{42}\left(\frac{15\beta Q}{4\sin\alpha}\right)^{\frac{2}{3}}\left(\frac{1}{\lambda}\right)^{\frac{5}{3}}. \tag{D.5}$$

If α minimizes the function $h_{\mathrm{m}}(\alpha)$, then we write the equation ${h_{\mathrm{m}}}'(\alpha) = 0$

$${h_{\mathrm{m}}}'(\alpha) = -\frac{1}{6}\left(\frac{15\bar{\beta}\bar{Q}}{4}\right)^{\frac{1}{3}}\frac{\cos\alpha}{(\sin\alpha)^{\frac{4}{3}}}\left(\frac{1}{\lambda}\right)^{\frac{1}{3}} \mp \frac{15\bar{Q}}{224\bar{\beta}}\frac{2mm'\sin\alpha - m^2\cos\alpha}{(\sin\alpha)^2}\frac{1}{\lambda} + O\left(\left(\frac{1}{\lambda}\right)^{\frac{5}{3}}\right) = 0, \tag{D.6}$$

where

$$m' = \mp\frac{\sin\alpha}{2m}. \tag{D.7}$$

We can find the solution of equation (D.6) in the form of an expansion

$$\alpha(\lambda) = \alpha_0(\lambda) + \alpha_1(\lambda), \tag{D.8}$$

where $\alpha_1(\lambda) \ll \alpha_0(\lambda)$. Substituting expansion (D.8) in (D.6) and keeping only the first term $\alpha_0(\lambda)$ and the main terms, we obtain

$$\frac{1}{2}\left(\frac{15\beta Q}{4}\right)^{\frac{1}{3}}\left(-\frac{1}{3}\right)\frac{\cos\alpha_0}{(\sin\alpha_0)^{\frac{4}{3}}}\left(\frac{1}{\lambda}\right)^{\frac{1}{3}} = 0 \tag{D.9}$$

hence

$$\alpha_0 = \frac{\pi}{2}. \tag{D.10}$$

To find the term $\alpha_1(\lambda)$, substituting expansion (D.8) in (D.6) and keeping only the main terms, we obtain

$$\alpha_1 = -\frac{3}{112}\left(\frac{30\bar{Q}}{\bar{\beta}^2}\right)^{\frac{2}{3}}\left(\frac{1}{\lambda}\right)^{\frac{2}{3}} \tag{D.11}$$

then, we have

$$\alpha_{\min} = \frac{\pi}{2} - \frac{3}{112}\left(\frac{30\bar{Q}}{\bar{\beta}^2}\right)^{\frac{2}{3}}\left(\frac{1}{\lambda}\right)^{\frac{2}{3}}. \tag{D.12}$$

From (D.12) we see that $\alpha_{\min} < \frac{\pi}{2}$, hence, $m^2 = \cos\alpha_{\min}$. Then the expression (D.5) takes the form

$$\begin{aligned} h_{\mathrm{m(min)}} = \frac{1}{2}\left(\frac{15\bar{\beta}\bar{Q}}{4}\right)^{\frac{1}{3}}\left(\frac{1}{\sin\alpha_{\min}}\right)^{\frac{1}{3}}\left(\frac{1}{\lambda}\right)^{\frac{1}{3}} - \frac{15\bar{Q}}{224\bar{\beta}}\cot\alpha_{\min}\frac{1}{\lambda} \\ - \frac{1}{42}\left(\frac{15\beta Q}{4}\right)^{\frac{2}{3}}\left(\frac{1}{\sin\alpha_{\min}}\right)^{\frac{2}{3}}\left(\frac{1}{\lambda}\right)^{\frac{5}{3}} \end{aligned} \tag{D.13}$$

then by substituting (D.12) in (D.13) we obtain

$$\begin{aligned} h_{\mathrm{m(min)}} = \frac{1}{2}\left(\frac{15\bar{\beta}\bar{Q}}{4}\right)^{\frac{1}{3}}\left(\frac{1}{\cos\alpha_1}\right)^{\frac{1}{3}}\left(\frac{1}{\lambda}\right)^{\frac{1}{3}} + \frac{15\bar{Q}}{224\bar{\beta}}\tan\alpha_1\frac{1}{\lambda} \\ - \frac{1}{42}\left(\frac{15\beta Q}{4}\right)^{\frac{2}{3}}\left(\frac{1}{\cos\alpha_1}\right)^{\frac{2}{3}}\left(\frac{1}{\lambda}\right)^{\frac{5}{3}}. \end{aligned} \tag{D.14}$$

For small α_1, we have the following expansions:

$$\left(\frac{1}{\cos\alpha_1}\right)^{\frac{1}{3}} = 1 + \frac{\alpha_1^2}{6} + \frac{\alpha_1^4}{24} + O\left(\alpha_1^6\right), \tag{D.15}$$

$$\tan\alpha_1 = \alpha_1 + \frac{\alpha_1^3}{3} + \frac{2\alpha_1^5}{15} + O\left(\alpha_1^7\right), \tag{D.16}$$

$$\left(\frac{1}{\cos\alpha_1}\right)^{\frac{2}{3}} = 1 + \frac{\alpha_1^2}{3} + \frac{\alpha_1^4}{9} + O\left(\alpha_1^6\right). \tag{D.17}$$

Substituting (D.15)–(D.17) in (D.14), we obtain

$$h_{\mathrm{m(min)}} = \frac{1}{2}\left(\frac{15\bar{\beta}\bar{Q}}{4}\right)^{\frac{1}{3}}\left\{1 + \frac{\alpha_1^2}{6}\right\}\left(\frac{1}{\lambda}\right)^{\frac{1}{3}} + \frac{15\bar{Q}}{224\bar{\beta}}\alpha_1\frac{1}{\lambda} - \frac{1}{42}\left(\frac{15\beta Q}{4}\right)^{\frac{2}{3}}\left(\frac{1}{\lambda}\right)^{\frac{5}{3}}. \tag{D.18}$$

Substituting (D.11) in (D.18), finally we get

$$h_{\mathrm{m(min)}} = \frac{1}{2}\left(\frac{15\bar{\beta}\bar{Q}}{4}\right)^{\frac{1}{3}}\left(\frac{1}{\lambda}\right)^{\frac{1}{3}} - \frac{1}{42}\left(\frac{15\bar{\beta}\bar{Q}}{4}\right)^{\frac{2}{3}}\left(1+\frac{135\bar{Q}}{896\bar{\beta}^{3}}\right)\left(\frac{1}{\lambda}\right)^{\frac{5}{3}}. \tag{D.19}$$

Appendix E

Errors in Section V of Davis and Hocking [29]

In this Appendix we describe the errors we found in Section V of Davis and Hocking [29] results for a two-dimensional fluid sheet flowing down an inclined porous substrate as described in Subsection 1.6.4.

The free surface equation (34) in Davis and Hocking [29] was written as

$$\mu \frac{\partial h'}{\partial t'} + \frac{\partial Q'}{\partial x'} = k' H(x') \left(\sigma \frac{\partial^2 h'}{\partial x'^2} - \rho g h' \cos\theta \right), \tag{E.1}$$

$$\mu Q' = \frac{1}{3} h'^3 \left(\sigma \frac{\partial^3 h'}{\partial x'^3} - \rho g \cos\theta \frac{\partial h'}{\partial x'} + \rho g \sin\theta \right), \tag{E.2}$$

where μ, h', Q', k', H, t, σ, ρ, g and θ denote the viscosity, free surface profile, volume flux, permeability of the substrate, Heaviside unit function, time, surface tension, density, magnitude of gravity and inclination angle of the substrate, respectively.

Note that there is a missing pair of brackets around $\partial h'/\partial t' + \partial Q'/\partial x'$ in the first line of their equation (34) (*i.e.* (E.1)), and therefore the corrected version of the equation

(34) in Davis and Hocking [29] is

$$\mu\left(\frac{\partial h'}{\partial t'}+\frac{\partial Q'}{\partial x'}\right)=k'H(x')\left(\sigma\frac{\partial^2 h'}{\partial x'^2}-\rho g h'\cos\theta\right), \tag{E.3}$$

$$\mu Q'=\frac{1}{3}h'^3\left(\sigma\frac{\partial^3 h'}{\partial x'^3}-\rho g\cos\theta\frac{\partial h'}{\partial x'}+\rho g\sin\theta\right). \tag{E.4}$$

Davis and Hocking [29] non-dimensionalise and scale the variables by writing:

$$x'=\frac{h_0}{\beta\tan\theta}x,\quad h'=h_0 h,\quad k'=Kk. \tag{E.5}$$

Setting $\partial h'/\partial t'=0$ and substituting (E.4) and (E.5) in the corrected version of equation (34) in Davis and Hocking [29] (*i.e.* (E.3)), equation (E.3) becomes

$$\frac{\mathrm{d}}{\mathrm{d}x}\left[h^3\left(\frac{\sigma\beta^3\tan^3\theta}{\rho g\sin\theta h_0^2}\frac{\mathrm{d}^3h}{\mathrm{d}x^3}-\beta\frac{\mathrm{d}h}{\mathrm{d}x}+1\right)\right]=\frac{3\mu KkH(x)}{h_0\mu\beta\tan\theta}\left[\frac{\sigma\beta^2\tan^2\theta}{\rho g\sin\theta h_0^2}\frac{\mathrm{d}^2h}{\mathrm{d}x^2}-\frac{h}{\tan\theta}\right]. \tag{E.6}$$

By setting $\sigma\beta^3\tan^3\theta/(\rho g\sin\theta h_0^2)=1$ and $K=h_0\beta^2\tan^2\theta/3$, we get

$$\frac{\mathrm{d}}{\mathrm{d}x}\left[h^3\left(\frac{\mathrm{d}^3h}{\mathrm{d}x^3}-\beta\frac{\mathrm{d}h}{\mathrm{d}x}+1\right)\right]=kH(x)\left[\frac{\mathrm{d}^2h}{\mathrm{d}x^2}-\beta h\right], \tag{E.7}$$

which is the same as equation (37) in Davis and Hocking [29]. Therefore, the correct scaling for the permeability and the correct definition of the Bond number B is

$$k'=\frac{h_0\beta^2\tan^2\theta}{3}k\quad\text{and}\quad B=\left(\frac{\rho g\sin\theta h_0^2}{\sigma}\right)=(\beta\tan\theta)^3, \tag{E.8}$$

which is different than the corresponding expressions given by Davis and Hocking [29], namely

$$k'=\frac{\mu h_0\beta^{2/3}\tan^{2/3}\theta}{3}k\quad\text{and}\quad B=\left(\frac{\rho g\cos\theta h_0^2}{\sigma}\right)=(\beta\tan\theta)^3. \tag{E.9}$$

Using the correct expression for k', the correct expression for the survival distance a' is

$$a'=\frac{h_0^2\tan\theta}{2k'}, \tag{E.10}$$

which is in exact agreement with the our expression for the length of an infinitely-wide sessile sheet flowing over and through a permeable membrane given by (3.75), and, in particular, gives $a' \sim (k')^{-1} h_0^2$.

Note that if we use the incorrect k' (*i.e.* (E.9)) given by Davis and Hocking [29] to find their version of this result, we get

$$a' = \frac{\mu h_0^2 \tan\theta}{2k'} \left(\frac{\sigma}{\rho g h_0^2 \cos\theta} \right)^{4/9}, \tag{E.11}$$

which gives $a' \sim (k')^{-1} g^{-4/9}$, which in turn is different to that which Davis and Hocking [29] gave (*i.e.* $a \sim (k')^{-1} g^{-1/3}$), but, even assuming that they meant to write a rather than a', this would give

$$a = \frac{\mu h_0^2 \tan\theta}{2k'} \left(\frac{\sigma}{\rho g h_0^2 \cos\theta} \right)^{1/9}, \tag{E.12}$$

which gives $a \sim (k')^{-1} g^{-1/9}$, which still is not what they gave.

Appendix F

Solution for Small ρ with the Disjoining Pressure of the Form (4.43)

In this Appendix, we seek an asymptotic solution to (4.45)–(4.47) in the case of $\Pi_{\mathrm{LR}}(h,x)$ given by (4.43), namely

$$\Pi_{\mathrm{LR}}(h,x) = \frac{1}{h^6} - \frac{1+\rho\sin(2\pi x)}{h^3}. \tag{F.1}$$

In particular, we seek an expansion of the form

$$h(x) = \bar{h} + \rho h_1(x) + O(\rho^2), \tag{F.2}$$

where

$$\int_0^1 h_1(x)\,\mathrm{d}x = 0. \tag{F.3}$$

Substituting (F.2) into (F.1) and expanding, we have

$$\Pi(h,x) = \frac{1}{\bar{h}^6} - \frac{1}{\bar{h}^3} + \left(-\frac{6h_1(x)}{\bar{h}^7} - \frac{\sin(2\pi x)}{\bar{h}^3} + \frac{3h_1(x)}{\bar{h}^4} \right)\rho + O(\rho^2). \tag{F.4}$$

Substituting into (4.12) and collecting the $O(\rho)$ terms, we have

$$\epsilon^2 \frac{d^2}{dx^2} h_1(x) - \frac{6h_1(x)}{\bar{h}^7} - \frac{\sin(2\pi x)}{\bar{h}^3} + \frac{3h_1(x)}{\bar{h}^4} + C = 0, \tag{F.5}$$

where

$$C = -\int_0^1 \left[-\frac{6h_1(x)}{\bar{h}^7} - \frac{\sin(2\pi x)}{\bar{h}^3} + \frac{3h_1(x)}{\bar{h}^4} \right] \mathrm{d}x = 0, \tag{F.6}$$

by using equation (F.3).

Solving (F.5) with the boundary conditions

$$h_1(0) = h_1(1), \quad h_{1x}(0) = h_{1x}(1), \tag{F.7}$$

yields the solution

$$h_1(x) = -\frac{\bar{h}^4 \sin(2\pi x)}{4\pi^2 \bar{h}^7 \epsilon^2 - 3\bar{h}^3 + 6}. \tag{F.8}$$

Therefore

$$h(x) = \bar{h} - \frac{\bar{h}^4 \sin(2\pi x)\, \rho}{4\pi^2 \bar{h}^7 \epsilon^2 - 3\bar{h}^3 + 6} + O(\rho^2). \tag{F.9}$$

Note that a similar procedure can be used to determine the asymptotics solution for small ρ with the disjoining pressure of the form (4.44).

Appendix G

$O(2)$ Symmetry Breaking by Spatial Non-Homogeneity

In this Appendix, we present an argument that shows that when the wettability contrast is present, *i.e.* when $\rho \neq 0$, the breaking of the $O(2)$ symmetry which equation (4.45) with the periodic boundary conditions (4.47) has for $\rho = 0$, leaves only two steady-state solutions.

This is, in principle, a known result (see, for example, Chillingworth [20]), but, since we are not aware of an easily accessible reference, we give the details here. As before, we set $G(x) = \sin(2\pi x)$. We provide the proof for Π_{SR} given by (4.44), the proof for Π_{LR} given by (4.43) is similar.

For the case of Π_{SR}, let us rewrite the boundary value problem (4.45) in the form

$$\epsilon^2 h_{xx} + f_1(h) + \rho f_2(h)G(x) - \int_0^1 [f_1(h) + \rho f_2(h)G(x)]\,\mathrm{d}x = 0, \quad 0 < x < 1, \tag{G.1}$$

where

$$f_1(h) = \frac{1}{h^6} - \frac{1}{h^3} \tag{G.2}$$

and

$$f_2(h) = \frac{1}{h^6}, \tag{G.3}$$

i.e. we separate the spatially homogeneous and spatially non-homogeneous components of the disjoining pressure. Equation (G.1) is subject to the periodic boundary conditions (4.47).

Suppose that when $\rho = 0$ there is an orbit of steady-state solutions, *i.e.* a continuous closed curve of solutions $h_{0,s}(x)$, parameterised by $s \in \mathbb{R}/[0,1]$, such that $h_{0,s}(x) := h_0(x+s)$, for some function $h_0(x)$, *i.e.* all these solutions are related by translation. We aim to understand what remains of this orbit for small non-zero ρ.

Fix $s \in \mathbb{R}/[0,1]$. We write

$$h(x) = h_{0,s}(x) + \rho h_1(x) + O(\rho^2). \tag{G.4}$$

Substituting this expansion into (G.1) and collecting the $O(\rho)$ terms, we have

$$\begin{aligned} \epsilon^2 h_{1,xx} &+ (f_1'(h_{0,s}) + f_2'(h_{0,s}))h_1 - \int_0^1 \left[f_1'(h_{0,s}) + f_2'(h_{0,s})\right] h_1 \,\mathrm{d}x \\ &= -f_2(h_{0,s})G + \int_0^1 f_2(h_{0,s})G \,\mathrm{d}x, \end{aligned} \tag{G.5}$$

where, just like $h_{0,s}(x)$, $h_1(x)$ also satisfies the periodic boundary conditions (4.47). Now set

$$Ku := \epsilon^2 u_{1,xx} + (f_1'(h_{0,s}) + f_2'(h_{0,s}))u - \int_0^1 [f_1'(h_{0,s}) + f_2'(h_{0,s})]u \,\mathrm{d}x, \tag{G.6}$$

and let $D(K)$, the domain of K, be

$$D(K) = \left\{ f \in C^2([0,1]) \mid f(0) = f(1), f'(0) = f'(1) \right\}. \tag{G.7}$$

The operator K is self-adjoint with respect to the $L^2([0,1])$ inner product. Invoking the Fredholm Alternative [90, Theorem 7.26], we conclude that (G.5) has 1-periodic solutions if and only if the right-hand side of (G.5) is orthogonal in $L^2([0,1])$ to the solutions of $Ku = 0$.

Next, we show that $u := h_{0,s}'$ solves $Ku = 0$. Indeed, by differentiating (G.1) with

$\rho = 0$ with respect to x, we find that u solves the equation

$$\epsilon^2 u_{xx} + (f_1'(h_{0,s}) + f_2'(h_{0,s}))u = 0. \tag{G.8}$$

Integrating this equation over the interval $[0, 1]$, we have that

$$\int_0^1 (f_1'(h_{0,s}) + f_2'(h_{0,s}))u \, \mathrm{d}x = 0. \tag{G.9}$$

Hence

$$\begin{aligned} 0 &= \epsilon^2 u_{xx} + (f_1'(h_{0,s}) + f_2'(h_{0,s}))u \\ &= \epsilon^2 u_{xx} + (f_1'(h_{0,s}) + f_2'(h_{0,s}))u + \int_0^1 (f_1'(h_{0,s}) + f_2'(h_{0,s}))u \, \mathrm{d}x \\ &= Ku. \end{aligned} \tag{G.10}$$

Also note that as $h_{0,s}(x)$ satisfies periodic boundary conditions,

$$\int_0^1 h_{0,s}'(x) \, \mathrm{d}x = 0. \tag{G.11}$$

Hence the solvability condition for (G.5) is

$$\int_0^1 h_{0,s}'(r) \left[-f_2(h_{0,s})G + \int_0^1 f_2(h_{0,s})G \, \mathrm{d}x \right] \mathrm{d}r = 0. \tag{G.12}$$

By (G.11), this condition reduces to

$$\int_0^1 f_2(h_{0,s})h_{0,s}' G \, \mathrm{d}x = 0. \tag{G.13}$$

Now recall that $h_{0,s}(x) = h_0(x + s)$, so if we write $F(x + s) = f_2(h_0(x + s))h_0'(x + s)$, the function $F(\cdot)$ is 1-periodic in x with zero mean. Hence

$$F(z) = \sum_{k=1}^{\infty} \alpha_k \sin(2k\pi z) + \beta_k \cos(2k\pi z). \tag{G.14}$$

Therefore for $G(x) = \sin(2\pi x)$, the solvability condition for (G.5) becomes

$$\alpha_1 \sin(2k\pi s) - \beta_1 \cos(2\pi s) = 0, \tag{G.15}$$

which has two solutions $s \in \mathbb{R}/[0,1]$, from which we conclude there is a solution $h_1(x)$ only for two choices of $s \in \mathbb{R}/[0,1]$, that is, that only two solutions to (G.1) remain from the entire $O(2)$ orbit that exists for $\rho = 0$.

Bibliography

[1] Kinera Coatings AS. URL: https://www.kinera.eu/dip-coated-products.html. Accessed 12th September 2021.

[2] V. S. Ajaev, E. Y. Gatapova, and O. A. Kabov. Stability and break-up of thin liquid films on patterned and structured surfaces. *Adv. Coll. Int. Sci.*, 228:92–104, 2016.

[3] R. F. Allen and C. M. Biggin. Longitudinal flow of a lenticular liquid filament down an inclined plane. *Phys. Fluids*, 17:287–291, 1974.

[4] A. S. Alshaikhi, M. Grinfeld, and S. K. Wilson. Patterns formed in a thin film with spatially homogeneous and non-homogeneous derjaguin disjoining pressure. Published online in Euro. J. Appl. Math. 2021. DOI:10.1017/S0956792521000267.

[5] A. S. Alshaikhi, S. K. Wilson, and B. R. Duffy. Rivulet flow down a slippery substrate. *Phys. Fluids*, 32:072011, 2020.

[6] A. S. Alshaikhi, S. K. Wilson, and B. R. Duffy. Rivulet flow over and through a permeable membrane. *Phys. Rev. Fluids*, 6:104003, 2021.

[7] A. Amini and G. M. Homsy. Evaporation of liquid droplets on solid substrates. I. Flat substrate with pinned or moving contact line. *Phys. Rev. Fluids*, 2:043603, 2017.

[8] F. Aurelian, M. Patrick, and H. Mohamed. Wall slip effects in (elasto) hydrodynamic journal bearings. *Tribol. Int.*, 44:868–877, 2011.

[9] P. W. Bates and P. C. Fife. Spectral comparison principles for the Cahn-Hilliard and phase-field equations, and time scales for coarsening. *Physica D*, 43:335–348, 1990.

[10] G. S. Beavers and D. D. Joseph. Boundary conditions at a naturally permeable wall. *J. Fluid Mech.*, 30:197–207, 1967.

[11] M. Bentwich, D. Glasser, J. Kern, and D. Williams. Analysis of rectilinear rivulet flow. *AIChE J.*, 22:772–779, 1976.

[12] A. L. Bertozzi, G. Grün, and T. P. Witelski. Dewetting films: Bifurcations and concentrations. *Nonlinearity*, 14:1569–1592, 2001.

[13] B. Birnir, K. Mertens, V. Putkaradze, and P. Vorobieff. Morphology of a stream flowing down an inclined plane. Part 2. Meandering. *J. Fluid Mech.*, 607:401–411, 2008.

[14] L. Biswal, S. K. Som, and S. Chakraborty. Thin film evaporation in microchannels with interfacial slip. *Microfluid. Nanofluid.*, 10:155–163, 2011.

[15] S. J. Bolaños and B. Vernescu. Derivation of the Navier slip and slip length for viscous flows over a rough boundary. *Phys. Fluids*, 29:057103, 2017.

[16] B. J. Brasjen and A. A. Darhuber. Dry-spot nucleation in thin liquid films on chemically patterned surfaces. *Microfluid. Nanofluid.*, 11:703–716, 2011.

[17] B. J. Brasjen, H. Gu, and A. A. Darhuber. Dewetting of thin liquid films on chemically patterned substrates: Front propagation along narrow lyophobic stripes and stripe arrays. *Microfluid. Nanofluid.*, 14:669–682, 2013.

[18] H. C. Brinkman. A calculation of the viscous force exerted by a flowing fluid on a dense swarm of particles. *Flow, Turbul. Combust.*, A1:27–34, 1949.

[19] Y. Chao, Z. Ding, and R. Liu. Dynamics of thin liquid films flowing down the uniformly heated/cooled cylinder with wall slippage. *Chem. Eng. Sci.*, 175:354–364, 2018.

[20] D. Chillingworth. Bifurcation from an orbit of symmetry. In S. N. Pnevmatikos, editor, *Singularities and Dynamical Systems*, pages 285–294. Elsevier, 1985.

[21] C.-H. Choi and C.-J. Kim. Large slip of aqueous liquid flow over a nanoengineered superhydrophobic surface. *Phys. Rev. Lett.*, 96:066001, 2006.

[22] P. Chossat and R. Lauterbach. *Methods in Equivariant Bifurcations and Dynamical Systems.* World Scientific, Singapore, 2000.

[23] A. Clarke, T. D. Blake, K. Carruthers, and A. Woodward. Spreading and imbibition of liquid droplets on porous surfaces. *Langmuir*, 18:2980–2984, 2002.

[24] P. Coussot and S. Proust. Slow, unconfined spreading of a mudflow. *J. Geophys. Res.*, 101:25217–25229, 1996.

[25] S. Couvreur and A. Daerr. The role of wetting heterogeneities in the meandering instability of a partial wetting rivulet. *Euro. Phys. Lett.*, 99:24004, 2012.

[26] J. B. Culkin and S. H. Davis. Meandering of water rivulets. *AIChE J.*, 30: 263–267, 1984.

[27] A. Daerr, J. Eggers, L. Limat, and N. Valade. General mechanism for the meandering instability of rivulets of Newtonian fluids. *Phys. Rev. Lett.*, 106:184501, 2011.

[28] H. P. G. Darcy. *Les Fontaines publiques de la ville de Dijon.* V. Dalamont, 1856.

[29] S. H. Davis and L. M. Hocking. Spreading and imbibition of viscous liquid on a porous base. *Phys. Fluids*, 11:48–57, 1999.

[30] E. J. Doedel and B. E. Oldeman. *Auto-07p: Continuation and Bifurcation Software for Ordinary Differential Equations.* Concordia University, Montreal, 2009.

[31] B. R. Duffy and H. K. Moffatt. Flow of a viscous trickle on a slowly varying incline. *Chem. Eng. J.*, 60:141–146, 1995.

[32] H. L. Dylla and K. R. Hansen. Porous asphalt pavements with stone reservoirs. Technical Report, U. S. Department of Transportation, Federal Highway Administration. Office of Asset Management, Pavements and Construction, FHWA-HIF-15-009, 2015.

[33] J. C. Eilbeck, J. E. Furter, and M. Grinfeld. On a stationary state characterization of transition from spinodal decomposition to nucleation behaviour in the Cahn-Hilliard model of phase separation. *Phys. Lett. A*, 135:272–275, 1989.

[34] L. Espín and S. Kumar. Droplet spreading and absorption on rough, permeable substrates. *J. Fluid Mech.*, 784:465–486, 2015.

[35] L. Espín and S. Kumar. Droplet wetting transitions on inclined substrates in the presence of external shear and substrate permeability. *Phys. Rev. Fluids*, 2: 014004, 2017.

[36] B. Fotovvati, N. Namdari, and A. Dehghanghadikolaei. On coating techniques for surface protection: A review. *J. Manuf. Mater. Process.*, 3:28, 2019.

[37] K. B. Glasner and T. Witelski. Collision versus collapse of droplets in coarsening of dewetting thin films. *Physica D*, 209:80–104, 2005.

[38] M. Golubitsky and D. G. Scheaffer. *Singularities and Groups in Bifurcation Theory, Vol. I.* Springer, 1985.

[39] H. P. Greenspan. On the motion of a small viscous droplet that wets a surface. *J. Fluid Mech.*, 84:125–143, 1978.

[40] R. W. Griffiths. The dynamics of lava flows. *Annu. Rev. Fluid Mech.*, 32:477–518, 2000.

[41] J. K. Hale. *Asymptotic Behavior of Dissipative Systems.* American Mathematical Society, 2010.

[42] P. J. Haley and M. J. Miksis. The effect of the contact line on droplet spreading. *J. Fluid Mech.*, 223:57–81, 1991.

[43] P. He, J. Cao, H. Ding, C. Liu, J. Neilson, Z. Li, I. A. Kinloch, and B. Derby. Screen-printing of a highly conductive graphene ink for flexible printed electronics. *ACS Appl. Mater. Interfaces*, 11:32225–32234, 2019.

[44] M. A. Herrada, A. M. Gañán-Calvo, and J. M. Montanero. Theoretical investigation of a technique to produce microbubbles by a microfluidic T junction. *Phys. Rev. E*, 88:033027, 2013.

[45] G. C. Holmes. The use of hyperbolic cosines in solving cubic polynomials. *Math. Gaz.*, 86:473–477, 2002.

[46] C. Honisch, T.-S. Lin, A. Heuer, U. Thiele, and S. V. Gurevich. Instabilities of layers of deposited molecules on chemically stripe patterned substrates: Ridges versus drops. *Langmuir*, 31:10618–10631, 2015.

[47] P. D. Howell, H. Kim, M. G. Popova, and H. A. Stone. Rivulet flow over a flexible beam. *J. Fluid Mech.*, 796:285–305, 2016.

[48] C. Huh and L. E. Scriven. Hydrodynamic model of steady movement of a solid/liquid/fluid contact line. *J. Coll. Interf. Sci.*, 35:85–101, 1971.

[49] B. Inaglory. URL: https://commons.wikimedia.org/wiki/File:Lava_channel_with_overflows_edit_4.jpg. Accessed 12th September 2021.

[50] H. Ji and T. P. Witelski. Finite-time thin film rupture driven by modified evaporative loss. *Physica D*, 342:1–15, 2017.

[51] P. Joseph, C. Cottin-Bizonne, J.-M. Benoit, C. Ybert, C. Journet, P. Tabeling, and L. Bocquet. Slippage of water past superhydrophobic carbon nanotube forests in microchannels. *Phys. Rev. Lett.*, 97:156104, 2006.

[52] K. Kargupta and A. Sharma. Templating of thin films induced by dewetting on patterned surfaces. *Phys. Rev. Lett.*, 86:4536–4539, 2001.

[53] K. Kargupta and A. Sharma. Mesopatterning of thin liquid films by templating on chemically patterned complex substrates. *Langmuir*, 19:5153–5163, 2003.

[54] D. J. Knox, S. K. Wilson, B. R. Duffy, and S. McKee. Porous squeeze-film flow. *IMA J. Appl. Math.*, 80:376–409, 2015.

[55] D. J. Knox, B. R. Duffy, S. McKee, and S. K. Wilson. Squeeze-film flow between a curved impermeable bearing and a flat porous bed. *Phys. Fluids*, 29:023101, 2017.

[56] R. Konnur, K. Kargupta, and A. Sharma. Instability and morphology of thin liquid films on chemically heterogeneous substrates. *Phys. Rev. Lett.*, 84:931–934, 2000.

[57] E. Lauga, M. P. Brenner, and H. A. Stone. Microfluidics: The no-slip boundary condition. In C. Tropea, A. L. Yarin, and J. F. Foss, editors, *Springer Handbook of Experimental Fluid Mechanics*, pages 1219–1240. Springer, 2007.

[58] R. S. Laugesen and M. C. Pugh. Linear stability of steady states for thin film and Cahn-Hilliard type equations. *Arch. Ration. Mech. Anal.*, 154:3–51, 2000.

[59] R. S. Laugesen and M. C. Pugh. Properties of steady states for thin film equations. *Euro. J. Appl. Math.*, 11:293–351, 2000.

[60] M. Le Bars and M. G. Worster. Interfacial conditions between a pure fluid and a porous medium: Implications for binary alloy solidification. *J. Fluid Mech.*, 550: 149–173, 2006.

[61] N. Le Grand-Piteira, A. Daerr, and L. Limat. Meandering rivulets on a plane: A simple balance between inertia and capillarity. *Phys. Rev. Lett.*, 96:254503, 2006.

[62] T. Lee, E. Charrault, and C. Neto. Interfacial slip on rough, patterned and soft surfaces: A review of experiments and simulations. *Adv. Coll. Int. Sci.*, 210: 21–38, 2014.

[63] H. Li, A. Li, Z. Zhao, M. Li, and Y. Song. Heterogeneous wettability surfaces: Principle, construction, and applications. *Small Struct.*, 1:2000028, 2020.

[64] M. M. Ling and Z. Bao. Thin film deposition, patterning, and printing in organic thin film transistors. *Chem. Mater.*, 16:4824–4840, 2004.

[65] R. Liu and Q. Liu. Instabilities of a liquid film flowing down an inclined porous plane. *Phys. Rev. E*, 80:036316, 2009.

[66] W. Liu and T. P. Witelski. Steady states of thin film droplets on chemically heterogeneous substrates. *IMA J. Appl. Math.*, 85:980–1020, 2020.

[67] A. Maali and B. Bhushan. Measurement of slip length on superhydrophobic surfaces. *Phil. Trans. R. Soc. A*, 370:2304–2320, 2012.

[68] G. McKay. The Beavers and Joseph condition for velocity slip at the surface of a porous medium. In B. Straughan, R. Greve, H. Ehrentraut, and Y. Wang, editors, *Continuum Mechanics and Applications in Geophysics and the Environment*, pages 126–139. Springer, 2001.

[69] D. E. Moulton and J. Lega. Effect of disjoining pressure in a thin film equation with non-uniform forcing. *Euro. J. Appl. Math.*, 24:887–920, 2013.

[70] T. G. Myers, H. X. Liang, and B. Wetton. The stability and flow of a rivulet driven by interfacial shear and gravity. *Int. J. Non-linear Mech.*, 39:1239–1249, 2004.

[71] T. Nakagawa. Rivulet meanders on a smooth hydrophobic surface. *Int. J. Multiphase Flow*, 18:455–463, 1992.

[72] T. Nakagawa and J. C. Scott. Stream meanders on a smooth hydrophobic surface. *J. Fluid Mech.*, 149:89–99, 1984.

[73] C. Neto, D. R. Evans, E. Bonaccurso, H.-J. Butt, and V. S. Craig. Boundary slip in Newtonian liquids: A review of experimental studies. *Rep. Prog. Phys.*, 68:2859–2897, 2005.

[74] J. M. P. Nicholson, H. Power, O. Tammisola, S. Hibberd, and E. D. Kay. Fluid dynamics of the slip boundary condition for isothermal rimming flow with moderate inertial effects. *Phys. Fluids*, 31:033602, 2019.

[75] R. W. D. Nickalls. A new approach to solving the cubic: Cardan's solution revealed. *Math. Gaz.*, 77:354–359, 1993.

[76] K. Nong and D. M. Anderson. Thin film evolution over a thin porous layer: Modeling a tear film on a contact lens. *SIAM J. Appl. Math.*, 70:2771–2795, 2010.

[77] J. A. Ochoa-Tapia and S. Whitaker. Momentum transfer at the boundary between a porous medium and a homogeneous fluid-I. Theoretical development. *Int. J. Heat Mass Transfer*, 38:2635–2646, 1995.

[78] T. Ondarcuhu and J. P. Aimé. *Nanoscale Liquid Interfaces: Wetting, Patterning and Force Microscopy at the Molecular Scale.* Jenny Stanford Publishing, 2013.

[79] A. Oron and S. G. Bankoff. Dewetting of a heated surface by an evaporating liquid film under conjoining/disjoining pressures. *J. Coll. Interf. Sci.*, 218:152–166, 1999.

[80] J. Ou, B. Perot, and J. P. Rothstein. Laminar drag reduction in microchannels using ultrahydrophobic surfaces. *Phys. Fluids*, 16:4635–4643, 2004.

[81] K.-C. Park, S. S. Chhatre, S. Srinivasan, R. E. Cohen, and G. H. McKinley. Optimal design of permeable fiber network structures for fog harvesting. *Langmuir*, 29:13269–13277, 2013.

[82] J. P. Pascal. Linear stability of fluid flow down a porous inclined plane. *J. Phys. D: Appl. Phys.*, 32:417–422, 1999.

[83] C. Paterson, S. K. Wilson, and B. R. Duffy. Pinning, de-pinning and re-pinning of a slowly varying rivulet. *Euro. J. Mech. B/Fluids*, 41:94–108, 2013.

[84] C. Paterson, S. K. Wilson, and B. R. Duffy. Rivulet flow round a horizontal cylinder subject to a uniform surface shear stress. *Quart. J. Mech. Appl. Math.*, 67:567–597, 2014.

[85] C. A. Perazzo and J. Gratton. Navier–Stokes solutions for parallel flow in rivulets on an inclined plane. *J. Fluid Mech.*, 507:367–379, 2004.

[86] L. M. Pismen. Mesoscopic hydrodynamics of contact line motion. *Coll. Surf. A*, 206:11–30, 2002.

[87] S. R. Quake and A. Scherer. From micro- to nanofabrication with soft materials. *Science*, 290:1536–1540, 2000.

[88] G. Z. Ramon, H. E. Huppert, J. R. Lister, and H. A. Stone. On the hydrodynamic interaction between a particle and a permeable surface. *Phys. Fluids*, 25:073103, 2013.

[89] J. P. Rothstein. Slip on superhydrophobic surfaces. *Annu. Rev. Fluid Mech.*, 42: 89–109, 2010.

[90] B. P. Rynne and M. A. Youngson. *Linear Functional Analysis*. Springer, 2008.

[91] I. M. R. Sadiq and R. Usha. Thin Newtonian film flow down a porous inclined plane: Stability analysis. *Phys. Fluids*, 20:022105, 2008.

[92] I. M. R. Sadiq, R. Usha, and S. W. Joo. Instabilities in a liquid film flow over an inclined heated porous substrate. *Chem. Eng. Sci.*, 65:4443–4459, 2010.

[93] P. G. Saffman. On the boundary condition at the surface of a porous medium. *Stud. Appl. Math.*, 50:93–101, 1971.

[94] D. Schäffel, K. Koynov, D. Vollmer, H.-J. Butt, and C. Schönecker. Local flow field and slip length of superhydrophobic surfaces. *Phys. Rev. Lett.*, 116:134501, 2016.

[95] P. Schmuki and M. Laso. On the stability of rivulet flow. *J. Fluid Mech.*, 215: 125–143, 1990.

[96] L. W. Schwartz and R. R. Eley. Simulation of droplet motion on low-energy and heterogeneous surfaces. *J. Coll. Interf. Sci.*, 202:173–188, 1998.

[97] A. Sehgal, V. Ferreiro, J. F. Douglas, E. J. Amis, and A. Karim. Pattern-directed dewetting of ultrathin polymer films. *Langmuir*, 18:7041–7048, 2002.

[98] R. Shamey and X. Zhao. *Modelling, Simulation and Control of the Dyeing Process*. Woodhead Publishing Series in Textiles. Woodhead Publishing, 2014.

[99] A. Sharma, R. Konnur, and K. Kargupta. Thin liquid films on chemically heterogeneous substrates: Self-organization, dynamics and patterns in systems displaying a secondary minimum. *Physica A*, 318:262–278, 2003.

[100] R. K. Singh, J. E. Galvin, and X. Sun. Three-dimensional simulation of rivulet and film flows over an inclined plate: Effects of solvent properties and contact angle. *Chem. Eng. Sci.*, 142:244–257, 2016.

[101] R. K. Singh, J. E. Galvin, G. A. Whyatt, and X. Sun. Breakup of a liquid rivulet falling over an inclined plate: Identification of a critical Weber number. *Phys. Fluids*, 29:052101, 2017.

[102] T. Sochi. Slip at fluid-solid interface. *Polym. Rev.*, 51:309–340, 2011.

[103] J. M. Sullivan, S. K. Wilson, and B. R. Duffy. A thin rivulet of perfectly wetting fluid subject to a longitudinal surface shear stress. *Quart. J. Mech. Appl. Math.*, 61:25–61, 2008.

[104] A. J. Tanasijczuk, C. A. Perazzo, and J. Gratton. Navier–Stokes solutions for steady parallel-sided pendent rivulets. *Euro. J. Mech. B/Fluids*, 29:465–471, 2010.

[105] U. Thiele, L. Brusch, M. Bestehorn, and M. Bär. Modelling thin-film dewetting on structured substrates and templates: Bifurcation analysis and numerical simulations. *Euro. Phys. J. E*, 11:255–271, 2003.

[106] U. Thiele, B. Goyeau, and M. G. Velarde. Stability analysis of thin film flow along a heated porous wall. *Phys. Fluids*, 21:014103, 2009.

[107] K.-K. Tio and S. S. Sadhal. Boundary conditions for Stokes flows near a porous membrane. *Appl. Sci. Res.*, 52:1–20, 1994.

[108] G. D. Towell and L. B. Rothfeld. Hydrodynamics of rivulet flow. *AIChE J.*, 12: 972–980, 1966.

[109] E. C. Tredenick, T. W. Farrell, W. A. Forster, and S. T. P. Psaltis. Nonlinear porous diffusion modeling of hydrophilic ionic agrochemicals in astomatous plant cuticle aqueous pores: A mechanistic approach. *Front. Plant Sci.*, 8:746, 2017.

[110] D. Tribe. URL: https://theconversation.com/no-need-to-get-browned-off-edible-films-keep-fruit-fresh-18150. Accessed 12th September 2021.

[111] D. Truog. URL: http://www.davidtruog.com/photo/2018oct25a. Accessed 25th October 2018.

[112] A. Vanderbauwhede. Symmetry and bifurcation from multiple eigenvalues. In W. N. Everitt and B. D. Sleeman, editors, *Ordinary and Partial Differential Equations*, pages 356–365. Springer, 1981.

[113] D. C. Venerus. Squeeze flows in liquid films bound by porous disks. *J. Fluid Mech.*, 855:860–881, 2018.

[114] D. Wang, Y. Song, J. Tian, E. Shiju, and G. Haidak. Research on the fluid film lubrication between the piston-cylinder interface. *AIP Adv.*, 8:105330, 2018.

[115] W. Wang, C. Du, C. Wang, M. Hirtz, L. Li, J. Hao, Q. Wu, R. Lu, N. Lu, Y. Wang, H. Fuchs, and L. Chi. High-resolution triple-color patterns based on the liquid behavior of organic molecules. *Small*, 7:1403–1406, 2011.

[116] S. J. Weinstein and K. J. Ruschak. Coating flows. *Annu. Rev. Fluid Mech.*, 36: 29–53, 2004.

[117] G. S. White, C. J. W. Breward, P. D. Howell, and R. J. S. Young. A model for the screen-printing of Newtonian fluids. *J. Eng. Math.*, 54:49–70, 2006.

[118] S. D. R. Wilson and S. L. Burgess. The steady, spreading flow of a rivulet of mud. *J. Non-Newt. Fluid Mech.*, 79:77–85, 1998.

[119] S. K. Wilson and B. R. Duffy. On the gravity-driven draining of a rivulet of viscous fluid down a slowly varying substrate with variation transverse to the direction of flow. *Phys. Fluids*, 10:13–22, 1998.

[120] S. K. Wilson and B. R. Duffy. A rivulet of perfectly wetting fluid draining steadily down a slowly varying substrate. *IMA J. Appl. Math.*, 70:293–322, 2005.

[121] S. K. Wilson and B. R. Duffy. Unidirectional flow of a thin rivulet on a vertical substrate subject to a prescribed uniform shear stress at its free surface. *Phys. Fluids*, 17:108105, 2005.

[122] S. K. Wilson, J. M. Sullivan, and B. R. Duffy. The energetics of the breakup of a sheet and of a rivulet on a vertical substrate in the presence of a uniform surface shear stress. *J. Fluid Mech.*, 674:281–306, 2011.

[123] H. Wu and S. Zheng. Global attractor for the 1-D thin film equation. *Asympt. Anal.*, 51:101–111, 2007.

[124] W. Xin, M. Yonggang, Z. Xiangjun, and W. Shizhu. Experimental research on boundary slip of confined liquids at micro/nano scale and effect of shear rate and viscosity. In J. Luo, Y. Meng, T. Shao, and Q. Zhao, editors, *Advanced Tribology*, pages 542–543. Springer, 2009.

[125] D. Yang and D. Ma. Development of organic semiconductor photodetectors: From mechanism to applications. *Adv. Optical Mater.*, 7:1800522, 2019.

[126] H. Zhang, J. Yue, G. Chen, and Q. Yuan. Flow pattern and break-up of liquid film in single-channel falling film microreactors. *Chem. Eng. J.*, 163:126–132, 2010.

[127] Y. Zhu and S. Granick. Rate-dependent slip of Newtonian liquid at smooth surfaces. *Phys. Rev. Lett.*, 87:096105, 2001.